# Image Quality in MAP SPECT Reconstructions

A Dissertation Presented

by

Santosh Kulkarni

to

The Graduate School

in Partial Fulfillment of the Requirements

for the Degree of

Doctor of Philosophy

in

Electrical Engineering

Stony Brook University

August 2009

Stony Brook University

The Graduate School

Santosh Kulkarni

We, the dissertation committee for the above candidate for the
Doctor of Philosophy degree, hereby recommend
acceptance of this dissertation.

Dr. Gene R. Gindi
Advisor
Associate Professor of Electrical & Computer Engineering and Radiology

Dr. Petar Djuric
Chairperson of the Defense
Professor of Electrical & Computer Engineering

Dr. Muralidhara SubbaRao
Professor of Electrical & Computer Engineering

Dr. Klaus Mueller
Associate Professor of Computer Science

This dissertation is accepted by the Graduate School.

Lawrence Martin
Dean of the Graduate School

# Abstract of the Dissertation

# Image Quality in MAP SPECT Reconstructions

by

Santosh Kulkarni

Doctor of Philosophy

in

Electrical Engineering

Stony Brook University

2009

SPECT (Single Photon Emission Tomography) is a noninvasive nuclear medical imaging modality commonly used in the clinic for diagnosis of disease. It is a tomographic modality that displays two-dimensional slices of the three-dimensional spatial distribution of injected radiopharmaceutical within the patient body. The radionuclide in the radiopharmaceutical emits gamma-ray photons that can pass through the body and get detected by a position-sensitive detector. The photons emitted from the radionuclide have a Poisson noise characteristic leading to noisy collected data. Limitations on patient dose mean that few photons are collected and so this photon noise is significant. In addition, the anatomical variability and variations in radiotracer uptake within the bodily anatomical structures is itself a form of noise,"object variability", akin to clutter in radar imaging. A tomographic statistical Bayesian reconstruction algorithm is used to estimate the patient image. The reconstruction algorithm must incorporate

an accurate forward model of the imaging system. An inaccurate model results a third type of noise,"model error". All three noise mechanisms propagate into the reconstruction.

In medical imaging "image quality" is assessed by how well information about a task of interest can be obtained from a given image. In my work, the medically relevant task is that of detection of a signal in a noisy background. The signal could be a local increase in radiotracer uptake, for example, indicating the presence of a tumor or other lesion.

My goal in this thesis is to analyze the effects of the three noise sources on detection task performance when the signal is deterministic i.e. its form and location are known. We focus on the use of mathematical model observers that emulate human performance (such as the Channelized Hotelling Observer CHO) in a binary detection task, where the signal is deemed either present or absent. We analyze the CHO and compare it to human performance in an experiment to investigate the optimal (in the sense of maximizing image quality) smoothing in a SPECT MAP (maximum *a posteriori*) reconstruction. We also observe that in the presence of object variability, CHO and human performance correlate well. We also address another concern regarding the efficacy of a Bayesian reconstruction incorporating an anatomical prior for lesion detection. The anatomical prior uses information regarding the different radiotracer uptake in different organs. Using the CHO we investigate whether this prior information leads to improved detection performance when the only noise source in the data is photon noise. Our results showed no difference in lesion detectability with and without the anatomical information. Finally, we mathematically investigate model error that accounts for noise due to

scattered photons in SPECT. We develop theoretical expressions to rapidly compute certain measures of image quality, the reconstructed mean, covariance, and local point-spread function, for SPECT MAP reconstructions. We conclude that this model error adds variance to the reconstructed image above and beyond that due to photon noise.

These investigations are useful in potentially comparing and optimizing both imaging hardware and reconstruction algorithms to achieve better task performance. Even incremental gains in task performance can lead to more favorable diagnostic outcomes for many patients.

**To my father and in the memory of my mother**

# Contents

## List of Acronyms

| | |
|---|---|
| **2AFC** | Two-Alternative-Forced-Choice |
| **2D** | Two-Dimensional |
| **3D** | Three-Dimensional |
| **ART** | Algebraic Reconstruction Technique |
| **AUC** | Area Under the ROC curve |
| *AUC* | Area Under the ROC curve |
| **BKE** | Background-Known-Exactly |
| **BKS** | Background-Known-Statistically |
| **BP** | Backprojection |
| **BSREM** | Block Sequential Regularized Expectation Maximization |
| **CHO** | Channelized Hotelling |
| **CHO** | Channelized Hotelling |
| **CNPW** | Channelized Non-prewhitening |
| **CNR** | Contrast-to-Noise Ratio |
| **COR** | Center Of Rotation |
| **COSEM** | Complete-data Ordered Subset Expectation Maximization |
| **CT** | Computed Tomography |
| **CZT** | Cadmium Zinc Telluride |
| **DFT** | Discrete Fourier Transform |
| **ECD** | Ethyl Cysteinate Dimer |
| **ECT** | Emission Computed Tomography |

| | |
|---|---|
| **EM** | Expectation-Maximization |
| **ET** | Emission Tomography |
| **FBP** | Filtered Back-Projection |
| **FDG** | Fluoro-deoxy-glucose |
| **FFT** | Fast Fourier Transform |
| **FOM** | Figure Of Merit |
| **FPF** | False Positive Fraction |
| **keV** | kilo electron Volts |
| **HEAP** | High-energy All-purpose |
| **HMPAO** | Hexamethylpropyleneamine Oxime |
| **HO** | Hotelling |
| **IQ** | Image Quality |
| **IQM** | Image Quality Metric |
| **LEAP** | Low-energy All-purpose |
| **LEHR** | Low-energy High-resolution |
| **LPSF** | Local Point Spread Function |
| **LRT** | Likelihood Ratio Test |
| **MAP** | Maximum *A Posteriori* |
| **MC** | Monte Carlo |
| **MDP** | Methylene Diphosphonate |
| **MEAP** | Medium-energy All-purpose |
| **ML** | Maximum Likelihood |
| **MMSE** | Minimum Mean Square Error |
| **MRI** | Magnetic Resonance Imaging |
| **MVG** | Multivariate Gaussian |
| **NED** | Normalized Energy Distance |

| | |
|---|---|
| **NPW** | Non-prewhitening |
| **OS** | Ordered Subsets |
| **OSEM** | Ordered Subsets EM |
| **PCG** | Preconditioned Conjugate Gradient |
| **PET** | Positron Emission Tomography |
| **PHA** | Pulse Height Analyzer |
| **PMT** | Photo-Multiplier Tube |
| **ROC** | Receiver Operating Characteristic |
| **ROI** | Region of Interest |
| **SART** | Simultaneous Algebraic Reconstruction Technique |
| **SC** | Scatter Correction |
| **SIMSET** | Simulation Software for Emission Tomography |
| **SKE** | Signal-known-exactly |
| **SKS** | Signal-Known-Statistically |
| **SNR** | Signal-to-Noise Ratio |
| **SPR** | Scatter-to-Primary Ratio |
| **SPECT** | Single-Photon Emission Computed Tomography |
| **TEW** | Triple Energy Window |
| **TNF** | True Negative Fraction |
| **TPF** | True Positive Fraction |
| **WSC** | Window-based Scatter Correction |

# List of Figures

## Acknowledgments

First, I would like to thank my dissertation adviser, Gene Gindi, for his guidance and encouragement in all my dissertation work. This dissertation truly would not have been possible without his effort. I would also like to thank the rest of my dissertation committee - Petar M. Djuric, Murali Subbarao, and Klaus Mueller - for their precious time and valuable suggestions.

I would also like to acknowledge support for this work by the National Institute of Health (NIH) via grant NIH-NIBIB R01EB02629.

All the members of the Medical Imaging Processing Laboratory at Stony Brook University contributed in many ways to this dissertation: Parmeshwar Khurd for introducing me to the various software packages and for the helpful, profound and inspiring discussions on concepts, ideas, and mathematical techniques; Ing-Tsung Hsiao for helpful discussions and literature survey on anatomical priors; Lili Zhou for helpful discussions; Yuxiang Xing for the initial introduction to a few software packages; Jorge Oldan for conducting 2AFC tests; Chintu Pandya for technical support. I am thankful to those who volunteered as subjects for the human observer studies: Lili Zhou, Jorge Oldan, Parmeshwar Khurd, Jennifer Segui and Gene Gindi. I highly appreciate their contributions to this work. I would like to thank the University of Arizona Center for Gamma Ray Imaging for their technical assistance and 2AFC software.

I would like to thank Chintu Pandya, Parmeshwar Khurd, Bhaskar Mukherjee, Abhishek Datta, Prasad Kerkar and Baljit Singh for making my daily life in Stony Brook interesting and enjoyable.

Finally, I would like to thank my father Pramod Kulkarni for his support and encouragement in all my educational endeavors. I also deeply thank my sisters, cousins, uncles and aunts for their emotional support and accompanying my father while I was pursuing my Ph.D. degree at Stony Brook.

# Chapter 1

# Introduction and Background

Nuclear Medical Imaging is a non-invasive modality of medical imaging for producing a 3D spatial distribution of emitting radio-pharmaceutical in the human body [1]. The 3D spatial distribution is viewed by a radiologist to glean useful diagnostic information. A radiopharmaceutical labeled with a radionuclide, e.g $^{99m}$Tc-sestamibi, is administered to the patient to tag a specific biochemical function with regards to a specific target organ [2]. Depending on the its bio-kinetic properties, the radiotracer distributes within the body to give the functional state of the target organ [3]. Two important emission tomographic (ET) imaging modalities are SPECT (Single Photon Emission Computed Tomography) [4] and PET (Positron Emission Tomography) [5]. In this dissertation, we will focus on SPECT.

Here, we give a brief introduction to the SPECT imaging process. This will be revisited in greater detail in later chapters. The radionuclide atom of the pharmaceutical emits photons [6] having sufficient energy to penetrate tissue and escape from the human body in significant numbers. The number of photons emanating from a certain region within the body reflects the spatial distribution information of radiopharmaceutical within the patient. Out of all the photons that make their way out of the body only those photons traveling in a specific direction hit a detector, an Anger camera [7], that has a large NaI (thallium-doped sodium iodide) crystal preceding an array of photomultiplier tubes (PMTs). This direction specific detection is made possible by a collimator which is a thick sheet of heavy metal (like lead) perforated like a honeycomb by long thin channels. The collimator does this by absorbing gamma photons traveling in directions other than those specified by the collimator. When a photon hits and interacts with the NaI crystal it ionizes the atoms withing the crystal causing an optical scintillation event. Light from this scintillation is detected by the array of PMTs and an electronic circuit estimates the location of interaction of the incident photon within the crystal by evaluating the signals from the PMTs. A histogram of the incident photons binned with respect to their estimated position on the face of the Anger camera constitutes a single two-dimensional planar image known as a projection [2]. It is a projection in the sense that it is a 2-D line integral of the 3-D object. This 2D image indirectly portrays the *in vivo* distribution of the radiopharmaceutical within the body. Several such 2D projections evaluated at different positions of the camera face form the data used in emission tomography. In emission tomography a 3D map of the radiopharmaceutical density within the body is digitally reconstructed from these multiple views. A 2D image of a slice extracted from this reconstructed 3D radiotracer distribution is then made available for the physician's perusal.

Nuclear imaging has the ability to image qualitatively and quantitatively dynamic physiological process of the body [3]. This ability is important because anatomical or morphological changes due to pathological conditions are often preceded by physiological or biochemical alterations. It makes possible the study of various biological functions such as blood flow and metabolism. It has has become an important tool in the clinic over the last several decades. Another part of its overall attraction is that it enables the study of dynamic body functions without trauma to the subject.

SPECT is a form of imaging in which one uses a radionuclide which emits a single gamma photon. The radiopharmaceutical is administered usually by injection or sometimes by inhalation [8]. The Anger camera detects and records gamma ray positions emitted by the radiopharmaceutical as a product of radioactive decay. There are two forms of single-photon emission imaging: planar and tomographic. SPECT is tomographic imaging with single-photons. A planar image depicts a single projection of a radiotracer distribution in a subject; a tomographic image is a slice from a volume of reconstructed radiotracer distribution computed from multiple 2D planar images acquired from multiple camera positions. The radiopharmaceuticals used in SPECT are labeled with radionuclides, i.e. atoms that emit gamma($\gamma$) rays. One of the most important radionuclides used in SPECT imaging is Technetium-99m or $^{99m}$Tc which emits 140Kev gamma photons with a half life of 6.03 hours [8]. The half life is the time in which the nuclei of one-half of a given population of atoms undergo radioactive decay. Thallium-201 or $^{201}$TI is another radionuclide used in SPECT which emits photons with 70Kev photons and whose half life is 73 hours [8].

## 1.1 Basics of Image Formation in SPECT and Planar Imaging

### 1.1.1 Planar Imaging

We first describe conventional planar imaging. In planar imaging the 3D distribution of radiopharmaceutical within the subject's body is imaged onto a planar surface producing a 2D projection image. The introduction of the scintillation camera by Hal Anger [7] was the driving force for planar imaging which later led to the SPECT modality. This camera uses a large NaI (Tl) crystal (typically 40cm in diameter) [1] coupled to an array of PMT's to record the position and energy of a incident gamma photons. Figure 1.1 illustrates the schematic structure of an Anger camera.

The gamma photons emitted by the internally distributed radionuclide penetrate through the patient's body. While traversing through the body the photons can interact with the intervening tissue. The photons undergo two effects, photoelectric absorption and Compton scattering, which will be discussed in the next chapter. It is

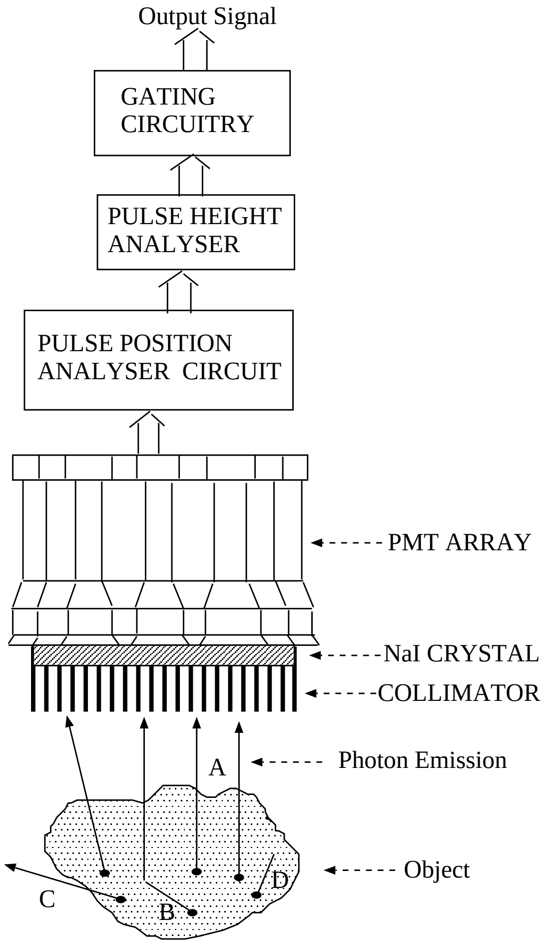

Figure 1.1: Basic components of an Anger camera.

those photons that do not interact and pass through the body that are used to obtain the image.

The directionally isotropic emission of gamma photons from within the body and the fact that gamma rays cannot be focused by lenses or electromagnetic field necessitates the use of collimators to confine the direction of the incident photons reaching the scintillation camera and thereby to localize the site of the emitting source. The collimator is usually made out of a perforated plate of heavy metal having high atomic number like lead or tungsten which can absorb the photons. If the apertures of the

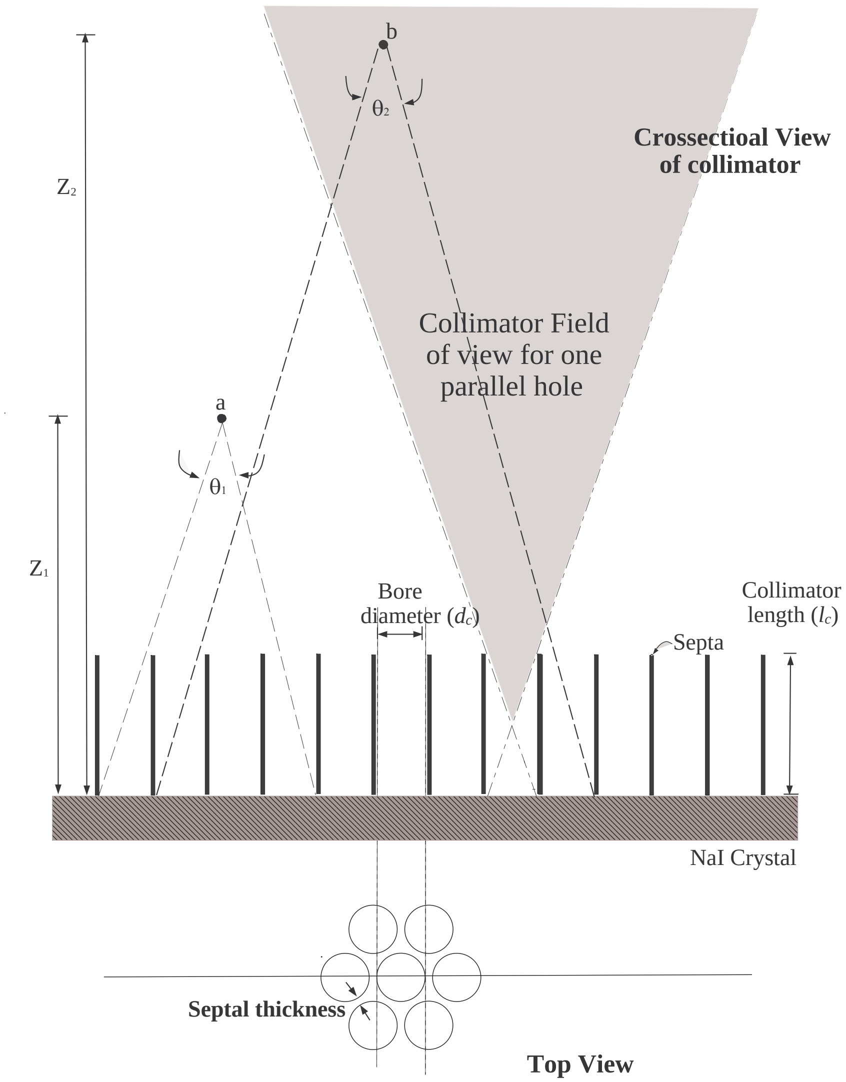

Figure 1.2: Basics of a parallel-hole collimator geometry: The hexagonal array in the bottom part of the figure is the top view of a few bores of a typical collimator. A cross-sectional view through the center of the hexagonal array is shown in the top part of the figure. The figure is not to scale relative to a clinically used collimator. The photons emitted from point 'a' spread over a smaller area of the crystal as compared to photons emitted from point 'b'. The acceptable angle of photon rays are limited by the collimator ($\theta_1$ for point 'a' and $\theta_2$ for point 'b'). The shaded area illustrates the field of view for one bore. To a good approximation, only photons emitted from locations within this field of view can be detected by the corresponding bore.

collimator are all parallel to each other, then the collimator is called a parallel hole collimator as shown in the Figure 1.2. For a parallel-hole collimator, incident photons are confined to directions approximately perpendicular to the collimator face. Incident rays approximately normal to the collimator reach the detector, while other photons will hit the collimator vanes or septa. The figure also gives the various parameters of the collimator such as collimator length ($l_c$), bore diameter ($d_c$), and septal thickness. A given bore will allow only those photons whose direction vectors lie in its field of view to hit the detector. The acceptance angle a function of the bore diameter and bore length is the parameter that describes the field of view subtended by the bore. Although most collimators have parallel holes, some collimators have hole patterns that converge or diverge [8, 9]. Depending upon the radionuclide being imaged and the desired sensitivity/resolution trade-off (this tradeoff is discussed in more detail in Chapter 2), a variety of lead parallel-hole collimators are commonly used in conjunction with the Anger gamma camera in the clinic: LEHR (low-energy, high-resolution), LEAP (low-energy, all-purpose), MEAP (medium-energy, all-purpose) and HEAP (high-energy, all-purpose) [8].

The collimated photon hits the NaI (thallium doped sodium iodide) crystal and deposits some energy by ionizing the atoms within the crystal at the point of incidence. The deposited energy is converted to a visible light photons. The image of a scintillation event at the exit face of the crystal is not a tiny bright dot but rather is a broadly spread region of light, with the brightest part of the region coinciding roughly with the location at which the gamma photon interacted with the crystal. The intensity of the visible light flash created by the scintillation event is proportional to the energy of the incident photon. This scintillation light is guided towards the photocathode of the PMT's coupled to the crystal.

The PMT consists of a photocathode, an anode and around 10 dynodes. The photocathode absorbs the flash of light impinging on it and emits photoelectrons. The number of electrons generated from the photocathode are proportional to the intensity of light impinging on it. The dynodes are coated with material that emits secondary electrons when struck by another electron. Electrons are multiplied at each dynode resulting in a burst of millions electrons at the output of the PMT. The output of each the PMT is proportional to the amount of light impinging on it. The output of the PMT's is amplified by the preamplifier circuit. The current pulses from the various PMT's is given to an analog or digital pulse-position analysis circuit to estimate the position of the scintillation event. This is then discretized to give a quantized position on the camera face. Such a quantized position on the camera face is known as "bin".

The current pulses from the PMT's are combined to give a net signal proportional to the total energy deposited in the crystal by the scintillation event. The height of the combined pulses gives an estimate of energy of the detected photon. There is an uncertainty in the estimate of energy of detected photon due to the uncertainty in the pulse heights from the PMT's and preamplifier. This uncertainty is responsible for the energy resolution of the camera. Thus for a typical camera, a pencil beam of 140KeV photons will produce energies $140 \pm 14$ KeV. The uncertainty in the combined pulse height is because of the following [8, 3] reasons: (1) uncertainty in the number of optical photons produced during a scintillation-event within the crystal (2) losses of light intensity during crystal transmission (3) fluctuations in number of photoelectrons released from the photocathode of the PMT (4) variations in the electron multiplication factors at the dynodes of the PMT and (5) imperfections in the linearity of the preamplifier. A pulse height analyzer (PHA) specifies an energy window so that only pulses within this window are accepted for counting. Thus only events within the range (corresponding to uncertainty in the energy estimation procedure) of known radionuclide energy result in a unit increment of a memory location specific to the quantized location of each of those events. The array of resulting counts, displayed as a 2D image, is known as projection or planar image.

### 1.1.2 Planar Imaging versus Tomography

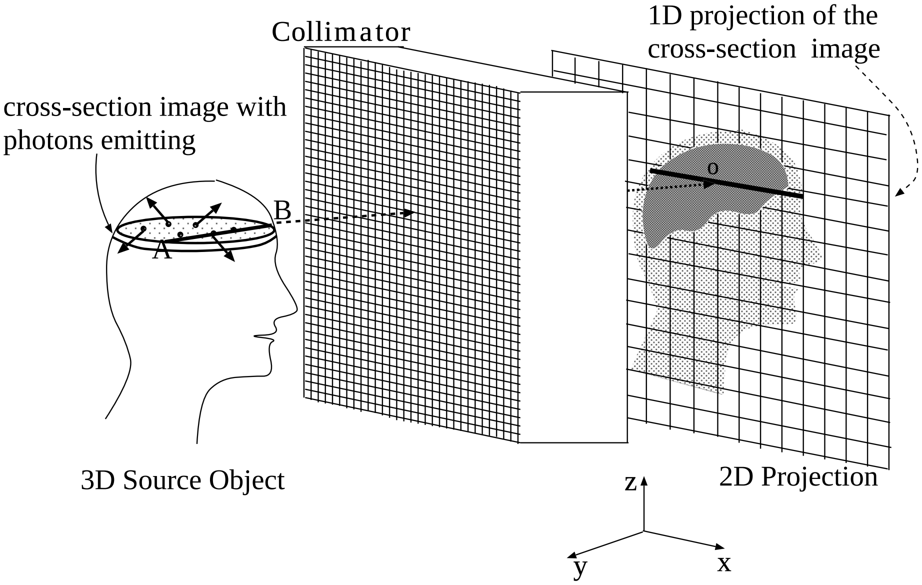

Figure 1.3: A 2D projection from a 3D object. The line AB on a cross-section (slice) is pictured to be a projection at point "o". A slice perpendicular to detector plane forms an image along one line (1D projection profile). Stacking 1D projections of slices together forms a 2D projection of a 3D object.

Figure 1.3 schematically shows the 2D projection image of a 3D radionuclide distribution within the body. The photons emitted get collimated and only those whose direction is nearly perpendicular to the detector get accepted. From the Figure 1.3 we can see that any photon moving in the direction of line segment AB will be recorded. Also all the photons that are emitted by the radionuclide along segment AB will be recorded at the point 'O'. Consequently all the photons emitted from the 2D cross-section containing AB and moving along the direction of AB will be summed and recorded as a 1D projection on the camera face. Following the same principle, a stack of 2D cross sections stacked along the $z$-axis and perpendicular to the camera face will be imaged as a stack of 1D projections on the camera face. Hence an entire 3D radiotracer density will project onto the camera face as a 2D projection image.

Since every point on the 2D projection image accumulates the radioactivity along an approximate normal at that point on the detector, any information of depth through the 3D radiotracer distribution is lost. Hence the underlying and overlying structures in a 3D

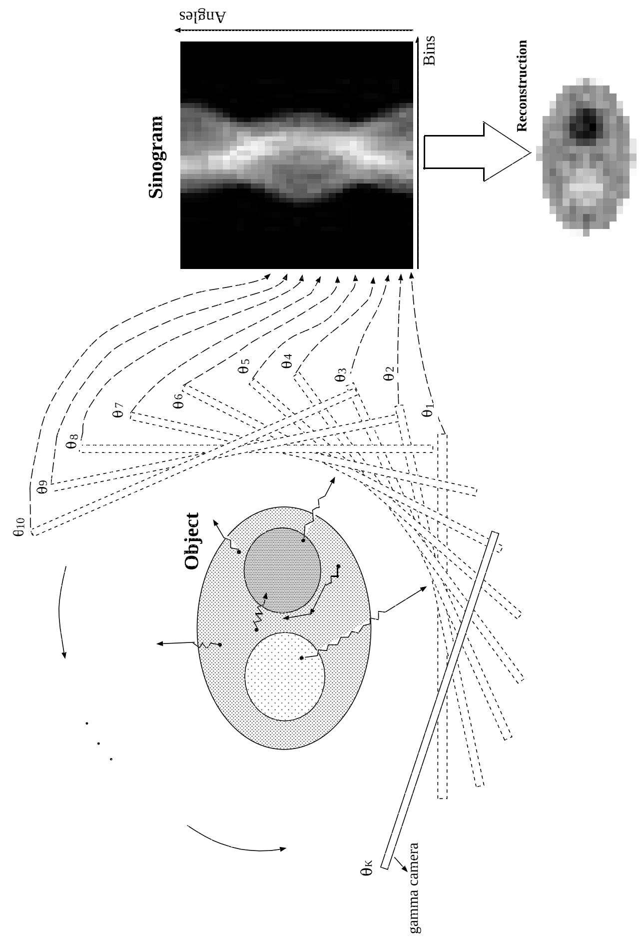

Figure 1.4: The basic principle of SPECT. A gamma camera rotates around the object and acquires many projection views at equidistant angles. These projection views together form a sinogram from which the object is mathematically reconstructed by a reconstruction algorithm.

object are overlapped in a 2D planar image. As in other tomographic modalities such as CT, we sense line integrals of the object, not the object itself. This overlap makes the image difficult to interpret.

The aim of SPECT is to provide a 3D distribution of gamma emitting radionuclide instead of a 2D projection image as in planar imaging. In tomography, one acquires projection views at many angles all around the object [10]. By combining these projection views mathematically, the 3D structure of the object can be obtained from its many 2D projections, or, a 2D structure from many 1D projections. The camera is rotated around the patient to get 2D planar images (projections) at various angles. In SPECT, a gamma camera is designed to rotate up to $360^o$ around the patient stopping at equidistant angular samples to collect and record gamma photons. The total time needed to complete the data acquisition for one patient is the number of stops times the accumulation time per stop. Typical study time is around 20 minutes for brain imaging and also bone imaging [8] and 20-30 minutes for ventilation and perfusion studies [8]. Once the projection data are acquired and stored, a computer system will process the data to reconstruct the original radioactivity distribution of the object.

Figure 1.4 illustrates the basic principle of operation of a 2D SPECT system, i.e., only one cross-section of an object is studied. The 1D camera is shown at many angular positions $\theta_k$. A 1D projection is measured at each position $\theta_k$. As shown in Figure 1.4, initially, the camera is in position $\theta_1$, photons are collected to bins and the resulting projection profile fills in the first line of the projection data with 1 being its index for angle. Then, the camera is rotated to the next position $\theta_2$. Its projection profile is placed next to the line from $\theta_1$, i.e., fills in the second line of the projection data with angle index 2. Then, camera goes to $\theta_3$ for the third line of the projection data. Extending this, the camera covers the full $360^o$(sometimes $180^o$) of the orbit, i.e.

completes the collection of photons at $K$ sampling angles in total as shown in Figure 1.4. All of these projection profiles are thus sequentially stacked to a 2D image with the abscissa being the digitized detector coordinate “bin” and the ordinate being the index of the sample angle. This 2D digital image is referred to as the “sinogram”.

A typical “sinogram” is shown in Figure 1.4. We can see that the sinogram is itself not visually interpretable by a radiologist. Therefore, before serving a diagnostic purpose, another step needs to be performed. This step is called reconstruction. A reconstruction algorithm attempts to transform a sinogram to a meaningful image of the original radioactivity distribution in its original coordinate frame. The digitized sinogram data is fed to a computer system on which the reconstruction algorithm is executed. The reconstructed digital images are what we present to physicians for diagnostic or therapeutic purposes. The upper right image in Figure 1.4 shows a the reconstruction of the data in the upper left sinogram in Figure 1.4.

## 1.2 Applications of SPECT

SPECT has been used in bone imaging [11, 12, 13, 14], clinical evaluation of cardiac disease [15, 16, 17, 18], brain perfusion studies [19] and in other clinical applications. Both $^{201}$Tl and $^{99m}$Tc labeled pharmaceuticals are used for SPECT myocardial perfusion imaging [8]. A common version of such studies involves the characterization of a patient’s heart with the patient at rest using $^{201}$Tl-TlCl and under stress using $^{99m}$Tc-sestamibi or tetrofosmin. Its is an invaluable aid for diagnosis and management of coronary artery disease (CAD).

Technetium-labeled methylene diphosphonate ( $^{99m}$Tc-MDP) is the tracer commonly used for bone imaging. It is used to detect focal uptake (localized uptake that is different in magnitude from uptake in neighboring bone) which may present an abnormality. If the focal uptake is greater that uptake in the neighboring bone, this may indicate arthritis, a fracture or metastasis. Focal uptake that is less than the neighboring bone may indicate necrotic tumor (due to accumulation of dead cells) or a sequela (consequence) of radiation therapy.

Technetium labeled hexamethylpropleneamine oxime (HMPAO) and $^{99m}$Tc-ECD (Ethyl Cysteinate Dimer) are most commonly used for brain SPECT scan for investigating clinical indications of cerebrovascular disease, dementia, or seizure. In [20], SPECT imaging was done for a renal region. SPECT has received wide interest for clinical applications and is a standard imaging procedure in all Radiology departments.

SPECT also serves as an important imaging technology for imaging molecular events for research in molecular biology [21]. The use of microSPECT to locate and characterize tumor cells with the intent to change these processes by gene manipulation in small animals is of interest [8]. The progress of a disease can be monitored and/or molecular changes due to gene expression can be detected. This information is particularly important in the area of gene therapy, where the imaging system can assess the success of tracer delivery and obtain accurate time curves of gene expression [22]. Such studies often use novel radiopharmaceuticals specially developed for *in vivo* imaging of the biomolecular event of interest at the cellular level [21]. Several high resolution small animal tomographic gamma-ray imaging systems have been developed in recent years based on scintillators [23, 24] and based on semiconductor arrays [22, 25].

## 1.3 Anatomical images: MRI and CT

Other imaging modalities like MRI (magnetic resonance imaging) and X-ray CT (Computed Tomography) have higher resolution than SPECT and PET. These modalities give anatomical information while SPECT provides functional information. (In certain cases MRI and CT can provide forms of functional information, but these

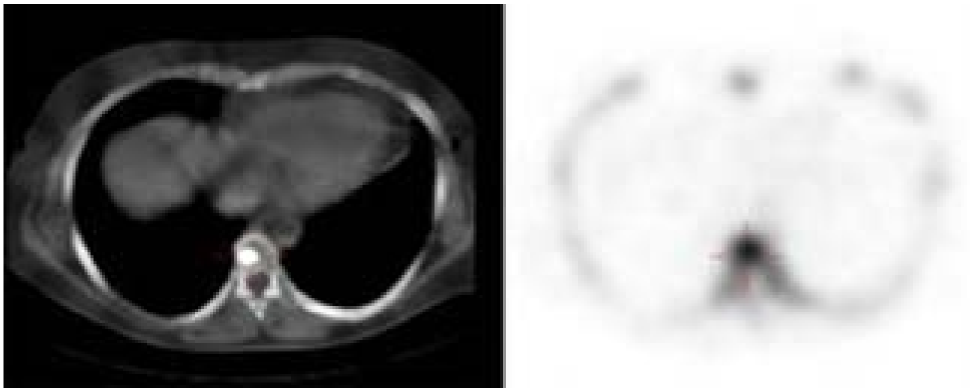

Figure 1.5: Traverse Thoracic image from CT and coresponding $^{99m}$Tc-FDP SPECT image showing increased Focal uptake in thoracic spine.

modalities are used primarily for anatomical information.) Magnetic resonance imaging (MRI) uses radio-frequency waves along with a strong magnetic field [26] and CT uses X-rays [2] to give high resolution anatomical images. The image of a reconstructed X-ray CT slice is the map of linear attenuation coefficients of the tissue within the corresponding slice in the body. As the X-ray beam passes through the body it gets attenuated by absorption and scattering processes. The degree of attenuation depends on the energy spectrum of the X-rays as well as on the average atomic number and mass density of the tissue its passing through. Since each tissue has different mass and average atomic number, X-ray CT results in a detailed anatomical map. CT is termed as “transmission tomography” since the X-ray source is external while SPECT is termed as “emission tomography” since the source of the radiation is inside the body. There is often high correlation between functional images (from SPECT or PET) and coregistered anatomical images (from MRI or CT) since function follows anatomy. Figure 1.5 showing anatomical detail of a slice through the thorax from CT and the focal uptake in the corresponding slice using SPECT image. Figure 1.6 shows slice through the parathyroid using (a) CT image and (b) SPECT image. The anatomical information can be used to improve emission reconstruction. We discuss the use of this information for image reconstruction in Chapter 6.

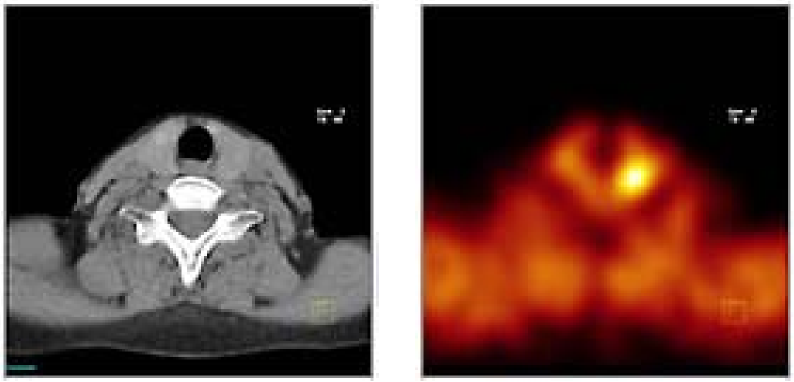

(a) (b)

Figure 1.6: (a) a CT slice showing anatomical detail in a traverse section through the parathyroid, and (b)a slice from a single-photon computed tomography (SPECT) image showing function. The bright spot is a benign tumor.

## 1.4 Tasks in Nuclear Imaging

As described in previous sections, a reconstructed image is the interface between a SPECT system and a physician. In order to improve the imaging system or reconstruction method or to compare imaging systems or reconstruction methods we need a way of measuring the amount of improvement. Most image reconstruction methods have one or two free parameters for tuning a given algorithm to a specific imaging problem. An imaging system has parameters such as collimator bore diameter and bore length that need to be optimally adjusted for a specific imaging problem. These parameters need to be tuned according to some criteria of image quality to get better images. In order to do so one must be able to quantify the image quality of images resulting from these imaging systems or reconstruction methods. This objective assessment of image quality must be task based. The image quality is measured on the basis of how well an imaging system or reconstruction method allows an observer to perform a specified task [27].

Tasks can be conveniently divided into estimation and classification. In estimation one seeks to accurately derive the value of some scalar parameter of interest e.g. a patient's cardiac ejection fraction (percentage of blood that's pumped out of a filled ventricle with each heartbeat) or quantitatively estimate the average tracer uptake in a particular organ or region of interest for the purpose of patient management, including staging and monitoring for effects of therapeutic intervention. Classification involves determining to which of two or more categories an image must belong. A detection task is a special case of a classification task in which one decides whether or not a signal is present. For a physician, the "signal" of interest might be a tumor or some type of lesion. Figure 1.7 shows examples of signal present and absent images of reconstructed slices of a digital test phantom. Another common form of "signal" is the absence of counts (a "cold spot") in an organ which has absorbed a certain amount of tracer. An example of cold spot would be in cardiac imaging and lung imaging, where the absence of radioactivity is a sign of impaired perfusion. Detection is not necessarily a binary decision problem. Instead of having just two hypothesis (absent/present) there can be $L+1$ hypothesis. The classifier has to decide whether the observed image contains a signal and if so which of $L$ signal classes the signal belongs. For example, the classes might represent $L$ different signals, all in same location or one signal in one of $L$ possible locations [28]. In this thesis, we will focus on binary detection tasks.

Image quality is based on performance of an observer with respect to the task. An observer is an entity which performs the task. For a detection task in a clinic the observer would be a physician. An observer could also be implemented as a mathematical operator. The familiar matched filter is a simple mathematical observer

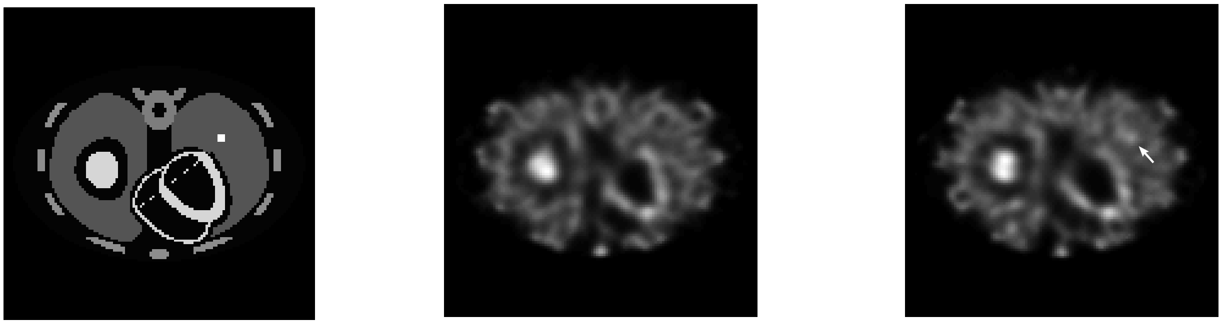

(a) (b) (c)

Figure 1.7: Anecdotal reconstruction of(a) a slice of a test object, (b) without lesion (c) with lesion (marked by arrow). The lesion was a 3 × 3 lesion of contrast 2:1 with the background.

for the case of detection of a known signal in uncorrelated Gaussian noise.

We would like to make the distinction between the imaging system and reconstruction algorithm. The imaging system delivers the raw projection data. The reconstruction algorithm transforms this data into an image for the physician to examine. To quantify image quality in an imaging system we need to measure the detection performance of an observer which works on the raw data and as argued in [29] the observer should be based on some optimal criterion. However, for a reconstruction algorithm, we need an observer that works on the reconstructed image and is based on the criteria which a human (physician) would apply while viewing the images. The best observer for this purpose is the human itself. We are restricting ourselves to the performance of observers for evaluating different reconstruction methods. But optimizing a reconstruction method based on the performance of humans is extremely time-consuming. Thus mathematical model observers that emulate human performance [27, 30] are extremely useful. In order to optimize or compare reconstruction algorithms a computable scalar figure of merit (FOM) for image quality is needed [31, 32, 33]. The uncertainty (noise) in the images as well as the observer performing the task play a vital role in calculating a FOM as a measure of performance. Thus a fast method that uses mathematical observers to theoretically predict the human observer performance is useful in rapidly culling the parameter search space for reconstruction optimization.

## 1.5 Overview of Dissertation

Chapter 2 explains the mathematical model of the SPECT imaging system. This is the forward projection model incorporating the physical effects of the SPECT system. In Chapter 3 we discuss the inverse problem of image reconstruction from projection data. Here we try to estimate the underlying source distribution from the measured noisy data using statistical methods. In Chapter 4 we describe the basics of a detection task and FOMs' of a few model observers. We discuss the noise characteristics of the reconstructed images obtained from projection data corrupted by a primary source of photon noise and theoretical methods to obtain them. In Chapter 5 we compared the performance of a human emulating model observer to that of human observers in order to determine an optimal smoothing parameter (controlling the noise/resolution trade-off) in SPECT reconstruction. In Chapter 6 we talk of how outside information made available by an anatomical scan can be incorporated into the image reconstruction. We give a theoretical method for evaluating expressions required for computing a detection FOM using model observers for studying the effect of the use of anatomical side information on a lesion detection task. It also has simulation details and results describing the efficacy of this anatomical prior information. In Chapter 7 we develop theoretical expressions to rapidly calculate certain measures of image quality, the reconstructed mean, covariance, and local point-spread function, for SPECT reconstructions. These expressions account for two sources of noise, (1) a model error along with (2) a primary source of photon noise. We also perform an elaborate simulation to validate our theoretical expressions with sample methods. In Chapter 8 we conclude this thesis with a discussion and some avenues for future work.

# Chapter 2

# SPECT Imaging Model

In this chapter we describe a mathematical model for the formation of projection data in SPECT. (Henceforth, we use the term "projection data" to mean the collection of planar images formed at different angular positions of the camera. For a simple 2D case, the sinogram in Figure 1.4 is an example of projection data.) This entails discussing the physics of the SPECT imaging system. It is important to have a mathematical forward model for the SPECT data to address the ensuing inverse problem of image reconstruction. The inverse problem of image reconstruction from the acquired SPECT data is dealt with in the next chapter.

## 2.1 Notational Conventions

Here we summarize notation. Lower-case (non-bold) letters are used to specify scalar variables and scalar valued functions. Vector and vector-valued functions are represented by lower-case bold letters. For example, $f_n, n = 0, 1, \cdots, N-1$ are the elements of a $N$-dimensional vector $\mathbf{f}$. Whether a vector or scalar is random or non-random will be made clear from context. A matrix is denoted by an upper-case letter and square brackets with appropriate subscripts is used to denote its element. For example, $[\mathcal{H}]_{mn}$ is the $mn^{th}$ element of a $M \times N$ matrix $\mathcal{H}$. The $m^{th}$ element of a matrix-vector product $\mathcal{H}\mathbf{f}$ is given by $[\mathcal{H}\mathbf{f}]_m$, where $[\mathcal{H}\mathbf{f}]_m = \sum_{n=0}^{N-1} [\mathcal{H}]_{mn} f_n$. A matrix-matrix product of an $L \times M$ matrix $\mathcal{B}$ with an $M \times N$ matrix $\mathcal{H}$ is denoted as $\mathcal{B}\mathcal{H}$, where $[\mathcal{BH}]_{ln}$ is its $ln^{th}$ element. An $M \times M$ diagonal matrix with an $M$-dimensional vector $\mathbf{g}$ as its diagonal is given by diag($\mathbf{g}$). Another operation involved between two matrices is an element-by-element multiplication, which is denoted by $\odot$. Two $M \times N$ matrices $\mathcal{Y}$ and $\mathcal{A}$ will have the $mn^{th}$ element of the element-by-element product $\mathcal{Y} \odot \mathcal{A}$ given by $[\mathcal{Y} \odot \mathcal{A}]_{mn} = [\mathcal{Y}]_{mn}[\mathcal{A}]_{mn}$. The element-by-element vector division of two M-dimensional vectors $\mathbf{a}$ and $\mathbf{g}$ is $\frac{\mathbf{a}}{\mathbf{g}}$ with $\frac{a_m}{g_m}$ is its $m^{th}$ element. The transpose of the matrix $\mathcal{H}$ is denoted by $\mathcal{H}^T$.

An image can be represented as a vector such that each element of the vector gives the intensity of an image pixel. We can lexicographically order a 2D or 3D image to a vector. Lexicographical ordering assigns the intensity of the $ij^{th}$ pixel of a 2D $I \times J$ image to the $n^{th}$ element of an $N$-dimensional vector $\mathbf{f}$ where $N = I \times J$. The index $n$ can be from a column-by-column or row-by-row raster scan of the locations $ij$ of the image. A $I \times J \times K$ 3D data-set can be lexicographically ordered into a vector $\mathbf{f}$ by assigning the intensity of $ijk^{th}$ element to $f_n$ where the index $n$ can be calculated as $kIJ + iJ + j$, or $kIJ + jI + i$, or $iJK + jK + k$, or $iJK + kJ + j$, or $jIK + iK + k$, or $jIK + kI + i$.

Because of the statistical feature of this work, the concepts of means and variances for random variables come up frequently in later chapters. We denote means by the decoration of a bar. For a random variable $a$, if its probability density function is $p(a)$, its mean is defined as:

$$\bar{a} = \int a p(a) \mathtt{d} a \tag{2.1}$$

and variance as:

$$\sigma_a^2 = \int (a - \bar{a})^2 p(a) \mathtt{d} a \tag{2.2}$$

Sometimes, we will also use $\langle a \rangle$ to denote its mean. Similarly, for a random vector $\mathbf{g}$ with its probability density function $p(\mathbf{g})$ (or, for a discrete valued random vector a joint probability $\Pr(\mathbf{g})$), its mean is denoted by $\bar{\mathbf{g}}$ with each element $\bar{g}_m$ computed as following:

$$\bar{g}_m = \int_{g_{M-1}} \cdots \int_{g_1} \int_{g_0} g_m p(g_0, g_1, \cdots, g_{M-1}) \,\mathtt{d}g_0 \,\mathtt{d}g_1 \cdots \,\mathtt{d}g_{M-1} \tag{2.3}$$

Its covariance matrix is denoted as $\mathcal{K}_{\mathbf{g}}$ with element $[\mathcal{K}_{\mathbf{g}}]_{nn'}$:

$$[\mathcal{K}_{\mathbf{g}}]_{nn'} = \int_{g_{M-1}} \cdots \int_{g_1} \int_{g_0} (g_n - \bar{g}_n)(g_{n'} - \bar{g}_{n'}) p(g_0, g_1, \cdots, g_{M-1}) \,\mathtt{d}g_0 \,\mathtt{d}g_1 \cdots \,\mathtt{d}g_{M-1} \tag{2.4}$$

If the random variable (vector) is discrete, the integration is replaced by summation. Another decoration used is the carat ( ˆ ). We denote an estimate of random vector $\mathbf{f}$ by $\hat{\mathbf{f}}$.

## 2.2 Image Formation

Once the radiopharmaceutical is introduced inside the subject's body it gets distributed within the body according to the physiological function it is targeting. It is this emitting distribution within the body that we do not know and are trying to estimate. The amount of radioactivity in the body is constantly reducing with time because of (1) the physical decay of the radionuclide and (2) the biological elimination of the radiopharmaceutical. Physically, the radionuclide is constantly decaying with an exponential decay law. This is because the fraction of radioactive decays is constant per unit time. Given $N_0$ atoms present initially, the number of atoms remaining after time $t$ is:

$$N(t) = N_0 e^{-\lambda t} \tag{2.5}$$

where $\lambda$ is the decay constant. The physical half-life ($T_p = 0.693/\lambda$) is a measure of the decay rate and is equal to the length of time required for the radionuclide atoms to reduce to half the original number of atoms. The radionuclide also undergoes a biological washout. The biological half-life ($T_b$) is the time required for the body to eliminate one half of the dose of any substance by regular process of elimination. The physical half-life ($T_p$) along with the biological half-life ($T_b$) contribute to the effective half-life ($T_e$) of the radioactive substance within the body. It is calculated as $T_e = \frac{T_p \times T_b}{T_p + T_b}$ as given in [3]. The biologic half-life always decreases the effective half-life to a value less than the physical half-life. We shall assume that the effective half-life of the radionuclide is much longer than the fixed observation time interval. This is often not true for some types of studies, there is a steady decline of radioactivity associated with radioactive decay or a significant washout. In this case, the projection data have to be corrected [3, 34] for half-life decay correction to ensure comparable count statistics throughout the scan. After accounting for this effect we can assume that the total number of radioactive atoms with the body do not change during the scan.

However, the radionuclide itself might move within the body due to physiological interactions with the body causing temporal variations on radionuclide distribution. Dynamic imaging is used to identify these temporal variations in the radiotracer concentration revealing information about organ physiology and is a prominent research topic [35, 8]. Further, patient motion and involuntary motions due to cardiac and respiratory cycles lead to a changes with time of the radionuclide distribution. Voluntary motion can be compensated for by means of infrared motion tracking [36, 37] and other techniques. Cardiac motion is captured in gated SPECT [38] which synchronizes the acquisition of tomography data with the cardiac cycle, thus permitting the reconstruction of a time sequence of images instead of a single motion blurred image. Though the radionuclide distribution can move, we will consider only a temporally static scenario. We assume the patient does not move and the radiotracer densities within the body are not changing in space during the imaging process. For many studies, the assumption of a temporally static distribution is a good one [8, 39].

In SPECT what we have is the data given by a number of 2D planar images (projections) taken at equidistant angles as described is Chapter 1. The entity we want to know is the true 3D spatial density distribution of the radionuclide. It is proportional to the average number of radionuclide disintegrations into $4\pi$ steradians per unit volume per unit time of the radionuclide distribution. This average gamma-emission rate (as a measure of radioactivity) per unit volume is a continuous function of 3D Euclidean space. We denote it as $f(x, y, z)$ with units of counts/(unit time, unit volume) and with $(x, y, z)$ the Euclidean coordinates of spatial position. The number of photons emitted from the radionuclide in volume $\mathtt{d}x\, \mathtt{d}y\, \mathtt{d}z$ during a finite interval of time is a random quantity and follows a Poisson distribution [6, 40]. The mean number of emissions per unit time is thus $f(x, y, z)\, \mathtt{d}x\, \mathtt{d}y\, \mathtt{d}z$. This is proportional to the concentration of radionuclide in the volume $\mathtt{d}x\, \mathtt{d}y\, \mathtt{d}z$. The higher the concentration, the more gamma photons per unit time will be emitted on average. Thus, estimating the Poisson means of the 3D emission rates is equivalent to estimating the spatial density distribution of the radionuclide. We will term $f(x, y, z)$ as the "object" and its estimate as the "object estimate".

The SPECT projection data are already in discrete form since each bin contains a positive integer number of photon counts. Thus the sinogram is discrete spatially (discrete bins) as well as in intensity (discrete in photon counts). The planar image at each of $\Theta$ angles is made of $L$ bins and $P$ slices. Thus the projection data has $M = \Theta L P$ elements which can be lexicographically ordered into a $M$ element vector $\mathbf{g}$. The quantity $g_m$ specifies the *number* of photons counted for a quantized position given by $l^{th}$ bin and $p^{th}$ slice on the Anger camera face at angle $\theta$ so that $\mathbf{g}$ is integer valued. The index $m$ can be $p\Theta L + \theta L + l$ (one of six ways in which a 3D data set can be lexicographically ordered). Due to the limited quantity of radiopharmaceutical that can be administered to the patient and the fact that only about 1 in $10^4$ photons emanating from the object gets detected, the typical bin counts $g_m$ are of the order of 1 to 10. This results in noisy data.

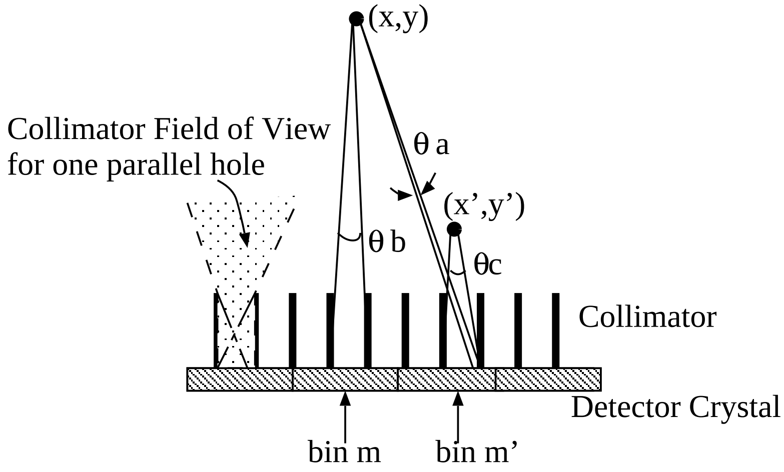

Figure 2.1: Collimator effects on the probability of photon detection: the probability of the photon detected by a detector bin $m$ is proportional to the angle limited by the collimator. Since $\theta_b$ is bigger than $\theta_a$, it's more probable for a photon emanated from $(x, y)$ is detected by detector bin $m$ than by $m'$. The angle is source-position dependent. The angle $\theta_c$ is bigger than $\theta_a$. The shaded area illustrates the field of view for one parallel hole of the collimator, i.e., photons started inside this area have a chance of being detected by this detector bin.

Photons are emitted into $4\pi$ steradians. The probability that a photon emitted from $f(x, y, z)\mathtt{d}x\,\mathtt{d}y\,\mathtt{d}z$ would be detected by a bin $m$ is dependent on location $(x, y, z)$ relative to the bin $m$ and other factors of the imaging system. One important geometric factor governing this acceptance probability is position relative to the collimator. Figure 2.1 shows how the angle subtended by the collimator varies among detector bins relative to a single location. The subtended angle is one factor that governs the probability that a photon from $(x, y, z)$ is detected or not detected at bin $m$. It is a function of both source position and bin size and location. We denote this probability density as $h_m(x, y, z)$. For $m = 0, 1, \cdots, M-1$, the functions $h_m(x, y, z)$

are called system sensitivity functions [29, 33] as they describe the sensitivity of a given detector to different spatial locations. The Bernoulli probability of detection at the $m^{th}$ bin of a photon from volume $\mathtt{d}x\,\mathtt{d}y\,\mathtt{d}z$ at $(x, y, z)$ is $h_m(x, y, z)\mathtt{d}x\,\mathtt{d}y\,\mathtt{d}z$. We already know that the number of photons emitted from $(x, y, z)$ is Poisson distributed with mean $f(x, y, z)\mathtt{d}x\,\mathtt{d}y\,\mathtt{d}z$. It turns out that a cascade of a Poisson process with mean $\lambda$ and a Bernoulli process with mean $q$ gives another Poisson process with its mean decreased to $q\lambda$ [41, 40]. Thus the number of photons detected at bin $m$ due to the radioactivity in volume $\mathtt{d}x\,\mathtt{d}y\,\mathtt{d}z$ at $(x, y, z)$ has a Poisson distribution with mean $h_m(x, y, z)f(x, y, z)\mathtt{d}x\,\mathtt{d}y\,\mathtt{d}z$.

The total number of photons counted at bin $m$ is the accumulation of the contribution from locations over the entire object. This involves the integration of $h_m(x, y, z)f(x, y, z)\mathtt{d}x\,\mathtt{d}y\,\mathtt{d}z$ over the entire object. Since the summation of many Poisson random variables is Poisson with mean equal to the sum of the all the means, the total number of photon counts detected at $m$ follows a Poisson distribution with mean $\bar{g}_m$, where $\bar{g}_m$ is given by

$$\bar{g}_m = \int\int\int h_m(x, y, z)f(x, y, z)\mathtt{d}x\,\mathtt{d}y\,\mathtt{d}z \tag{2.6}$$

The number of counts in each bin is random and independently Poisson distributed [40] due to the random feature of the emission of photons and the detection process. The sinograms we acquire in SPECT imaging are sample values of the Poisson random vector.

For computational convenience we will now discretize the object $f(x, y, z)$ and subsequently approximate the continuous system sensitivity functions $h_m(x, y, z)$ in a system matrix H. We use voxels as the basis functions for transforming the object from the continuous to the discrete domain. Other basis functions such as Gaussian basis functions can also be used [42]. We discretize $f(x, y, z)$ into an array of rectanguloid voxels having a total number of $N$ voxels of size $(\Delta x, \Delta y, \Delta z)$. This array is lexicographically ordered into a vector $\mathbf{f}$ with each $n^{th}$ element $(n = 0, \ldots, N-1)$, given by

$$f_n = \int_{x_n-\frac{\Delta x}{2}}^{x_n+\frac{\Delta x}{2}} \int_{y_n-\frac{\Delta y}{2}}^{y_n+\frac{\Delta y}{2}} \int_{z_n-\frac{\Delta z}{2}}^{z_n+\frac{\Delta z}{2}} f(x,y,z)\, \mathtt{d}x\, \mathtt{d}y\, \mathtt{d}z \tag{2.7}$$

where the integration is taken over the volume of the $n^{th}$ voxel centered at $(x_n, y_n, z_n)$. The intensity value of a voxel $f_n$ represents the expected number of emissions from the $n^{th}$ voxel. Therefore, for the cubic or rectanguloid voxels the original continuous object is approximated by a discrete representation $\mathbf{f}$ with elements $f_n$ given by

$$f(x,y,z) \approx \sum_{n=0}^{N-1} f_n \mathrm{rect}\,(\frac{x-x_n}{\Delta x})\mathrm{rect}(\frac{y-y_n}{\Delta y}\mathrm{rect}(\frac{z-z_n}{\Delta z}) \tag{2.8}$$

Applying the system transformation (2.6) to (2.8), we can obtain:

$$\begin{aligned} \bar{g}_m &= \int\int\int \sum_{n=0}^{N-1} f_n \mathrm{rect}(\frac{x-x_n}{\Delta x})\mathrm{rect}(\frac{y-y_n}{\Delta y})\mathrm{rect}(\frac{z-z_n}{\Delta z}) h_m(x,y,z)\, \mathtt{d}x\, \mathtt{d}y\, \mathtt{d}z \\ &= \sum_{n=0}^{N-1} [\mathrm{H}]_{mn} f_n \end{aligned} \tag{2.9}$$

where H, with elements $\mathrm{H}_{mn} = \int\int\int h_m(x,y,z)\mathrm{rect}(\frac{x-x_n}{\Delta x})\mathrm{rect}(\frac{y-y_n}{\Delta y})\mathrm{rect}(\frac{z-z_n}{\Delta z})\, \mathtt{d}x\, \mathtt{d}y\, \mathtt{d}z$, is called the system matrix. The quantity $\mathrm{H}_{mn}$ is the Bernoulli probability that a photon emitted from voxel $m$ is detected at bin $n$.

Since counts in each detector bin are independent [40], the joint probability of the number of detected counts $\mathbf{g}$ conditioned on $\mathbf{f}$ is given by an independent Poisson distribution as

$$\Pr(\mathbf{g}|\mathbf{f}) = \prod_{m=0}^{M-1} \frac{e^{-[\mathrm{H}\mathbf{f}]_m}}{g_m!}([\mathrm{H}\mathbf{f}]_m)^{g_m} \tag{2.10}$$

with mean

$$E\{\mathbf{g}\} \equiv \bar{\mathbf{g}} = \mathrm{H}\mathbf{f} \tag{2.11}$$

Due to the Poisson nature of (2.10), the covariance of $\mathbf{g}$ for a given $\mathbf{f}$ is a diagonal matrix [43] with variances along the diagonal given by $\sigma_{g_m}^2 = \bar{g}_m = [\mathrm{H}\mathbf{f}]_m$. Thus, for a given object $\mathbf{f}$, the conditional covariance $\mathcal{K}_{\mathbf{g}|\mathbf{f}}$ is

$$\mathcal{K}_{\mathbf{g}|\mathbf{f}} = \mathrm{diag}(\mathrm{H}\mathbf{f}) \tag{2.12}$$

We naturally consider the case where $\mathbf{g}$ is measured and $\mathbf{f}$ unknown. In this case, (2.10) is a likelihood.

Given (2.11), we can express the forward projection model as a linear system of equations:

$$\mathbf{g} = \mathrm{H}\mathbf{f} + \mathbf{n} \tag{2.13}$$

where $\mathbf{g}$ is an instance of a (Poisson) noise vector with mean $\mathrm{H}\mathbf{f}$ and $\mathbf{n}$ is the noise component. Note that the Poisson noise is signal dependent, yet we are still able to express this noise as an additive term in (2.13). The vectors $\mathbf{g}$ and $\mathbf{n}$ are random, and $\mathbf{f}$ is the nonrandom (parameter) vector we try to estimate. In later chapters we will consider $\mathbf{f}$ to be random.

In practice, $\mathrm{H}_{mn}$ will only need to be proportional to the probability of receiving a count in $m$ emanating from $n$. For 3D SPECT with a $128 \times 128 \times 32$ object and data acquired over 128 angles using a 192-bin detector and 32-slices, the size of the system matrix stored in single-precision format is over 1 TB ($128 \times 128 \times 32 \times 128 \times 192 \times 32 \times 4$ bytes). Storing and directly using such a huge matrix for example, in computing matrix vector products during reconstruction is impractical. The matrix is either computed on the fly or stored in some efficient way using specialized formats for sparse matrices. Specialized functions have to be used to compute matrix vectors such as $\mathrm{H}\mathbf{f}$.

## 2.3 System Matrix H and its Approximation $\mathcal{H}$

The system matrix H models the overall physical effects of the imaging system, such as geometrical response of the detector discussed earlier and the interaction of the gamma photons with the human body and the detector. The matrix H comprises many factors, some known only approximately via external measurements. It is often convenient, especially in reconstruction, to use an approximate system matrix. In Section 2.3.3 we explain computations of the the matrix $\mathcal{H}$ that approximate H by modelling some of the physical effects contained in H.

Note that the imaging equation (2.13) is linear. In this thesis we do not consider non-linear effects such as dead time. The dead-time [44, 45] refers to the time required by the detector to process individual detected events. Its is also known as pulse resolving time. It is due to the finite scintillation rise and decay times, and time required by the processing electronics. While a detected event is being processed, the detector is not able to process another event. Therefore, if a second signal pulse occurs before the first has disappeared, it does not generate a detected signal. The effect of dead-time causes the loss of detected photons reducing sensitivity and limiting the count rates. The mean projection data is no longer $\mathbf{Hf}$. The measurement data would no longer be Poisson distributed since the inter-arrival times between detected events do not remain exponentially distributed. In a typical camera, dead-time is on the order of microsecond [8, 3, 46]. The fraction of counts lost due to dead-time is proportional to the true count rate in low to moderate count rates, but is non-linear at high count rates [47]. For almost all SPECT studies, the average count rate is relatively low, thus it is a good approximation to ignore dead-time.

### 2.3.1 Attenuation and Scatter

The H matrix incorporates the object-dependent physical effects of attenuation and scatter as mentioned in Section 1.1.1, When a beam of photons passes through the human body, it becomes weaker or attenuated as it interacts with the intervening tissue. Given the energies of SPECT photons (70Kev-394Kev) [1] and the material properties (mostly water) of the body, this attenuation takes place mainly in two ways: photoelectric effect and Compton effect [3]. The **photoelectric effect** [48] occurs when an incident gamma photon (primarily of low energy) interacts with an inner-orbital electron, the entire energy of the gamma photon is transferred to the electron, and the gamma photon is totally absorbed. The electron, called a photo-electron, is released from its energy shell and the atom. The photo-electron will itself be absorbed. The photoelectric interaction only occurs when the energy of the incident gamma photon is higher than the binding energy of the electron. As far as the imaging system is concerned, the photon simply disappears at the absorption site.

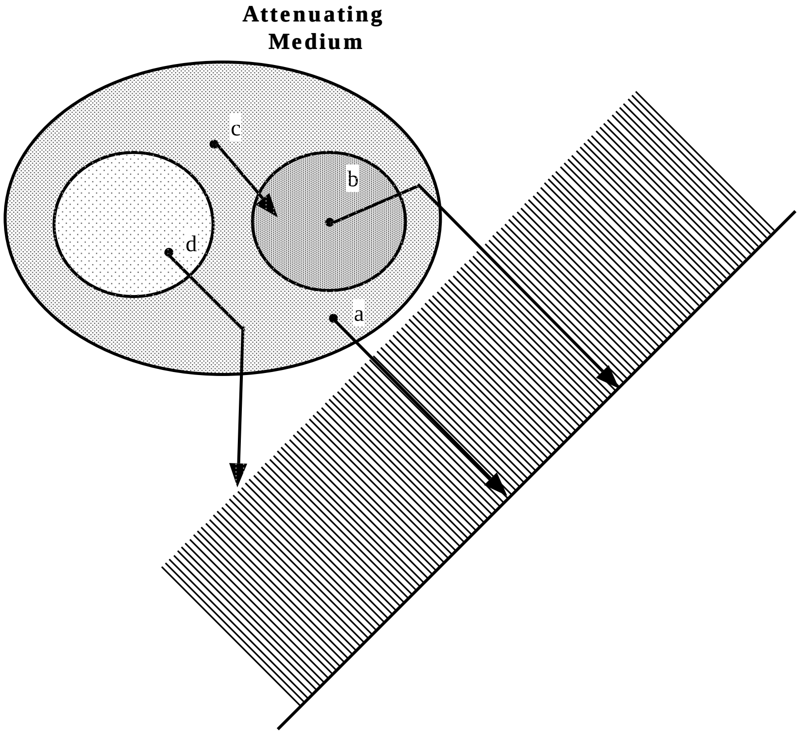

Figure 2.2: Illustration of attenuation and scatter in SPECT imaging. The attenuation object with several emission point scources is shown in the figure. Photon “a” is detected directly. Photon “c” is stopped because of photoelectric absorption. Photon “d” is scattered and stopped by the collimator. Photon “b” flies originally in an undetectable direction but is scattered and then detected.

The **Compton effect** [48] occurs when an incident gamma photon interacts with an outer-shell electron and some energy of the gamma photon is transferred to the electron, and the electron is ejected from its orbit. The gamma photon, with reduced energy, emerges from the atom with a change in direction. The relationship between the fractional energy loss of the photon and the scattering angle is given by the Klein-Nishna equation [48]. This scattered photon may undergo further photoelectric absorption, or be rescattered or go undetected or get detected.

In order for a photon to be detected, it must escape the body in a direction that enables it to get through the collimator as discussed earlier. However, due to the effects of photoelectric absorption and Compton scatter, photons can disappear (get absorbed) or get deflected (scattered). If a gamma photon that would otherwise be detected is either totally absorbed or scattered to a direction undetectable to any detector, we classify the event as "attenuation". In other words, photon attenuation denotes the loss of photons because of interaction with the tissue of the human body. Figure 2.2 shows an attenuation object with several emission point sources. It shows the interaction of 4 emitted photons 'a', 'b', 'c' and 'd' with the attenuating medium. The attenuation process is illustrated by photons 'c' and 'd' which fail to reach the detector. If a photon that wouldn't be detected gets detected after scattering then such a photon is known as scatter photon. The photon 'b' in Figure 2.2 is an example of a scatter photon. A photon that does not undergo either photo-electric interaction or Compton scatter while traversing the body and is detected is termed a primary photon. An example of a primary photon is the photon 'a' in Figure 2.2.

Attenuation is measured by a linear attenuation coefficient $\mu$ with units of $\text{cm}^{-1}$. It is a measure of the probability of attenuation per unit length along a thin beam passing through tissue. The attenuation coefficient depends on the energy spectrum of the photons as well as on the average atomic number of the tissue it passes through. Let $N_0$ be the number of photons incident into a uniform medium of thickness $\Delta x$ and attenuation coefficient $\mu$, and $N$ be the number of photons leaving the medium from the other side. In general, the transmittance $\frac{N}{N_0}$ can be obtained by using Beer's law

[1]:

$$\frac{N}{N_0} = \exp(-\mu \Delta x) \tag{2.14}$$

In (2.14), we have considered a $\mu$ which is independent of position and also suppressed the energy dependence $\mu(E)$ of $\mu$. The linear attenuation coefficient $\mu$ is the sum of attenuation coefficient for photoelectric absorption $\mu^{pe}$ and attenuation coefficient for Compton scatter $\mu^{c}$ [48]. A more detailed description of the attenuation coefficient is available in [6] where the attenuation coefficient is given by

$$\mu = \mu^{pe} + \mu^{C}_{en} + \mu^{C}_{s} \tag{2.15}$$

$$\mu^{absorption} = \mu^{pe} + \mu^{C}_{en} \tag{2.16}$$

The term $\mu^{absorption}$ occurs because energy is transfered to the medium due to (1) photoelectric effect and (2) a part of the energy of the scattered photon is transfered to the recoil electron during Compton scatter; $\mu^{pe}$ is due to photoelectric effect; $\mu^{C}_{en}$ is due to energy imparted as kinetic energy to the recoil electrons and $\mu^{C}_{s}$ is due to the energy imparted to emerging scattered photon.

To account for attenuation of the photons emitted by a monoenergetic radionuclide in a non-homogeneous medium, we use the obvious generalization of Beer's law:

$$\frac{N}{N_0} = \exp(-\int_0^d \mu(l)\mathtt{d}l) \tag{2.17}$$

where $d$ is the distance inside the medium along the ray connecting the emitting radionuclide and the detector bin. Here $\mu(l)$ is the variation of $\mu$ along the ray. Equation (2.17) would be applicable where a photon might travel through different tissues (lung, soft tissue, bone), each with different $\mu$, before leaving the body and getting detected. At 140Kev ($^{99m}$Tc) the attenuation coefficient of soft tissue (mostly consisting of water) is 0.153cm$^{-1}$, lung is 0.05 cm$^{-1}$ and bone is 0.335 cm$^{-1}$. Half the incident photons are absorbed after passing through only 4.53 cm of water. This means in a human body where the photons have to travel through water, bone and lung for a distance of several centimeters to tens of centimeters, the attenuation effects will be fairly severe.

Scatter interactions cause a deflection of the radiation, which can cause a misleading indication of each gamma ray's initial propagation direction. Photons that have been scattered before reaching the detector give misplaced information of the point of origin. This causes an object dependent distortion [1] i.e. dependent on both activity and attenuation blur in the sinogram . This results in poor contrast in the reconstructed SPECT image.

For a detector with perfect energy discrimination, the scatter photons can be totally rejected. For a perfect detector system, in the absence of Compton scattering effects, photons from a mono-energetic source with a specific energy should be detected with exactly one energy and the energy spectrum should appear as a delta function centered at the specified energy. However this is not the case since the detection system is not perfect as explained in Section 1.1.1, resulting in an approximate energy-estimation procedure which is characterized by a finite energy resolution. Thus if we shot a pencil beam of mono-energetic 140Kev gamma rays at a single bin and recorder the estimated energies of only the primary photons, we would get the bell-shaped energy histogram shown as the dotted line in Figure 2.3. If we also recorded the energies of scattered photons, we would obtain the dong-tailed histogram shown by the dashed-dotted line in Figure 2.3. Note that the histogram overlap. Therefore, while some low energy scattered photons can be eliminated by energy thresholding, other scattered photons have energies comparable to those in the "photopeak window" (bell shaped curve) and are more difficult to reject. In Chapter 7, we discuss further this scatter rejection problem. The width of this energy window is approximately equal to the twice the energy resolution of the detector. The width of the energy resolution of a NaI crystal detector for a $^{99m}$Tc source is about 10% FWHM which scales with the width of photopeak window. For a typical study the scatter fraction, equal to the ratio of scatter to primary photons in the photopeak window is around is 20%-40% [49]. For multienergy radionuclides like $Ga^{67}$ there is more than one line of energy and thus more than one photopeak window. In such case a photon of higher energy can get scattered and lose energy and so get detected in the lower energy photopeak window. This scattered photon is rejected by the higher energy photopeak window but gets detected as a primary photon of the lower energy. Thus phenomenon is known as down-scatter. In this thesis we will not focus on downscatter.

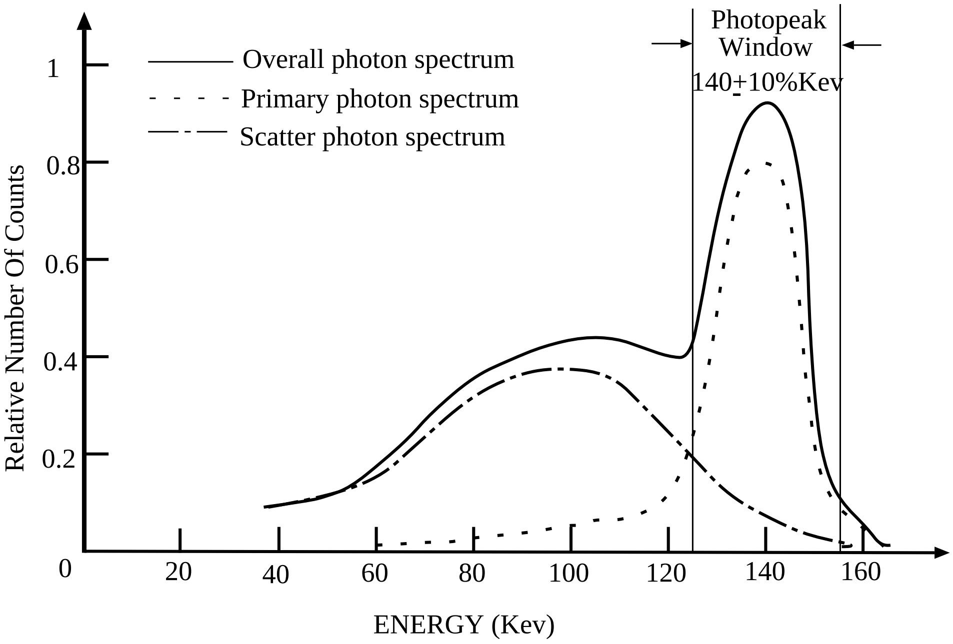

Figure 2.3: Illustration of the energy spectrum of detected photons for $^{99m}$Tc. The dotted line shows the spectrum of primary photons which directly hit the detector without being scattered. The finite width of the dotted curve is due to the limited energy resolution of the detector. The dashed dotted line shows the spectrum of scattered and then detected photons. The overall energy spectrum (sum of two curves) is displayed as the solid line. Counts with energy outside the primary window are rejected.

From our earlier explanation we know that the photons detected in the photopeak window are contributions from both scatter photons and photons that are not attenuated (primary photons). Thus the mean projection data $\mathrm{H}\mathbf{f}$ in the photopeak window is a sum of a primary component $\mathrm{H}^P\mathbf{f}$ in the photopeak and a scatter component $\mathrm{H}^S\mathbf{f}$ in the photopeak. Consequently, the system matrix H can be written as the sum of these two matrices and hence $\mathrm{H} = \mathrm{H}^P + \mathrm{H}^S$.

### 2.3.2 Geometric Response

The geometric response of the gamma camera is an important effect to to be modeled in the system matrix. Here we give a qualitative account for geometrical response and later give a mathematical account. In absence of an attenuating medium a point source in a 3D imaging system will get imaged as a 2-D Gaussian blob [50] rather than a sharp point. A complete specification of such 2-D blobs for various positions of the point source gives us the geometrical response of the gamma camera. The geometrical response includes collimator blur effects and intrinsic detector blur effects.

From Section 1.1 we know that for a parallel-hole collimator, incident photons are confined to directions approximately perpendicular to the collimator face. A given bore (see Figure 1.2) will allow only those photons whose direction vectors lie in its field of view, to hit the detector. As seen in Figure 1.2, the point source ‘a’ is close to the collimator, the area of the detector it sees is small while the point source ‘b’ is farther from the collimator so the area of the detector it sees is larger. The point spread function (PSF) of point ‘a’ is seen in Figure 2.4(a) and the PSF of point ‘a’ is seen in Figure 2.4(b). The counts under both the surfaces (2D curves) are the same, hence for a point source with no attenuating medium the counts are preserved independent of its distance from the collimator. The FWHM of the PSF’s for a point source at a certain distance is a measure of collimator resolution at that distance. The collimator resolution decreases as the detector to source distance increases. The figure also gives the various parameters of the collimator such as collimator length ($l_c$), bore diameter ($d_c$), and septal thickness. The figure is not to scale. Typical values of collimator parameters would be $l_c = 2.0$cm, $d_c = 0.1$cm and septal thickness of 0.01cm. These parameters would result in a collimator resolution of 2cm at a distance of 30cm from the collimator face. The acceptance angle a function of the bore diameter and bore length is the parameter that describes the field of view subtended by the bore. The mathematical models for 3D parallel-hole collimators were analyzed in [51, 52].

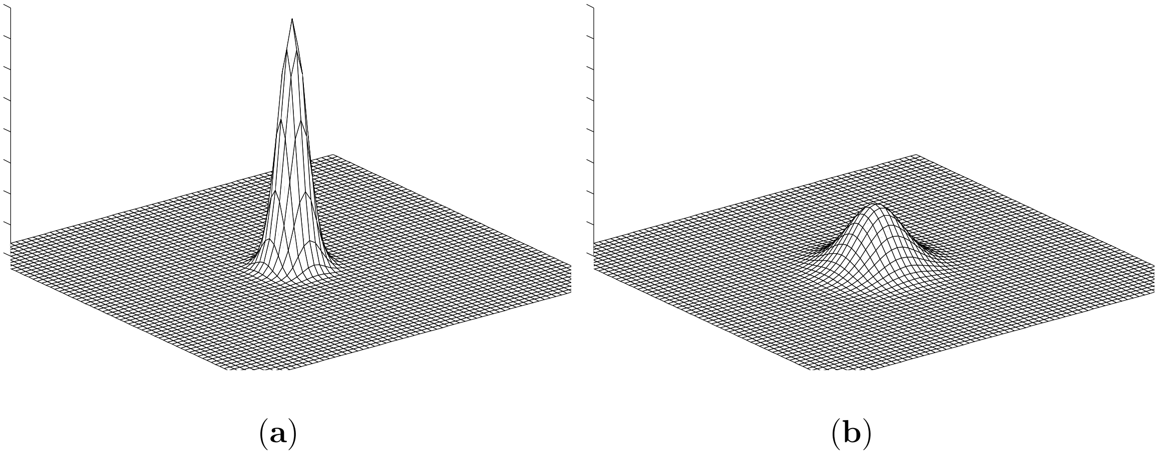
**(a)** **(b)**

Figure 2.4: (a) PSF's of a point closer to the collimator, (b) PSF's of point farther away from the collimator. Note that the area under both the PSF's is the same. Thus mean number of counts are for either points are preserved in the absence of attenuation and scatter.

The geometric response of a collimator is affected by both the collimator bore diameter ($d_c$) and the bore length ($l_c$). The bore length ($l_c$) depends on the collimator material, the energy of the radiation and the typical source distances [8]. For a radioactive source in a fixed distance from the detector, the smaller the collimator hole (small $d_c$), the smaller the acceptance angle, therefore, the smaller the collimator blur and the detector space resolution distance. On the other hand, the wider the collimator holes (large $d_c$), the the bigger the acceptance angle, subsequently, the worse the collimator blur and the detector space resolution. A collimator with a bigger acceptance angle (more blur) collects more counts hence reducing the noise and increasing sensitivity. A collimator with a smaller acceptance angle (less blur) collects less counts hence increasing the noise and reducing sensitivity. This leads to a resolution-noise trade-off. The system resolution is greatly determined by the collimator blur. Reducing the collimator blur means improving the system resolution.

Apart from the collimator blur there is a limitation to the resolution of the detector itself. This intrinsic spatial resolution is due to the uncertainty propagated through the detector chain discussed earlier. The intrinsic resolution is due to a number of factors (a) variations in depth of gamma photon-crystal interaction (b) variations in surface optical properties of the crystal and (c) multiple scattering of some gamma photons within the crystal result in the flash of visible light to be centered away from the site of initial photon-crystal interaction. But, the primary degrading factor in the detector resolution is the Poisson noise in the number of photons produced during the photon-crystal scintillation event. The noise (due to noise in number of photoelectrons and secondary electrons) in the outputs of the PMT's which see the (noisy) scintillation event leads to noise in the position estimate of the detected gamma-photon. The error in this position estimation procedure manifests itself as intrinsic detector blur. Usually the intrinsic detector blur is modeled as a depth independent Gaussian function and is typically on the order of 3 to 4mm [47]. The intrinsic detector blur is usually combined with collimator blur to obtain an overall model of geometrical blur. The overall blur is a convolution of the collimator psf and the intrinsic camera psf.

So far, we have discussed attenuation, scatter and geometrical response (comprising intrinsic detector response and collimator response). We have discussed their physical bases, but have *not* discussed how to incorporate these linear effects in the approximation $\mathcal{H}$. Before we discuss H, we point that there are other physical effects that we have not discussed. One is septal penetration, in which a gamma ray passes through a septum and hits the detector . Septal penetration effects can be measured and approximated as a component in the overall geometrical response. Another effect is the generation of lead X-rays via the interaction of $\gamma$-rays with the lead present in some collimator. This is a small effect and can ignore it. Another effect is detector efficiency, discussed in Section 2.3.3.

There is no practical procedure to compute the exact system matrix H. Given the attenuation map and the geometrical response parameters, Monte Carlo (MC) simulators such as SIMSET, SIMIND or GEANT [46, 8] may be used to compute a good approximation to the system matrix H. The MC simulator is a program which models the transport of photons within an object by randomly sampling from certain probability density functions. These pdfs model the physical processes involved in photon interaction with matter. By performing a simulation ( starting with a large number of source events) with a point source at the $n^{th}$ pixel within the object to get the projection of in the photopeak window, one can calculate the columns of H which models all attenuation, scatter and geometrical response. The accuracy is dependent on the number of photons (source events) transported through the object. A larger number of source events improves the accuracy but entails larger computation times. This approach would require large data storage capacity and long computation time. Instead of an MC simulation we can perform a data acquisition on real scanner with a point source at every point in a phantom to measure the matrix H.

### 2.3.3 Approximations to the System Matrix in the Absence of Scatter

We obtain successively more accurate analytical approximations to the true system matrix $\mathrm{H}^{P}$ by incorporating one physical effect at a time. We shall denote the approximate system matrix as $\mathcal{H}$. The matrix $\mathcal{H}$ will not account for scatter in the photopeak window.

### Basic Line Integral

A simplified version of $\mathcal{H}$ is represented by $\mathcal{Y}$ which gives the system matrix without the effects of photon interactions within the body and with the detector. The element of system matrix $\mathcal{Y}_{mn}$ is the projection of the $n^{th}$ voxel on the $m^{th}$ bin. In other words it is the volume of overlap of a strip emanating out of bin $m$ and the voxel $n$. We approximate this by the intersecting length $l_{mn}$ at the intersection of the projection ray from the center of bin $m$ and the voxel $n$ (see Figure 2.5). Thus, for a particular central projection ray of bin $m$, (where ray $m$ is associated with detector bin $m$), it intersects several of the pixels.

The dark line in Figure 2.5 passes through pixels associated with ray $m$. As illustrated in Figure 2.5, among those pixels intersecting this central ray, the length of the intersecting chord of a pixel $n$ with central ray of bin $m$ is denoted as $\mathcal{Y}_{mn}$. For those pixels $n'$ which do not intersect with this ray, the corresponding $\mathcal{Y}_{mn'}$ equals to zero. Hence, we may write :

$$\bar{g}_m = \sum_{n=0}^{N-1} [\mathcal{Y}]_{mn} f_n \tag{2.18}$$

In matrix form,

$$\bar{\mathbf{g}} = \mathcal{Y}\mathbf{f} \tag{2.19}$$

Equation (2.19) thus summarizes our model of idealized projection into a linear algebraic form. Obviously, if the intersecting chord is long, such as the first or last pixel along ray $m$ in Figure 2.5, it means that big portion of this pixel can be "viewed" by detector bin $m$, i.e., the photon emitted from this pixel is more probably detected by bin $m$. If the intersecting line is short, such as $[\mathcal{Y}]_{mn_2}$ in Figure 2.5, it means that only small portion of this pixel can be "viewed" by detector bin $m$, i.e., the photon

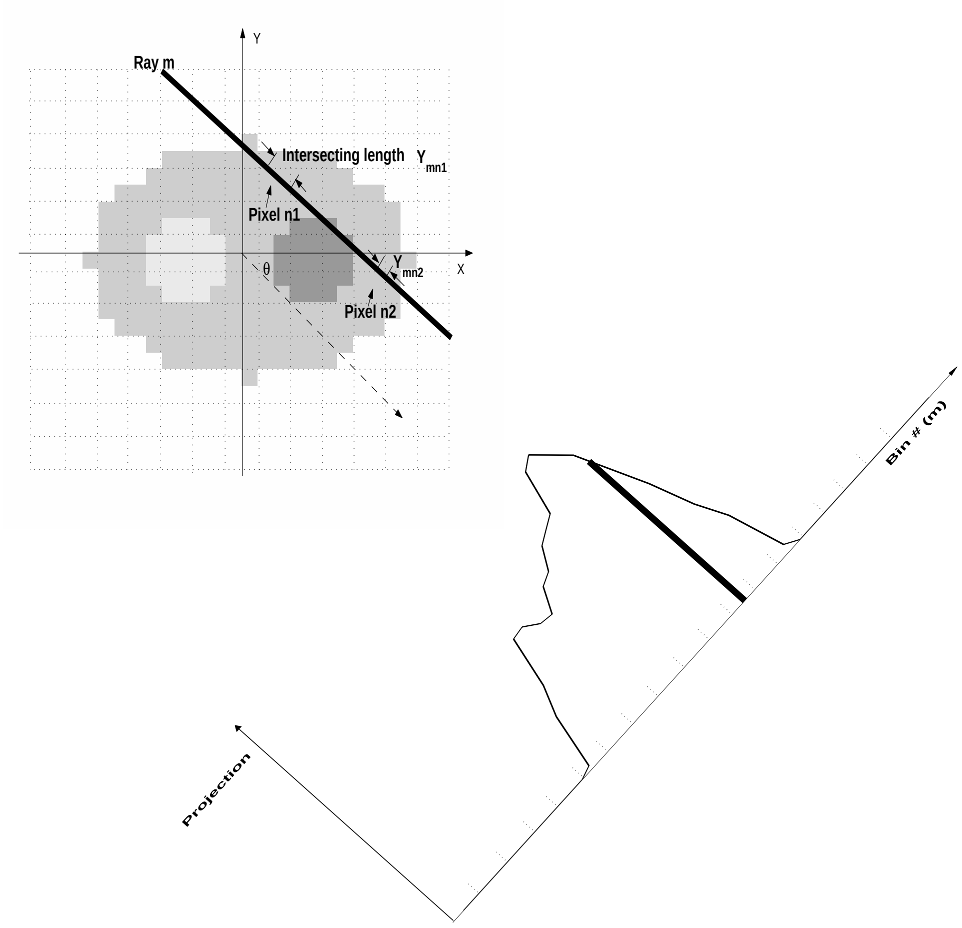

Figure 2.5: Line integral approximation for discretized 2D projection: An object is discretized to $N$ pixels (dotted lines). A line integral is used to model the idealized geometry of a SPECT system. The dark line is a central ray, indexed by $m$, that is perpendicular to the detector array and intersects it at $\iota_m$, the center of bin $m$. Without considering degradation factors, each element of the system matrix $[\mathcal{H}]_{mn}$ is approximated by the intersection length $[\mathcal{Y}]_{mn}$ of the central ray $m$ with pixel $n$. The dashed line shows the projection profile at this angle.

emitted from this pixel is less probably detected by bin $m$. Therefore, the intersecting chord length $[\mathcal{Y}]_{mn}$ is a reasonable choice to crudely approximate the corresponding system matrix element $[\mathcal{H}]_{mn}$, i.e.

$$\mathcal{H} \approx \mathcal{Y} \tag{2.20}$$

for a system without any other degradation factors. As we see in Figure 2.5, each ray only intersects with limited number of pixels. Also photons emitted from each pixel are only possibly detected by limited number of detector bins (in the order of the number of angles $K$). Thus, the $\mathcal{Y}$ matrix is a very sparse matrix for this idealized model. From now on, we will use $\mathcal{Y}$ to delineate the system matrix with these idealized geometrical effects only.

### Modelling Attenuation in $\mathcal{H}$

To model attenuation in a system matrix, we consider the path (including the attenuation coefficient along the path) that photons pass through. It starts from the pixel from which the photon is emitted and ends at the bin where it is detected, thus attenuation factors depend on both pixel position and bin position. We use the $M \times N$ matrix $\mathcal{A}$ to cover all possible pixel-bin pairs of attenuation factors. The element $\mathcal{A}_{mn}$ is the value the attenuation factor connecting pixel $n$ and detector bin $m$. That means, with the attenuation effect, the original detection probability of photons from pixel $n$ to bin $m$ is reduced by $\mathcal{A}_{mn}$. Assuming that the attenuation map with attenuation coefficients $\mu_n$ of the object is from a transmission scan, the value of $\mathcal{A}_{mn}$ is given by :

$$\mathcal{A}_{mn} = \exp\left( - \sum_{n' \in path(m,n)} \mu_{n'} \mathcal{Y}_{mn'} \right) \tag{2.21}$$

where, $path(m, n)$ is the set of pixels that intersect with the ray starting from pixel $n$ and ending at bin $m$, and $\mathcal{Y}_{mn'}$ is, as we defined before, the chord length of the intersection between this ray and pixel $n'$.

Thus, the system matrix with only an attenuation model added to the basic line integration approximation is given by

$$\mathcal{H}^{(a)} = \mathcal{Y} \odot \mathcal{A} \tag{2.22}$$

Modelling Geometric Response

For modelling geometric response we need to consider both the collimator blur and the intrinsic spatial resolution of the detector. We can approximate the average collimator response by a depth-dependent Gaussian kernel [50]. We know that the intrinsic resolution of a detector is independent of the collimator blur and system resolution cannot get any better than the intrinsic resolution. Usually the intrinsic detector blur is modeled as a depth independent Gaussian function (with standard deviation $\sigma_0$) and is typically on the order of 3 to 4mm [47]. The collimator response is depth-dependent and is well modelled by a Gaussian whose standard deviation grows linearly with depth. The standard deviation of the geometric response blur can thus be modelled by a $\sigma(d) = \alpha d + \sigma_0$, a curve which is a linear function of the depth $d$.

For 2D SPECT a depth-dependent blur kernel given by vector $\mathbf{b}$ with parameters $\sigma(d)$ and $\sigma_0$ specifying the amount of Gaussian blurring is given by

$$[\mathbf{b}(d)]_m = \frac{1}{\sqrt{2\pi(\sigma(d)^2 + \sigma_0^2)}} \exp\left(-\frac{\iota_m^2}{2(\sigma(d)^2 + \sigma_0^2)}\right) \tag{2.23}$$

Here $\iota_m$ is the center of bin $m$ as given in the caption of Figure 2.5. For implementing this depth-dependent blur kernel, the entire object is be divided into $L$ zones parallel to the camera face at the $k^{th}$ angle with incrementally increasing distance from the camera face. The projection of all the voxels in the $l^{th}$ zone are convolved with the corresponding depth-dependent blur kernel $\mathbf{b}(d(l))$ . Each of these projection are then added to get the projection of the entire object on the camera face at the $k^{th}$ angle. The entire details of implementing the system matrix with only the geometrical effect, called $\mathcal{H}^{(dd)}$, is given in [9].

When attenuation is considered each element of $\mathcal{H}^{(dd)}$, $[\mathcal{H}^{(dd)}]_{mn}$, is attenuated by the corresponding attenuation factor $[\mathcal{A}]_{mn}$, resulting in a new system matrix which we denote by $\mathcal{H}^{(dd,a)}$ :

$$\mathcal{H}^{(dd,a)} = \mathcal{H}^{(dd)} \odot \mathcal{A} \tag{2.24}$$

Here, we use the superscript $^{(dd,a)}$ denotes that both attenuation and depth-dependent blur are modeled. The validity of (2.24) is based on the central ray approximation [9]. For 3D SPECT, the scheme is similar, but (2.23) becomes a radially symmetric 2D Gaussian. Details are given in [50].

In (2.24) we haven't modelled detector efficiency. Detector efficiency is the probability that the photon gets recorded when entering the crystal, and it depends on the density and thickness of the scintillation crystal [3]. This it is a pure detector effect. The detector efficiency is measured through system calibration using a flood image (homogeneous photon fluence density over the field of view). It can be modelled by the diagonal matrix diag($\mathbf{c}$) where $M$-dim vector $\mathbf{c}$ accounts for flood correction applied to the sinogram. The approximate system matrix $\mathcal{H}$ is then given by:

$$\mathcal{H}^{(dd,a)} = \mathrm{diag}(\mathbf{c})(\mathcal{H}^{(dd)} \odot \mathcal{A}) \tag{2.25}$$

We have discussed how to model the effects of attenuation, geometric response and detector efficiency and how to approximately capture them in our system matrix $\mathcal{H}$. Our approximate system matrix $\mathcal{H}$ does not model the effect of scatter in the photopeak window. We will discuss of modelling effects of scatter in Chapter 7 but below we give an overview of the modelling approach.

### 2.3.4 Modelling scatter

As mentioned earlier, it is not possible to obtain computationally efficient analytic approximation to the system matrix that accounts for scatter. Some groups have derived efficient Monte Carlo methods to approximate SPECT projections (i.e., computations of the form H$\mathbf{f}$ for any object $\mathbf{f}$) and used them in iterative statistical reconstruction techniques [53, 54, 55], but these methods still tend to be computationally very expensive. MC or physical calculation of H are useful, but these methods are far too cumbersome to use for reconstruction. Reconstruction involves repeated multiplications of $\mathrm{H}\hat{\mathbf{f}}^k$, where $\hat{\mathbf{f}}^k$ is an object estimate at the iteration $k$. Since H is too large to store, it is common to replace this product $\mathrm{H}\hat{\mathbf{f}}^k$ with $\mathcal{H}\hat{\mathbf{f}}^k$ where $\mathcal{H}$ is an approximation to H. Though $\mathcal{H}$ is a matrix, we typically do not store it, but instead compute it on the fly repeatedly as needed.

In Chapter 7, we will model scatter as an affine term that is independent of the object $\mathbf{f}$. Let $\mathbf{s} = \mathrm{H}^S\mathbf{f}$ denote the true scatter that would be observed in the noise-free data. Therefore, $\bar{\mathbf{g}} = \mathrm{H}^P\mathbf{f} + \mathbf{s}$. We shall obtain an estimate $\hat{\mathbf{s}}$ of the affine true scatter term $\mathbf{s}$ using various energy-window techniques as discussed in Chapter 7 and use it in the approximate affine imaging model given below:

$$\mathbf{g} \sim \mathrm{Poisson}(\mathcal{H}\mathbf{f} + \hat{\mathbf{s}}) \tag{2.26}$$

This affine imaging model and the degrading effects of using such an approximate imaging model in the reconstruction are discussed in greater detail in Chapter 7. As a digression, we note that affine likelihood models similar to (2.26) have also found applicability in PET [56]. Often, we will use a simplified imaging model that totally ignores the effects due to scatter:

$$\mathbf{g} \sim \mathrm{Poisson}(\mathcal{H}\mathbf{f}) \tag{2.27}$$

In Chapters 6 and 5, we shall use this simplified imaging model.

# Chapter 3

# Image Reconstruction

Given the projection data **g**, and given a system matrix $\mathcal{H}$ which approximates H, the reconstruction problem is to estimate the emission density **f** (the mean of the Poisson emission rates at each pixel) of the source object via a reconstruction algorithm. We model this estimation process in general with a reconstruction operator $\mathcal{O}$ as:

$$\hat{\mathbf{f}} = \mathcal{O}\{\mathbf{g}\} \tag{3.1}$$

where $\hat{\mathbf{f}}$ is the estimate of **f**.

Emission tomography is a count starved modality due to attenuation, detector efficiency and short observation times which leads to high statistical noise in the data. A method for image reconstruction which models the statistical nature of the noisy data is expected to produce "better" images than deterministic methods. Effects like attenuation, detector blur and scatter can be modeled in the system matrix which is another reason to adopt statistical methods. Modelling these effects becomes a serious issue in SPECT where attenuation, for example can cause severe artifacts if it is not suitably accounted for. In addition to accounting for the noise in the data, statistical reconstruction techniques can be used to incorporate the probabilistic models of the image itself by using Bayesian methods. In later chapters, we will discuss what we mean by "better". In this chapter we discuss MAP (maximum *a* *posteriori*) and ML maximum likelihood estimates for reconstruction. Our focus will be statistical methods, but we also discuss very briefly deterministic methods for the inverse problem of reconstruction in Section 3.2.

## 3.1 Statistical Methods for Reconstruction

### 3.1.1 Likelihood

A likelihood $p(b|a)$ is a measurement of the likelihood that the presence of $a$ causes $b$ to occur. In this case, (2.10) is a likelihood with $b$ presumed known and $a$ unknown. The logarithm of the likelihood is known as *log likelihood.* The *maximum likelihood* (ML) *estimate* $\hat{\mathbf{f}}$ is the value of $\mathbf{f}$ that most likely causes the acquired projection data $\mathbf{g}$, i.e.

$$\begin{aligned} \hat{\mathbf{f}} &= \arg \max_{\mathbf{f} \geq \mathbf{0}} \Pr(\mathbf{g}|\mathbf{f}) \qquad (3.2) \\ &= \arg \max_{\mathbf{f} \geq \mathbf{0}} \log \Pr(\mathbf{g}|\mathbf{f}) \end{aligned}$$

Note that the estimate is subject to a positivity constraint $\mathbf{f} \geq \mathbf{0}$ consistent with the physical nature of $\mathbf{f}$. Since the logarithm is monotonic the second equality is true. We define $\Phi_L(\mathbf{f};\mathbf{g}) \equiv \log(\Pr(\mathbf{g}|\mathbf{f}))$ as the log-likelihood. Substituting (2.10) and omitting the terms independent of $\mathbf{g}$ we get

$$\begin{aligned} \hat{\mathbf{f}} &= \arg \max_{\mathbf{f} \geq \mathbf{0}} \Phi_L(\mathbf{f};\mathbf{g}) \qquad (3.3) \\ &= \arg \max_{\mathbf{f} \geq \mathbf{0}} \sum_{m=0}^{M-1} [g_m \log \bar{g}_m - \bar{g}_m] \\ &= \arg \max_{\mathbf{f} \geq \mathbf{0}} \sum_{m=0}^{M-1} \left[ g_m \log \big( \sum_{n=0}^{N-1} [\mathcal{H}]_{mn} \mathbf{f}_n \big) - \big( \sum_{n=0}^{N-1} [\mathcal{H}]_{mn} \mathbf{f}_n \big) \right] \qquad (3.4) \end{aligned}$$

In (3.4), we use $\mathcal{H}$, the approximation to H, since the arg max operation will be iterative and involve many vector products of the form $\mathcal{H}^T\mathbf{g}$ and $\mathcal{H}\mathbf{f}$. Using H in these products would be computationally infeasible.

Iterative optimization is needed since a closed form solution is not available. It is found that the ML estimation problem is ill-posed and hence the estimates at higher iterations tend to be noisy. One solution to this problem is to stop the iterative process at an earlier stage when the estimates appear to be most stable according to some criterion [57]. Post-smoothing [58, 59] of the ML estimate is also a way to tackle the problem. Another solution to the instability is the use of Bayesian methods [60] to get a maximum *a posteriori* (MAP) estimate. The MAP estimate is equivalent to a penalized ML reconstruction.

The MAP estimate $\hat{\mathbf{f}}$ for the data $\mathbf{g}$ is given by

$$\hat{\mathbf{f}} = \arg \max_{\mathbf{f}\geq\mathbf{0}} p(\mathbf{f}|\mathbf{g}) = \arg \max_{\mathbf{f}\geq\mathbf{0}} \log p(\mathbf{f}|\mathbf{g}) = \arg \max_{\mathbf{f}\geq\mathbf{0}} \log\left(\Pr(\mathbf{g}|\mathbf{f})p(\mathbf{f})\right) \tag{3.5}$$

where $p(\mathbf{f})$ is the prior probability of the object $\mathbf{f}$. The MAP objective is

$$\begin{aligned} \Phi(\mathbf{f};\mathbf{g}) &= (\log \Pr(\mathbf{g}|\mathbf{f}) + \log p(\mathbf{f})) \\ &\equiv (\Phi_L(\mathbf{f};\mathbf{g}) + \beta\Phi_P(\mathbf{f})) \end{aligned} \tag{3.6}$$

where $\Phi_P$ is the regularizer or prior, $\Phi_L$ is the likelihood and $\beta > 0$ is the scalar regularizing factor that controls the relative influence of the prior.

### 3.1.2 Regularizer

Many priors have been proposed [61, 62, 63, 64, 65]. The Gibbs distribution has been adopted as a suitable prior in an attempt to capture the locally structured properties of object [66]. The generalized form of the Gibbs distribution [67]:

$$P(\mathbf{f}) = \frac{1}{Z}\exp(-\beta\mathcal{U}(\mathbf{f})) \tag{3.7}$$

where $\beta > 0$ is a weight to adjust the influence of the prior. The choice of $\beta$ plays an important role in MAP regularized with this Gibbs prior. The term $Z$ is a normalization factor (partition function) that plays no role in the MAP reconstruction. The non-negative function $\mathcal{U}(\mathbf{f})$ is the Gibbs energy function or "potential" of the prior, is a sum of potentials, each of which is a function of a subset of cliques. The cliques for a particular neighborhood system must satisfy the condition that each pair of sites in each clique are mutual neighbors. When image $\mathbf{f}$ meets the prior assumptions, $\mathcal{U}(\mathbf{f})$ reaches its minimum and the prior function is maximized. The energy function can be rewritten as

$$\mathcal{U}(\mathbf{f}) = \sum_{n} \sum_{j \in \mathcal{N}(n)} \phi_{nj}(\mathbf{f}). \tag{3.8}$$

In (3.8), $\mathcal{N}(n)$ defines a neighborhood system of pixel $j$ while $\phi_{nj}(\mathbf{f})$ is the potential function which is dependent on $\mathcal{N}(n)$. The potential functions $\phi_{nj}(\mathbf{f})$ attempt to reflect the local smoothness among neighboring pixels. For a 2-D object, a four-pixel nearest neighborhood system (4NN) is shown in Figure 3.1 where the set of pixels that pixel $f_n$ is related with, $\mathcal{N}(n)$, includes $f_{j_1}$, $f_{j_2}$, $f_{j_3}$ and $f_{j_4}$. Another is an eight-nearest-pixel neighborhood system (8NN) with the corresponding $\mathcal{N}(n)$ including $f_{j_1}$, $f_{j_2}$, $\cdots$, $f_{j_8}$. These apply to 2D objects, and equivalent neighborhoods are used for 3D systems. For example, in 3D there are 26NN (including diagonal neighbors).

Figure 3.1: Illustration of neighborhood systems

The energy function for a quadratic smoothing membrane (MM) prior [68, 40] defined as the weighted summation of the quadratic function of the difference between neighboring pixels is equal to the negative of the prior:

$$\Phi_P(\mathbf{f}) = -\mathcal{U}(\mathbf{f}) = -\sum_{n=0}^{N-1} \sum_{j\in\mathcal{N}(n)} \frac{1}{2}\omega_{nj}(f_n - f_j)^2 \tag{3.9}$$

where $\mathcal{N}(n)$ is the neighborhood of pixel $n$ and $\omega_{nj} > 0$ is the weight related to each pair of neighboring pixels. Usually $\omega_{nj}$ is chosen to be proportional to the inverse of the distance between pixel $n$ and $j$, reflecting the fact that nearby pixels are more important. Note that $\omega_{nj} = \omega_{jn}$. The regularizer $\Phi_P(\mathbf{f})$ incorporates the quadratic membrane energy function.

The quadratic prior $\Phi_P(\mathbf{f})$ can be expressed in a quadratic [69] form $-\frac{1}{2}\mathbf{f}^T\mathcal{R}\mathbf{f}$, where a $N \times N$ matrix $\mathcal{R}$ is the Hessian of $\Phi_P(\mathbf{f})$. The elements of $\mathcal{R}$ for prior in (3.9) are given by

$$[\mathcal{R}]_{nj} = \frac{\partial^2}{\partial f_n \partial f_j}\left[\sum_{n=0}^{N-1} \sum_{j\in\mathcal{N}(n)} \frac{1}{2}\omega_{nj}(f_n - f_j)^2\right] \tag{3.10}$$

Thus,

$$[\mathcal{R}]_{nj} = \begin{cases} \sum_{j'\in\mathcal{N}(n)} 2\omega_{nj'} & j = n \\ -2\omega_{nj} & j \in \mathcal{N}(n) \\ 0 & j \notin \mathcal{N}(n) \quad \text{and} \quad j \neq n \end{cases} \tag{3.11}$$

Note that for such quadratic priors, $\mathcal{R}$ is independent of the object. This quadratic form will later serve as a mathematical convenience.

The Gibbs distribution with quadratic membrane prior is

$$p(\mathbf{f}) = \frac{1}{Z}\exp(-\beta \sum_{n=0}^{N-1} \sum_{j\in\mathcal{N}(n)} \omega_{nj}(f_n - f_j)^2) \tag{3.12}$$

Taking the logarithm of $p(\mathbf{f})$ and then dropping the terms $\log\frac{1}{Z}$ and $\beta$ in (3.9), the overall MAP objective becomes

$$\Phi(\mathbf{f},\mathbf{g}) = \sum_{m=0}^{M-1}\left[g_m \log(\sum_{n=0}^{N-1}[\mathcal{H}]_{mn}\mathbf{f}_n) - (\sum_{n=0}^{N-1}[\mathcal{H}]_{mn}\mathbf{f}_n)\right] - \beta\sum_{n=0}^{N-1} \sum_{j\in\mathcal{N}(n)} \frac{1}{2}\omega_{nj}(f_n - f_j)^2 \tag{3.13}$$

and the MAP estimate becomes

$$\hat{\mathbf{f}} = \arg\max_{\mathbf{f}\geq\mathbf{0}} \Phi(\mathbf{f},\mathbf{g}) \tag{3.14}$$

### 3.1.3 Optimization Techniques to Maximize the Objective Function

The maximizations in (3.3) and (3.14) are constrained optimizations. In principle, any standard optimization algorithm can be applied to get the estimates. However, it is difficult to simply apply a textbook algorithm to this problem. For MAP the reconstruction $\hat{\mathbf{f}}$ is termed the "fixed point" of the objective and will be unique and independent of initial condition for the convex prior in (3.9). For ML reconstructions that are terminated early to control noise, the result *does* depend on the algorithm and the final estimate is not technically and ML estimate. We will give a brief discussion of a few optimization algorithms that have been applied in statistical reconstruction for emission tomography. The description of the algorithms is cursory since it is not a focus of the thesis. The reader is referred to the references for more detail.

### 3.1.4 Preconditioned Conjugate Gradient Algorithm

The PCG algorithm belongs to a class of optimization methods known as gradient methods. At each iteration the objective function is optimized along a search direction. For $k = 0, 1, 2, \cdots$

- Compute gradient $\nabla\Phi(\mathbf{f}^k)$, where $\nabla\Phi(\mathbf{f}^k) = \mathcal{H}^T\left(\frac{\mathbf{g}}{\mathcal{H}\mathbf{f}^{(k)}} - \mathbf{1}\right) - \beta\mathcal{R}\mathbf{f}^{(k)}$
- Compute $\mathbf{p}^k = \mathcal{M}^k\nabla\Phi(\mathbf{f}^k)$
- Compute direction vector $\mathbf{d}^k$:

  If $k = 0$, $\mathbf{d}^0 = \mathbf{p}^0$

  else

  - Compute $\lambda^k = \frac{\left(\nabla\Phi(\mathbf{f}^k) - \nabla\Phi(\mathbf{f}^{k-1})\right)^T\mathbf{p}^k}{\left(\nabla\Phi(\mathbf{f}^{k-1})\right)^T\mathbf{p}^{k-1}}$ (from Polak-Ribiere form)
  - $\mathbf{d}^k = \left(\mathbf{p}^k\right)^T + \lambda^k\mathbf{d}^{k-1}$
- Line search $x^k = \arg\ \max_\alpha \Phi(\mathbf{f}^k + \alpha\mathbf{d}^k)$

- Update $\hat{\mathbf{f}}^{k+1} = \hat{\mathbf{f}}^k + x^k \mathbf{d}^k$

Note that projection and backprojection operations are involved in PCG. These must be implemented by custom software. The direction vectors are $\mathbf{Q}$-orthogonal i.e. $\mathbf{d}^k\mathbf{Q}\mathbf{d}^k$=0. The matrix $\mathcal{M}^k$ is called the preconditioner and can be used to reduce the number of iterations. Considerable effort has been devoted to the design of preconditioners [70, 71, 72, 73]. PCG in itself does not preserve positivity.

### 3.1.5 Expectation Maximization Algorithm

The expectation maximization (EM) algorithm is another iterative technique that has been applied to the maximum-likelihood estimate. The ML-EM technique was first presented by Dempster *et al.* [74] in its full generality. Later, its application in emission tomography was proposed independently by Shepp and Vardi [75] and Lange and Carson [76]. The ML-EM update for the $(k+1)^{th}$ iteration $\hat{\mathbf{f}}^{k+1}$ is given by:

$$\hat{f}_n^{k+1} = \frac{\hat{f}_n^k}{\sum_m \mathcal{H}_{mn}} \sum_m \mathcal{H}_{mn} \frac{g_m}{[\mathcal{H}\hat{\mathbf{f}}^k]_m} \tag{3.15}$$

The ML-EM algorithm is preserves positivity and is easy to implement. One drawback is its slow convergence. As in other iterative ML techniques the noise increases as the number of iterations increase. MAP can solve this latter problem.

The prior in MAP causes coupling between different voxels. The EM-type updates are no longer separable, but a surrogate method introduced in [77, 78] solves this problem. The MAP update for (3.14) becomes

$$\hat{f}_n^{k+1} = \frac{-B + \sqrt{B^2 - 4AC}}{2A} \tag{3.16}$$

where $A = 4\beta \sum_{n' \in \mathcal{N}(n)} \omega_{nn'}$,$B = -\sum_{n' \in \mathcal{N}(n)} 2\beta\omega_{nn'}(\hat{f}_n^k - \hat{f}_{n'}^k) + \sum_m \mathcal{H}_{mn}$ and $C = -\hat{f}_n^k \sum_m \mathcal{H}_{mn} \frac{g_m}{[\mathcal{H}\hat{\mathbf{f}}^k]_m}$

One problem with the EM-ML and EM-MAP algorithms described above is that they are slow to converge. It has been found that the convergence speed of the EM algorithm can be considerably improved using the "ordered-subsets" (OS) technique [79]. In the ordered-subsets technique, the projection data $\mathbf{g}$ is divided into subsets $S_l, l = 1, \cdots, L$ and a sub-iteration loop indexed by $l$ is added inside the main iteration. The typical method of selecting the subsets is as follows : Suppose the projection data were collected over 64 angles, and we decide to use 16 subsets. Then the first subset will corresponds to the projection data over the angles $\theta_1, \theta_{17}, \theta_{33}, \theta_{49}$, the second subset corresponds to the projection data of the angles $\theta_2, \theta_{18}, \theta_{34}, \theta_{50}$ and the $l^{th}$ subset $S_l$ corresponds to $\theta_l, \theta_{16+l}, \theta_{2(16)+l}, \theta_{3(16)+l}$ and so on. The subsets are chosen so that the projection data in each subset could have been obtained from a tomographic scan at a coarser angular spacing. Each inner iteration corresponds to a subset and all projections and backprojections required by the iterative update are performed only over that subset. The object estimate is updated during each inner iteration or *subiteration*. A version of the EM algorithm using OS is the popular OSEM algorithm [79]. Its update is similar to (3.15) and is given by

$$\hat{f}_n^{(k,l)} = \frac{\hat{f}_n^{(k,l-1)}}{\sum_{m \in S_l} \mathcal{H}_{mn}} \sum_{m \in S_l} \mathcal{H}_{mn} \frac{g_m}{[\mathcal{H}\hat{\mathbf{f}}^{(k,l-1)}]_m} \tag{3.17}$$

where $\hat{f}_n^{(k,l-1)}$ is the estimate from the $k^{th}$ iteration and $(l-1)^{th}$ subiteration, used to get the update for the $k^{th}$ iteration and $l^{th}$ subiteration. One full iteration, indeed by $k$, comprises one pass through all the subsets i.e. all the $L$ subiterations. The OSEM algorithm is fast but does not technically converge to the ML estimate. In a later development, a row-action maximum likelihood algorithm (RAMLA) [80] was proposed by including strong under relaxation in a modified version of OSEM that converges to the ML estimate. For the MAP case (Block Sequentially regularized EM) BSREM [81] and modified BSREM [82] were proposed which also require setting a relaxation schedule to achieve convergence.

Other algorithms, the Complete Data Ordered Subset Expectation Maximization (COSEM) for ML [83] and MAP [84] have been developed in our group. We use this algorithm for Chapter 6. Although it is slightly slower than the BSREM algorithm, it does not require a relaxation schedule to ensure convergence and hence has fewer free parameters and is easy to use. The derivation, convergence proof and implementation of the are found in [85].

Though the algorithm is complex, we list the MAP version in detail there since we will use it extensively for many of the MAP reconstructions of the ensuing chapters. For simplicity, we drop the carat over $\mathbf{f}$ in object estimates so that $f_n^{k,l}$ is understood to be the estimate of $f_n$ at iteration $k$ and the subiteration $l$. Below is the pseudocode for COSEM-MAP.

```
• **The COSEM-MAP Algorithm**
• Initialize $\{f_n^{(0,0)} = f_n^{\text{init}}, \forall n \in \{1, \dots, N\}\}$
• Initialize $\{c_{mn}^{(0,0)}, \forall m \in S_l, \forall l \in \{1, \dots, L\}$ and $\forall n \in \{1, \dots, N\}\}$ by
  $c_{mn}^{(0,0)} = g_m \frac{\mathcal{H}_{mn} f_n^{(0,0)}}{\sum_n \mathcal{H}_{mn} f_n^{(0,0)}}$
• $B_n^{(0,0)} = \sum_{l'=1}^{L} \sum_{m \in S_{l'}} c_{mn}^{(0,0)}, \forall n$
• **Begin** k-loop $[k \in \{0, 1, \dots\}]$
    – $c_{mn}^{(k,0)} = c_{mn}^{(k-1,L)}, \forall m,\, n\, \text{and}\, k > 0.$
    – $B_n^{(k,0)} = B_n^{(k-1,L)}, \forall n\, \text{and}\, k > 0.$
    – $f_n^{(k,0)} = f_n^{(k-1,L)}, \forall n\, \text{and}\, k > 0.$
    – **Begin** l-loop $[l \in \{1, \dots, L\}]$
        * $c_{mn}^{(k,l)} = g_m \frac{\mathcal{H}_{mn} f_n^{(k,l-1)}}{\sum_{n'} \mathcal{H}_{mn'} f_{n'}^{(k,l-1)}}, \forall m \in S_l, \forall n$ .
        * $c_{mn}^{(k,l)} = c_{mn}^{(k,l-1)}, \forall m \notin S_l, \forall n$
        * $B_n^{(k,l)} = \sum_{m \in S_l} (c_{mn}^{(k,l)} - c_{mn}^{(k,l-1)}) + B_n^{(k,l-1)}, \forall n$
        * $f_n^{(k,l)} = \frac{-B + \sqrt{B^2 - 4AC}}{2A}, \quad \forall n \in \{1, \dots, N\}$
          where
            · $A = 8\lambda \sum_{n' \in \mathcal{N}(n)} w_{nn'}$,
```

```
            · $B = \sum_m \mathcal{H}_{mn} - 4\lambda \sum_{n' \in \mathcal{N}(n)} w_{nn'}(f_n^{(k,l-1)} + f_{n'}^{(k,l-1)})$ and
            · $C = -B_n^{(k,l)}$.
        – End l-loop
    • End k-loop
```

## 3.2 Deterministic methods

Deterministic methods search for a solution $\hat{\mathbf{f}}$ directly from the deterministic model of projection $\mathbf{g} = \mathcal{H}\mathbf{f}$. This deterministic model is obtained simply by removing the noise in (2.13). Thus $\mathbf{g}$ becomes deterministic (although it is actually a single noise realization). Thus deterministic methods for SPECT attempt to invert an inconsistent system of linear equations. As opposed to statistical methods, they do not model the noise in projection data, but they can easily incorporate a system matrix $\mathcal{H}$.

### 3.2.1 Algebraic Reconstruction Technique

The algebraic reconstruction technique (ART) is a method which can be applied to any system of linear equations. In particular, it can be applied to the system $\mathbf{g} = \mathcal{H}\mathbf{f}$. In 1970, it was applied by Gordon *et.al* [86] as a tomographic reconstruction method. ART is an iterative method which includes a forward projection and correction back projection in the $k$th iteration [87]:

$$f_n^{k+1} = f_n^k + \frac{[\mathcal{H}]_{mn}(g_m - [\mathcal{H}\mathbf{f}^k]_m)}{\sum_n [\mathcal{H}]^2_{mn}} \qquad m = k(mod\, M) \tag{3.18}$$

SART, a simultaneous version of ART [86, 87] was developed:

$$f_n^{k+1} = f_n^k + t \sum_m \frac{[\mathcal{H}]_{mn}(g_m - [\mathcal{H}\mathbf{f}^k]_m)}{\sum_n [\mathcal{H}]^2_{mn}} \tag{3.19}$$

where $t > 0$ is chosen to ensure $\mathcal{I} - t\mathcal{H}^T\mathcal{H}$ is positive definite. ART is slow to converge which prevents its wide use in clinical applications. Linear algebraic methods such as ART and SART [2] are advantageous in that they can incorporate sophisticated imaging models via the $\mathcal{H}$ matrix, but their deterministic model is equivalent to an (incorrect) assumption of uniform Gaussian noise as the noise model. This implicit noise model is inaccurate for photon-limited imaging systems (such as SPECT) and hence statistical methods are more useful [2]

### 3.2.2 Filtered Back Projection

The most famous and popular reconstruction method is filtered backprojection (FBP). It is naturally derived in continuous space and so is a method for obtaining (for a 2-D case) $f(x, y)$ from an analytic version of the sinogram. Many versions of FBP exist for different acquisition geometries, but here we summarize the well-known case for a 2D parallel ray projections [10, 88]. It assumes that the observed sinogram is a continuous 2-D function and that is a Radon transform of the underlying object, i.e.,

$$g(t,\theta) = \int_{-\infty}^{\infty}\int_{-\infty}^{\infty} f(x,y)\delta(xcos\theta + ysin\theta - t)dxdy \tag{3.20}$$

where $\theta$ is the projection angle and $t$ is the projection bin. It can be shown that the Radon transform can be inverted with the following operations:

1. Ramp Filtering

$$\begin{aligned} \text{Fourier Transform of Data:} \quad G(\rho,\theta) &= \int_{-\infty}^{\infty} g(t,\theta)\exp(-j2\pi t\rho)dt && (3.21)\\ \text{Apply Ramp Filter:} \quad Q(\rho,\theta) &= |\rho|G(\rho,\theta) && (3.22)\\ \text{Inverse Fourier Transform:} \quad q(t,\theta) &= \int_{-\infty}^{\infty} Q(\rho,\theta)\exp(-j2\pi t\rho)d\rho && (3.23) \end{aligned}$$

2. Backprojection

$$\hat{f}(x,y) = \int_0^{\pi} q(t,\theta)|_{t=xcos\theta+ysin\theta}d\theta \tag{3.24}$$

Discretization of the above inversion formulae gives us the filtered backprojection (FBP) algorithm used often in the clinic. The ramp filtering operation can be performed in the frequency domain with a Fast Fourier Transform (FFT). To mitigate the effects of noise, an apodizing filter is often used in addition to the ramp filter in the above equations.

FBP is popular due to its speed, but it models only parallel ray projection (essentially our $\mathcal{Y}$ matrix) and not any other physical effects in H. It can be modified, however, to approximately account for some of these physical effects. To compensate for depth-dependent collimator blur, we may apply to the observed data an inverse filter based on the approximate frequency-distance relation [89, 9] between the observed data and its Radon counterpart. The form of the frequency-distance relation is highly dependent on the geometry of the collimator and the orbit of rotation of the camera. To compensate for non-uniform attenuation, an empirical data-correction technique such as the Chang method [90, 9] is often used. The accuracy of these methods is highly-dependent on the geometry of the collimator and the camera orbit.

By contrast, all geometrical and physical effects including non-circular orbits can be simply included in the $\mathcal{H}$ matrix in statistical and linear algebraic reconstructions. The price one pays for this is speed - FBP is less than one iteration, while MAP, ART and other algorithms can take 10's of iterations. For SPECT, the data sets are not that large and reconstruction speed is not a problem if a modern high-speed cluster is used.

# Chapter 4

## Model Observers for the Detection Task

One of the most important criteria in assessing the quality of a medical image is how well does the image allow a human observer to perform a certain task. Often the task is a detection task in which the observer has to detect the presence or absence of signal (lesion) in the background (underlying object). An image obtained is "better" than another if the probability of correctly detecting or rejecting the presence of the signal using this image is greater than that using an image from a different imaging system or reconstruction algorithm.

In this chapter we will be giving a basic background on detection theory and discussing some common figures of merit as a measure of the detection task performance. In our discussion we assume the signal to be deterministic, i.e. its size, contrast and location are known. With the signal fixed we discuss two types of tasks. In the first, we assume that the background to be known and fixed. The only type of noise in the reconstructed images is that propagated via the reconstruction from the photon noise in the projection data. Such a simplified detection task is known as a signal-known-exactly/background-known-exactly (SKE/BKE) detection task and allows for analytical computation of figures of merit. In the second, slightly more realistic task known as the signal-known-exactly/background-known-statistically (SKE/BKS) detection task, we assume the signal to known and fixed and the background to be random but known statistically.

Assessment of task performance involves an observer. It could be a human, or a mathematical observer that emulates human performance or an ideal mathematical observer whose verdict is based on an optimal decision criteria. As mentioned earlier in Section 1.4 we are concerned with the detection performance of human observers. Since detection studies using human observers are laborious, there has been an extensive effort [27] to substitute mathematical "model" observers, derived from signal processing theory and psychophysics, to emulate human observers. A scalar figure of merit (FOM) has to be determined as a measure of performance of the observer in the detection task. It may be used to quantitatively compare or optimize different imaging system parameters or different reconstruction algorithms in the context of the detection task.

In the SKE/BKE task the only source of noise corrupting the reconstructed images is the Poisson noise in the raw projection data. In the SKE/BKS task the projection data has two components of noise (1) due background variability in the underlying object and (2) the Poisson noise in the image formation process. Background variability is the statistical variability in the uptake $\mathbf{f}$, now considered random. It occurs on different spatial scales. Background variability found in real human patient distribution includes anatomical variability [91], organ uptake variability and small scale local fluctuations [92] which can be referred as "texture". Since radionuclide tends to localize roughly uniformly in different anatomical organs, the shape/size variability of organs in a patient population is a source of so-called anatomical variability. In addition, the average uptake level per organ can vary amongst populations, so that uptake variability is another source of object uncertainty. Perhaps most important are small scale "textural variations" due to small scale anatomical uptake variations in the object. This texture noise can easily mask detection of a lesion that would otherwise be easily seen against a uniform background. In the radar and remote-sensing literature this form of background variability is known as "clutter". Because small scale textural variability is such an important effect we shall henceforth imply this kind of variability when speaking of object variability. Random backgrounds that use variability due to anatomical structures are generally too complex to be dealt with analytically, though sample based methods can be used in this case.

A number of works have used models for texture variability based on random processes from which the first and second moments can be derived analytically. One example of such analytic models is the "Lumpy" backgrounds [93, 94, 29] derived by convolving a two-dimensional Poisson spatial point process with a "lump" profile. In another example [95], we modeled textural background variability as additive zero mean multivariate Gaussian noise. It was obtained by blurring iid Gaussian noise with a Gaussian kernel. In [33, 30] variability was simulated using a stationary Gaussian process with a noise power spectrum which follows an inverse-power law over a range of spatial frequencies.

In Chapter 5 we will be considering the task of detecting a signal in a statistically known background. In our group we have also done original work on signal-known-statistically/background-known-statistically (SKS/BKS) [28, 96, 97] but we do not discuss it here. In the following sections, we first describe the FOM in general. Then, the commonly used model observers, the Hotelling and the Channelized Hotelling observers that are developed in Section 4.2. The model observers described in this Chapter and used in this thesis need only the first and second order statistics of the reconstructed images for both the SKE/BKE and SKE/BKS cases. For this we address the topic of noise propagation through the reconstruction in Section 4.3.

## 4.1 Figures of merit

One of the simplest detection problems is the binary hypothesis testing problem of detecting a signal in noise [98]. The first hypothesis, denoted by $H_0$ and called the null hypothesis, corresponds to the absence of signal. The second hypothesis, denoted by $H_1$ and called the alternate hypothesis corresponds to the signal-present case. For each image, the observer (receiver or detector) calculates a scalar test statistic $\lambda$ known as the observer response which represents the degree of agreement with $H_1$. The observer then compares this quantity to some threshold $\gamma$ and decides in favour of hypothesis $H_1$ if $\lambda \geq \gamma$ and hypothesis $H_0$ if $\lambda < \gamma$. The probability density function of the observer response conditioned on the underlying hypotheses $H_0$ and $H_1$ are denoted by $p(\lambda|H_0)$ and $p(\lambda|H_1)$, respectively. Such conditional pdf's are shown in Figure 4.1.

In general the observer will classify some of the images correctly and some of then incorrectly. For a particular decision threshold $\gamma$ the classification performance can be summarized as follows

$$\begin{aligned} \text{TPF} &= \Pr(\lambda \geq \gamma|H_1) \qquad (4.1)\\ \text{FPF} &= \Pr(\lambda \geq \gamma|H_0) \\ \text{TNF} &= 1 - \text{FPF} \\ \text{FNF} &= 1 - \text{TPF} \end{aligned}$$

The TPF, or “true positive fraction”, is the probability of guessing that the signal is present when it is indeed present. The FPF, or “false positive fraction”, is the probability of guessing that the signal is present when it is in fact absent. The TNF, or “true negative fraction”, is the probability of guessing that the signal is absent when it is indeed absent. The FNF, or “false negative fraction”, is the probability of guessing that the signal is absent when it is in fact present. Obviously TPF+FNF=1

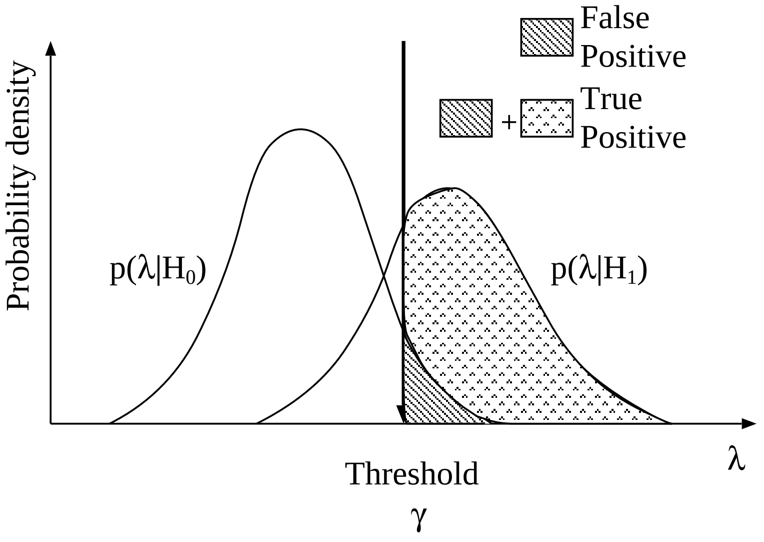

Figure 4.1: The decision making diagram. As indicated in the legend, the shaded areas under the curves represent the false positive and true positive decision probabilities for the threshold shown. The areas of the shaded regions form one point on the ROC curve. As $\gamma$ is swept, the ROC curve is generated.

and TNF+FPF=1, so only two of the 4 quantities are independent. TPF and TNF are also known as sensitivity and specificity, respectively. A plot of all possible pairs of TPF and FPF obtained as the threshold $\gamma$ is varied is called the receiver operating characteristic (ROC) curve [98, 99]. The ROC curve can be generated by sweeping the threshold $\gamma$ as shown in Figure 4.1 and measuring the areas below the $p(\lambda|H_0)$ and $p(\lambda|H_1)$ to the right of the threshold. The area under this ROC curve (AUC) is commonly used [29] as a figure of merit (FOM) to assess observer performance. Figure 4.2 shows several ROC curves. The best possible ROC curve (solid line), shown in Figure 4.2, has an AUC=1, and more realistic ROC curves (dot-dashed and long dashed), shown in Figure 4.2, have $0.5 < \text{AUC} \leq 1$. The small dashed (diagonal line) curve is the worst possible ROC curve. Its area, 0.5, is tantamount to two observer response curves that overlap with no separation.

Another FOM for signal detection is the detectability $d_A$ [29, 33]. This FOM is defined as a nonlinear transformation of the AUC. The relation is given by

$$d_A = 2\text{erf}^{-1}(2\text{AUC} - 1) \tag{4.2}$$

where $\text{erf}^{-1}(\cdot)$ denotes the inverse error function.

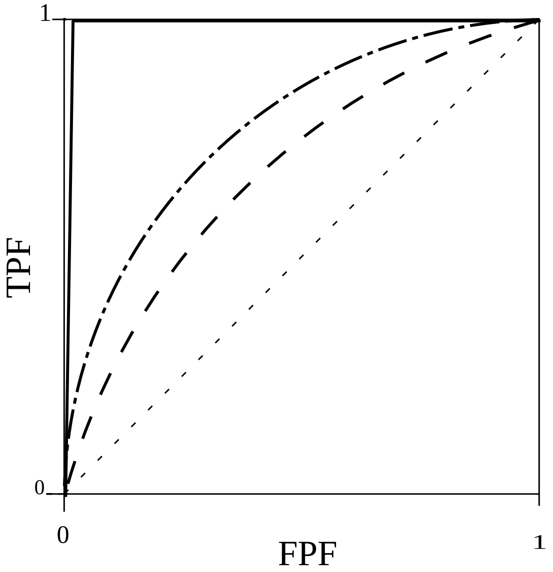

Figure 4.2: Plots of TPF vs FPF showing a few ROC curves. The solid curve has a AUC=1, and is the best possible curve. The linear diagonal curve has an AUC=0.5 and is the worst. More realistic ROC curves are displayed as the dash-dot and dashed curves.

Another available FOM for detection tasks, found to have a monotonic relationship to AUC under certain conditions, is the observer signal-to-noise ratio (SNR)

$$\text{SNR}^2 = \frac{(\langle\lambda|H_1\rangle - \langle\lambda|H_0\rangle)^2}{\frac{1}{2}\Big(var(\lambda|H_1) + var(\lambda|H_0)\Big)} \tag{4.3}$$

where $\langle\lambda|H_1\rangle$ and $\langle\lambda|H_0\rangle$ are means of $\lambda$ under hypotheses $H_1$ and $H_0$, $var(\lambda|H_1)$ and $var(\lambda|H_0)$ are the variances of $\lambda$ under hypotheses $H_1$ and $H_0$. The SNR is a way to measure the separability of the two lumps of the probability density functions. The bigger the difference between their means and the smaller their variance is, the more separable they are. If they are highly separable, then the probability of a correct decision is increased. Notice that SNR only requires the information of the first and second moments of $p(\lambda|H_0)$ and $p(\lambda|H_1)$, thus is less representative but easier to be quantified than AUC. If the observer response has a Gaussian distribution under each hypothesis then the SNR is related to AUC by [100]

$$\mathrm{SNR} = 2\mathrm{erf}^{-1}(2\mathrm{AUC} - 1) = d_A \tag{4.4}$$

We do not need equal variances for 4.4 to hold.

## 4.2 Model Observers

To evaluate the performance for a detection task one would have to perform a human observer study using well-established ROC testing methodologies [101, 102] and then assess performance using the AUC. ROC testing is labor intensive, and if one is to optimize a reconstruction algorithm over many parameters or a wide range of one parameter, the amount of labor required becomes formidable. Model (computational) observers [27] that emulate human performance have been proposed, and the hope is that these may be used to lower this burden. While not meant to replace human observers, model observers might be used, in principle, to rapidly cull the parameter search space down to a few select candidates that can be addressed by ROC testing. That is, if one seeks to optimize some parameter(s) by ROC testing, one might well use model observers to cull the parameter space to a size manageable by human ROC testing. Our focus will be on such mathematical model observers wherein the test statistic can be derived from an explicit formula.

For both the SKE/BKE and SKE/BKS tasks we express the two hypothesis as

$$H_1: \quad \mathbf{f} = \mathbf{b} + \mathbf{s} \tag{4.5}$$

$$H_0 : \qquad \mathbf{f} \;=\; \mathbf{b}$$

where $\mathbf{b}$ is the (possibly random) background and $\mathbf{s}$ deterministic signal. The hypothesis $H_0$ is the signal-absent hypothesis and hypothesis $H_1$ is the signal-present hypothesis. For the SKE/BKE task the background is also fixed. Since for SKE/BKE the underlying object $\mathbf{f}$ is fixed under the two hypothesis, hence $\Pr(\mathbf{g}|H_0) = \Pr(\mathbf{g}|\mathbf{f}, H_0)$ and $\Pr(\mathbf{g}|H_1) = \Pr(\mathbf{g}|\mathbf{f}, H_1)$. We know that $\Pr(\mathbf{g}|\mathbf{f}, H_0)$ and $\Pr(\mathbf{g}|\mathbf{f}, H_1)$ are Poisson with means $\mathcal{H}\mathbf{f}_1$ and $\mathcal{H}\mathbf{f}_2$ respectively. It will be henceforth convenient to use the notation $\mathbf{f}_1$ and $\mathbf{f}_2$ for the signal-absent and signal-present objects, respectively, for both the SKE/BKE and SKE/BKS cases. Thus the expressions $\Pr(\mathbf{g}|\mathbf{f}, H_0)$ and $\Pr(\mathbf{g}|\mathbf{f}_1)$ are equal, as are $\Pr(\mathbf{g}|\mathbf{f}, H_1)$ and $\Pr(\mathbf{g}|\mathbf{f}_2)$.

Note that we have denoted the Poisson means above as $\mathcal{H}\mathbf{f}_1$ and $\mathcal{H}\mathbf{f}_2$. For the same reasons we use $\mathcal{H}$ instead of H in reconstruction algorithms, we shall use $\mathcal{H}$ instead of H in observer expressions in this chapter. The reasons ultimately have to do with computational tractability. That is, by conducting detectability experiments using $\mathcal{H}$ in place of H we greatly ease the computational burden.

For the SKE/BKS task the background $\mathbf{b}$ is a realization from a stochastic random process with mean $\boldsymbol{\mu}_b$ and covariance $\mathcal{K}_b$. The probability density function of the underlying object under the two hypothesis is $p(\mathbf{f}|H_0)$ and $p(\mathbf{f}|H_1)$. The probability distribution of $\mathbf{g}$ conditioned on the underlying object $\mathbf{f}$ (which is a realization of a random process) and respective hypothesis, is given by $\Pr(\mathbf{g}|\mathbf{f}, H_0)$ and $\Pr(\mathbf{g}|\mathbf{f}, H_1)$, is Poisson with mean $\mathcal{H}\mathbf{f}_1$ and $\mathcal{H}\mathbf{f}_2$ respectively. The overall probability of the raw projection data $\mathbf{g}$ under the two hypothesis is

$$\Pr(\mathbf{g}|H_0) = \int_{f_{N-1}} \cdots \int_{f_0} \Pr(\mathbf{g}|\mathbf{f}, H_0) p(\mathbf{f}|H_0) \mathtt{d}f_0 \cdots \mathtt{d}f_{N-1} \tag{4.6}$$

$$\Pr(\mathbf{g}|H_1) = \int_{f_{N-1}} \cdots \int_{f_0} \Pr(\mathbf{g}|\mathbf{f}, H_1) p(\mathbf{f}|H_1) \mathtt{d}f_0 \cdots \mathtt{d}f_{N-1} \tag{4.7}$$

The observer is to inspect the reconstruction $\hat{\mathbf{f}}$ and decide to which hypothesis $H_0$ or $H_1$ it belongs. To do this model observer computes a scalar test statistic $\lambda$ via $\lambda = w(\hat{\mathbf{f}})$, where $w$ is some operation (linear or non-linear) on $\hat{\mathbf{f}}$. Then $\lambda$ is compared to $\gamma$ and a hypothesis chosen. Observers can be classified on whether the test statistic is optimal or suboptimal or whether $w$ is a linear or non-linear operation.

### 4.2.1 Ideal Observer

For the two-class decision problem, the ideal observer yields optimal task performance in that it achieves maximum AUC, maximum TPF for a fixed FPF (the Neyman Pearson lemma), and minimum Bayes' risk [29]. As explained in [99, 103], the choice of ideal observer is independent of costs associated decisions. The likelihood ratio test is the optimal decision strategy. The ideal observer is given by the log of the likelihood ratio test

$$\lambda = w(\hat{\mathbf{f}}) = \ln\left[\frac{(p(\hat{\mathbf{f}}|H_1))}{(p(\hat{\mathbf{f}}|H_0))}\right] \tag{4.8}$$

The computation of the ideal observer's performance requires full knowledge of the probability distributions for the random quantities it operates on (here, the reconstruction) under the competing hypothesis. The expressions $p(\hat{\mathbf{f}}|H_0)$ and $p(\hat{\mathbf{f}}|H_1)$ are usually too difficult to express analytically.

For imaging system optimization it is interesting to note [33, 29] that the ideal observer can also be applied to the raw projection data $\mathbf{g}$ instead of the reconstruction $\hat{\mathbf{f}}$. The ideal observer would be given in this case by

$$w(\mathbf{g}) = \ln\left[\frac{(\Pr(\mathbf{g}|H_1))}{(\Pr(\mathbf{g}|H_0))}\right] \tag{4.9}$$

$\Pr(\mathbf{g}|H_1)$ and $\Pr(\mathbf{g}|H_0)$ in (4.9) for SKE/BKS tasks are given by (4.7) and (4.6). Computation of the likelihood ratio for SKE/BKS task modelling textural variability in the form of lumpy background is described in [104] and modelling large scale anatomical variability are described in [105]. The ideal observer acting on $\mathbf{g}$ sets an upper bound on the maximum achievable AUC. The detectability of the ideal observer acting on the reconstructed images $\hat{\mathbf{f}}$ will be less than or equal to the detectability of the ideal observer acting in the projection data $\mathbf{g}$. If the reconstruction operation is invertible in the sense that the original projection data is recoverable then the ideal observer acting on the reconstructed image or the projection data will give the same result [106, 29].

We want to use model observers that are *sub*optimal in that they emulate human performance. Thus, even if an ideal observer of the form (4.8) where available, we'd be interested instead in a model observer that emulates human performance. Ideal observers are nonlinear except in few simple circumstances. Our human emulating observers will be linear. We first consider a general class of linear observers, then specialize these to human-emulating observers.

### 4.2.2 Hotelling Observer

Since the Bayesian ideal observer is intractable in many situations, one often considers the optimal linear or Hotelling observer. Linear observers have the general form $\lambda = \mathbf{w}^T\hat{\mathbf{f}}$ where the $N$-dimensional vector $\mathbf{w}$ is referred to as the observer template. (Note that if the reconstructed image $\hat{\mathbf{f}}$ had a Gaussian distribution with same covariance under both hypotheses then the ideal observer would be linear and would be the same as the Hotelling observer [33, 29]. But this is not the case in real tomographic systems.) The Hotelling Observer template $\mathbf{w}$ requires knowledge and the first order statistics $\bar{\hat{\mathbf{f}}}_2$ and $\bar{\hat{\mathbf{f}}}_1$ under the hypothesis $H_1$ and $H_0$, respectively. It also requires knowledge of the average covariance $\mathcal{K}_{\hat{\mathbf{f}}}$ defined as $\mathcal{K}_{\hat{\mathbf{f}}} = \frac{1}{2}(\mathcal{K}_{\hat{\mathbf{f}}|H_0}+\mathcal{K}_{\hat{\mathbf{f}}|H_1}) \equiv \frac{1}{2}(\mathcal{K}_{\hat{\mathbf{f}}_1}+\mathcal{K}_{\hat{\mathbf{f}}_2})$ . The Hotelling observer corresponds to $\mathbf{w} = \mathcal{K}_{\hat{\mathbf{f}}}^{-1}(\bar{\hat{\mathbf{f}}}_2 - \bar{\hat{\mathbf{f}}}_1)$. It turns out that the Hotelling SNR$^2$ is given [33] by :

$$\text{SNR}_{HO}^2 = (\bar{\hat{\mathbf{f}}}_2 - \bar{\hat{\mathbf{f}}}_1)^T\mathcal{K}_{\hat{\mathbf{f}}}^{-1}(\bar{\hat{\mathbf{f}}}_2 - \bar{\hat{\mathbf{f}}}_1) \tag{4.10}$$

The Hotelling observer models the data as Gaussian regardless of the data's true statistics.

As in the case for the ideal observer, the Hotelling observer can also be applied to the raw projection data instead of the reconstructed images. If the reconstruction operation does not remove information from the raw data, i.e. if it is invertible, then the $\mathrm{SNR}_{HO}$ from the raw data will be the same as that from the reconstructed images. The rationale for computing $\mathrm{SNR}^2_{HO}$ in the data domain is that the expression in (4.10) for the reconstruction domain is much more computationally intense. The $\mathrm{SNR}^2_{HO}$ expressed in the data domain is

$$\mathrm{SNR}^2_{HO} = (\bar{\mathbf{g}}_2 - \bar{\mathbf{g}}_1)^T(\mathcal{K}_{\mathbf{g}}^{-1})(\bar{\mathbf{g}}_2 - \bar{\mathbf{g}}_1) \tag{4.11}$$

where $\bar{\mathbf{g}}_2$,$\bar{\mathbf{g}}_1$ are the mean data for signal present, absent, respectively, and

$$\mathcal{K}_{\mathbf{g}} = \frac{1}{2}(\mathcal{K}_{\mathbf{g}|H_0} + \mathcal{K}_{\mathbf{g}|H_1}) \tag{4.12}$$

We now consider the $\mathrm{SNR}^2_{HO}$ for the SKE/BKE case as expressed in the data domain. Clearly $\bar{\mathbf{g}}_2 = \mathcal{H}(\mathbf{b}+\mathbf{s})$ and $\bar{\mathbf{g}}_1 = \mathcal{H}(\mathbf{b})$ where $\mathbf{b}$ is the fixed background, so that $\bar{\mathbf{g}}_2 - \bar{\mathbf{g}}_1 = \mathcal{H}\mathbf{s}$. The covariance of $\mathbf{g}$ is $\mathcal{K}_{\mathbf{g}|H_0} = \mathrm{diag}(\mathcal{H}\mathbf{f}_1)$ and $\mathcal{K}_{\mathbf{g}|H_1} = \mathrm{diag}(\mathcal{H}\mathbf{f}_2)$ under the two hypotheses, respectively. Using (4.11) and (4.12) the Hotelling SNR for the SKE/BKE case becomes

$$\mathrm{SNR}^2_{HO} = \frac{1}{2}(\mathcal{H}\mathbf{s})^T(\mathrm{diag}\{\mathcal{H}(\mathbf{f}_2+\mathbf{f}_1)\})^{-1}(\mathcal{H}\mathbf{s}) \tag{4.13}$$

We now consider the SKE/BKS case. Here $\mathbf{f}_1 = \mathbf{b}$ and $\mathbf{f}_2 = \mathbf{b}+\mathbf{s}$ where $\mathbf{b}$ is now random with the mean $\boldsymbol{\mu}_{\mathbf{b}}$, and $\mathbf{s}$ is deterministic. The mean projection data is thus $\bar{\mathbf{g}}_2 = \mathcal{H}(\boldsymbol{\mu}_{\mathbf{b}}+\mathbf{s})$ and $\bar{\mathbf{g}}_1 = \mathcal{H}(\boldsymbol{\mu}_{\mathbf{b}})$. Thus $\bar{\mathbf{g}}_2 - \bar{\mathbf{g}}_1 = \mathcal{H}\mathbf{s}$. To compute SNR, we need an expression for $\mathcal{K}_{\mathbf{g}|H_0}$ and $\mathcal{K}_{\mathbf{g}|H_1}$. This is given in [29] as

$$\begin{aligned} \mathcal{K}_{\mathbf{g}|H_0} &= \mathrm{diag}(\mathcal{H}\boldsymbol{\mu}_{\mathbf{b}}) + \mathcal{H}^T\mathcal{K}_b\mathcal{H} && (4.14) \\ \mathcal{K}_{\mathbf{g}|H_1} &= \mathrm{diag}(\mathcal{H}(\boldsymbol{\mu}_{\mathbf{b}}+\mathbf{s})) + \mathcal{H}^T\mathcal{K}_b\mathcal{H} && (4.15) \end{aligned}$$

Using (4.14) and (4.15) and the expressions for $\bar{\mathbf{g}}_2$ and $\bar{\mathbf{g}}_1$, we obtain for the SKE/BKS case. The Hotelling SNR is given by

$$\mathrm{SNR}^2_{HO} = \frac{1}{2}(\mathcal{H}\mathbf{s})^T(\mathcal{K}_{\mathbf{g}|H_0} + \mathcal{K}_{\mathbf{g}|H_1})^{-1}(\mathcal{H}\mathbf{s}) \tag{4.16}$$

### 4.2.3 Channelized Hotelling Observer

The human visual system is suboptimal for detection. For SPECT, the ideal and Hotelling observers are not always good predictors of actual human performance. The channelized Hotelling observer (CHO) [29] is found to be a good predictor of human performance in detecting lesions in correlated noisy backgrounds such as those in SPECT reconstructions [39, 30, 59, 107, 108]. Abbey and Barrett [30] found agreement in human and CHO performance in SKE tasks to investigate the effects of regularization in tomographic images. Gifford [39] *et al.* found correlation between CHO and human observers to evaluate the impact of detector-response compensation on tumor detection in SPECT.

The CHO is a Hotelling observer modified with the use of anthropomorphic channels $\mathcal{T}$ to track human observer performance. It performs a detection task after reducing the image to a smaller set of response variables. The human visual system processes an image through frequency-selective channels to extract features. In the CHO, in order to model the human visual mechanism, each feature is obtained by applying a channel template at the lesion location. After reducing the input stimulus to a small set of channel responses, these responses are combined using an optimal linear combination rule (Hotelling). The loss of information due to channelization results in suboptimal performance.

To perform the feature extraction step the human visual system acts as if it operates on the Fourier transform of the retinal image. To extract each feature, the Fourier transform of the retinal image is integrated over the corresponding bandpass channel filter. This is mathematically equivalent to the inner product in the spatial domain of the image and the impulse response of the bandpass channel filter. The impulse response of the bandpass channel filter is the spatial domain representation of the channel.

The CHO observes a single 2D slice image extracted from the 3D reconstruction, as does a human observer. Let $\mathcal{L}$ be a linear slice extraction operator which is an $N_{2D} \times N$ matrix with $N_{2D}$ the number of pixels in the extracted image. The CHO applies anthropomorphic bandpass channels to reduce the $N_{2D}$-dim image into $N_c$ channel responses (features). The feature reduction step is carried out by the dot product of the image with each of the $N_c$ channel templates, similar to the description above for the human visual system. Since $N_c$ is usually around 3-6, the number of features is far less than the number of pixels $N_{2D}$. If the vector $\mathbf{t}^i$ is the $i^{th}$ channel template centered at the lesion center, then the corresponding $i^{th}$ channel response is $\hat{u}^i = (\mathbf{t}^i)^T \mathcal{L} \hat{\mathbf{f}}$. The feature vector is given by $\hat{\mathbf{u}} = \mathcal{T}^T \mathcal{L} \hat{\mathbf{f}}$, where $\mathbf{t}^i$ is the $i^{th}$ column of $\mathcal{T}$, and $\mathcal{T}$ is an $N_{2D} \times N_c$ matrix.

For SKE/BKE let $\bar{\hat{\mathbf{f}}}_1$ and $\bar{\hat{\mathbf{f}}}_2$ represent the mean (over data noise) reconstructions for the signal-absent and signal-present hypotheses respectively. Since, the background is fixed we have $\mathcal{K}_{\hat{\mathbf{f}}|H_0} = \mathcal{K}_{\hat{\mathbf{f}}|\mathbf{f},H_0} = \mathcal{K}_{\hat{\mathbf{f}}_1}$ and $\mathcal{K}_{\hat{\mathbf{f}}|H_1} = \mathcal{K}_{\hat{\mathbf{f}}|\mathbf{f},H_1} = \mathcal{K}_{\hat{\mathbf{f}}_2}$ under the two hypothesis respectively. The covariance $\mathcal{K}_{\hat{\mathbf{f}}} = \frac{1}{2}(\mathcal{K}_{\hat{\mathbf{f}}_1} + \mathcal{K}_{\hat{\mathbf{f}}_2})$. For SKE/BKS let $\bar{\hat{\mathbf{f}}}_1$ and $\bar{\hat{\mathbf{f}}}_2$ represent the mean reconstructions averaged over data noise and background variability for the signal-absent and signal-present hypotheses respectively. The (overall) covariance of $\hat{\mathbf{f}}$ under each hypothesis is given by $\mathcal{K}_{\hat{\mathbf{f}}|H_0} = \mathcal{K}_{\hat{\mathbf{f}}_1}$ and $\mathcal{K}_{\hat{\mathbf{f}}|H_1} = \mathcal{K}_{\hat{\mathbf{f}}_2}$, respectively. For SKE/BKS case, analytic methods to calculate $\mathcal{K}_{\hat{\mathbf{f}}_1}$ and $\mathcal{K}_{\hat{\mathbf{f}}_2}$ from $\mathcal{K}_{\mathbf{g}|H_0}$ and $\mathcal{K}_{\mathbf{g}|H_1}$ are given in [109, 94]. The covariance $\mathcal{K}_{\hat{\mathbf{f}}} = \frac{1}{2}(\mathcal{K}_{\hat{\mathbf{f}}_1} + \mathcal{K}_{\hat{\mathbf{f}}_2})$.

We now consider the calculation of the first and second order moments of the feature vector. The quantities $\hat{\mathbf{f}}_1$, $\hat{\mathbf{f}}_2$ and $\mathcal{K}_{\hat{\mathbf{f}}}$ have been defined for the SKE/BKE and SKE/BKS. The mean feature vectors $\bar{\hat{\mathbf{u}}}_2$ and $\bar{\hat{\mathbf{u}}}_1$ are obtained from $\bar{\hat{\mathbf{f}}}_1$ and $\bar{\hat{\mathbf{f}}}_2$, respectively.

$$\bar{\hat{\mathbf{u}}}_2 = \mathcal{T}^T \mathcal{L} \bar{\hat{\mathbf{f}}}_2 \qquad \bar{\hat{\mathbf{u}}}_1 = \mathcal{T}^T \mathcal{L} \bar{\hat{\mathbf{f}}}_1 \tag{4.17}$$

Let $\mathcal{K}_{\hat{\mathbf{u}}}$ be the average of the lesion-absent and lesion-present channel response covariance matrices.

$$\mathcal{K}_{\hat{\mathbf{u}}_2} = \mathcal{T}^T \mathcal{L} \mathcal{K}_{\hat{\mathbf{f}}_2} \mathcal{L}^T \mathcal{T} \qquad \mathcal{K}_{\hat{\mathbf{u}}_1} = \mathcal{T}^T \mathcal{L} \mathcal{K}_{\hat{\mathbf{f}}_1} \mathcal{L}^T \mathcal{T} \tag{4.18}$$

The channel covariance matrix is thus $\mathcal{K}_{\hat{\mathbf{u}}} = \mathcal{T}^T \mathcal{L} \mathcal{K}_{\hat{\mathbf{f}}} \mathcal{L}^T \mathcal{T}$. Then a measure of detectability, the CHO SNR, is given by [33]

$$\mathrm{SNR}^2 = (\bar{\hat{\mathbf{u}}}_2 - \bar{\hat{\mathbf{u}}}_1)^T (\mathcal{K}_{\hat{\mathbf{u}}})^{-1} (\bar{\hat{\mathbf{u}}}_2 - \bar{\hat{\mathbf{u}}}_1) \tag{4.19}$$

and the overall template is given by

$$\mathbf{w}_{\text{CHO}} = (\mathcal{K}_{\hat{\mathbf{u}}})^{-1} (\bar{\hat{\mathbf{u}}}_2 - \bar{\hat{\mathbf{u}}}_1) \tag{4.20}$$

Because of the transformation by $\mathcal{T}$, the dimensions of $\mathcal{K}_{\hat{\mathbf{u}}}$ are small ($N_c \times N_c$) and the necessary inverse is easy to calculate.

We use radially symmetric channels since the noise covariance and the signal profiles the reconstructions used in this thesis are approximately radially symmetric. Examples of the frequency domain bandpass channel filters and their spatial domain representations are given in Figure 4.3. Figure 4.3(a) displays the frequency domain radial profiles, of three difference-of-Gaussian (DOG) [33, 30] channel filters of dyadically increasing widths. Figure 4.3(b) shows the 2-D spatial version of the first channel template and figure 4.3(c) its central profile. Figure 4.3(d) displays the frequency domain radial profile, showing non-overlapping square channels of increasing bandwidths, while Figure 4.3(e) shows the 2D spatial version of one of the channels along with a central profile in Figure 4.3(f).

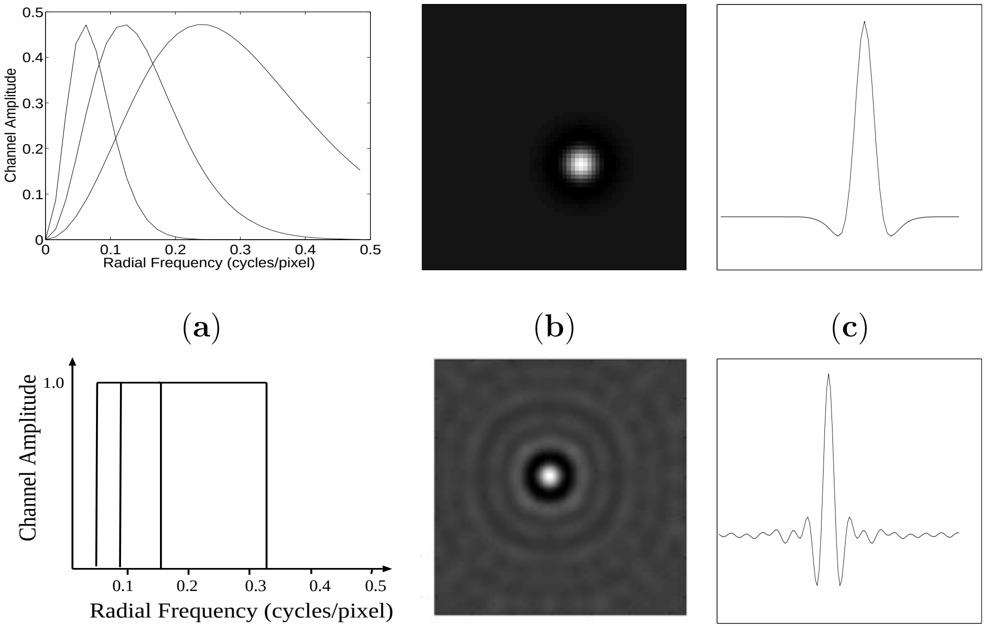

(**a**) (**b**) (**c**)

(**d**) (**e**) (**f**)

Figure 4.3: Radial profile of (a) DOG channels, (d) Radial profile of square channels in frequency space. (b) 2D space domain channel template (corresponding to the first DOG channel in (a)) displayed here as a $64 \times 64$ grey scale image. (c) Central profile of the channel template in (b). (e) 2D space domain channel template (corresponding to the third square channel in (d)) displayed here as a $128 \times 128$ grey scale image. (f) Central profile of the channel template in (e).

### 4.2.4 Sample Methods

We can calculate the CHO SNR with sample methods. First we reconstruct an ensemble of noisy reconstructions $\hat{\mathbf{f}}_1^k$ and $\hat{\mathbf{f}}_2^k$, where $k = 1, \cdots, N_{samp}$ indexes sample number. For SKE/BKE tasks, each sample reconstruction is calculated from projection data obtained by adding Poisson noise to the noiseless projection of fixed $\mathbf{f}$. For SKE/BKS tasks, projection data obtained by adding Poisson noise to the projection of a random realization of the underlying background is used as the input for calculating each sample reconstruction. Then we obtain the channel response $\hat{\mathbf{u}}_2^k = \mathcal{T}^T\mathcal{L}\hat{\mathbf{f}}_2^k$ and $\hat{\mathbf{u}}_1^k = \mathcal{T}^T\mathcal{L}\hat{\mathbf{f}}_1^k$ by applying the channel matrix at the lesion location on the extracted slice.

The sample means of the signal-present and -absent channel responses are given by

$$\bar{\hat{\mathbf{u}}}_2 = \frac{1}{N_{samp}}\sum_k \hat{\mathbf{u}}_2^k \quad \text{and} \quad \bar{\hat{\mathbf{u}}}_1 = \frac{1}{N_{samp}}\sum_k \hat{\mathbf{u}}_1^k \tag{4.21}$$

and the sample covariance of the channel responses is given by

$$\begin{aligned}\mathcal{K}_{\hat{\mathbf{u}}} = & \frac{0.5}{N_{samp}-1}\sum_k(\hat{\mathbf{u}}_2^k - \bar{\hat{\mathbf{u}}}_2)(\hat{\mathbf{u}}_2^k - \bar{\hat{\mathbf{u}}}_2)^T \\ & + \frac{0.5}{N_{samp}-1}\sum_k(\hat{\mathbf{u}}_1^k - \bar{\hat{\mathbf{u}}}_1)(\hat{\mathbf{u}}_1^k - \bar{\hat{\mathbf{u}}}_1)^T\end{aligned} \tag{4.22}$$

Since $\mathcal{K}_{\hat{\mathbf{u}}}$ is $N_c \times N_c$, calculating its inverse is trivial. To get a good estimate of $\mathcal{K}_{\hat{\mathbf{u}}}$ and its subsequent inverse, $N_{samp}$ should $10 \sim 100$ times $N_c$ [110]. We can then substitute (4.21) and (4.22) into (4.19) to obtain the sample SNR. We use jackknifing approach [111] to compute the variance of the estimated SNR. A brief description is given below.

For the jackknifing approach we use a "leave one out" methods to calculate an SNR value $\text{SNR}^{(1)}$ without the the first sample noisy reconstructions $\hat{\mathbf{f}}_1^1$ and $\hat{\mathbf{f}}_2^1$, an SNR value $\text{SNR}^{(2)}$ without $\hat{\mathbf{f}}_1^2$ and $\hat{\mathbf{f}}_2^2$ but including $\hat{\mathbf{f}}_1^1$ and $\hat{\mathbf{f}}_2^1$, SNR value $\text{SNR}^{(k)}$ without $\hat{\mathbf{f}}_1^k$ and $\hat{\mathbf{f}}_2^k$ and so forth. The standard deviation of SNR is calculated for the set $\text{SNR}^{(1)}$,$\text{SNR}^{(2)}$,$\cdots$,$\text{SNR}^{(k)}$,$\cdots$,$\text{SNR}^{(N_{samp})}$ from the formula [111]:

$$\hat{\sigma}\text{SNR} = \sqrt{\frac{N_{samp}-1}{N_{samp}}\sum_{i=1}^{N_{samp}}\left(\text{SNR}^{(i)} - \frac{1}{N_{samp}}\sum_{j=1}^{N_{samp}}\text{SNR}^{(j)}\right)^2} \tag{4.23}$$

### 4.2.5 Internal Noise

To better emulate human performance the CHO can be modified with internal noise. If a human is presented with exactly the same image on two different occasions, the human may decide "signal-present" sometimes and "signal-absent" at others. A model observer will, by contrast, always give a consistent result. This inconsistency by humans is modelled by a form of noise termed "internal noise" [33]. One way to model internal noise [33] is by addition of a zero mean random variable to each of the $N_c$ channel-responses. This results in the addition of an internal noise covariance $\mathcal{K}_\epsilon$ to the channel response covariance $\mathcal{K}_{\hat{\mathbf{u}}}$. The resulting SNR is obtained by replacing the term $\mathcal{K}_{\hat{\mathbf{u}}}^{-1}$ in (4.19) by $(\mathcal{K}_{\hat{\mathbf{u}}} + \mathcal{K}_\epsilon)^{-1}$. The effect of $\mathcal{K}_\epsilon$ on the CHO SNR is described extensively in Section 5.5.1.

## 4.3 Mean and covariance of MAP estimates

In order to evaluate the $\mathrm{SNR}_{\mathrm{CHO}}$, we need the first and second order statistics of the reconstructed images. Note that $\mathrm{SNR}_{HO}$ can be calculated in the sinogram space, but $\mathrm{SNR}_{CHO}$ must be calculated in the reconstruction space. MAP is a nonlinear estimator for the Poisson noise model hence the propagation of photon noise into the reconstruction is not straightforward. Here we give the theoretical expressions for mean and variance of the MAP estimate using the approach introduced by [112]. These theoretical expressions enable the fast computation of the mean and covariance of MAP reconstructions, which in turn are conducive to the rapid evaluation of detection FOMs. This avoids the laborious generation of large number of sample reconstructions as per Section 4.2.4. The evaluation of the statistical properties of MAP reconstructions in emission tomography have been extensively analyzed in [112, 69, 113, 114, 115, 116].

The MAP solution in Eq. 3.14 can be expressed as a nonlinear operator $\mathcal{O}\{\mathbf{g}\}$ on the observed data $\mathbf{g}$. Using a first-order Taylor series expansion about mean data $\bar{\mathbf{g}}$, we get

$$\hat{\mathbf{f}} = \mathcal{O}\{\mathbf{g}\} \approx \mathcal{O}\{\bar{\mathbf{g}}\} + \nabla_{\mathbf{g}}\mathcal{O}\{\bar{\mathbf{g}}\}(\mathbf{g} - \bar{\mathbf{g}}) \tag{4.24}$$

here, $\nabla_{\mathbf{g}} = [\frac{\partial}{\partial g_1} \cdots \frac{\partial}{\partial g_M}]$ denotes the gradient vector. The term $\mathcal{O}\{\mathbf{g}\}$ is an $N$-dimensional vector because it is an estimate of $\mathbf{f}$. The derivative operation with respect to a $M$-dimensional vector $\mathbf{g}$ makes $\nabla_{\mathbf{g}}\mathcal{O}\{\mathbf{g}\}$ an $N \times M$ matrix. The elements of $\nabla_{\mathbf{g}}\mathcal{O}\{\mathbf{g}\}$ are given by

$$[\nabla_{\mathbf{g}}\mathcal{O}\{\mathbf{g}\}]_{nm} = \frac{\partial}{\partial g_m}[\mathcal{O}\{\mathbf{g}\}]_n \tag{4.25}$$

Hence, the reconstruction operator in (4.24) is approximated as linear. To the extent that the variation of $\mathbf{g}$ about $\bar{\mathbf{g}}$ is small, the linearity approximation in (4.24) holds.

From the linearized operation in Eq. (4.24), we can obtain the mean of $\hat{\mathbf{f}}$ for a nonlinear reconstruction:

$$\bar{\hat{\mathbf{f}}} = \langle \mathcal{O}\{\mathbf{g}\}\rangle_{\mathbf{g}} \approx \mathcal{O}\{\bar{\mathbf{g}}\} \tag{4.26}$$

where the $\langle\rangle_{\mathbf{g}}$ denotes the mean over $\mathbf{g}$. From the linearized approximation of Eq. 4.24, we can also get the covariance of $\hat{\mathbf{f}}$ conditioned on the underlying object $\mathbf{f}$ under the hypothesis $H_k$ as follows:

$$\mathcal{K}_{\hat{\mathbf{f}}|\mathbf{f},H_k} \approx \nabla_{\mathbf{g}}\mathcal{O}\{\bar{\mathbf{g}}\}\mathcal{K}_{\mathbf{g}|\mathbf{f},H_k}[\nabla_{\mathbf{g}}\mathcal{O}\{\bar{\mathbf{g}}\}]^T \tag{4.27}$$

Thus, obtaining $\nabla_{\mathbf{g}}\mathcal{O}\{\bar{\mathbf{g}}\}$ will solve Eq. 4.27. The unconditional covariance of $\hat{\mathbf{f}}$ under the hypothesis $H_k$ is given as follows:

$$\mathcal{K}_{\hat{\mathbf{f}}|H_k} \approx \nabla_{\mathbf{g}}\mathcal{O}\{\bar{\mathbf{g}}\}\mathcal{K}_{\mathbf{g}|H_k}[\nabla_{\mathbf{g}}\mathcal{O}\{\bar{\mathbf{g}}\}]^T \tag{4.28}$$

We will lose the conditional notation on $H_k$ for the rest of this section. The quantities in (4.27) and (4.28) will have to be calculated for each of the hypothesis.

The first derivative at the fixed point in the case of the concave MAP objective given in Eq. 3.13 is

$$\frac{\partial}{\partial \mathbf{f}}\Phi(\mathbf{f};\mathbf{g})|_{\mathbf{f}=\hat{\mathbf{f}}} = \mathbf{0} \tag{4.29}$$

Using notation

$$\nabla^2_{\mathbf{ff}}\Phi(\hat{\mathbf{f}};\mathbf{g}) \equiv \frac{\partial^2\Phi(\hat{\mathbf{f}};\mathbf{g})}{\partial \mathbf{f}^2} \quad \text{and} \quad \nabla^2_{\mathbf{fg}}\Phi(\hat{\mathbf{f}};\mathbf{g}) \equiv \frac{\partial^2\Phi(\hat{\mathbf{f}};\mathbf{g})}{\partial \mathbf{f}\partial \mathbf{g}} \tag{4.30}$$

and applying chain rule and using results from [112] at point of expansion $\bar{\mathbf{g}}$ , we get

$$\nabla_{\mathbf{g}}\mathcal{O}\{\bar{\mathbf{g}}\} = -[\nabla^2_{\mathbf{ff}}\Phi(\mathcal{O}\{\bar{\mathbf{g}}\};\bar{\mathbf{g}})]^{-1}\nabla^2_{\mathbf{fg}}\Phi(\mathcal{O}\{\bar{\mathbf{g}}\};\bar{\mathbf{g}}) \tag{4.31}$$

For a Gibbs prior with its potential function defined as in Eq. (3.9), the second derivation (Hessian) of the prior is:

$$\nabla^2_{\mathbf{ff}}\Phi_P = \frac{\partial^2\Phi_P}{\partial\mathbf{f}^2} = \mathcal{R} \tag{4.32}$$

For the case of SPECT, the derivatives of $\Phi(\mathbf{f};\mathbf{g})$ (with a quadratic smoothing prior) evaluated at $\bar{\mathbf{g}}$ and $\bar{\hat{\mathbf{f}}}$ are [112]

$$\begin{aligned}
\nabla^2_{\mathbf{ff}}\Phi(\bar{\hat{\mathbf{f}}};\bar{\mathbf{g}}) &= -\mathcal{H}^T\text{diag}\Big(\frac{\bar{\mathbf{g}}}{(\mathcal{H}\bar{\hat{\mathbf{f}}})^2}\Big)\mathcal{H} - \beta\mathcal{R} && (4.33)\\
\nabla^2_{\mathbf{fg}}\Phi(\bar{\hat{\mathbf{f}}};\bar{\mathbf{g}}) &= \mathcal{H}^T\text{diag}\Big(\frac{1}{\mathcal{H}\bar{\hat{\mathbf{f}}}}\Big) && (4.34)
\end{aligned}$$

Therefore the right side of (4.27) becomes,

$$\Big[\mathcal{H}^T\text{diag}\Big(\frac{\bar{\mathbf{g}}}{(\mathcal{H}\bar{\hat{\mathbf{f}}})^2}\Big)\mathcal{H} + \beta\mathcal{R}\Big]^{-1}\mathcal{H}^T\text{diag}\Big(\frac{\bar{\mathbf{g}}}{(\mathcal{H}\bar{\hat{\mathbf{f}}})^2}\Big)\mathcal{H}\Big[\mathcal{H}^T\text{diag}\Big(\frac{\bar{\mathbf{g}}}{(\mathcal{H}\bar{\hat{\mathbf{f}}})^2}\Big)\mathcal{H} + \beta\mathcal{R}\Big]^{-1} \tag{4.35}$$

Hence the conditional covariance is given by

$$\mathcal{K}_{\hat{\mathbf{f}}|\mathbf{f}} = [\mathcal{F} + \beta\mathcal{R}]^{-1}\mathcal{F}[\mathcal{F} + \beta\mathcal{R}]^{-1} \tag{4.36}$$

where $\mathcal{F} = \mathcal{H}^T\text{diag}\big(\frac{\bar{\mathbf{g}}}{(\mathcal{H}\bar{\hat{\mathbf{f}}})^2}\big)\mathcal{H} \approx \mathcal{H}^T\text{diag}\big(\frac{1}{(\mathcal{H}\mathbf{f})}\big)\mathcal{H}$

To the extent that the object variability is small scale (low-amplitude textural background variability) the overall covariance of the reconstructions for BKS case can be calculated using the approach in [109, 94] and is given by

$$\mathcal{K}_{\hat{\mathbf{f}}} \approx \nabla_{\mathbf{g}}\mathcal{O}\{\bar{\mathbf{g}}\}\mathcal{K}_{\mathbf{g}}[\nabla_{\mathbf{g}}\mathcal{O}\{\bar{\mathbf{g}}\}]^T \tag{4.37}$$

Substituting (4.15),(4.31),(4.33) and (4.34) into (4.37)we get

$$\mathcal{K}_{\hat{\mathbf{f}}} = [\mathcal{F} + \beta\mathcal{R}]^{-1}[\mathcal{F} + \mathcal{F}\mathcal{K}_{\mathbf{b}}\mathcal{F}][\mathcal{F} + \beta\mathcal{R}]^{-1} \tag{4.38}$$

Apart from the mean and the covariance, another important statistic is a measure of resolution of the imaging system known as the local point spread function or the generalized point spread function or the local impulse response. For a space-invariant reconstruction operator, the point spread function is invariant to position. For our non-linear shift-variant reconstruction, it depends upon position, the object and the noise level, so we must characterize it locally. The local point spread function (lpsf) is defined in [69] as:

$$\bar{\hat{\mathbf{e}}}_j \equiv \lim_{\delta \to 0} \frac{1}{\delta}( < \mathcal{O}\{\mathbf{g}(\mathbf{f} + \delta \mathbf{e}_j)\} > - < \mathcal{O}\{\mathbf{g}(\mathbf{f})\} > ) \tag{4.39}$$

Here, $\mathbf{e}_j$ denotes a unit impulse at location $j$ and $\bar{\hat{\mathbf{e}}}_j$ denotes the lpsf at location $j$. It is the mean reconstruction of the object with a small point source at $j$ minus the same reconstruction without the point source. Using (4.24) and (4.26), the above expression may be simplified as:

$$\begin{aligned}
\bar{\hat{\mathbf{e}}}_j &\approx \lim_{\delta \to 0} \frac{1}{\delta}(\mathcal{O}\{\bar{\mathbf{g}}(\mathbf{f} + \delta \mathbf{e}_j)\} - \mathcal{O}\{\bar{\mathbf{g}}(\mathbf{f})\}) \\
&\approx \lim_{\delta \to 0} \frac{1}{\delta} \nabla_{\mathbf{g}} \mathcal{O}\{\bar{\mathbf{g}}(\mathbf{f})\}(\bar{\mathbf{g}}(\mathbf{f} + \delta \mathbf{e}_j) - \bar{\mathbf{g}}(\mathbf{f})) \\
&= \nabla_{\mathbf{g}} \mathcal{O}\{\bar{\mathbf{g}}(\mathbf{f})\} \mathcal{H} \mathbf{e}_j
\end{aligned} \tag{4.40}$$

Using (4.31),(4.33),(4.34), we get

$$\bar{\hat{\mathbf{e}}}_j = (\mathcal{F} + \beta \mathcal{R})^{-1} \mathcal{F} \mathbf{e}_j \tag{4.41}$$

We observe that the expression for $\mathcal{K}_{\hat{\mathbf{f}}|\mathbf{f}}$ in equations (4.36) is a matrix too large for practical computation. As in the case of (4.18) for a signal located at a particular location $j$, one generally is interested in constructs of the form $\mathcal{K}_{\hat{\mathbf{f}}|\mathbf{f}} \mathbf{x}_j$ or $\mathbf{x}_j^T \mathcal{K}_{\hat{\mathbf{f}}|\mathbf{f}} \mathbf{x}_j$ where $\mathbf{x}_j$ is a vector centered around $j$. For a point $j$, one can form a triply block-circulant approximation $\mathcal{K}_{\hat{\mathbf{f}}|\mathbf{f}}^{(j)}$ that closely approximates $\mathcal{K}_{\hat{\mathbf{f}}}$ in the vicinity of $j$. The main step in forming $\mathcal{K}_{\hat{\mathbf{f}}|\mathbf{f}}^{(j)}$ is to approximate $\mathcal{F}$ by a local triply block-circulant approximation $\mathcal{F}^{(j)}$. The $i^{th}$ column of both $\mathcal{F}$ and $\mathcal{F}^{(i)}$ is $\mathcal{H}^T \mathrm{diag}\Big(\frac{\bar{\mathbf{g}}}{(\mathcal{H}\hat{\mathbf{f}})^2}\Big) \mathcal{H} \mathbf{e}_i$, and the remaining columns of $\mathcal{F}^{(i)}$ are shifted versions of this $i^{th}$ column. Note that the key computations in computing this $i^{th}$ column are a projection of a point source and a full backprojection. For uniform quadratic prior (3.9), the Hessian of the prior $\mathcal{R}$ given by (3.10), is triply block circulant (shift invariant if we ignore the edge pixels). Using the properties of circulant matrices the eigenvalues of $\mathcal{R}$ and $\mathcal{F}(j)$ can be computed using a 3-D DFT [88]. We know that the Fisher information matrix $\mathcal{F}$ as well as $\mathcal{R}$ is positive semi-definite [114], i.e. its eigenvalues are real and non-negative. In order to enforce this condition only the real part of the eigenvalues is used and negative components are clipped to zero [116, 106]. Now (4.36) becomes

$$\mathcal{K}^{(j)}_{\hat{\mathbf{f}}|\mathbf{f}} = \mathcal{Q}^{-1}\text{diag}\left[\frac{\boldsymbol{\nu}^j}{(\boldsymbol{\nu}^j + \beta\boldsymbol{\eta})^2}\right]\mathcal{Q} \tag{4.42}$$

where $\mathcal{Q}$ is the 3D DFT operator, $\boldsymbol{\nu}^j$ and $\boldsymbol{\eta}$ are the lexicographically ordered eigenvalues of the matrices $\mathcal{F}(j)$ and $\mathcal{R}$ respectively. The (4.18) for channel centered around $j$ would become

$$(\mathcal{T}^T\mathcal{L}\mathcal{K}_{\hat{\mathbf{f}}}\mathcal{L}^T\mathcal{T}) = \mathcal{T}^T\mathcal{L}\mathcal{Q}^{-1}\text{diag}\left[\frac{\boldsymbol{\nu}^j}{(\boldsymbol{\nu}^j + \beta\boldsymbol{\eta})^2}\right]\mathcal{Q}\mathcal{L}^T\mathcal{T} \tag{4.43}$$

A triply block-circulant approximation to the overall covariance (4.38) is given

$$\mathcal{K}^{(j)}_{\hat{\mathbf{f}}} = \mathcal{Q}^{-1}\text{diag}\left[\frac{\boldsymbol{\nu}^j}{(\boldsymbol{\nu}^j + \beta\boldsymbol{\eta})^2}\right]\mathcal{Q} + \mathcal{Q}^{-1}\text{diag}\left[\frac{\boldsymbol{\nu}^j}{(\boldsymbol{\nu}^j + \beta\boldsymbol{\eta})}\right]\mathcal{Q}\mathcal{K}_{\mathbf{b}}\mathcal{Q}^{-1}\text{diag}\left[\frac{\boldsymbol{\nu}^j}{(\boldsymbol{\nu}^j + \beta\boldsymbol{\eta})}\right]\mathcal{Q} \tag{4.44}$$

In case if the background variability is multivariate Gaussian obtained by filtering iid Gaussian noise then $\mathcal{Q}\mathcal{K}_{\mathbf{b}}\mathcal{Q}^{-1}$ would be a diagonal matrix.

The lpsf in (4.41) has the form $(\mathcal{F} + \beta\mathcal{R})^{-1}\mathbf{v}_j$ where $\mathbf{v}_j = \mathcal{F}\mathbf{e}_j$. The lpsf is given by

$$\bar{\hat{\mathbf{e}}}_j = \mathcal{Q}^{-1}\text{diag}\left[\frac{\boldsymbol{\nu}^j}{(\boldsymbol{\nu}^j + \beta\boldsymbol{\eta})}\right]\mathcal{Q}\mathbf{e}_j \tag{4.45}$$

The above mentioned formulae ignore the positivity constraint in reconstruction. Methods to account for the positivity constraint are discussed in [114]. These formulae are also limited in the sense that they consider the effects only due to primary photon noise. Various generalizations of these analytical formulae are often necessary. In Section 7.5.1, we derive similar formulae that deal with the noise in the scatter estimates in SPECT. The CHO observer described in this chapter will be used in Chapter 5 for predicting human performance to determine the optimal smoothing parameter $\beta$ of MAP reconstructions. The CHO is also used to assess the efficacy of anatomical prior information in MAP reconstruction in Chapter 6.

# Chapter 5

# Channelized Hotelling and Human Observer Study of Optimal Smoothing in SPECT MAP Reconstruction

In Chapter 4 we have discussed the human emulating CHO. In Chapter 3 we discussed the MAP reconstruction where the scalar smoothing parameter $\beta$ is the weight of the prior $\Phi_P$ which is used as a regularizer in the MAP objective. In this chapter we perform a human observer study to assess the effect of this regularization parameter $\beta$ on lesion detectability . Since $\beta$ controls the noise-resolution tradeoff in the reconstruction, it is a natural parameter to study. We compared the performance of CHO to that of the human observer and then modified the CHO with internal noise to give a better prediction of the human observer performance. This chapter is based on our work in [95]. Though I appear as a second author on this paper, I had contributed in the theory and in computation of all the calculations involving CHO SNR's (i.e. generating sample reconstructions, calculation of CHO SNR's, choosing internal noise parameters, calculation of error bars, studying the effects of quantization). I was in charge of the generating the figures and $\LaTeX$ing the manuscript. The human observer study was conducted by the first author.

## 5.1 Introduction

FOM's of human observer ROC testing methodologies are the most accepted testing standard for optimization of reconstruction parameters with respect to a detection task. Model observers [27] described in Chapter 4 that are known to emulate humans can be used to reduce the many possible cases that arise in an optimization study down to a few select candidates that can be addressed by the more time-consuming ROC testing. Model observers might also be used to "prototype" a study to glean preliminary information regarding FOM variation with signal contrast, location or noise level. This prototyping can be used to further narrow the conditions of the subsequent human study. In this work, we focus on one particular model observer, the channelized Hotelling observer (CHO) [117]. The CHO has become a widely adopted [118][39][59] model observer in applications involving optimization of reconstruction strategies in ECT.

From Chapter 3 we know that MAP reconstruction methods incorporate (a) the models of both the imaging system and data noise, (b) a prior to stabilize the ill-posed reconstruction and to model object properties such as smoothness. The reconstruction is obtained by optimizing an objective function that comprises a weighted sum of a data-fit term and a some form of smoothing penalty. The relative influence of each term is controlled by a scalar parameter $\beta$. In recent years, efforts have been made to adjust the penalty in order to achieve desired image quality in the reconstruction. For example, in [69] (and a series of follow up works) this strategy was used to obtain uniform spatial resolution, and in [113] the strategy was used to optimize a contrast-to-noise ratio in the reconstruction. In [119] the authors design penalty functions to improve lesion detectability measured by the CHO.

We explore the possibility of maximizing a detection FOM by controlling $\beta$, using human and model observer tests. We limit ourselves to SKE/BKE detection task and also include some comments for SKE/BKS tasks. A two-alternative forced-choice (2AFC) test was used for assessing the human performance as a function of the smoothing parameter $\beta$. In a single trial of a 2AFC test, the observer is presented with two images and asked to identify which image contains the signal. Each trial with a different pair of signal-present signal-absent images (on each trial) is repeated several times in a test to eventually deliver a percent-correct ($P_C$) which approaches the AUC [33] as number of pair samples increases. The CHO observer performance was calculated using sample methods involving many reconstructions as described in Section 4.2.4.

In this study we consider an SKE/BKE SPECT MAP detection problem, and explore detection FOM's vs $\beta$ with sample (CHO) and human observers. In addition, we explore an issue regarding the use of floating-point reconstructions versus quantized reconstructions. This issue arises because humans actually view reconstructions that are quantized for display purposes. We discuss the issue of whether the CHO internal noise parameters tuned to the human data for a particular location can be generalized to give CHO results that track human results for a different locations and different signal contrasts. We also discuss the effect of $\beta$ on the CHO and human observer performance when object variability is added to the task. In Secs. 5.3 and 5.4 we describe experiments using human observers and sample observers, respectively, and in Section 5.5 we compare human vs model observer performance. We conclude in Section 5.6 with a discussion.

## 5.2 Details of SPECT Reconstruction and the CHO

As in Chapter 4 for the SKE/BKE and SKS/BKS tasks we define $\mathbf{f}_1 = \mathbf{b}$ and $\mathbf{f}_2 = \mathbf{b} + \mathbf{s}$ as signal-absent and signal-present objects with $\mathbf{b}$ and $\mathbf{s}$ denoting a background and fixed signal, respectively. For the SKE/BKE study we used two signals, signal A and signal B, at two different locations and contrasts. Figures 5.1(a),(b) shows our $\mathbf{f}_2$ for each signal.

A MAP reconstruction optimizes the MAP objective (3.6). The quadratic penalty used in the (3.6) is given by (3.9) with the neighbourhood system $\mathcal{N}(n)$ defined over the 8 nearest-neighbors and with $\omega_{nj}$ chosen to be proportional to the inverse of the distance between pixels $n$ and $j$. The crucial scalar $\beta > 0$ controls the degree of regularization (i.e. smoothing), and so we will use the notation $\hat{\mathbf{f}}(\beta)$ when emphasizing the dependence of the reconstruction on $\beta$. Our reconstructions are obtained by maximizing the objective using a positivity constraining preconditioned conjugate gradient algorithm.

The $128 \times 128$ pixel (each pixel is 0.25 cm) chest phantom in Figure 5.1 comprises lung:soft-tissue:cardiac regions of relative intensity ratio 1:2:4. Signal A, in Figure 5.1(a), is a $3 \times 3$ square pixel region whose contrast relative to local surround is 2:1. A second signal, signal B, depicted in Figure 5.1(b) has a contrast relative to local surround of 2.3:1. We included the effects of depth-dependent blur where the blur kernel FWHM varied linearly from 1.97 to 5.36 detector bin lengths. Attenuation effects were also included using attenuation coefficients 0.153 $\text{cm}^{-1}$ and 0.0558 $\text{cm}^{-1}$ in the soft tissue and lung region, respectively. The average count level was 525K. Data was collected via a parallel hole collimator at 128 equispaced angles.

For the SKE/BKS study we used signal A added to a multivariate Gaussian background as shown in Figure 5.2. Zero-mean multivariate Gaussian noise with correlation width $\sigma = 6$ pixels and amplitude 0.2133 was added to the signal A signal present/absent phantom. The attenuation map and rest of SPECT imaging system parameters were same as those for the SKE/BKE task.

The reconstruction $\hat{\mathbf{f}}(\beta)$ is naturally a floating point entity, yet the reconstruction is quantized ( typically by an 8-bit ADC) before display. In our human trials, the observer views this 8-bit image, further modified by the physical effects of the display monitor. For our sample observer, we shall use reconstructions quantized to 8 bits, but the sample reconstructions will not be further modified to include monitor effects.

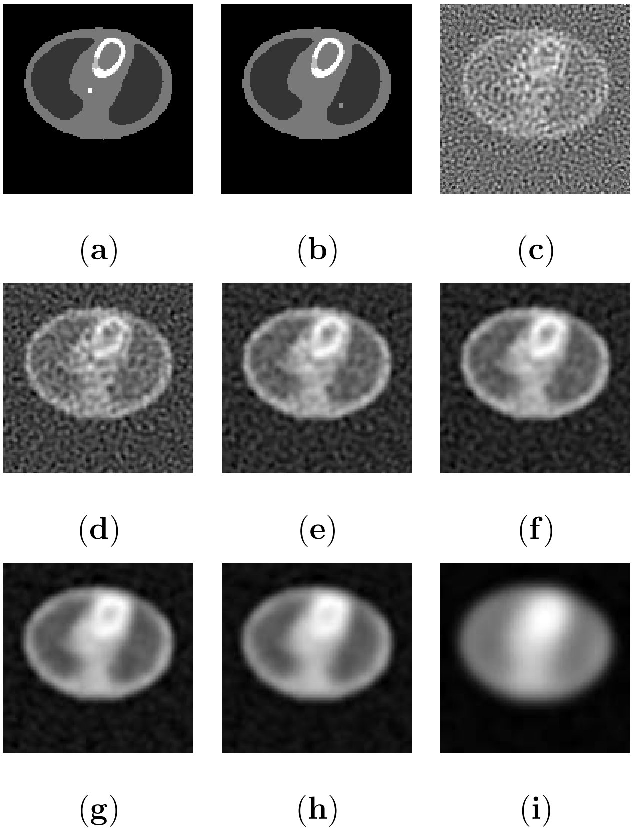

Figure 5.1: Reconstructions without object variability (a)Background plus signal A (b)Background plus signal B. The remaining panels show anecdotal signal-present reconstructions for signal A at (c) $\beta = 0.01$ (d) $\beta = 0.1$ (e) $\beta = 0.5$ (f) $\beta = 1.0$ (g) $\beta = 5.0$ (h) $\beta = 10.0$ (i) $\beta = 100.0$

For human trials, additional scaling steps, described in Section 5.3, are applied before display.

We consider a wide range of $\beta$ in our reconstructions, ranging from obviously noisy reconstructions to absurdly smooth ones. Figure 5.1(c)-(i) displays, for signal A, signal-present anecdotal reconstructions for the seven values of $\beta$ (0.01, 0.1, 0.5, 1.0, 5.0, 10.0, 100.0) used in this study. Clearly the signal, is difficult to detect in these reconstruction.

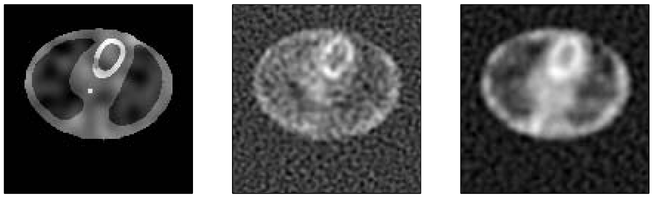

(a) (b) (c)

Figure 5.2: Reconstructions with object variability (OV). (a) Phantom with small 3×3 pixel lesion having contrast 2:1 over the local background with one realization of a Gaussian random background added (amplitude is 16% of local surround, correlation length is 6 pixels.), (c)(d) Signal-present MAP reconstructions of the OV phantom at $\beta = 0.1, 1.0$. Signal is very difficult to detect in the case of SKE/BKS.

In Figure 4.3, we display the ($N_c$=3) channelization scheme used in our studies. (In Section 5.4 we will describe how we arrived at this channel scheme.) The lesion-centered channels are real-valued and radially symmetric in both the spatial and Fourier domains. Figure 4.3(d) displays the channel radial profiles, showing square profiles of increasing radius in the frequency domain, while Figure 4.3(e) shows the 2D spatial version of the third channel template and Figure 4.3(f) its central profile. As described in Section 4.2.3 the CHO SNR is calculated using (4.19). Since the CHO SNR is calculated for different values of $\beta$ we use the notation $\mathrm{SNR}^2(\beta)$ to emphasize its dependence on $\beta$.

## 5.3 Human Observer Trials

### 5.3.1 Testing Procedure

Human observer SKE/BKE studies were done on reconstructed images using the 7 values of $\beta$ and for two different combinations of signal location and contrast. For each $\beta$, we used a 56-image training set to familiarize human observers with the image set's characteristics, and a 180-image test set to obtain test data. Each observer underwent a total of 3 sessions, two for three $\beta$'s each, and the third for $\beta = 100$. For the two sessions with three $\beta$'s, the observer took a significant rest between $\beta$'s . This strategy, along with the choice of the number of training and test images, avoided observer fatigue. The sets corresponding to different $\beta$'s were presented in different orders to different observers so as to avoid learning effects on $\beta$. Persons inside the lab (including the paper authors) and the Stony Brook Health Sciences Center were used as observers. There were a total of $N_{obs} = 6$ observers.

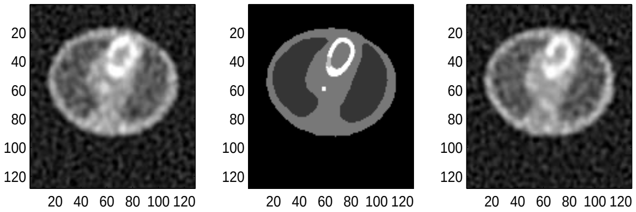

Figure 5.3: Typical display as seen by an observer during a 2AFC test. This reconstruction was done at $\beta = 0.5$ and for signal A. The image pair here clearly shows the lesion in the left panel. In practice, such easy discrimination was rarely possible.

The trials used a 2AFC (two-alternative-forced-choice) methodology. The 2AFC methodology can be used in place of standard ROC methodologies to obtain AUC estimates and related FOM's. To implement the 2AFC, we modified software from the 'Test2AFC' MATLAB scripts provided by the University of Arizona's Center for Gamma-Ray Imaging (an NIH Resource). For each $\beta$, the 2AFC tests were conducted as follows. As seen in Figure 5.3, each person was presented with three black and white 128x128 images on a standard CRT monitor. The center panel always displayed the background with signal in order to help the human observer localize the potential signal locations in the test images. The left and right panels displayed two noisy reconstructions on the sides. One panel contained a noisy reconstruction with the lesion absent, the other a noisy reconstruction with the lesion present. The panel with the lesion was randomly determined (via a randomization function that consulted the system clock) to be either on the right or the left side. The size of all three pictures as measured together on the monitor together was 38.1 cm wide by 17.78 cm high. Each individual picture was square, measuring 8.25 cm on a side. The expansion of the 128x128 picture to fit the 8.25 cm square entailed a default interpolation in MATLAB.

The observer had to choose with a right or left mouse-button click which side they thought the picture (with lesion) was on. The observer had as much time as they needed to observe the images, and was free to move their head position and viewing distance as they saw fit. The average viewing distance was about 38 cm and we noted that actual viewing distances did not dramatically differ from this average. The correctness of their answer was immediately reported, as was their total percent correct ($\hat{P_C}$) when they finished the experiment. Room lights were turned off, but any additional specular reflection onto the monitor from ambient light around the lab was decreased with a cardboard hood that enclosed the monitor and observer's head.

To map the reconstructions $\hat{\mathbf{f}}(\beta)$ to the display, we used the following strategy: For a given pair of 2AFC images, a histogram of the floating-point values of both images was created. The pixels corresponding to the top 0.5% and bottom 0.5% of the histogram were set to 255(white) or 0(black). The remaining pixels were mapped to occupy 256 equispaced values within the 0-255 range. We did not calibrate the monitor brightness in any particular way, but the brightness and contrast knobs were held fixed, throughout all experiments.

### 5.3.2 Calculation of $d_A^2$ for human observers

After the results were obtained for all six observers, we calculated a FOM, the squared detectability, $d_A^2$. This FOM is commensurate with the SNR$^2$ for the CHO observer as explained in Section 5.4. The calculation was done as follows. Let $r$ index the observer, so that $\hat{P}_{C,r}$ is the percent correct (as measured by 2AFC) of the $r^{th}$ observer (we note that $P_C = \text{AUC}$). Let $\hat{d}_{A,r}$ be the detectability of the $r$th observer. These are related [110] by :

$$\hat{d}_{A,r} = 2\text{erf}^{-1}(2\hat{P}_{C,r} - 1) \tag{5.1}$$

Since we were attempting to compare human performance to model observer SNR$^2$, we need to calculate an estimate of squared detectability. To do this, we simply squared $\hat{d_{A,r}}$ to obtain:

$$\hat{d}^2_{A,r} = (\hat{d}_{A,r})^2 \tag{5.2}$$

The justification is as follows: $\hat{P}_{C,r}$ is the ML (maximum likelihood) estimate of $P_{C,r}$, the underlying "ability" of the $r^{th}$ observer. The quantity $\hat{d}^2_A$ is related to $\hat{P}_C$ via the invertible transformation of (5.1) and (5.2). Since the ML estimate of a transformed quantity equals the transformation (if invertible) of the ML estimate, we can say that $\hat{d}^2_{A,r}$ is the ML estimate of $(\hat{d}_{A,r})^2 = \left[2\text{erf}^{-1}(2\hat{P}_{C,r} - 1)\right]^2$. Figure 5.4 shows $d^2_A$ vs $\beta$ for the 6 human observers for the signal A experiment. Error bars represent 68% confidence intervals. The plots for signal B (not shown) were qualitatively similar, with individual observer performance consistent across signals A and B.

Error bars for $\hat{d}^2_A$, the squared detectability averaged over all observers, were calculated using the standard error of the mean-squared detectability [33]:

$$\hat{\sigma}_{\hat{d}^2} = \left[\frac{1}{N_{obs}(N_{obs} - 1)} \sum_{r=1}^{N_{obs}} (\hat{d}^2_{A,r} - \bar{\hat{d}}^2_A)^2\right]^{\frac{1}{2}} \tag{5.3}$$

where $\bar{\hat{d}}^2_A$ was the average squared detectability in the experiment:

$$\bar{\hat{d}}^2_A = \frac{1}{N_{obs}} \sum_{r=1}^{N_{obs}} \hat{d}^2_{A,r} \tag{5.4}$$

and $\hat{d}^2_{A,r}$ was obtained from (5.1) and (5.2). The human-observer $\hat{d}^2_A$ values are plotted in Figure 5.10 (for signal A) and Figure 5.11 (for signal B). The error bars correspond to ±1 standard deviation, as calculated in (5.3).

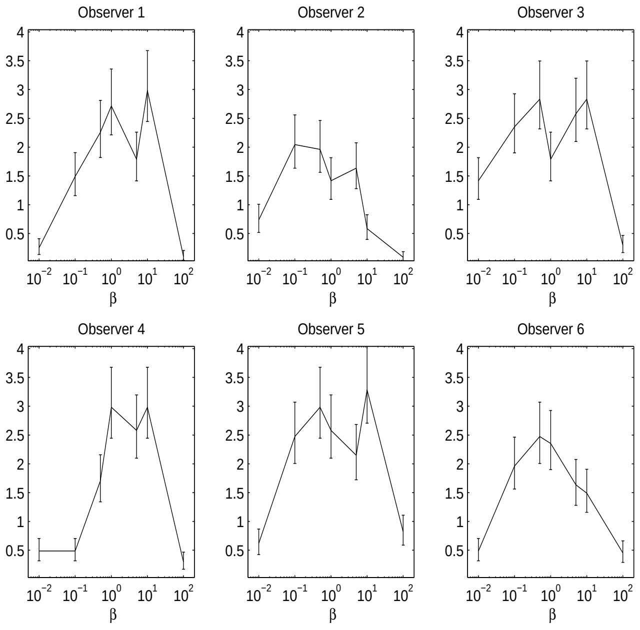

Figure 5.4: $d_A^2$ versus $\beta$ for individual human observers. Error bars are 68% confidence interval.

## 5.4 Sample Observer Trials

### 5.4.1 Details of SNR Calculation

The sample method used for calculation of the CHO SNR is as given in Section 4.2.4 with one additional step involved. The $N_{samp}$ signal-present and signal-absent reconstruction for a particular beta are quantized to 8 bits i.e. 256 quantization levels before applying the channel templates $\mathcal{T}$. For quantization we compute the global $\hat{f}_{max}$ and $\hat{f}_{min}$ from *all* $2N_{samp}$ samples, and set $\Delta q = \frac{\hat{f}_{max} - \hat{f}_{min}}{256}$. Then we quantize each sample using step size $\Delta q$ to obtain $\hat{\mathbf{f}}_1^k(\beta)$ and $\hat{\mathbf{f}}_2^k(\beta)$. After applying the channel templates $\mathcal{T}$ to the $2N_{samp}$ quantized reconstructions, we use (4.21) and (4.22) into (4.19) to get the CHO sample SNR. We used $N_{samp} = 416$ which is adequate to give a stable estimate for SNR. Note that $N_{samp} = 416$ is greater than the 180 samples used for human observers.

The signal, object and count level were chosen so that the histograms of model observer response with and without signal showed considerable overlap. Figure 5.5 shows typical model observer response curves for the signal-absent and signal-present cases for signal A. Other trials for different $\beta$ and for signal B showed a similar degree of overlap and a similar approximate Gaussian shape. If model observer responses for signal-present and signal-absent images are Gaussian in form, the model observer signal-to-noise ratio is equivalent to the detectability $d_A$ for humans [30]. As seen in Figure 5.5, the histograms of the observer responses are indeed approximately Gaussian. We thus compared the model observer SNR$^2$ to the human observer ${d_A}^2$.

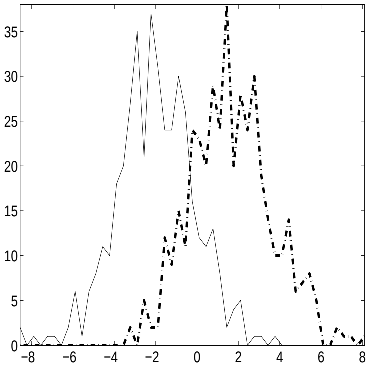

Figure 5.5: Histogram of the observer responses for signal absent (bold line)and signal present (dotted line) cases for $\beta$=1.0 and signal A. Histograms for other values of $\beta$ showed a similar degree of overlap.

### 5.4.2 Channelization Scheme

A wide variety of radial channel profiles are possible; but we limit our study to square channel profiles, which result in annular regions in the frequency domain. We also restricted ourselves to dyadic channels, in which the width of the bandpass channels increases by a factor of two. In order to properly select these channels so as to approximate the function of the human eye, we must pick the frequency boundaries of the channel appropriately.

A minimum limit is set by the ability of the human eye to detect low-frequency patterns (it has fairly low response below a given level). A reconstruction study [33] used a minimum limit of 0.48 cycles per degree as a frequency cutoff. We used this value as an approximate start point in designing our channels. To use this value, we must convert it to units of cycles/pixel. Our average viewing distance $\delta_{view}$ was about 38 cm and our displayed image width 8.25 cm. Thus the pixel width was $\delta_{pix}$ 0.0645 cm, since our images comprised 128 by 128 pixels. Using the formula [33] relating frequency in units of $\text{deg}^{-1}(\rho_{degree})$ to $\text{pixel}^{-1}(\rho_{pix})$

$$\rho_{degree} = \frac{\delta_{view}}{\delta_{pix}} \frac{2\pi}{360} \rho_{pix} \tag{5.5}$$

we obtain 0.05 cycles per pixel as the minimum frequency corresponding to the cutoff figure in [33] 0.48 cycles/deg. The maximum $\rho_{degree}$ is set by the Nyquist frequency $\rho_{pix} = 0.5$. Plugging $\rho_{pix} = 0.5$ into (5.5), we get a maximum $\rho_{degree} = 5.154$. To explore channel schemes we used the following procedure. We picked a low frequency cutoff $\rho_{pix}^{min}$. The bandpass limits in the dyadic scheme become $(\rho_{pix}^{min}, 2\rho_{pix}^{min})$, $(2\rho_{pix}^{min}, 4\rho_{pix}^{min})$, $(4\rho_{pix}^{min}, 8\rho_{pix}^{min})$, etc. We choose as many such bandpass channels as would fit below the Nyquist limit $\rho_{pix} = 0.5$. Thus $\rho_{pix}^{min}$ indexes each channel scheme. We took multiples of the value $\rho_{pix}^{min} = 0.05$ to explore different schemes. In particular we formed channels using $\gamma\rho_{pix}^{min}$ for $\gamma = 0.3$, 0.4, 0.5, 0.6, 0.7, 0.8, 0.9, 1.0 and 1.25. For each $\gamma$, we could fit $\text{N}_C = 3$ or $\text{N}_C = 4$ channels within the Nyquist limit; we derived the channels, and applied the resulting CHO to sample reconstructions to obtain an $\text{SNR}^2$ vs $\beta$ curve.

In Figure 5.6, these $\text{SNR}^2(\beta)$ curves are compared to the one obtained for the signal A human observers. We decided to choose the curve that looked qualitatively closest to the human curve. We settled on a value of $\gamma = 0.8$ corresponding to

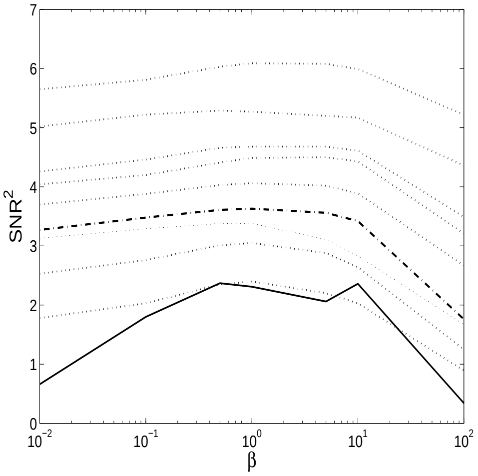

Figure 5.6: Choosing a best channel scheme. The solid line is the $d_A^2$ for humans. The dotted lines correspond to SNR's obtained for various values of $\gamma$, while the dashed curve is the SNR$^2$ curve for our chosen ($\gamma = 0.8$) channel scheme.

minimum frequency of 0.04 cycles per degree; 3 channels brought us to a maximum frequency of 0.32 cycles per degree or 64% of the Nyquist. This actual channel scheme is the one displayed in Figure 4.3. The dotted curve in Fig. 5.6 is thus the CHO SNR$^2(\beta)$ curve unmodified for effects of internal noise. We will call this observer with its chosen channel scheme and lack of internal noise model the "unmodified observer". For this observer we calculated error bars obtained via a jackknife procedure [111] as explained in Section 4.2.4. The resulting SNR$^2(\beta)$ curve is displayed in Figure 5.10 along with the human observer results for comparison.

## 5.5 Comparison of Human and model observer performance

### 5.5.1 Internal Noise Models

As seen in Figure 5.6 for signal A, our CHO outperforms our human observers did; the CHO has an SNR$^2$ of about 3.5 for most values, corresponding to a performance of about 91 percent correct, whereas human observers scored anywhere from 58 to 90 percent correct on the trials (average numbers obviously varied with $\beta$ and with observer). In addition the unmodified CHO is less specific in its prediction of a range for $\beta$. In order to 'handicap' the CHO so that its performance was more similar to that of a human observer, we used three types of internal noise models. Each of these models works via an addition to the diagonal elements of the covariance matrix. This is equivalent to altering the prewhitening so as to incorporate an assumption of increased channel variance. Our strategy was to apply internal noise models to the signal A CHO curve in attempt to match it to the human curve.

The first type of noise consists of an addition of a multiple $\alpha_1$ of the diagonal elements of the covariance matrix to the diagonal, resulting in multiplication of the diagonal of the covariance matrix by $1 + \alpha_1$:

$$[\mathcal{K}_u]_{ii} \rightarrow [\mathcal{K}_u]_{ii} + \alpha_1 [\mathcal{K}_u]_{ii} \tag{5.6}$$

We observed that this sort of noise generally creates a smoothing and lowering of the curve, decreasing the CHO's performance and also decreasing differences between performance at different values of $\beta$. This is seen in Figure 5.7. This sort of noise was employed by Abbey and Barrett [30] in their work on ramp-spectrum noise.

The second noise mechanism, described in [33] is more complicated. Here, constants proportional to the maximum of the diagonal are added to each diagonal element of the covariance matrix:

$$[\mathcal{K}_u]_{ii} \rightarrow [\mathcal{K}_u]_{ii} + \alpha_2 \max_j [\mathcal{K}_u]_{jj} \tag{5.7}$$

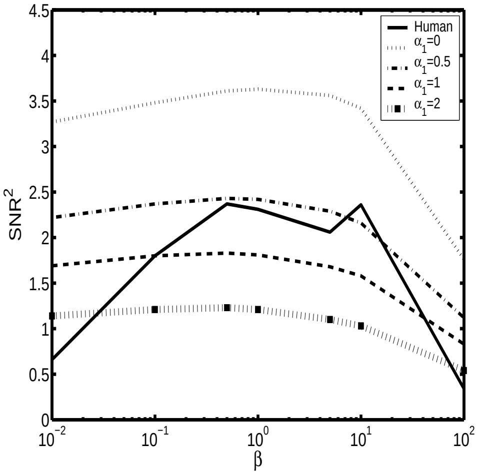

Figure 5.7: Different values of the $\alpha_1$ parameter. Note the relative flatness of the curves.

As seen in Figure 5.8 this type of noise approximates the shape of the human observer much more closely, having a peak at $\beta = 0.5$ and decaying at similar rates on both sides.

The third internal noise model, used in [120] is relatively simple. It involves a multiple $\alpha_3$ of the identity matrix added to the covariance matrix as follows:

$$\mathcal{K}_u \rightarrow \mathcal{K}_u + \alpha_3 I \tag{5.8}$$

This sort of noise gives a CHO SNR$^2$ curve that does not match well with that for the humans as shown in Figure 5.9.

The noise we used to 'handicap' the CHO was a combination of $\alpha_1$ and $\alpha_2$ noise. We examined a range of linear combinations of $\alpha_1$ and $\alpha_2$ noise and searched for the ones which gave us the minimum absolute ($\alpha_1 = 0.25$,$\alpha_2 = 0.25$) and minimum squared ($\alpha_1 = 0.15$, $\alpha_2 = 0.3$) errors. As our final (best) CHO observer, we chose one corresponding to the MSE. In Fig. 5.10 we plot the SNR$^2(\beta)$ for this final CHO observer and include error bars obtained using a jackknife procedure [111]. The error

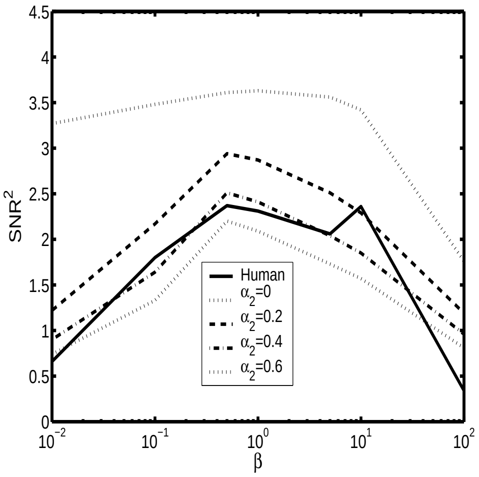

Figure 5.8: Different values of the $\alpha_2$ parameter. Note the relatively close approximation to the human shape.

bars correspond to ±1 standard deviation. On the same figure, we superimpose the results for human observers. We will call this sample observer, with its internal noise component, the "modified" CHO.

We repeated the human and CHO trails for location B. The unmodified CHO in this case was the same as that used for signal A. We then modified the CHO using the *same* $\alpha_1$ and $\alpha_2$ internal noise parameters as was used for signal A. In Fig. 5.11, we plot the $\mathrm{SNR}^2(\beta)$ curve for the modified and unmodified observers, and also the $d_A^2$ results for the human tests. All error bars were calculated as before.

So far, all reconstructions $\mathbf{f}(\hat{\beta})$ used in calculating SNR were 8-bit quantized versions. For theory observers, one must use floating point versions of $\mathbf{f}(\hat{\beta})$ in the ensemble formulae. This might make a difference in SNR, and indeed, such effects were reported in Narayanan [59] for the case of optimization of OSEM iterations and FWHM 3-D Gaussian post-filtering. To test whether quantization effects affected our MAP reconstruction trials, we recomputed $\mathrm{SNR}^2(\beta)$ using floating point samples of

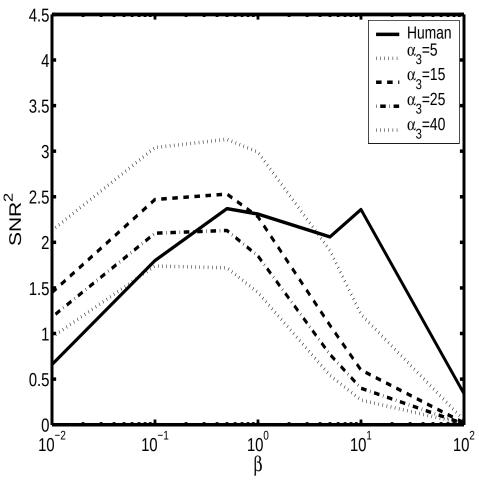

Figure 5.9: Different values of the $\alpha_3$ parameter. Note the partial plateau.

$\hat{\mathbf{f}}(\beta)$ and compared the results to that using the quantized versions. Figure 5.12 shows the SNR$^2$ vs $\beta$ curve for the unmodified CHO at location A applied to 8-bit quantized data and also to floating point data. As seen in Fig.5.12 there is a very slight divergence at $\beta = 100$ where the smoothness of the images exacerbates quantization effects. At all other values of $\beta$, the curves were indistinguishable. (The $\beta$'s differed by less than 0.3% except at $\beta = 100$, where they differed by 6.9%)

## 5.6 Discussion

We have investigated the ability of CHO observers to mimic human observers for our application of interest: SKE/BKE lesion detection as a function of smoothing in a MAP reconstruction. As seen in Figures 5.10 and 5.11 both the human and CHO show that detectability is rather insensitive to $\beta$ over a broad range, but the CHO's unmodified for internal noise predict a broader range than that of humans. For both signal A and B, the human response achieved a high plateau in $d_A^2$ covering the $\beta$ values 0.5, 1.0, 5.0 and 10.0. The unmodified CHO extended this plateau range to

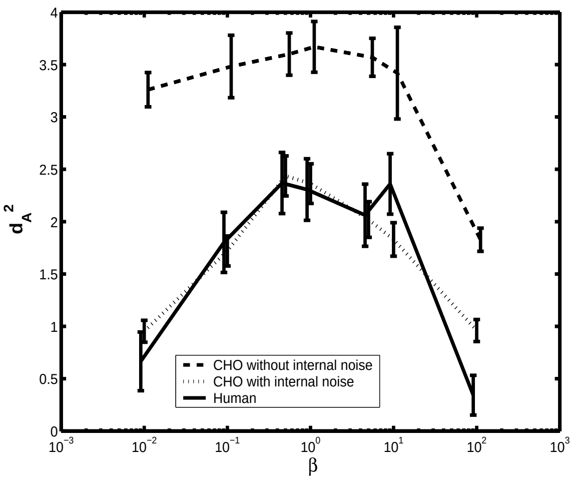

Figure 5.10: Comparison of $d_A^2$ and SNR$^2$ versus $\beta$ for human, unmodified and modified CHO for signal A

include $\beta = 0.01$ and 0.1.

For signal A, we modified the CHO for internal noise so that, as seen in Figure 5.10, the response matches that of the human rather well, with both modified CHO and human responses significantly high at $\beta = 0.5$, 1.0, 5.0 and 10.0. Can this internal noise modification be generalized to work for different locations and signal contrasts? Figures 5.11 shows the CHO at B modified using the internal noise parameters from A. While the human and modified CHO curves no longer match, the modified CHO does yield a plateau region ($\beta$ = 0.5-10.0) that matches the human. These results seem to imply that while internal noise is needed for CHO's to narrow the range of sensitivity to $\beta$, perhaps some form of generic internal noise could be used that achieves the range narrowing but does not require a human trial to calculate parameters such as $\alpha_1$ and $\alpha_2$. In terms of even a crude rank order prediction, even the unmodified CHO, though not perfect, is not far off from the human response. In [120] the issue of needing a human observer study to set model observer internal

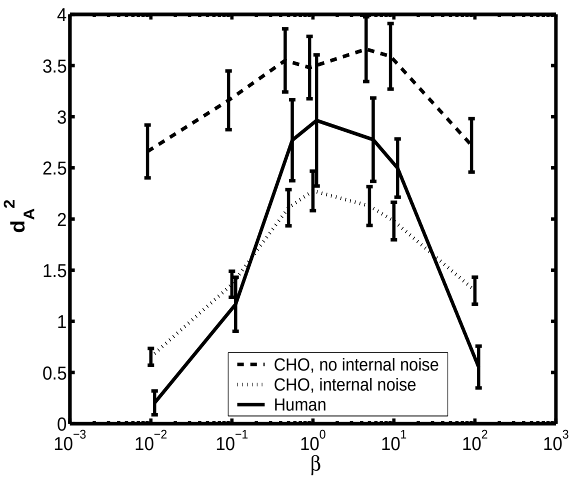

Figure 5.11: Comparison of $d_A^2$ and $\mathrm{SNR}^2$ versus $\beta$ for human unmodified and modified CHO for signal B .

noise parameters was discussed. A follow up on this work in [121] concluded that the inclusion of internal noise did not change the ranking of the CHO AUC values. In [121] the CHO predicts a narrow range of optimal OSEM iteration parameters as compared to a human ROC study which predicts a much broader range of optimal number of iterations.

One limitation of the study was the restriction to square-channel profiles. We tried two versions of 3-channel DOG (Difference-of-Gaussian) filters intended to approximately cover the same frequency bands of our square-channel filters. The results for the DOG were not qualitatively different. Both unmodified DOGs showed very flat $\mathrm{SNR}^2$ response over the entire range of $\beta$, and when modified by $\alpha_1$ and $\alpha_2$ internal noise parameters, a narrowing of the $\beta$ range similar to that seen with the square channels.

The results are shown in Fig. 5.13 for the SKE/BKS test, both $d_A$ and SNR are lowered (as expected) compared to the SKE/BKE results in Fig. 5.10, but the

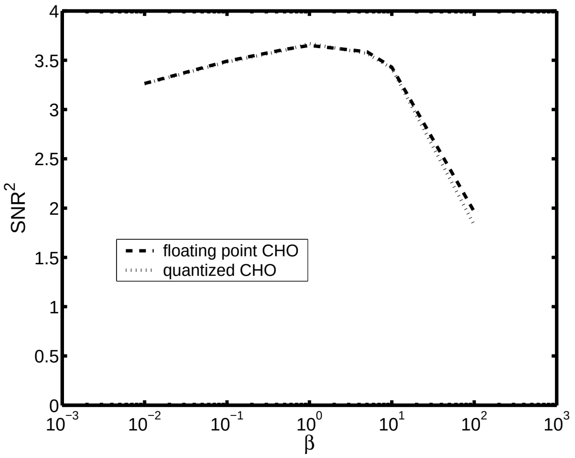

Figure 5.12: SNR$^2$ vs $\beta$ curve with and without quantization effects.

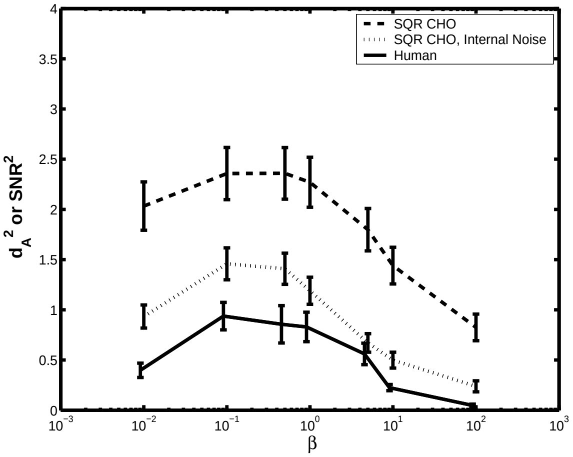

Figure 5.13: With background variability the CHO and human observer performance correlates well even without the addition of internal noise

CHO and human IQM's were well correlated even without the addition of an internal noise mechanism. The results in Fig. 5.13 show that at $\beta = 0.1$ (vz. Figure 5.1(d)) that performance was not much affected, but that $\beta = 1.0$ (vz. Figure 5.1(e)) the previous high SNR/$d_A$ values for SKE/BKE were lowered significantly, and at $\beta = 10.0$, corresponding to the smooth image of Figure 5.1(h), the performance dropped tremendously. For this very limited SKE/BKS study, unmodified CHO's appeared to track the human performance. Thus OV dramatically changed the $\beta$-response curve. We plan a more thorough investigation of this issue in the future.

# Chapter 6

# A Channelized Hotelling Observer Study of Lesion Detection in SPECT MAP Reconstruction Using Anatomical Prior

The use of *a priori* information in image reconstruction to reduce the noise in an ML estimate has been discussed in chapter 3. One might expect that a prior that reflects the nature of the underlying radionuclide distribution might give an improved reconstruction. Such a prior can be obtained by incorporating "side-information" made available from anatomical images. This chapter is based on our work [122], which focused on exploring the efficacy of such side information for lesion detection as a function of boundary proximity. In section 6.1 we give the impetus for using anatomical side-information for improving image reconstruction in the context of a detection task. We also give a brief overview of previous work done by other authors. In section 6.2, we present a simple way to incorporate anatomical information into the MAP reconstruction. In section 6.3 we show how to rapidly calculate detection performance using analytic methods. Our simulation results are shown in section 6.4. In the discussion section 6.5.1, we summarize our work. In our discussion in section 6.5.2, we place our work in the context of efforts by others to improve lesion detectability using anatomical information.

## 6.1 Introduction

In emission tomography (ET) one tries to determine the underlying radiotracer distribution of radiopharmaceutical within the patient body. This tracer concentration has high correlation with the underlying anatomy. The high correlation is due to the fact that different anatomical structures have different physiological function and hence we expect to see a difference in tracer uptake between these anatomical regions. A common assumption on anatomy-function correlation is that activity uptake tends to be slowly varying within an organ or anatomical region, but can suffer a discontinuity at a region boundary. This general observation is borne out in high resolution autoradiographic images in which functional images also clearly reveal the morphology of the underlying structures [123]. In some cases, lesion boundaries can also be observed in the anatomical scan [124], and so lesion boundary information can be used to aid in determining whether there is a significant uptake in the lesion versus its surround. This high correlation with anatomy would lead one to expect an improvement in the functional image quality with the use of this anatomical "side-information" in the image reconstruction process. Such anatomical side information can be made available from coregistered MR (for brain) and from CT (whole body) images. For instance, high resolution magnetic resonance MR images are acquired as a part of basic epilepsy presurgical evaluation protocols [125]. Furthermore, the advent of multi-modality imaging systems like PET/CT [126] and SPECT/CT [127] increase the availability of coregistered anatomical images. Many ways of improving the ET reconstruction by incorporating anatomical side information have been proposed, but the improvement in the ET images must be evaluated based on the performance with respect to a chosen task - in our case, a detection task.

A common theme for imposing anatomical information is based on applying some sort of smoothing withing anatomical boundaries while preserving discontinuities across boundaries. Keeping this theme in mind one might intuitively expect an improvement in lesion detectability, if lesion boundary information with the precise extent of the lesion is used for the reconstruction of a hot lesion in a weaker background. This intuition comes from the fact that the suspension of smoothness across boundaries prevents the blurring of the lesion into the surrounding tissue, thus possibly enhancing detection. (Any reconstruction will have a noise-resolution tradeoff, leading to a somewhat blurred reconstructed lesion.) In support of this, see Figure 6.1 for an example using noiseless reconstructions.

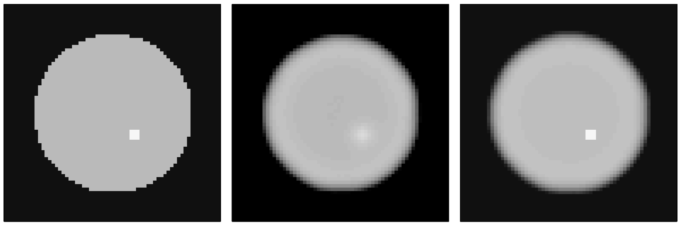

(**a**) (**b**) (**c**)

Figure 6.1: (a) Phantom with lesion present. Lesion contrast is 1.333:1 (b) Noiseless lesion-present MAP reconstruction without anatomical boundary information. (c) Noiseless lesion present MAP reconstruction with anatomical boundary information placed precisely along the lesion boundary. The figure supports the intuition that with the presence of a boundary information, we expect the detectability of the lesion to be enhanced.

Based on the above discussion, one might intuitively expect lesion detectability to be improved by anatomical side information if the lesion were proximate to an anatomical boundary; and less improved if the lesion was distant from the boundary. To address this question, we use an SKE/BKE (signal-known-exactly/background-known-exactly) detection task, and a CHO (channelized Hotelling observer) which is a numerical observer whose detection performance emulates that of humans for this task. To investigate lesion proximity effects, we therefore vary lesion and boundary locations and calculate an SNR, a scalar figure of merit for detection. In our study, our results show that these intuitions are incorrect for an SKE/BKE detection task with a channelized Hotelling numerical observer and our SPECT MAP reconstruction.

Though there are many ways to impose anatomical information, we choose a MAP (maximum *a posteriori*) reconstruction method in which a simple smoothing prior can be modified to incorporate organ and lesion boundary information. Such a method lends itself to very rapid calculation of the SNR by using analytic methods, and so allows us to perform many more experiments than we could using sample methods.

Previous work can be categorized based on the use of the side-information either in the image reconstruction step or in post-processing the reconstructed image. A limited survey follows. In [128, 129, 130, 131] a post-processing method for brain imaging using a convolution-based approach was discussed. The approaches in the former category use Bayesian estimation techniques to introduce the anatomical side-information into the reconstruction processes. In recent work in Comtat *et al.* [132] and Bruyant *et al.* [124], segmented anatomical labels were used to manipulate the weighting of a quadratic prior. Baete *et al.* [133] have developed an anatomy-based MAP algorithm for PET brain imaging. The algorithm takes into account the knowledge that the activity in the white matter (WM) has a fairly uniform spatial distribution with an unknown mean and the activity in the cerebrospinal fluid (CSF) is known *a-priori* to be negligible. This “A-MAP” scheme uses an edge-preserving concave prior [134] for the grey matter (GM) and Gaussian priors for white matter (WM) and CSF. The rationale of using a prior based on relative difference is that, since glucose metabolism in GM is not uniform but locally varying throughout the entire brain, the amount of penalty should not be based on the absolute, but rather on the relative difference of activity of neighboring pixels. Gindi *et al.* [123], Leahy and Yan [135], Lipinski *et al.* [136] and Ouyang *et al.* [137] used an edge-preserving Gibbs prior where the anatomical boundary information was used to control the formation of discontinuities in the emission reconstruction. These methods estimate pixel values as well as “line sites” (discontinuity formation) [67]. A low line-site value penalizes pixel difference whereas a high value allows difference. A spatially varying weight for the formation of line-sites modulates the Gibbs potential so as to encourage the formation of discontinuities in the emission reconstruction at sites corresponding to discontinuities in the anatomical image. Ardekani *et al.* [138] proposed an minimum cross-entropy reconstruction algorithm that incorporates multi-spectral MR data into a cross-entropy prior, which performs edge preserving smoothing based on the anatomical information. An interesting MAP approach by Hsu and Leahy [139] used a segmented anatomical image to impose a graded form of smoothing in inter-region areas where partial volume effects limit one’s ability to impose sharp continuity breaks. An elaborate hierarchical Bayesian approach was proposed by Bowsher [140] to jointly estimate anatomical side information as well as functional tracer uptake. Sastry and Carson [141] suggested a label-based tissue composition model to impose a Gaussian distribution within a tissue region. The exact tissue fractions for each pixel were provided from segmented MR brain images. Rangarajan *et al.* [142] used a joint-mixture framework to incorporate anatomical information. In [143] Bowsher *et al.* considered registration of the (MRI/CT) anatomical images with the (SPECT/PET) emission grid via optimization of an (SPECT/PET) reconstruction objective function which included the registration parameters. They provide a natural framework for calculating joint uncertainties in registration parameters and radiotracer activity. Much of the previous work reports improvement with anatomical priors in terms of ROI quantitation tasks. Baete *et al.* [125] & Bruyant *et al.* [124] address improvements for a detection task.

## 6.2 Background

### 6.2.1 Quadratic Prior With Anatomical Information

We assume the anatomical information (from a segmented preregistered anatomical image) to be present in the form of a tissue label map, where label $l_n$ is the tissue class of voxel $n$. The quadratic prior given in (3.9) can be modified to capture anatomy-function correlation by smoothing within an organ or lesion boundary while suspending smoothing across boundaries. The prior, similar to ones used in [124] and [132] , is given by

$$\Phi_P(\mathbf{f}) = -\sum_n \sum_{j \in \mathcal{N}(n)} \frac{1}{2} \frac{\omega_{nj}(l_n, l_j)}{d_{nj}} (f_n - f_j)^2 \tag{6.1}$$

where $\mathcal{N}(n)$ defines neighbors of pixel $n$, $d_{nj}$ is the Euclidean distance between voxels $n$ and $j$, and the penalty weight $\omega_{nj}(l_n, l_j)$ is dependent on the anatomical labels of voxels $n$ and $j$ as follows:

$$\omega_{nj}(l_n, l_j) = \begin{cases} 1, & \text{if} \quad l_n = l_j, \\ 0, & \text{else} \end{cases} \tag{6.2}$$

Thus, if $n$ and $j$ belong to different anatomical regions, $\omega_{nj}$ is set to 0, thus "breaking continuity" between voxels $n$ and $j$. Note that if want to turn off anatomical information, we simply set $\omega(l_n, l_j) = 1$ unconditionally and thus obtain a uniform space-invariant quadratic prior exactly as the one in (3.9). For the 2D 4NN neighborhood system in Fig. 6.2 the voxel $n$ and $j_2$ belong to different tissue classes. Hence the anatomical boundary formed between the two pixel results in a smoothing discontinuity reflected by $\omega_{nj_2} = 0$. The smoothing between voxel $n$ and voxels $j_1$, $j_3$, $j_4$ is retained since they belong to the same tissue class as $n$. In the 8NN system in Fig. 6.2 the penalty weight between voxel $n$ and the voxels $j_2$, $j_7$, $j_6$ is set to zero since they belong to a tissue class other than that of $n$. The Euclidean distance of $j_7$ and $j_6$ is taken care of by the term $d_{nj}$ in (6.1). The smoothing between $n$ and $j_1$, $j_3$, $j_4$, $j_5$ and $j_8$ is retained since they belong to the same tissue class.

The anatomical prior in (6.1) would reduce noise by smoothing within anatomical regions and preserve edges by not blurring across different anatomical regions. It will be convenient to re-express the prior $\Phi_P(\mathbf{f})$ as a quadratic form $-\frac{1}{2}\mathbf{f}^T\mathcal{R}\mathbf{f}$, where the $N \times N$ matrix $\mathcal{R}$ is the Hessian of $-\Phi_P(\mathbf{f})$ with matrix elements given by

$$[\mathcal{R}]_{nj} = \begin{cases} \sum_{j' \in \mathcal{N}(n)} \frac{2}{d_{nj'}} \omega_{nj'}(l_n, l_{j'}) & j = n \\ -\frac{2}{d_{nj}} \omega_{nj}(l_n, l_j) & j \in \mathcal{N}(n) \\ 0 & j \notin \mathcal{N}(n) \text{ and } j \neq n \end{cases} \tag{6.3}$$

Although we considered the dimensionality of the anatomical images to be the same as that of $\mathbf{f}$, many times there is in fact, a resolution mismatch. Each voxel in a functional image encompasses a number of high-resolution segmented MR or CT voxels. Often several high-resolution anatomical voxels with disparate labels may constitute a single functional voxel resulting in a fractional tissue composition in the corresponding voxel. Due to this resolution mismatch there may not be a distinct anatomical boundary. If a voxel is composed of fractions of different tissue classes then the corresponding anatomical boundary between those classes gets diluted at this voxel. Often, convoluted anatomical structures have thicknesses less than the resolution of the reconstruction grid. It is difficult to resolve these anatomical structures given the finite axial and transaxial resolution of the functional images. This causes at least a few voxels to be composed of different tissue classes (partial volume voxels). Generally if not accounted for, this partial volume may lead to underestimation of tracer in that anatomical structure at those partial volume voxels. In [128, 129, 130, 131, 133, 134] techniques using anatomical information are used to minimize the partial volume effects (PVE) in the convoluted gray matter areas in brain imaging. Some segmentation algorithms give a fuzzy classification i.e. they return a probability that a voxel belongs to a certain tissue class. In this case even in

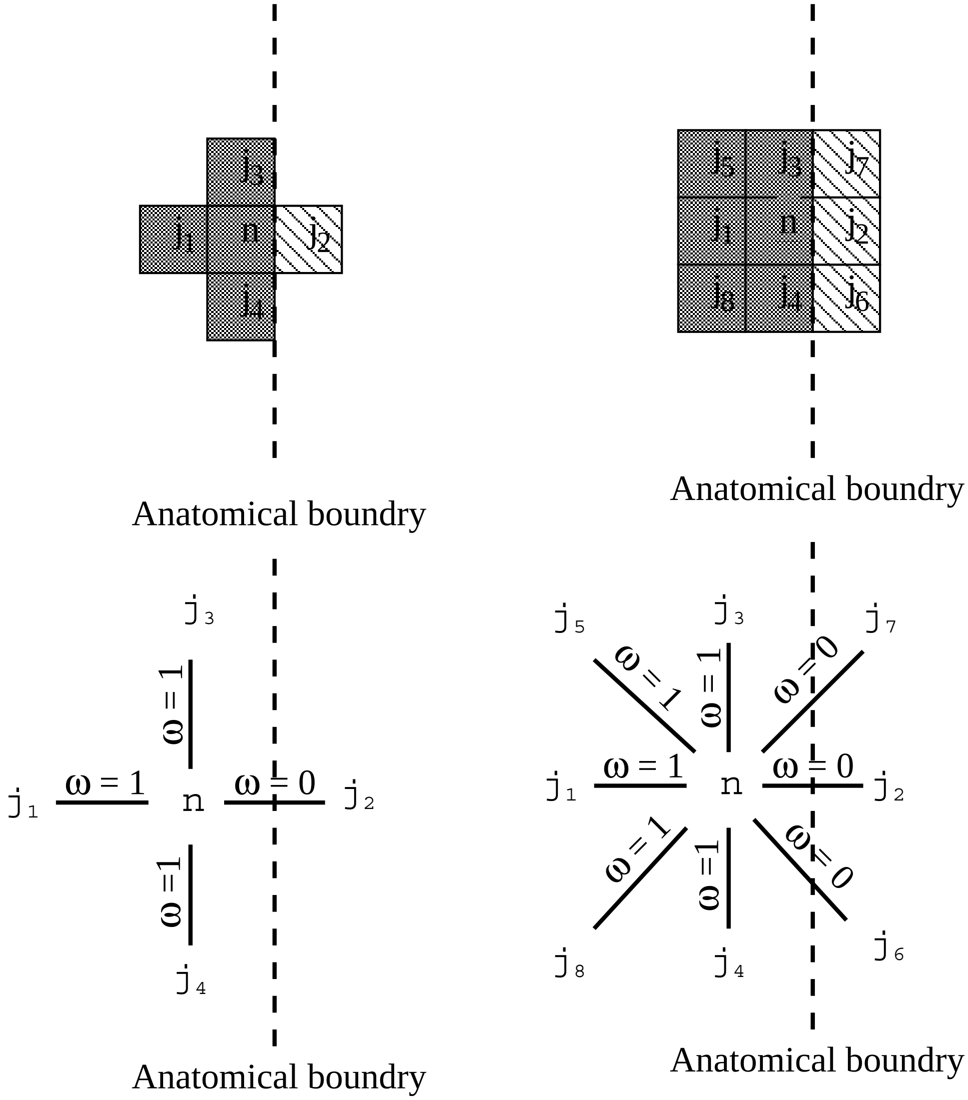

Figure 6.2: The figure illustrates the use of anatomical boundary information in a 4NN and 8NN neighbourhood system. The voxels on either side of anatomical boundary belong to different classes. The penalty weight for the voxels across the corresponding boundary is set to zero. Shading indicates tissue class.

the absence of function-anatomy resolution mismatch we would have partial volume voxels. Further, there may be small-scale misalignments due to errors in the registration of functional and anatomical images. Registration errors are typical for images of the same patient using two different imaging modalities. This inter-modality misalignment is less than a few pixel distances in the functional images since brain is a rigid registration. The registration errors in whole body image can be big. Miss-registered edges or blurred edges result in imperfect anatomical information. This imperfect side information would reduce the effectiveness of anatomical information. We assume that if boundary proximity effects are significant, they should show up in the idealized case where both effects are absent. Thus in our study we do not consider partial volume effect and our prior assumes each voxel to be assigned to only one tissue type, though it can accommodate partial volume effects with a slight modification, similar to the "blurred label" scheme in [132].

So far, we have implied a model in which different anatomical regions have different activity. But to complicate matters, there may be an emission discontinuity with no corresponding anatomical discontinuity. For example, a tumor avid lesion in an organ may not have an anatomical signature. In the same vein, an anatomical lesion boundary may not correspond to an emission hot-spot, e.g. a necrotic lesion that shows up in CT may not show up in SPECT. In our simulations we consider both such cases of false boundaries.

## 6.3 Methods

The CHO SNR calculations typically require sample methods as discussed in section 4.2.4. For each of the many cases (many lesion locations and many boundaries) we will consider, the calculation of SNR using sample methods requires a few hundred sample reconstructions. This is a formidable amount of computation. The SNR is applied to an SKE/BKE detection task since such a task can clearly elicit the effects of boundary proximity. In addition, SKE/BKE tasks lend themselves to rapid evaluation of SNR for the CHO using the theoretical methods. In this section, we focus on the theoretical methods used to rapidly obtain SNR.

From section 4.2.3 we know that $\mathcal{K}_{\hat{\mathbf{f}}}$ is an average covariance. For our SKE/BKE task and for the low contrast signals that we will use, it is a good approximation to use $\mathcal{K}_{\hat{\mathbf{f}}_1}$ for $\mathcal{K}_{\hat{\mathbf{f}}}$. We can justify this approximation because our analytically calculated SNR's (which use $\mathcal{K}_{\hat{\mathbf{f}}_1}$) are validated by sample-method SNR's (computed using $\frac{\mathcal{K}_{\hat{\mathbf{f}}_1}+\mathcal{K}_{\hat{\mathbf{f}}_2}}{2}$). The mean channel responses become $\bar{\hat{\mathbf{u}}}_2 = \mathcal{T}^T\mathcal{L}\bar{\hat{\mathbf{f}}}_2$ and $\bar{\hat{\mathbf{u}}}_1 = \mathcal{T}^T\mathcal{L}\bar{\hat{\mathbf{f}}}_1$. The covariance of these extracted 2D images is $\mathcal{L}\mathcal{K}_{\hat{\mathbf{f}}_1}\mathcal{L}^T$ and the corresponding covariance of the channel responses, $\mathcal{K}_{\hat{\mathbf{u}}}$, becomes $\mathcal{T}^T\mathcal{L}\mathcal{K}_{\hat{\mathbf{f}}_1}\mathcal{L}^T\mathcal{T}$. With the inclusion of slice extraction and the approximation $\mathcal{K}_{\hat{\mathbf{f}}} \sim \mathcal{K}_{\hat{\mathbf{f}}_1}$ in (4.19), the CHO SNR becomes

$$\mathrm{SNR}^2 = (\bar{\hat{\mathbf{f}}}_2 - \bar{\hat{\mathbf{f}}}_1)^T\mathcal{L}^T\mathcal{T}(\mathcal{T}^T\mathcal{L}\mathcal{K}_{\hat{\mathbf{f}}_1}\mathcal{L}^T\mathcal{T})^{-1}\mathcal{T}^T\mathcal{L}(\bar{\hat{\mathbf{f}}}_2 - \bar{\hat{\mathbf{f}}}_1) \tag{6.4}$$

We shall base our sample-method calculation of SNR on (4.19) and our analytic methods on (6.4).

We perform two types of studies. In the first, termed the "organ boundary" experiment, we place a lesion at varying distances from an organ boundary and evaluate the SNR vs. distance for the case of an anatomical prior and for an ordinary smoothing prior (no anatomy). In the second, termed a "lesion boundary" experiment, there were no organ boundaries, only a uniform background with a single lesion. We fix the functional lesion size and location but vary the anatomical boundary about the lesion so that its radius increases beyond the functional lesion. At its minimum radius, the anatomical boundary exactly encloses the lesion boundary. The maximum radius corresponds to no boundary. The lesion boundary experiment is also motivated by the following consideration: A perfect anatomical lesion boundary is the extreme case of isotropic boundary information at minimal proximity in all directions. We relax this “ultimate” anatomical information by increasing the radius of the boundary until there is no boundary, and then we assess the effects on SNR to gain insight.

### 6.3.1 Organ Boundary Experiment

Let $\mathbf{s}_j$ denote a lesion centered at $j$. Then, $\mathbf{f}_{2j} = \mathbf{b} + \mathbf{s}_j$ is the signal-present 3D object. Let $\bar{\hat{\mathbf{f}}}_{2j}$ be the the mean reconstruction of the object with $\mathbf{s}_j$. Denote $\mathcal{T}_j$ as the channel template matrix centered at $j$. From (6.4) the detectability of the lesion centered at $j$ is given by

$$\mathrm{SNR}_j^2 = (\bar{\hat{\mathbf{f}}}_{2j} - \bar{\hat{\mathbf{f}}}_1)^T \mathcal{L}^T \mathcal{T}_j (\mathcal{T}_j^T \mathcal{L} \mathcal{K}_{\hat{\mathbf{f}}_1} \mathcal{L}^T \mathcal{T}_j)^{-1} \mathcal{T}_j^T \mathcal{L} (\bar{\hat{\mathbf{f}}}_{2j} - \bar{\hat{\mathbf{f}}}_1) \tag{6.5}$$

The quantities $\bar{\hat{\mathbf{f}}}_{2j}$ and $\bar{\hat{\mathbf{f}}}_1$ are well approximated by noiseless reconstructions. The main theoretical computation is in the terms $(\mathcal{T}_j^T \mathcal{L} \mathcal{K}_{\hat{\mathbf{f}}_1} \mathcal{L}^T \mathcal{T}_j)$ in (6.5). This involves the difficult-to-compute covariance matrix $\mathcal{K}_{\hat{\mathbf{f}}_1}$. For our BKE MAP case, we rewrite (4.36) the theoretical expression for the covariance as

$$\mathcal{K}_{\hat{\mathbf{f}}_1} = (\mathcal{F} + \beta \mathcal{R})^{-1} \mathcal{F} (\mathcal{F} + \beta \mathcal{R})^{-1} \tag{6.6}$$

where $\mathcal{F} = \mathcal{H}^T \mathrm{diag}\left( \mathcal{H}\mathbf{f}_1 / (\mathcal{H}\bar{\hat{\mathbf{f}}}_1)^2 \right) \mathcal{H}$ is an $N \times N$ matrix that approximates the Fisher information matrix.

For uniform quadratic priors with no continuity breaking, the Hessian of the prior, $\mathcal{R}$, is triply block circulant (shift invariant if we ignore the edge pixels), hence $(\mathcal{T}_j^T \mathcal{L} \mathcal{K}_{\hat{\mathbf{f}}_1} \mathcal{L}^T \mathcal{T}_j)$ in (6.5) can be evaluated using a local shift invariance assumption and Fourier approximations [114, 116] as described in Section 4.3. But with the incorporation of continuity breaking, the matrices $\mathcal{R}$ become shift variant and hence we cannot use the Fourier tricks. Instead we use the following alternate method.

Substituting (6.6) in $(\mathcal{T}_j^T \mathcal{L} \mathcal{K}_{\hat{\mathbf{f}}_1} \mathcal{L}^T \mathcal{T}_j)$ we get

$$\mathcal{T}_j^T \mathcal{L} \mathcal{K}_{\hat{\mathbf{f}}_1} \mathcal{L}^T \mathcal{T}_j$$

$$
\begin{aligned}
&= \mathcal{T}_j^T \mathcal{L}(\mathcal{F}+\beta\mathcal{R})^{-1}\mathcal{F}(\mathcal{F}+\beta\mathcal{R})^{-1}\mathcal{L}^T\mathcal{T}_j \\
&\equiv \mathbf{X}_j^T \mathcal{F}\mathbf{X}_j && (6.7) \\
&= \mathbf{X}_j^T \mathcal{H}^T \mathrm{diag}\left(\mathcal{H}\mathbf{f}_1/(\mathcal{H}\bar{\bar{\hat{\mathbf{f}}}}_1)^2\right)\mathcal{H}\mathbf{X}_j && (6.8)
\end{aligned}
$$

where $\mathbf{X}_j \equiv (\mathcal{F}+\beta\mathcal{R})^{-1}\mathcal{L}^T\mathcal{T}_j$ is an $N \times N_c$ matrix. The $i^{th}$ column of matrix $\mathbf{X}_j$, given by vector $\mathbf{x}_j^i$, can be obtained by solving the following linear system

$$
(\mathcal{F}+\beta\mathcal{R})\mathbf{x}_j^i = \mathcal{L}^T\mathbf{t}_j^i \tag{6.9}
$$

where $\mathbf{t}_j^i$ is the $i^{th}$ channel template centered at $j$.

Equation (6.9) must be solved for all $i = 1, \ldots, N_c$ channels and $j = 1, \ldots, J$ locations. We can solve this matrix-vector equation for a given $\mathbf{x}_j^i$ using a preconditioned conjugate-gradient (PCG) method with a diagonal preconditioner [144]. Solving for one $\mathbf{x}_j^i$ is computationally equivalent to a few reconstructions. Thus (6.9) would involve an order of $JN_c$ reconstructions. In (6.8), the matrix $\mathcal{H}\mathbf{X}_j = \begin{bmatrix}\mathcal{H}\mathbf{x}_j^1 & \mathcal{H}\mathbf{x}_j^2 & \ldots & \mathcal{H}\mathbf{x}_j^{N_c}\end{bmatrix}$ is obtained by projecting each column of $\mathbf{X}_j$. (In this notation $\mathcal{H}\mathbf{x}_j^l$, the projection of $\mathbf{x}_j^l$ is the $l^{th}$ column of $\mathcal{H}\mathbf{X}_j$). Thus $\mathcal{H}\mathbf{X}_j$ entails $N_c$ projections. Given $\mathcal{H}\mathbf{X}_j$, each $mn^{th}$ element of the $N_c \times N_c$ matrix $\mathcal{T}_j^T\mathcal{L}\mathcal{K}_{\hat{\mathbf{f}}_1}\mathcal{L}^T\mathcal{T}_j$ can be calculated by the dot product of $\mathcal{H}\mathbf{x}_j^m$ and $\mathcal{H}\mathbf{x}_j^n$ weighted by diagonal elements of $\mathrm{diag}\left(\mathcal{H}\mathbf{f}_1/(\mathcal{H}\bar{\bar{\hat{\mathbf{f}}}}_1)^2\right)$. That is $\left[\mathcal{T}_j^T\mathcal{L}\mathcal{K}_{\hat{\mathbf{f}}_1}\mathcal{L}^T\mathcal{T}_j\right]_{mn} = (\mathcal{H}\mathbf{x}_j^m)^T\mathrm{diag}\left(\mathcal{H}\mathbf{f}_1/(\mathcal{H}\bar{\bar{\hat{\mathbf{f}}}}_1)^2\right)\mathcal{H}\mathbf{x}_j^n$. Thus in (6.8) we have shown how to compute the crucial $N_c \times N_c$ matrix $\mathcal{T}_j^T\mathcal{L}\mathcal{K}_{\hat{\mathbf{f}}_1}\mathcal{L}^T\mathcal{T}_j$. Since $N_c$ is small, the inversion of this $N_c \times N_c$ matrix is rapidly accomplished.

The terms $\bar{\bar{\hat{\mathbf{f}}}}_1$ and $\bar{\bar{\hat{\mathbf{f}}}}_{2j}$ in (6.5) can each be evaluated by a noiseless reconstruction [112] for each lesion location plus one noiseless reconstruction for a signal-absent case, requiring a total of $J+1$ reconstructions. Since (6.9) requires $\sim JN_c$ reconstructions, our theory method to calculate the CHO SNR at locations $j = 1, \cdots, J$ with varying proximity to a fixed boundary thus entails an order of $J(N_c+1)+1$ reconstructions, where $N_c$ is typically 3-5. Sample methods as described in section 4.2.4 would take

$(J+1)N_{samp}$ reconstructions, where $N_{samp}$ is the number of sample reconstructions for a given object. Since $N_{samp}$ should $10 \sim 100$ times $N_c$ [110], the net computational savings using theory vs. sample methods is thus roughly two orders of magnitude.

### 6.3.2 Lesion Boundary Experiment

In this scenario, we take $r = 1, \cdots, R$ spherical boundaries with varying radii circumscribing the fixed-location lesion $\mathbf{s}$. (The quantity $r$ is not the radius; it indexes the boundary radius as will be shown in Figure 6.3 below.) Our intent is to relax the boundary confinement (proximity) of the fixed lesion by surrounding it with continuity-breaking boundaries of increasing radii. To study the effects of $r = 1, \ldots, R$ different boundaries on the detectability of the lesion, we have to calculate the CHO SNR for the $r^{th}$ boundary given by

$$\mathrm{SNR}_r{}^2 = (\bar{\hat{\mathbf{f}}}_2^r - \bar{\hat{\mathbf{f}}}_1^r)^T \mathcal{L}^T \mathcal{T} (\mathcal{T}^T \mathcal{L} \mathcal{K}_{\hat{\mathbf{f}}_1^r} \mathcal{L}^T \mathcal{T})^{-1} \mathcal{T}^T \mathcal{L} (\bar{\hat{\mathbf{f}}}_2^r - \bar{\hat{\mathbf{f}}}_1^r) \tag{6.10}$$

where $\hat{\mathbf{f}}_2^r$ and $\hat{\mathbf{f}}_1^r$ are the reconstructions of $\mathbf{f}_2$ and $\mathbf{f}_1$ using the $r^{th}$ lesion boundary information in the prior. Figure 6.3 shows an example of varying anatomical boundaries for $r = 1, \ldots, 8$.

As in section 6.3.1, the main computation is in the terms $(\mathcal{T}^T \mathcal{L} \mathcal{K}_{\hat{\mathbf{f}}_1^r} \mathcal{L}^T \mathcal{T})$ in (6.10). Following (6.6), (6.7), (6.8), (6.9) in section 6.3.1 but for given $r$ instead of a given $j$, we can again compute $(\mathcal{T}^T \mathcal{L} \mathcal{K}_{\hat{\mathbf{f}}_1^r} \mathcal{L}^T \mathcal{T})$. Note that in (6.6), $\mathcal{R}$ becomes $\mathcal{R}^r$, i.e. the $\mathcal{R}$ prior matrix indexed by $r$, and $\mathcal{F}$ becomes $\mathcal{F}^r$, given by $\mathcal{F}^r = \mathcal{H}^T \mathrm{diag}\left(\mathcal{H}\mathbf{f}_1 / (\mathcal{H}\bar{\hat{\mathbf{f}}}_1^r)^2\right) \mathcal{H}$. Furthermore since the lesion is now centered at a single location, the channel matrices $\mathcal{T}_j$ becomes a single matrix $\mathcal{T}$. With this reindexing, and for $R$ lesion boundaries and $N_c$ channels, we obtain the following computational burden for the lesion boundary case. It takes $\sim RN_c$ reconstructions to obtain $(\mathcal{T}^T \mathcal{L} \mathcal{K}_{\hat{\mathbf{f}}_1^r} \mathcal{L}^T \mathcal{T})$ for $r = 1, \cdots, R$. For a single boundary, $\bar{\hat{\mathbf{f}}}_1^r$ and $\bar{\hat{\mathbf{f}}}_2^r$ can be calculated using 2 noiseless reconstructions. Therefore, for $R$ different boundaries, the theory method takes on the order of $RN_c +$

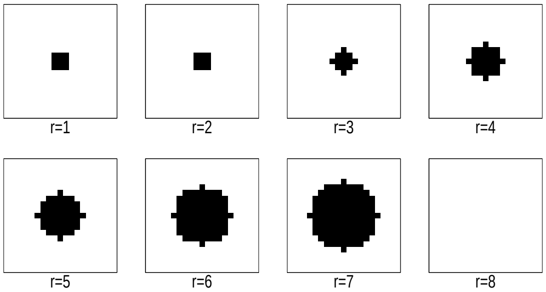

Figure 6.3: 2D cross-section of 3D spherical anatomical boundaries of increasing radii centered on a fixed small lesion. The radii are indexed by $r$. Note $r = 1$ corresponds to a boundary coincident with the lesion boundary and $r = 8$ to no boundary. Dark pixels are inside the boundary.

$2R$ reconstructions, while sample methods would involve $2RN_{samp}$ reconstructions. The net computational savings is again about two orders of magnitude.

## 6.4 Results

We conducted 3D SPECT simulations to explore the effects of boundary information. In all cases, we used $N_c = 3$ DOG bandpass channels in the radially symmetric CHO as shown in Figure 4.3(a)(b)(c). The center frequencies of the 3 DOG channels were 0.0625 cycles/pixel, 0.1250 cycles/pixel and 0.250 cycles/pixel. These channel parameters were chosen according to criteria described in our work [95]. These values would correspond to 0.625 cycles/degree, 1.25 cycles/degree and 2.5 cycles/degree if $\delta_{view} = 38$cm and $\delta_{pix} = 0.0645$cm as is in section 5.4.2. Though this would cause the displayed image width to be 4.2 cm. In [33] the center frequencies of the Sparse DOG channels correspond to 1 cycles/degree, 2 cycles/degree and 4 cycles/degree. We used the theoretical methods of section 6.3 to calculate SNR and validated the theory methods with sample methods.

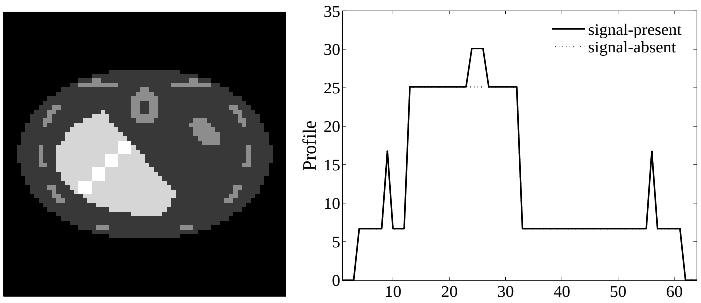

(a) (b)

Figure 6.4: (a) The $9^{th}$ slice of the phantom through the lesion center. The figure shows four of the ten prospective lesion locations. (b) Horizontal profile plot through center of second lesion from top. In the profile plot the lesion is easily seen, centered at pixel 25.

We performed an organ boundary experiment with a 3D MCAT [145, 146, 147] $64 \times 64 \times 16$ phantom with cubic voxels of size 0.625cm and an attenuation map at 140 KeV. The 16 slices comprised a region around the liver (The slices start where the lungs end and contain most of the liver). A depth-dependent collimator response was modeled as a Gaussian psf whose $\sigma$ was modeled as $\sigma\ (cm) = 0.013\ d\ (cm) + 0.0392\ cm$ where $d$ is depth measured from the collimator face. No scatter was simulated. Figure 6.4 shows the $9^{th}$ slice of the phantom with four prospective lesion locations in the liver at varying distances from the (inner edge) straight liver boundary. We used 10 lesion locations across the liver from one edge to the other. The lesion is a $3 \times 3 \times 3$ cube with the 8 corner voxels deleted and with a low-contrast lesion-to-background ratio of 6:5. We note that for SKE/BKE studies in ECT, low-contrast lesions are required to avoid unacceptably high SNR's. Each camera face comprised $96 \times 32$ square bins of size 0.625 cm and was placed at a distance of 30 cm from the center of rotation. We simulated a parallel-beam geometry with 65 equispaced projection angles. The total number of counts was 4.8M. The reconstructions with a regularization weight of $\beta = 0.001$ used the COSEM-MAP [84] algorithm with 16 subsets and were run till convergence. The smoothing parameter $\beta$ was chosen to obtain a reasonable noise-resolution tradeoff. Organ boundary information was applied using (6.2) in the reconstructions.

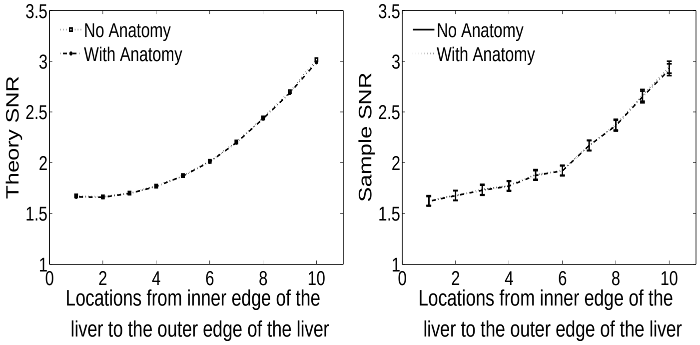

(a) (b)

Figure 6.5: (a) Theory SNR plotted as a function of location ranging from the inner edge of the liver to the outer edge. "Location" is proportional to distance from the inner edge. (b) Sample SNR along with error bars plotted as a function of location ranging from the inner edge of the liver to the outer edge. In each case, the curves for the anatomy and no-anatomy cases coincide almost exactly, so the plots appear as a single curve.

Figure 6.5(a) plots SNR vs. lesion location from the inner edge to the outer edge of the liver boundary for the cases of with/without anatomy. The CHO SNR's were calculated using the theoretical expressions for SNR in (6.5). There is no visible difference in the anatomy/no anatomy curves. One thousand two hundred lesion-present and lesion-absent reconstructions were used for the sample validation of the SNR using (4.21),(4.22) and (4.19). The sample SNR curves are shown in Figure 6.5(b). They show close correspondence with the theory curves in Figure 6.5(a). Error bars calculated using a jackknife procedure [111] as described in section 4.2.4 and displayed in Figure 6.5(b) represent a 68% confidence interval. As seen, there is no visible anatomy vs. no-anatomy difference in the SNR (for either sample or theory methods) even when the lesion is adjacent to either edge of the liver. Figures 6.6(a)(b) show signal-present anecdotal reconstructions with no anatomy information and with anatomy information, respectively. Figures 6.6(c)(d) are anecdotal signal-present reconstructions with the signal contrast enhanced for display purposes.

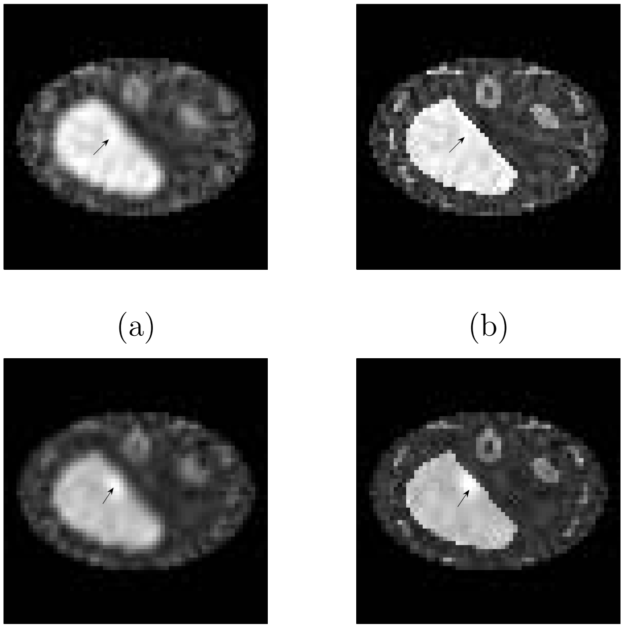
(a) (b)

(c) (d)

Figure 6.6: Slice from anecdotal signal-present reconstructions (a) without organ boundaries (b) with organ boundaries. Signal-present reconstructions with a signal contrast increased for visualisation (c) without and (d) with anatomical boundary discontinuities. Note (a)(b) share a common gray scale and (c)(d) share a common grey scale.

The bowing of the SNR curves is due to attenuation effects. The voxel corresponding to the location # 1 in Figure 6.5 is near the object center while that at location # 10 is near the edge of the object. Pixels near the center will suffer lower SNR relative to those near the edge, hence the bowing. This is because photons emanating from the voxel at the center of the object undergo attenuation on their path to the camera faces at each of the 65 projection angles, while those emanating from the edge of the object do not undergo attenuation on their path towards the camera faces closer to the corresponding edge. When attenuation is removed, the SNR curves in Figures 6.5(a)(b) become nearly flat.

One might suspect that our main conclusion for the organ boundary experiment, i.e. no separation of the anatomy and no-anatomy curves in Figure 6.5, would be altered with the inclusion of internal noise described in section 4.2.5 in the CHO. To address this we used an internal noise model summarized by the following transformation of the diagonal of $\mathcal{K}_{\hat{\mathbf{u}}}$ : $[\mathcal{K}_{\hat{\mathbf{u}}}]_{ii} \rightarrow [\mathcal{K}_{\hat{\mathbf{u}}}]_{ii} + \alpha_1 [\mathcal{K}_{\hat{\mathbf{u}}}]_{ii} + \alpha_2 \max_j [\mathcal{K}_{\hat{\mathbf{u}}}]_{jj}$ where $\alpha_1$, $\alpha_2$ were positive scalars as described in section 5.5. We tried 441 combinations of $(\alpha_1, \alpha_2)$. In each case, the curves in Figure 6.5 were lowered, but they remained coincident, so that internal noise did not affect our main conclusion.

Though the results in Fig. 6.5 were for a single $\beta$ we repeated the organ boundary experiment using theory methods, again for a high ($10\beta$) and low ($0.1\beta$) smoothing parameter. We observed the anatomy vs no-anatomy curves remained coincident for all values of $\beta$. In addition the low $\beta$ curve shifted downward about 30% and the high $\beta$ curve shifted upward roughly 5%.

For the organ boundary experiment we observed no difference in SNR for MAP with anatomy versus MAP without anatomy even when the lesion is at its closest distance to the anatomical boundary. One might expect a different result if instead of an non-anatomical MAP reconstruction, a post smoothed ML (psML) reconstruction was used. We investigated this issue using sample methods to compute SNR for post-smoothed ML (psML) and theory methods to compute SNR for MAP with our anatomical prior. For MAP, the SNR was plotted vs smoothing parameter $\beta$, and for psML, SNR was plotted vs $\sigma_{ps}$, the standard deviation of a 3-D Gaussian post-smoothing kernel. We used the case of that lesion in Figure 6.5(a) at minimal distance to the inner edge of the organ boundary. To obtain the psML results, we reconstructed the data with 90 iterations of OSEM with 16 subsets followed by 10 iterations of the ML-convergent COSEM-ML [84] algorithm with 16 subsets. A total of 2400 samples for the lesion present and -absent case were used. Figure 6.7 shows the SNR curve for MAP with anatomy compares favourably to the psML curve and the MAP peak is 12% above the psML peak. Since we also observed that the SNR for MAP with anatomy is equal to SNR for MAP without anatomy we can conclude that for the CHO, MAP reconstructions without anatomy outperform psML resonstructions. Qi in [148] came to the same conclusion.

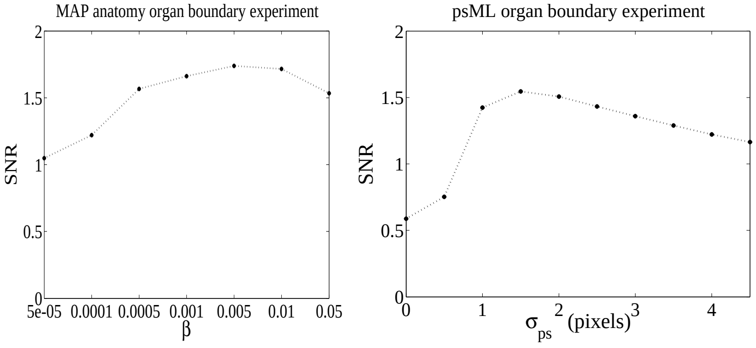

(a) (b)

Figure 6.7: SNR curves for a lesion from the organ boundary experiment closest to the inner edge of the liver.(a) Theory SNR as a function of $\beta$ for MAP with organ boundary information. (b) Sample SNR for post smoothed ML reconstruction as a function of $\sigma_{ps}$.

We performed a lesion boundary experiment using a $64 \times 64 \times 16$ object with cubic voxels of size 0.625 cm. Here, as seen in Figure 6.8(a), the background was uniform and the lesion was placed at the center of the object volume. The lesion, a $3 \times 3 \times 3$ cube with the 8 corner voxels removed, had a contrast of 1.345 relative to background. All other imaging and reconstruction parameters were as before except that a smoothing parameter $\beta = 0.002$ was used. The smoothing is reasonable in reducing the noise in the reconstruction without over-smoothing the reconstructed signal. Anatomical information in the form of $R$ spherical anatomical lesion boundaries indexed by $r = 1, \cdots, R$ was used in the reconstructions. Anatomical information is indexed by a parameter $r$, with $r = 1$ implying perfect knowledge of the functional lesion boundary, $r = 2$ imperfect knowledge where the radius of the surrounding anatomical lesion boundary is enlarged slightly, $r = 3, 4, 5, 6, 7$ even more imperfect knowledge with even larger radii as shown in Figure 6.3, and with $r = 8$ corresponding to no lesion boundary (no anatomical knowledge). MAP reconstructions with and without anatomical information were evaluated using our theoretical expressions for the SNR in (6.10). The observer is applied at the lesion site and evaluated vs. $r$. Nine hundred lesion-present and lesion-absent reconstructions for each $r$ were used for the sample validation of the SNR using (4.21), (4.22) and (4.19). Error bars calculated using a jackknife procedure [111] and displayed in Figure 6.8(b) represent a 68% confidence interval.

From Figure 6.8(b) we see that the SNR does not significantly vary with $r$ and that the theory and sample methods correspond well. This result belies the intuition discussed in Figure 6.1. That the SNR vs. $r$ curve is indeed flat is borne out by the anecdotal signal-present (+) and -absent (-) reconstructions shown in the first four rows of Figure 6.8(c). Note that even in the signal-absent cases, the lesion boundaries can induce false lesions as seen in the $4^{th}$ row of Figure 6.8(c). For signal-present

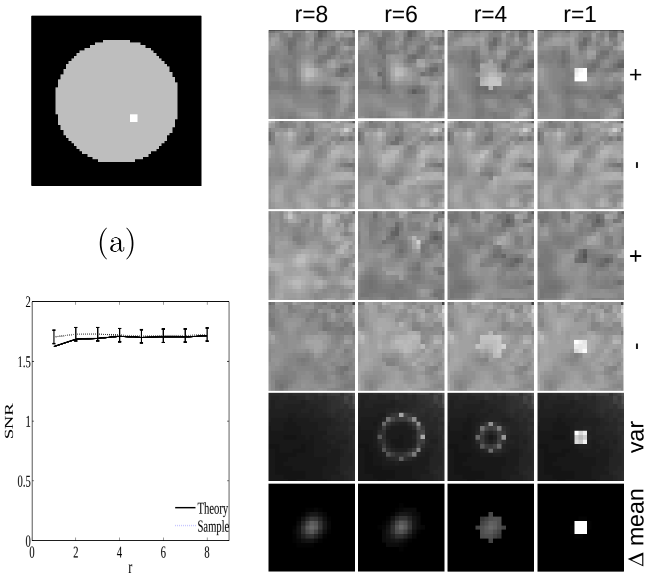

(a)

(b)

(c)

Figure 6.8: Effects of increasingly inaccurate boundary information about the lesion. (a) $9^{th}$ slice of the phantom through center of the lesion (b) SNR versus proximity of boundary with r=1 a perfect boundary and r=8 no boundary. Plot shows that SNR versus $r$ is relatively flat, with theory and sample methods in agreement. (c) Each column corresponds to a boundary indexed by r. The first four rows show anecdotal reconstructions with the lesion present (+) and absent (-). The fifth row plots variance at each pixel and the sixth row is the difference of reconstructions.

cases, the lesion boundaries can induce reverse contrast (cold) lesions in place of the hot-lesion signal. The fifth row of Figure 6.8(c) comprises the variance images (at a common gray scale) of the $9^{th}$ slice. The sixth row shows the $9^{th}$ slice of the noiseless reconstructions of the signal, given by $\mathcal{L}\bar{\hat{\mathbf{f}}}_2^r - \mathcal{L}\bar{\hat{\mathbf{f}}}_1^r$. Note that the variance level along the perimeter of the anatomical lesion boundary increases as the lesion boundary becomes more confining. This accounts for a typical result of a false positive lesion as seen in the fourth row, column $r$=1 and the cold lesion as seen in the third row, column

$r = 1$. A similar result of increased variance along the perimeter of the lesion boundary accompanied by false positive lesions is reported in [132]. The high variance can also lead to false negative reports as seen in the images in row 3, columns $r$=4,6 and 8. The last row illustrates that the anatomical lesion boundary restricts the spread of the mean reconstructed lesion and yields for noiseless images a higher contrast with more restricting boundaries. One would expect this latter effect to increase SNR as $r$ is reduced. However, tight boundaries also increase variance (row 5), and this decreases SNR. The trade-off of these two effects results in the slow variation of SNR with $r$ seen in Figure 6.8(b).

We repeated the lesion boundary experiment of figure 6.8(b), but with a smaller $1 \times 1 \times 3$ pixel lesion whose size in the plane of observation was less than the system resolution. The reason for doing this in the case of the lesion boundary experiment is to see if anatomical information assists lesion detection particularly when the functional lesion as well and the anatomical lesion boundary is smaller than the system spatial resolution. The FWHM at the center of rotation is $1.01cm$. We added one additional lesion boundary, indexed by $r = 0$, that exactly encompassed the smaller functional lesion ($0.625cm$ wide in the plane of observation). The resulting theory SNR vs $r$ curve was again invariant with $r$.

We again tested whether the inclusion of internal noise would affect our main conclusion - the invariance of SNR with $r$. As before, we used 441 combinations of $(\alpha_1, \alpha_2)$ in the internal noise modification of $\mathcal{K}_{\hat{\mathbf{u}}}$. We observed that inclusion of internal noise lowered the overall SNR($r$) curve, but did not change the invariance with $r$. Internal noise, therefore, did not alter our conclusions.

The Figure 6.8(b) shows the SNR($r$) for a single $\beta$ which is flat and the SNR$\approx=$ 1.7. We used theory to repeat this lesion boundary experiment for $10\beta$ and $0.1\beta$ and observed that curves remained fairly flat with $r$, but that the SNR for the low

$0.1\beta$ was much lower (SNR≈1.2) and the SNR for the higher $10\beta$ was slightly higher (SNR≈1.83).

For the lesion boundary experiment we observed that the SNR at $r = 1$ was equal to the SNR at $r = 8$. One might expect the SNR for a non-anatomical non-MAP psML reconstruction instead of a non-anatomical ($r = 8$) MAP reconstruction to be different from the SNR at $r = 1$. To investigate this issue we used sample methods to compute SNR for psML and theory methods to compute SNR for MAP with $r = 1$. To obtain the psML results, we reconstructed the data with 90 iterations of OSEM with 16 subsets followed by 10 iterations of the ML-convergent COSEM-ML algorithm with 16 subsets. We used a total of 1800 samples for signal-present and -absent reconstructions. The results are displayed in Figure 6.9.

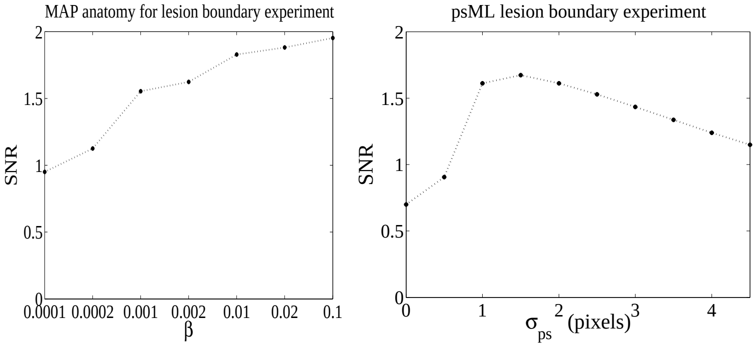

(a) (b)

Figure 6.9: For the lesion boundary experiment (a) SNR for MAP($r = 1$) plotted vs smoothing parameter $\beta$, (b) SNR for psML plotted vs $\sigma_{ps}$.

For the range of $\beta$ and $\sigma_{ps}$ in Figure 6.9 here, the peak SNR($\beta$) is 15% greater than that of SNR($\sigma_{ps}$). Since SNR for MAP with $r = 1$ is same as for MAP with $r = 8$ one could conclude that for a CHO, MAP reconstructions outperform psML reconstructions. A similar result is observed for a non-anatomical MAP reconstruction by Qi in [148] and for an anatomical MAP reconstruction in Nuyts in [149].

One observes that with no regularization (i.e $\beta = 0$ a.k.a psML with $\sigma_{ps} = 0$) the SNR is much lower for both organ boundary and lesion boundary experiments.

## 6.5 Discussion

### 6.5.1 Summary

We studied the effects of anatomical information on lesion detectability using anatomical and non-anatomical MAP priors, an SKE/BKE task, a CHO observer and a scalar figure of merit SNR. We investigated, in this context, whether SNR would be improved with the incorporation of organ boundary information. We further investigated whether this improvement in SNR would be a function of proximity of the lesion to an organ boundary. We concluded that SNR was unchanged with the addition of organ boundary information, and in particular, we found no change in SNR at any proximity.

We also investigated whether the incorporation of anatomical lesion boundaries coincident with the assumed functional lesion boundary (our $r = 1$ case) would improve SNR relative to no anatomical information (our $r = 8$ case). We further investigated whether SNR improvements, if any, would vary if the anatomical lesion boundary was less proximate (our $1 < r < 8$ case) to the assumed functional lesion boundary. We concluded that SNR was unaffected by the inclusion of perfect ($r = 1$) lesion boundaries. In particular, SNR was insensitive to $r$. This insensitivity may be due to the fact that for the low lesion contrast necessary for an SKE/BKE task, the detection performance is limited by the appearance of false positive and false negative lesions within anatomical lesion boundaries. This is caused by an increase in variance within the lesion boundary as seen in figure 6.8(c).

In sum, we found that anatomical boundary information did not affect SNR in our context, and that SNR was unaffected as proximity was varied. We note that related studies by others, discussed in section 6.5.2, do not include proximity effects. Hence any comparisons to our work involve only perfect ($r = 1$) lesion boundary information. In addition, comparisons involving organ boundaries do not take into account lesion location with respect to the organ boundary.

One can gain some insight into our negative results by noting that, for our reconstruction method, an optimal linear observer, the Hotelling observer (HO), would yield no SNR difference with anatomy versus without anatomy. Note that the CHO is a Hotelling observer applied to channel responses instead of directly to pixels. The HO is a limiting form of the CHO as we increase the number of channels so that a unit-weight channel template is applied to each pixel. Note that $\mathrm{SNR}^2_{HO} \geq \mathrm{SNR}^2_{CHO}$. Qualitatively, the smoothing prior without anatomy acts as a linear information-preserving slowly-varying smoothing filter in the reconstruction domain, and the HO is insensitive to this smoothing if the reconstruction step does not remove information. When we adjust $\mathcal{R}$ to incorporate anatomical information, it simply induces a form of smoothing on the reconstruction that yields sudden changes along anatomical loci and the HO is again insensitive to this form of smoothing. Yet another way to see that $\mathrm{SNR}_{HO}$ is insensitive to $\mathcal{R}$, and hence insensitive to anatomical priors, is to note that the $\mathrm{SNR}_{HO}$ can be expressed directly in the sinogram domain [150, 33, 29] as $\mathrm{SNR}_{HO} = \mathbf{s}^T \mathcal{H}^T \mathrm{diag}(\frac{1}{\mathcal{H}\mathbf{f}_1}) \mathcal{H}\mathbf{s}$. Therefore any difference in the anatomy versus no-anatomy results must be due to the inclusion of channels, though, as mentioned earlier, we have seen little difference with our CHO.

In [150] it was shown, for the SKE/BKE MAP case, that if $\mathcal{F}$ and $(\mathcal{F} + \beta\mathcal{R})$ were invertible, then $\mathrm{SNR}^2_{HO}$ as calculated in the reconstruction domain would be independent of the smoothing as encoded in $\mathcal{R}$. The result in [150] was derived using Fourier techniques and applied to forms of $\mathcal{R}$ that encoded simple space-invariant quadratic smoothing, but it is easy to generalize this argument to the form of $\mathcal{R}$, quadratic prior with continuity breaking vz (6.1), used for our anatomical priors. The $\text{SNR}^2_{HO}$ on applying the Hotelling observer to the reconstructed images is given by

$$\text{SNR}^2_{HO} = (\bar{\hat{\mathbf{f}}}_2 - \bar{\hat{\mathbf{f}}}_1)^T \mathcal{K}_{\mathbf{f}}^{-1} (\bar{\hat{\mathbf{f}}}_2 - \bar{\hat{\mathbf{f}}}_1) \tag{6.11}$$

where $\mathcal{K}_{\hat{\mathbf{f}}} = \frac{1}{2}(\mathcal{K}_{\hat{\mathbf{f}}_1} + \mathcal{K}_{\hat{\mathbf{f}}_1})$. As introduced by [150, 94] for an SKE/BKE case the difference between mean reconstructions is given by

$$(\bar{\hat{\mathbf{f}}}_2 - \bar{\hat{\mathbf{f}}}_1) \approx (\mathcal{F} + \beta\mathcal{R})^{-1} \mathcal{H}^T \text{diag}\left(\frac{1}{\mathcal{H}\bar{\hat{\mathbf{f}}}_1}\right) \mathcal{H}\mathbf{s}. \tag{6.12}$$

where $\mathcal{F} = \mathcal{H}^T \text{diag}\left(\mathcal{H}\mathbf{f}_1/(\mathcal{H}\bar{\hat{\mathbf{f}}}_1)^2\right)\mathcal{H}$. Substituting (6.12) and (6.6) in (6.11) we get

$$\begin{aligned} \text{SNR}^2_{HO} \;\approx\; & \mathbf{s}^T \mathcal{H} \text{diag}\left(\frac{1}{\mathcal{H}\bar{\hat{\mathbf{f}}}_1}\right) \mathcal{H}(\mathcal{F} + \beta\mathcal{R})^{-1} \left((\mathcal{F} + \beta\mathcal{R})^{-1} \mathcal{F} (\mathcal{F} + \beta\mathcal{R})^{-1}\right)^{-1} \\ & (\mathcal{F} + \beta\mathcal{R})^{-1} \mathcal{H}^T \text{diag}\left(\frac{1}{\mathcal{H}\bar{\hat{\mathbf{f}}}_1}\right) \mathcal{H}\mathbf{s}. \end{aligned} \tag{6.13}$$

Using the fact that $\mathcal{F} \approx \mathcal{H}^T \text{diag}(\frac{1}{\mathcal{H}\bar{\hat{\mathbf{f}}}_1})\mathcal{H} \approx \mathcal{H}^T \text{diag}(\frac{1}{\mathcal{H}\mathbf{f}_1})\mathcal{H}$ [69], we obtain

$$\text{SNR}^2_{HO} \approx \mathbf{s}^T \mathcal{H}^T \text{diag}\left(\frac{1}{\mathcal{H}\bar{\hat{\mathbf{f}}}_1}\right) \mathcal{H}\mathbf{s} \approx \mathbf{s}^T \mathcal{H}^T \text{diag}(\frac{1}{\mathcal{H}\mathbf{f}_1})\mathcal{H}\mathbf{s} \tag{6.14}$$

Indeed, it is possible, given the strictures on $\mathcal{F}$ and $(\mathcal{F} + \beta\mathcal{R})$, to calculate $\text{SNR}^2_{HO}$ using only sinogram quantities [150, 33] having nothing to do with $\mathcal{R}$.

We indeed verified in a 2D organ boundary experiment that the $\text{SNR}^2_{HO}$ was insensitive to the inclusion of anatomical information and was greater than $\text{SNR}^2_{CHO}$. We used a 64 × 64 rectangular phantom consisting of a hot region and cold region separated by a vertical edge which was used as an organ boundary in presence of anatomy. Figure 6.10(a) shows a horizontal profile of the phantom drawn across the vertical organ boundary. A single pixel lesion (contrast 6:1) was placed at various points along this horizontal profile on either side of the vertical edge. Attenuation effects and detector response were not modeled in the projection data. For each

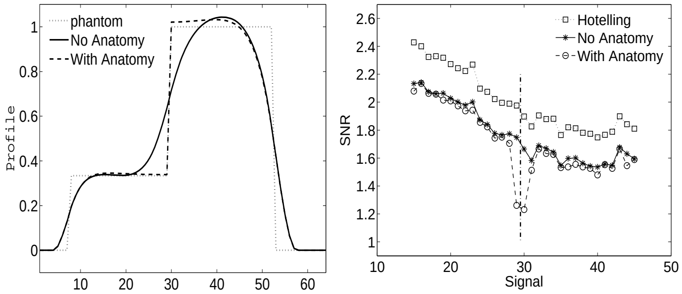

(a) (b)

Figure 6.10: (a) Horizontal profile (across a vertical organ boundary) of noiseless signal-absent reconstruction with/without organ boundary information. (b) SNR vs lesion location. The $\mathrm{SNR}_{HO}$ is observed to be same with and without boundary information. Hence a single curve for the Hotelling SNR is shown, represented by ‘$\cdots \Box \cdots$’. The two other curves lying below the Hotelling curve are the $\mathrm{SNR}_{CHO}$ with/without anatomy. Dashed dotted vertical line indicates boundary position.

lesion location, we computed both $\mathrm{SNR}^2_{HO}$ and $\mathrm{SNR}^2_{CHO}$ for the cases of with/without anatomy. For this test case without physics the $\mathrm{SNR}^2_{CHO}$ versus lesion location curves differed for anatomy versus no anatomy in the vicinity of the boundary. In contrast, the $\mathrm{SNR}^2_{HO}$ versus lesion distance curves coincided to several decimal places. Furthermore, the $\mathrm{SNR}^2_{HO}$ curve remained invariant when it was computed directly from sinogram data. Hence the $\mathrm{SNR}_{HO}$ is shown by a single curve in Figure 6.10(b) lying above $\mathrm{SNR}_{CHO}$ curves for with/without organ boundary. The $\mathrm{SNR}_{CHO}$ with organ boundary decreases near the boundary (dashed line).

Our selection of a 3-DOG channel scheme does not seem especially important and we have observed similar results with different channel schemes. For any reasonable $\beta$, the anatomy/no anatomy SNR curves remain in close agreement. We also observed that the inclusion of internal noise did not alter our conclusions. Our CHO used radially symmetric channels even near organ boundaries where a non-symmetric channel might be more appropriate. The use of radially symmetric channels is justified [30] when the signal profile and noise covariance is radially symmetric around the lesion. This is true for our lesion boundary experiment. But for the organ boundary experiments, the signal spread and the covariance are anisotropic and the use of anisotropic channels might give different performance. Partly to address this problem, we designed our somewhat artificial lesion boundary experiment to be completely isotropic in 3D. We again observed little difference in SNR as the anatomical lesion boundary radius was expanded to the point where the boundary disappeared.

Finally, this work should obviously be extended to human observer testing. Preliminary results using human experiments with a 2AFC methodology [29] to measure SNR showed agreement of human and model observer for our lesion boundary experiment, but far more work is needed.

### 6.5.2 Related Work

Any comparison of our results to other work must be couched in the context of the components of a generalized detection task. Thus one must specify the task (detection or detection plus localization or localization). The object model including signal (size, contrast, shape, location known or unknown) and background (variable or fixed) must be stated. The imaging modality (PET or SPECT) and imaging model (Monte Carlo vs analytical projector, modeling of scatter or other effects) must also be stated. One must consider the nature of the anatomical boundary information (the particular type of lesion and or organ boundary) and the reconstruction method (MAP with some anatomical or non-anatomical prior, post smoothed ML). To measure image quality, one must specify the observer + scalar figure of merit (CHO+SNR, NPW+SNR, scanning CNPW+ALROC, human+ALROC, human+localization accuracy.) Finally many studies focus on the variation of the figure of merit with some regularization parameter (smoothing weight $\beta$ in MAP, post smoothing kernel for ML, number of iterations).

It will be useful in our comparisons below to be more specific about our anatomical boundary taxonomy. We will consider 4 types of boundary: (i) organ boundaries (ii) perfect lesion boundaries as in our $r = 1$ case (we shall refer to these as “tight lesion boundaries”) (iii) organ + tight lesion boundaries (iv) hybrid boundaries, in which functional lesions are surrounded by complex anatomies that do not correspond to any of the cases (i)-(iii).

Others have assessed the effects of anatomical priors in PET and SPECT for pure detection, pure localization, and for detection plus localization tasks. None of these directly addressed our question of boundary proximity effects, but some of these works had conclusions that bore relation to our work. We first consider previous work that involved detection only.

The work most similar to ours is found in [149]. Nuyts *et al.* in [149] considered the detection of hypometabolic regions in brain PET using an SKE/BKE task and CHO+SNR. They compared SNR performance for their brain-specific AMAP anatomical reconstruction versus a non-anatomical post-smoothed ML (psML) reconstruction. Like our anatomical MAP prior, the prior in AMAP breaks continuity across anatomical boundaries but applies different forms of smoothing within grey matter, white matter and CSF. In phantom studies incorporating tight lesion boundaries, organ boundaries and hybrid boundaries, they found that AMAP at a variety of smoothing parameters $\beta$ outperformed psML at a variety of Gaussian post-smoothing kernels with standard deviation $\sigma_{ps}$. A related study by Baete *et al.* [133, 125] assessed SNR of hypometabolic brain regions in PET but used an NPW (Non-prewhitening) observer [29] rather than a CHO. Again AMAP was compared to psML. The brain phantom used here involved hybrid boundaries only. No significant difference was found between the optimal NPW SNR of AMAP and the optimal NPW SNR of psML. In [133]

Baete *et al.* again addressed the same PET problem using an NPW observer, but this time compared the performance of AMAP versus that of a MAP algorithm using a relative difference prior [134]. The NPW SNR was greater for AMAP than that of MAP-RD.

Since for our MAP with SKE/BKE and CHO+SNR, anatomical information essentially had no advantage, and since, in the various contexts listed above, AMAP *did* often show an advantage, one is motivated to reconcile these differences. In [149] AMAP did indeed outperform psML using a CHO and SKE/BKE detection task. However, the study was incommensurate with ours in that AMAP differed from our anatomical MAP and psML differed from our non-anatomical MAP. In [133] the MAP-RD prior is of interest because it is the natural non-anatomical Bayesian counterpart of AMAP. However, that study was again incommensurate with ours since the observer was an NPW. Despite incommensurabilities, one might well infer that a prior (such as AMAP) highly tuned to the anatomical correlates of the underlying radiotracer distribution might lead to improved performance in a detection-only task.

We now consider previous work [124, 151, 152, 153] involving a detection plus localization task for a Ga-67 SPECT torso simulation. The projection data were generated using a Monte Carlo package. These tasks involve model observers and a figure of merit radically different than ours and also necessarily involve lesion contrasts much higher than those required by SKE/BKE. The figure of merit was the area under the LROC curve (ALROC). These works used either human observers or a numerical scanning channelized NPW (CNPW) observer [154]. The observer was required to correctly detect the signal while also localizing it within a search tolerance. They addressed the case of SPECT with an imaging model similar to ours. They encoded anatomical information using a MAP objective identical to ours. Their lesion contrasts were high ranging from 12:1 to 30:1. They considered organ boundaries but with the lesion location, if the lesion was present, distributed uniformly throughout a search region. The results in [124], using their numerical observers, showed that the use of organ-boundary information did not increase ALROC relative to that obtained with non-anatomical psML. While scatter was not modeled in [124], it was included in [151, 152]. In [151], organ boundary information led to a mild increase in ALROC for the numerical observer relative to that of non-anatomical psML. In a human observer study in [153], they used, in addition to a non-anatomical psML reconstruction, a non-anatomical MAP reconstruction identical to the one in this paper. Scatter was included. An interesting conclusion was that for MAP reconstructions organ boundaries alone did not significantly improve ALROC. These papers also considered the case of organ + tight lesion boundaries. All four papers found significant ALROC increases with respect to their non-anatomical counterparts for this organ + tight lesion boundary case. In sum, organ boundaries alone did not help much, but organ + tight lesion boundaries were of significant help in detection plus localization studies. In a separate work by a PET brain group, in [125] Baete *et al.* used a pure localization task (signal always present but location unknown), human observers, and a figure of merit given by percent correctly localized signals in an MAFC study. They used a brain phantom whose hypometabolic lesions were surrounded by hybrid boundaries. The lesion contrast ranged from 5% -100%. In this context it was found that AMAP outperformed the non-anatomical psML reconstruction.

While none of the studies involving higher-order tasks, such as detection plus localization, directly addressed boundary proximity effects, it would be interesting to investigate these. For example, since the ALROC metric involves an aggregate detectability over all locations in a search region, it is not clear whether lesions nearer to boundaries contributed more to ALROC than other lesions.

Finally, we point out that previous studies discussed in this section have not included the important feature of statistically variable backgrounds. Aside from their realism, the inclusion of background variability might lead to a change in conclusions regarding the efficacy of anatomical priors in some task contexts.

# Chapter 7

# Statistical Properties of SPECT MAP Reconstruction Incorporating Window Based Scatter Correction

In this chapter, we derive analytical noise propagation formulae incorporating scatter effects in SPECT MAP reconstruction. This chapter is based on our work in [155, 156]. By accounting for noise in the reconstruction due to scatter, we can, in principle perform image quality tests under more realistic conditions, i.e. scatter noise in addition to photon noise and object variability.

## 7.1 Introduction

In SPECT imaging systems, scatter can account for a significant fraction of the counts detected within an allowed (photopeak) energy window whose width scales with the energy resolution of the detector. Energy windows we discussed in Chapter 2. The corresponding sinogram thus contains scatter counts, and when reconstructed, this scatter can lead to a degradation of image quality in addition to that due to other sources.

Many types of scatter correction (SC) methods have been proposed (see [8, 157, 158] for a good overview). In Section 7.2 we have a literature survey of the various scatter estimation and compensation techniques. Energy window-based SC (WSC) is a simple and oft-used method [159, 160, 161, 162, 163, 164, 165, 166, 167, 168, 169, 170, 171] in which counts collected in one or more satellite energy windows are used to estimate the scatter contribution in the photopeak window. Reconstruction-based SC methods [54, 53, 172, 173, 174, 175] start with an estimated source and attenuation map and calculate the contribution of scatter in the projection. The contribution is calculated using the underlying principles of scatter interactions and this contribution is used in the reconstruction. Transmission-dependent convolution subtraction methods [176, 177] use the photopeak data along with data from a transmission scan to estimate scatter in the photopeak. While the latter two SC methods are based on more sophisticated physical models of scatter than window based methods, WSC is more easily implemented and enjoys frequent use [178, 175, 179, 173]. In many cases, the performance of WSC methods is comparable to that of the more sophisticated and computationally complex methods [178, 175]. One of the more well-known WSC techniques is the TEW (Triple Energy Window) [162, 180] method and similar variants [181, 182, 183]. Here, counts in narrow satellite windows on either side of a photopeak window are used to estimate counts in the photopeak window. Our analysis will focus on TEW but is generally applicable to many WSC methods.

Often, in WSC, one simply subtracts the scatter estimate from the photopeak window and then reconstructs. However, one can incorporate WSC directly into a reconstruction, and there are reasons (discussed in section 7.3)) to prefer this over simple subtraction.

In Chapter 4 Section 4.3 we derived theoretical expressions for rapid evaluation of the first- and second-order moments of SPECT MAP reconstructions corrupted by Poisson noise in the absence of scatter. In this chapter we develop theoretical expressions that enable the rapid calculation of the mean, covariance and local point spread function (lpsf) of SPECT reconstructions that incorporate WSC. Theoretical calculation of these quantities (mean, covariance, lpsf) can be used to rapidly calculate figures of merit (FOM) that summarize performance of detection and estimation tasks for reconstructed images.

In [184], Qi and Huesman presented a similar theoretical analysis for propagating noise from a Monte Carlo (MC) estimated scatter sinogram into a PET mammographic reconstruction. The noise in the MC scatter estimate is due to the finite number of source events used for an MC run. They give an expression for the covariance of the reconstruction caused by photon noise and noise in the MC scatter estimate. In our work, we apply this approach to the case of WSC, where the noise in the scatter estimate is due to photon noise in photopeak and satellite energy windows. We use this to calculate an lpsf and mean as well as a covariance for the reconstructed image.

Reconstructions are noisy by virtue of photon noise propagated into the reconstruction and also by virtue of a necessarily noisy scatter estimate that comprises part of the imaging model. We develop theory expressions for mean, covariance and lpsf for SPECT MAP in the presence of these two sources of noise. Indeed similar theory expressions for the case of emission tomography but with only the photon noise were developed in [112, 69] and in section 4.3. Subsequent papers built on [112, 69] to develop expressions that enable rapid calculation of detection figures of merit FOMS [119, 150, 115, 94, 109, 96, 97] and quantitation FOMs [185, 186]. Some of these papers [119, 109, 69, 115, 119, 150, 94, 185, 186] modeled scatter but, unlike the work in this paper, did so as a known deterministic quantity. In [187], the effects of a systematic bias in $\mathrm{H}^S$ were analyzed in the context of PET.

Instead of fast theoretical expressions to evaluate mean, covariance and lpsf, one can instead evaluate these quantities by sample methods that entail numerous laborious reconstructions. Therefore one motive to develop the theory expressions is that they can be used to more rapidly (faster than sample) calculate lpsf, covariance and mean and thus more rapidly obtain useful FOMs. In section 7.6 we evaluate the speedup of our theory vs sample methods for the calculation of mean, covariance and lpsf.

In section 7.2 we present a literature survey on various scatter correction methods. In section 7.3 we give background information on MAP reconstruction and WSC methods. In section 7.4 we present our theoretical development. In section 7.5 we validate our theoretical expressions using sample methods. We conclude in section 7.6 with a discussion.

## 7.2 Literature Survey of Scatter Compensation Techniques

This rather exhaustive literature survey is meant as an aid to those familiar with scatter techniques. To the casual reader section 7.2 is difficult to follow since only limited space is available to describe the plethora of methods. However, in section 7.3 we shall focus on window based methods and build our mathematical development slowly and carefully.

Scatter correction methods can be divided into two categories. First category described in are the ones that use the acquired emission data to estimate the scatter contribution in the projection data. This acquired emission data could be from the energy spectrum (TEW or Compton Window) as described in Section 7.2.1 or a combination of the photopeak data and an approximation of the scatter PSF as described in Section 7.2.2. This scatter contribution can then be modeled before the reconstruction or during the reconstruction or after the reconstruction. The second category is the Reconstruction Based SC methods (RBSC) described in 7.2.3 consists of those that model the scatter during the reconstruction using the underlying principles of scattering interactions. In Section 7.2.4 we give a brief description of various works comparing the different Energy Window based scatter correction methods and RBSC methods.

### 7.2.1 Energy Window based Scatter Estimation Methods

The energy window based methods estimate the scatter contribution within the photopeak window using the photons detected the entire energy spectrum around the photopeak. The entire spectrum around the photopeak is used to correct for scatter due to the effect of down-scatter. A photon of higher energy can get down scattered into a low energy photopeak. These down-scattered photons can be corrected by using counts from an energy window on the higher side of the lower energy photopeak window. Convolution based methods described in Section 7.2.2 use the scatter estimate for scatter correction by convolving the photopeak data with a scatter PSF.

Compton window method (CW)

The method by Jaszczak in [159] is also known as dual energy window method or Compton window (CW) method. Two energy windows are used, the photopeak (127 keV-153 keV) and a secondary window (92-125keV). Projection data from the secondary window is multiplied by a scaling factor "$k$" and is then subtracted from the photopeak projection. The scaling factor is derived from calibration studies or from Monte Carlo (MC) simulation. The heuristic method gave a value of $\approx 0.5$ while MC gave a value or 0.57. His results are based on value of $k$ to be equal to 0.5.

It is observed that the value of "$k$" varies depending on radionuclide, energy-window definition, activity distribution and attenuation [188]. In [188] by Koral *et al* phantom studies are performed to investigate, first the effect of varying background levels around a spherical hot object on the "$k$" values and second, to relate the "$k$" value to body-size and location variations. Luo *et al* in [189] use Monte Carlo simulation to investigate VOI quantification of radioactive structures and the effect on that quantification of dual-energy- window scatter correction. They find values of $k$ for a variety of phantom geometries.

### Spectral fitting methods

The spectral fitting method in [161] involves establishing the shape of the energy spectrum for unscattered counts i.e. scatter-free spectrum (by calibration or MC). For every given pixel location in the projection data, the acquired energy spectrum can be assumed to be a sum of the scatter spectrum (this vector is unknown which we want to determine) and the a known bell shaped scatter-free spectrum times an unknown scalar parameter (which we want to determine). The authors have made another assumption that the scattered energy spectrum can be represented as a third order polynomial. Combining these two assumptions a system of equations can be written. A weighted least squares solution of this system gives the coefficients for the polynomial fitting and the unknown scalar multiplier. The multi window spectral fitting method in [161] employs 32 2keV windows from 108keV to 162 keV to estimate the unscattered component of the acquired data. The energy spectrum is analyzed in two stages. The first is an iterative peak-erosion algorithm. The result of successively reducing the peak height is an estimate of the Compton scattering spectrum.

The method described in [163] is similar to Koral *et al* [161], but does not assume a polynomial shape for the scatter component of the energy spectra. It requires knowledge of the camera energy resolution function (i.e. the detected ‘energy’ spread function for any true gamma ray energy). Instead of the polynomial fitting it assumes the scatter spectrum within the acquired data to be the convolution of the camera energy resolution function and the scatter energy distribution of the source. Knowing the camera energy response function, Wang *et al* [163] wrote a system of equations similar to those in [161] and then performed a penalized least square inverse operation to estimate the scatter. Monte-Carlo simulations on hot sphere in cold cylinders with $^{99m}$Tc and $^{131}$I were performed. Wang *et al* provide a data weighted least-square method and a unweighted least-square method.

### Dual photopeak Window (DPW)

In [164], King *et al* divide the photopeak window into two non-overlapping abutted energy windows. The ratio of counts in the lower to upper energy window is used as an input to a regression relation that gives the scatter fraction (ratio of scatter to primary) (SF) within the photopeak. The coefficients of the analytic function are obtained by calibration experiments for $^{99m}$Tc. Using the scatter fraction the scatter in the photopeak is estimated, this estimate is then low-pass filtered before being subtracted from the counts in the photopeak (sum of lower and upper energy windows). This method is not applicable to our analysis in this Chapter because it involves ratios of counts in the lower to upper energy window to get the scatter fraction. The use of ratios is not within out mathematical scope.

### Channel Ratio Method

The same windows used for Dual photopeak window (DPW)[164] SC were used here. The channel ratio method [165] assumes that the ratio of the number of unscattered photons detected in these two sub windows is constant value $\alpha$ and the ratio of the number of scattered photons in these two windows has a constant value $\beta$. Consequently, calibration of $\alpha$ and $\beta$ results in a system of four equations for four unknown values. Its solution leads to the number of unscattered photons in the photopeak window. Pretorius *et al* performed phantom calibration experiments with $^{99m}$Tc source in air and water to determine the values of $\alpha$ and $\beta$.

### Generalized Spectral Method (GS)

Haynor *et al* in [166], describe a multi-window method that uses a linear combination of counts in many energy windows to estimate the scatter contribution in each pixel. Moore *et al* in [171] refer to this as a generalized spectral method. This scatter contribution is then spatially smoothed and this smoothed scatter contribution at each pixel is subtracted from the total number of counts (summed over energy bins) for that pixel. A Rollo phantom was used to study linear scatter correction methods for $^{99m}$Tc and $^{201}$Tl sources. For $^{99m}Tc$ the acquisition window extended from 96.5-168.5 keV and was divided into 18 4 keV energy bins. For, $^{201}Tl$, the acquisition window extended from 39.7-120.7keV and was subdivided into 27 bins of 3 keV each. The authors give a procedure for obtaining the optimal the weight for every energy bin. In the "optimal" sense, it minimizes some normalized mean square error (NMSE) and error in region of interest (EROI) criteria. They also give a model-based adaptive scatter correction method which delivers a set of basis functions (the first basis function being the primary component) by performing principal component analysis on the lower order polynomials obtained from the energy spectra and the camera energy response function. They compare their optimal linear method to the model-based adaptive method along with the dual photopeak window method. The model-based adaptive method outperforms the other schemes.

The Compton window method and GS method used by Haynor is applicable to our analysis in this Chapter. Haynor *et al*'s model-based adaptive method is based on an obscure extension of Koral *et al* [161].

### Triple Energy Window TEW

The TEW method by Ogawa *et al* in [162], uses two satellite windows on either side of the photopeak window to estimate the scatter in the photopeak window for every pixel in the projection data. This scatter is then subtracted from the photopeak projection on a pixel by pixel basis. The same group in a later publication (Ichihara *et al* [180]) conducted physical evaluations of this method using experimental phantoms and also applied this method to patients in a clinical trial. They performed studies with a single isotope ($^{99m}$Tc) and a dual-isotope ($^{201}$Tl and $^{123}$I). The relation between the activity within a region of the reconstructed image vs the true activity (in mCi) is used as a tool for comparison. The TEW corrected images perform better than no scatter correction. Ichihara *et al* in [180] argue that overlapping windows are hard to acquire. The same argument is observed in Bong *et al* [181].

In Dewaraja *et al* [190] the accuracy of quantitative $^{131}$I SPECT with TEW SC is evaluated by phantom measurements. In $^{131}$I imaging the right satellite window is used to compensate for scatter by 637keV and 723keV. The photopeak width at centered at 364keV was set at 20%(72.8keV) and the left satellite windows at 6% (19keV) and right satellite window at 6% (25keV). The TEW scatter estimate is subtracted from the photopeak projection. Attenuation maps were generated from registered X-ray CT images using external markers in the physical phantom. Quantitaive accuracy in the post smooted EM reconstructed images with TEW was better than no scatter correction. A preliminary clinical trial to evaluate tumor activity of B-cell lymphoma patients with $^{131}$I radioimmunotherapy was also performed.

The Extended TEW method by Bong *et al* in [181] is a modification of TEW with the satellite window not abutted to the photopeak window. When the satellite windows are abutted to the photopeak the ETEW boils down to TEW. ETEW is compared to TEW using MC simulations for point sources as well as hot and cold spheres in a cylindrical water phantom. The scatter components were estimated using ETEW and TEW. NMSE, image contrast, activity recovery coefficients, and normalized standard deviation were calculated for evaluation and comparison of FBP reconstruction of the TEW and ETEW SC projections. Extended TEW method in [181] is tractable with our analysis in this Chapter.

As far as variants of the basic TEW, there are two: Bourguignon *et al* [182] and Li *et al* [183].

Ogawa *et al* in [167] employed a 3 layered artificial neural network (ANN) to estimate primary photons in the photopeak. Five 6keV windows with the energy range of 125-154keV were used. The ANN comprised of 5 input units, 5 hidden units and 2 output units. The inputs to the input units were the ratio of counts acquired by narrow windows to total counts acquired from 125-154keV. The outputs were scatter count ratios and primary count ratio. The neural network was trained with a backpropagation algorithm using calculated true energy spectra obtained by MC methods. Energy spectra from 3 projection angles was used resulting in 192 samples in the training set. They showed an accurate estimation of primary photons using an error ratio metric. They even analyzed the performance of the ANN for different network parameters (no. of input units and no. of hidden units) Ogawa *et al* [167]'s method is not tractable by our analysis. The given input to the ANN is the ratio of counts in the corresponding energy window to the total counts in all energy windows. The output is the ratio of scatter counts to the total counts in all energy windows.

Maksud *et al* in [191] use an ANN to simultaneously correct for attenuation and Compton scattering. The ANN used was a multilayer perceptron (MLP) featured with error backpropagation algorithm as learning tool. Three sets of experiments are conducted using data of radioactive sources with various shapes and distributions in the a homogeneous medium. They use metrics like RMSE, recovery and likelihood to compare CW, DPW and TEW SC schemes with their scheme. Fakhri *et al* in [168] used the ANN in [191] for scatter correction in $^{67}$Ga SPECT.

Holospectral Imaging

Holospectral Imaging described by Gagnon in [160] is a multiwindow SC method with typically 16 subwindows. The acquired projection data is rearranged into 16 frames where the $i^{th}$ frame corresponds to the projection data acquired in the $i^{th}$ energy window. A single bin in the projection data can be visualized as a point in $\mathbf{R}^{16}$ dimensional space. To analyze the relation between these 16 frames, the 16 frames are transformed into 16 principal component frames using the Hotelling transform. The eigenvectors corresponding to these principal component bear a certain relation to the contribution of primary, scatter and noise to the acquired data. The eigenvector with the maximum eigenvalue gives the direction of maximum variation in $\mathbf{R}^{16}$ space which would be due to the primary component of the projection data. The second largest eigenvalue corresponds to the variation due to the scatter component in the acquired data in $\mathbf{R}^{16}$ space. In order to reduce the scatter component of the acquired data, a filtering operation is performed on the principal components to eliminate the variations due to the second highest eigenvalue. The resulting principal components are then transformed back. To maintain positivity a nonlinear operation is further performed. Gagnon extended this work in [192].

### 7.2.2 Convolution based subtraction methods

These methods seek to estimate the scatter content of the projection data on the basis of the acquired photopeak data. This photopeak data is used to estimate of the source distribution and this source is projected using some model of the scatter point spread function in the projection space. Example of convolution subtraction [193], [194] and [195]

#### Scatter line-spread function

The scatter line-spread function (SLSF) method described in [196] and [197] is a convolution-subtraction technique that used spatially variant scatter line-spread functions in the modeling of the scatter component. The knowledge of the source distribution is necessary to select appropriate scatter functions. This information is obtained from reconstructed SPECT images since each voxel is an estimate of the given voxel in the object. This method estimates the scatter contribution from each voxel location in the object using the scatter LSF and the scatter-to-total fraction for that voxel location.

#### Transmission dependent convolution subtraction schemes

Meikle *et al* in [176] describe a method of scatter compensation that uses the photopeak data along with data from a transmission scan to estimate scatter in the photopeak. The scatter distribution is first estimated by convolving the projection data with a monoexponential scatter function. The subsequent scatter fraction to be used is then determined for each point in the projections based on the transmission scan. If the convolution operation is denoted by $\otimes$ then it is an iterative deconvolution operation given by $\mathbf{g}^k = \mathbf{g}_{obs} - K(\mathbf{g}^{k-1} \otimes sf)$ where $sf$ is the monoexponential scatter function, $\mathbf{g}^k$ is the scatter corrected projection at the $k^{th}$ iteration and $K$ is obtained from the transmission data. On a pixel by pixel basis in projection domain it can be written as $g^k(x, y) = g_{obs}(x, y) - K(x, y)[(g^{k-1}(x, y) \otimes sf(x, y)]$. Other groups [198, 199, 200, 177] have worked on optimized extensions of TDSC.

### 7.2.3 Reconstruction based scatter correction (RBSC)

In RBSC, scatter is included in the statistical model. With RBSC methods, compensation is achieved by mapping scattered photons back to their point of origin in the object instead of trying to determine a separate estimate of the scatter contribution to the photopeak projection data [174]. RBSC methods in some way try to perform the $\mathrm{H}^S\mathbf{f}$ operation at every iteration (or the scatter is estimated at every $p^{th}$ iteration). One drawback [175] of RBSC methods is that they cannot account for scattered photons that originate outside the SPECT camera field-of-view (FOV). Multi-energy window based methods can correct for these scattered photons that originate outside the FOV.

### Effective Scatter Source estimate (ESSE)

Frey and Tsui proposed the ESSE scatter model of RBSC in [54] The ESSE scatter model works by calculating an 'effective scatter source' form which the scatter contribution can be estimated using the same projector as for the primary photons. The effective scatter source is dependent upon the current image estimate, the attenuation map, the projection angle and ESSE scatter kernel. The current image estimate is blurred into an effective scatter source distribution. The effective scatter source is formed by taking into account the probability that a photon emitted at a given location will reach the scattering site, the photon there undergoes a scattering interaction that leads to it being detected, and finally that the scattered photon will interact in the crystal producing an event that is within the energy window used in imaging. The probability of it not being lost due to attenuation on its way from its last scattering site to the crystal is handled by the ($\mathrm{H}^P$) the projector that models attenuation and collimator blur for the primary photons. Computation of the effective scatter source can be broken into two parts (1) convolution of the current image estimate with the ESSE scatter kernel (this is done for the first three terms of a truncated Taylor series expansion of the exponential describing the probability of attenuation of the photon from the site of emission to the site of last scattering [54]) and (2) weighting by the relative density map to account for some of the effects of non-uniform attenuation. Advances to this method involving an incremental slice-by-slice blurring approach are provided by Zeng *et al* in [201] and Bai *et al* in [172].

In [202] the authors have applied a RBSC to Thallium-201 which a multi-energy isotope. The use ESSE [54] for scatter modeling.

### Monte Carlo Based Scatter Compensation

Beekman *et al* in [53] have developed a highly efficient Monte Carlo simulator to be used as the projector in iterative reconstruction algorithms. The method combines stochastic photon transport of the interactions within the patient with an analytic model of the detection by the camera, a technique they call convolution-based forced detection [203].

### Fast Implementation of fully 3D RBSC

Kadrmas *et al* in [174] provide a fast implementation of fully 3D RBSC using (i) a coarse-grid scatter model that makes use of the fact that scatter component of the projection data is dominated by low-frequency information and (ii) intermittent RBSC that limits the number of iterations during which scatter is modelled. The former leads to an order of magnitude reduction in processor time required to model the scatter response function SRF in an iterative algorithm. The later accelerates the reconstruction process by limiting the number of iterations during which scatter is modelled. Since, the scatter estimate tends to converge within the early iterations [174] it is kept constant after only 2 or 3 iterations for the remaining iterations. The coarse-grid scatter model is incorporated along with ESSE. They use an unmatched projector/backprojector that models scatter only during projection. The fast implementation was evaluated using a MC simulated experiment of a 3D MCAT phantom with a $^{99m}$Tc tracer and also using experimentally acquired data with $^{201}$Tl.

### 7.2.4 Comparisons of Scatter Correction Methods

Moore *et al* in [171] compared three energy window based SC methods, (1) CW (2) TEW and (3) generalized spectral method (GS) on the basis of the accuracy with which lesion and background activity concentration could be simultaneously estimated. They optimized the following parameters for each of the SC methods - (1)"k" factor in CW method (2) Window widths of the photopeak and satellite windows in TEW and (3) the energy weights for the seventeen 4keV windows used in the GS method. The optimization entailed minimizing the sum of mean-squared errors (MSE) of the estimates of the lesion and background activity ([ all operations performed in sinogram domain]). The 3 SC methods with optimal parameters where compared by calculating the bias, variance and RMSE of the activity estimates for lesions of different size, location and contrast. Along with the estimation of lesion and background activity he also included a more complex Bayesian estimation task in which lesion size was estimated. For CW the optimal value of "k" was found to be 0.4 and for the TEW methods the optimal photopeak and satellite windows were 124-157keV and 112-124keV (generally the satellite windows is like 2-6keV).

Narayan *et al* in [204] studied the effects of different compensation strategies SPECT reconstruction for improving accuracy of detection of coronary artery disease. Seven human observer were used to perform the ROC studies. The accuracy of detecting CAD was evaluated for following reconstruction strategies: FBP; OSEM with attenuation correction (AC); OSEM with AC and SC; and OSEM with AC, SC and resolution compensation (RC). Reconstruction parameters for OSEM were optimized by use of human-observer ROC studies, where as standard clinical parameters were used for FBP. TEW was the SC method used. OSEM with AC,SC and RC outperforms FBP.

Narayanan *et al* in [178] state the TEW method "as their current clinical standard". Narayanan *et al* compared the ESSE method with TEW method in a cardiac study. The area under the ROC curve was virtually identical for the LCx territory for the two methods, but was larger with ESSE for detection of coronary artery disease for the LAD territory and the RCA territory. The difference was statistically significant ($P < 0.05$) only for the ROC curves for the LAD territory. The authors of the study added several caveats, but stated: "*With TEW like scatter compensation strategies being easier to implement and having a minimal impact on reconstruction time compared to ESSE, the slightly better performance of ESSE with the clinical images of this study may not be enough to strongly favour its use clinically.*"

DeVries *et al* in [205] investigated the effect of DPW SC method on lesion detection and quantitation. The scatter estimate was smoothed with a Wiener low-pass filter before subtraction. A human observer SKE-ROC study was used to determine accuracy of tumor detection in the liver. The human results were compared to those of an NPW model observer and to activity quantitation metrics. SIMIND was used to generate noise free projection data. Projection data was reconstructed with FBP and multiplicative Chang AC and Butterworth lowpass filter. Images with low and high amount of scatter were compared with corresponding SC images and corresponding images with only primaries in the projection data. SC methods may improve lesion detection if there is a significant amount of scatter present. Their results are better summarized in Farncombe [179].

Beekman *et al* investigated effects of different scatter compensation methods in fully 3D iterative reconstruction. They compared (i) 'ideal scatter estimate - Noise free' (ISE-NF) (ii) 'ideal scatter estimate' (ISE) (iii) 'ideal scatter model' (ISM) (iv) 'no scatter compensation' (NSC) and (v) 'ideal scatter rejection' (ISR). This paper refrains from subtracting the scatter estimate and uses an affine term instead. ISE-NF uses a scatter estimate which is the scatter component of the noiseless projection data (made available by SIMSET or SIMIND or any in-house method for getting the noiseless primary and scatter projection data). ISE uses a scatter estimate which is a noisy version of the estimate used in ISE-NF. In [206] the noise level in the ISE estimate is that which would be expected from a CW estimate. ISM is an RBSC method in with the scatter response function is modeled at every iteration. The metrics of contrast recovery, normalized standard deviation and sum of squared differences was used to assess the five strategies. Ideal scatter rejection (ISR ) out performs all other methods. ISM is superior to ISE and performs approximately as well as ISE-NF. No scatter compensation performs the worst.

Ljungberg *et al* in [169] compared four SC methods with $^{99m}$Tc. The four schemes were (1)CW with $k = 0.5$ (2) DPW (3) TEW (4) and a convolution-subtraction method based on scatter line-spread function [196, 197]. Two forms of the TEW were used (a) TEW(1) with a right scatter window and (b) TEW(2) without a right scatter window. The comparison involved MC simulated data for point sources, hot or cold spheres of different diameter in cylinder of water, and a clinically realistic brain phantom. Projection data was reconstructed with FBP. The comparison between SC's was made using NMSE, image contrast, % recovery and scatter fraction. TEW(1) did tend to over estimate the scatter. It concluded that performing scatter correction is essential for accurate quantification, and that all four methods yeilds a good, but not perfect, scatter correction.

Buvat *et al* in [170] compared nine window based scatter correction methods. MC simulations were used to get the primary and scatter projection data in each energy bin for a realistic $^{99m}Tc$ phantom. Relative and absolute quantification and signal-to-noise ratio were assessed for each scatter corrected projection. They compared (1) No scatter correction (2) DPW (3) Channel Ratio method (4) Photopeak energy Distribution method (similar to DPW and Channel ratio method but the widths of the subwindows in the photopeaks needs to determined by calibration of MC simulation) (5) CW (6) TEW (7) TEW without the right satellite window (8) Constrained factor analysis methods (FAMIS) (9) Factor analysis of medical image sequence using target-apex seeking (FAMIS-TAS). The FAMIS and FAMIS-TAS require many smaller subwindows and involve a fit to the acquired data as do the methods in [161] and [163]. The new factor analysis outperformed the other methods. TEW and DPW are easy to implement and in terms of accuracy TEW is better than DPW.

King *et al* in [49] optimized the filter used to smooth the TEW scatter estimate. Using MC simulated projections of a MCAT phantom they investigated 2-D pre-reconstruction filtering by Wiener filter and Butterworth filters with various cutoffs. The scatter estimate was either subtracted or modeled as affine term in OS-ML reconstruction. Using the NMSE criteria between reconstructed and true slices they observed (1) lowpass filtering dramatically decreased NMSE compared to no filtering (2) the inclusion of scatter estimate as affine term results in a lower NMSE than subtraction of the scatter estimate from the photopeak window prior to reconstruction.

For $^{67}$Ga citrate SPECT study with lesions in the mediastinum Farncombe *et al* in [179] simulated SIMIND projections of an MCAT phantom. They first performed a SKEV CHO study to optimize the prereconstruction filter cutoff for the TEW estimate. The TEW estimate is modeled as affine term. (Through human LROC studies [207] showed that at clinical noise level, subtraction of the scatter estimate actually reduces the detectability as compared to no scatter correction). They compared five SC strategies (1) Perfect scatter rejection (PSR), (2) Ideal scatter compensation (ISC) using $\mathrm{H}^S\mathbf{f}$ as the affine term, (3) TEW (4) ESSE (a reconstruction based SC method) and (5) post reconstruction scatter subtraction (PSSR) where they subtract the reconstruction of the TEW estimate from the reconstruction of the photopeak data. The optimal filter for TEW estimate was obtained using a SKEV-CHO study. Then they performed s human LROC study to optimize the number of iteration for RBI and the FWHM of the Gaussian postsmoothing. Both TEW and ESSE SC methods were able to significantly improve lesion detectability over no SC.

Dewaraja *et al* in [175], compared a TEW against an accurate Monte Carlo based scatter modeling (MCBS) scheme using 3-D OSEM reconstruction of $^{131}$I SPECT. The scatter estimate is included as an affine term. In MCS, a simple multiple window-based estimate is used for the initial iterations and in later iterations the Monte Carlo estimate is used for several iterations before it is updated. (So in [175] one will use the TEW estimate for first 20 iterations, then generate the MC estimate and update it at the $20^{th}$ iteration then use it for 4 iterations and then update it at the $24^{th}$ iteration and so on.) He used NMSE, normalised standard deviation and % bias as the metric for comparing TEW and MCS. The accuracy and noise of the reconstructed images was superior with MCS compared to TEW. However the improvement was not large, and some may not justify the large compuational requirements of MCS. They observed the the TEW tends to overestimate the scatter and show that TEW correction could be improved by applying a suitably chosen scaling factor to the scatter estimate. )

The authors of [175] state in the conclusion section of the paper - "*In general, the accuracy and noise of the images reconstructed with MCS were superior to images reconstructed with TEW. However, the improvement was not large, and in some cases may not justify the large computational requirements of MCS.*"

Xiao *et al* in [173] compares Monte Carlo based scatter correction which is a type of Reconstruction based scatter correction described in [53], versus TEW versus no scatter correction. He compared performance of the algorithms in terms of noise properties, contrast-to-noise ratios, and contrast separability of cold defects. The found that MCBS to be superior to TEW for their imaging context.

Nartia *et al* in [177] compared results from TEW SC with their TDSC method and concluded that their TDSC method produced a much smoother scatter estimate, and the resulting signal to noise ratio was better that with TEW correction.

## 7.3 Background

For WSC, one often simply subtracts the scatter estimate and reconstructs the remaining counts. This subtraction method has several problems. It could lead to negative counts. Also the Poisson nature of the sinogram is lost thus making likelihood-based reconstruction methods more difficult [208]. One way to avoid these problems [49, 179, 206] involves eschewing the subtraction step in favor of modeling scatter directly in a likelihood function using an affine term, and then performing a maximum likelihood (ML) or penalized-likelihood (a.k.a. MAP or maximum *a posteriori*) reconstruction. A second improvement recommended in [49, 179, 206] is to spatially smooth the noisy scatter estimate. Several investigators [49, 207, 179, 206] have compared reconstructions (both MAP and other methods) obtained with scatter subtracted sinograms with reconstructions obtained by modeling scatter in a likelihood term. The inclusion of scatter estimate as affine term results in a lower noise levels and improved image quality. Below we describe MAP reconstruction with scatter and also give relevant details for the TEW WSC method.

### 7.3.1 MAP Reconstruction with Scatter

Let the object be denoted by the $N$-dim lexicographically ordered vector $\mathbf{f}$ and sinogram for the photopeak window by $M$-dim vector $\mathbf{g}$. Thus $f_n : n = 1 \ldots N$ is the value of the $n^{th}$ voxel and $g_m : m = 1 \ldots M$ is the integer value of the $m^{th}$ detector bin. Denote the reconstruction by $\hat{\mathbf{f}}$ with $\hat{f}_n$ the value of the $n^{th}$ reconstructed voxel. Let the system matrix be denoted by $\mathrm{H}$ so that $\mathrm{H}_{mn}$ is proportional to the probability that a count emanating from voxel $n$ is received in bin $m$. The sinogram $\mathbf{g}$ is independently

Poisson distributed at each bin. The mean sinogram is given by

$$\bar{\mathbf{g}} = \mathrm{H}\mathbf{f} \tag{7.1}$$

In (7.1) matrix H incorporates all effects including attenuation, camera resolution, collimator resolution and scatter. We split H into $\mathrm{H}^S$, the part of H that models scatter only, and $\mathrm{H}^P$, the sparse matrix that models all other effects:

$$\mathrm{H} = \mathrm{H}^P + \mathrm{H}^S \tag{7.2}$$

We can approximate with good accuracy forward projection operations such as $\mathrm{H}^P\mathbf{f}$ and $\mathrm{H}^S\mathbf{f}$ by using a photon tracking MC Monte Carlo simulator such as SIMIND [46] or SIMSET [209] applied to a discrete but fine-grained version of $\mathbf{f}$. In iterative reconstruction algorithms one would have to compute projections $\mathrm{H}\mathbf{f}$ and backprojections $\mathrm{H}^T\mathbf{g}$ (where $T$ means transpose). One problem with doing this is that projections and backprojections with $\mathrm{H}^S$ are exceedingly computationally intensive.

WSC circumvents this problem by forming an estimate of scatter in the sinogram photopeak window rather than repeatedly computing it via matrix multiplication with $\mathrm{H}^S$. Define the $M$-dim vector $\mathbf{s}$ to be the sinogram of scattered photons in the photopeak. Then WSC delivers an *estimate* of $\mathbf{s}$ which we denote by $\hat{\mathbf{s}}$. Since we do not have knowledge of $\mathbf{s}$ itself we replace the imaging model (7.1),(7.2) with

$$\bar{\mathbf{g}} = \mathrm{H}^P\mathbf{f} + \hat{\mathbf{s}} \tag{7.3}$$

where the estimated scatter $\hat{\mathbf{s}}$ is treated for reconstruction purposes as a constant independent of $\mathbf{f}$. From (7.1),(7.2) and (7.3), one can see that $\hat{\mathbf{s}}$ is an approximation to the correct model term $\mathrm{H}^S\mathbf{f}$, and for WSC the value of $\hat{\mathbf{s}}$ will change on each photon noise realization. Thus (7.3) incorporates a form of model error : $\hat{\mathbf{s}} = \mathrm{H}^S\mathbf{f} + \delta\mathrm{H}^S\mathbf{f}$ with $\delta\mathrm{H}^S\mathbf{f}$ a model error. This model error is a source of noise different than that of photon noise or object variability.

We note that with this model, the reconstruction $\hat{\mathbf{f}}$ is corrupted by *two* sources of noise. The first is Poisson photon noise in the photopeak $\mathbf{g}$. The second source is in $\hat{\mathbf{s}}$ which is noisy because it is obtained, as described in section 7.3.2 below, from noisy counts in satellite energy windows surrounding the photopeak. Let $\mathcal{O}$ be a reconstruction operator so that $\hat{\mathbf{f}} = \mathcal{O}(\mathbf{g}, \hat{\mathbf{s}})$. For MAP this can be written as an optimization

$$\begin{aligned} \hat{\mathbf{f}} &= \mathcal{O}\{\mathbf{g}, \hat{\mathbf{s}}\} = \arg\max_{\mathbf{f}\geq\mathbf{0}} \Phi(\mathbf{f}, \mathbf{g}, \hat{\mathbf{s}}) \\ &= \arg\max_{\mathbf{f}\geq\mathbf{0}} \left(\Phi_L(\mathbf{f}, \mathbf{g}, \hat{\mathbf{s}}) + \Phi_P(\mathbf{f})\right) \end{aligned} \tag{7.4}$$

where $\Phi$ is a MAP objective with $\Phi_L$ the log likelihood and $\Phi_P$ the log prior (regularizer). In this work we use a simple quadratic smoothing prior given by $\Phi_P(\mathbf{f}) = -\frac{\beta}{2}\sum_n \sum_{n'\in\mathcal{N}(n)} w_{nn'}(f_n - f_{n'})^2$. The term $\mathcal{N}(n)$ denotes a local neighbourhood of voxels about $n$ and $w_{nn'}$ is the inverse Euclidean distance between $n$ and $n'$. For $\mathcal{N}(n)$ we shall use the 27 nearest 3D neighbours of $n$. The scalar $\beta > 0$ weights the prior and effectively controls the reconstructed-noise resolution tradeoff. Note that the regularizing term can be written as the quadratic form $\Phi_P(\mathbf{f}) = -\frac{\beta}{2}\mathbf{f}^T\mathcal{R}\mathbf{f}$ where $\mathcal{R}$ is a triply block-circulant matrix (for a $3D$ object). The elements of a spatially invariant $\mathcal{R}$ for a uniform quadratic prior are described in [69, 122].

The log likelihood $\Phi_L$ is due to the Poisson data noise whose mean is given by (7.3) and is thus given by

$$\begin{aligned} \Phi_L(\mathbf{f}, \mathbf{g}, \hat{\mathbf{s}}) &= \sum_m g_m \log(\sum_n \mathcal{H}_{mn} f_n + \hat{s}_m) \\ &\quad - \sum_m (\sum_n \mathcal{H}_{mn} f_n + \hat{s}_m) \end{aligned} \tag{7.5}$$

To be consistent with (7.3), one should use $\mathrm{H}^P_{mn}$ instead of $\mathcal{H}_{mn}$ in (7.5). However, the product $\mathrm{H}^P\mathbf{f}$ leads to computationally intensive operations if $\mathrm{H}^P$ is modelled realistically. Hence often one approximates $\mathrm{H}^P$ by a system matrix $\mathcal{H}$, an analytical projector that is efficiently computed.

### 7.3.2 Triple Energy Window Scatter Estimation

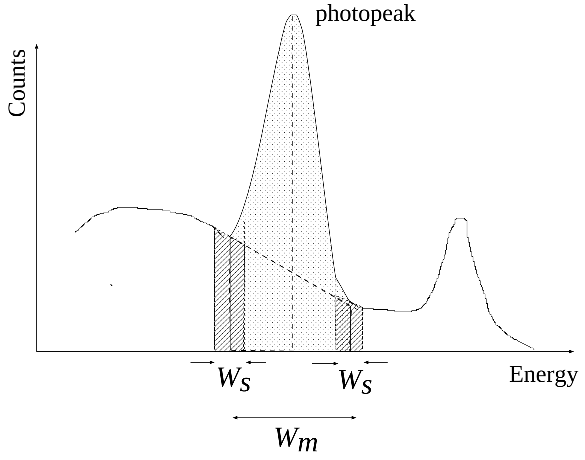

Figure 7.1: The TEW method. The solid curve shows the energy spectrum of scattered plus primary counts. The photopeak window of width $W_m$ and the two overlapping satellite windows of widths $W_s$ are shown. Primary counts in the photopeak window are estimated by subtracting counts in the trapezoid under the dotted line connecting the satellite windows.

We consider the well-known triple-energy window (TEW) method [162] for estimating scatter, though our method applies to any window-based method. As recommended in [49], we also allow the TEW sinogram to be spatially smoothed by a linear filtering operator represented by matrix **B**. In this case, the TEW scatter estimate (see Fig. 7.1) is given by

$$\hat{\mathbf{s}} = \frac{W_m}{2W_s}\mathbf{B}(\mathbf{g}_l + \mathbf{g}_r) \tag{7.6}$$

where $W_m$ is the width of the photopeak energy window and $W_s$ the width of narrower satellite windows. In (7.6), $\mathbf{g}_l$ and $\mathbf{g}_r$ are the counts (primary as well as scatter) collected in the left (low energy) and right (high energy) windows. We note that the satellite windows can partially overlap the photopeak window and thus include primary counts. For a monoenergetic isotope only a single left satellite window needs to be used. Because the right satellite window will be empty since there is no possibility of down-scatter form any other higher energy photon. For a multienergy isotope both left and right satellite windows must be used since the both the photopeak and right energy window will contain photon down-scattered from a higher energy. In some cases [180, 49, 169] only a single low-energy window $\mathbf{g}_l$ need be collected.

## 7.4 Theory

Our goal is to develop theoretical expressions for the mean reconstruction $\bar{\hat{\mathbf{f}}}$ and its covariance $\mathcal{K}_{\hat{\mathbf{f}}}$. In addition we develop a theoretical expression for the local point spread function (lpsf) [69] of the reconstruction. These, in turn, will depend on the mean and covariance of $\mathbf{g}$ and $\hat{\mathbf{s}}$.

The mean $\bar{\mathbf{g}}$ and covariance $\mathcal{K}_{\mathbf{g}}$ of $\mathbf{g}$ are given by $\bar{\mathbf{g}} = \mathrm{H}^P\mathbf{f} + \mathrm{H}^S\mathbf{f}$ and $\mathcal{K}_{\mathbf{g}} = \mathrm{diag}(\bar{\mathbf{g}})$. (Note that the alternative affine form $\bar{\mathbf{g}} = \mathrm{H}^P\mathbf{f} + \hat{\mathbf{s}}$ is used only in the optimization of the likelihood objective.) From (7.6), the mean $\bar{\hat{\mathbf{s}}}$ and the covariance $\mathcal{K}_{\hat{\mathbf{s}}}$ of the scatter estimate are given by

$$\bar{\hat{\mathbf{s}}} = \frac{W_m}{2W_s}\mathbf{B}(\bar{\mathbf{g}}_l + \bar{\mathbf{g}}_r) \tag{7.7}$$

$$\mathcal{K}_{\hat{\mathbf{s}}} = \frac{W_m^2}{4W_s^2}\mathbf{B}\mathrm{diag}\Big((\bar{\mathbf{g}}_l + \bar{\mathbf{g}}_r)\Big)\mathbf{B}^T \tag{7.8}$$

In (7.7) and (7.8), we use the fact that $\mathbf{g}_l$ and $\mathbf{g}_r$ are independent of one another and each is independently Poisson distributed. Note that the means $\bar{\mathbf{g}}$ and $\bar{\hat{\mathbf{s}}}$ and covariances $\mathcal{K}_{\mathbf{g}}$ and $\mathcal{K}_{\hat{\mathbf{s}}}$ are dependent on $\bar{\mathbf{g}}$, $\bar{\mathbf{g}}_l$ and $\bar{\mathbf{g}}_r$. Accurate estimates of these three mean sinograms can be obtained by propagating (using an MC simulator) a large number of source events into the appropriate energy windows.

We use a Taylor series approach to propagate noise from the scatter estimates. Using a first-order Taylor series expansion about the mean data and scatter estimate, we get

$$\begin{aligned}\hat{\mathbf{f}} &\approx \mathcal{O}\{\bar{\mathbf{g}},\bar{\hat{\mathbf{s}}}\} + \nabla_{\mathbf{g}}\mathcal{O}\{\bar{\mathbf{g}},\bar{\hat{\mathbf{s}}}\}(\mathbf{g}-\bar{\mathbf{g}}) \\ &\quad + \nabla_{\hat{\mathbf{s}}}\mathcal{O}\{\bar{\mathbf{g}},\bar{\hat{\mathbf{s}}}\}(\hat{\mathbf{s}}-\bar{\hat{\mathbf{s}}}) \end{aligned} \tag{7.9}$$

The term $\nabla_{\mathbf{g}}\mathcal{O}\{\bar{\mathbf{g}},\bar{\hat{\mathbf{s}}}\}$ is an $N \times M$ matrix whose $(n,m)$th element is given by $\frac{\partial[\mathcal{O}\{\bar{\mathbf{g}},\bar{\hat{\mathbf{s}}}\}]_n}{\partial g_m}$. A similar definition obtains for $\nabla_{\hat{\mathbf{s}}}\mathcal{O}\{\bar{\mathbf{g}},\bar{\hat{\mathbf{s}}}\}$. From (7.9), it is immediately evident that the mean reconstruction $\bar{\hat{\mathbf{f}}}$ is given by:

$$\bar{\hat{\mathbf{f}}} \approx \mathcal{O}\{\bar{\mathbf{g}},\bar{\hat{\mathbf{s}}}\} \tag{7.10}$$

Using techniques from [112, 184] and dropping (to avoid notational clutter) the dependence on the point of expansion $\{\bar{\mathbf{g}},\bar{\hat{\mathbf{s}}}\}$, we get

$$\nabla_{\mathbf{g}}\mathcal{O} = -[\nabla^2_{\mathbf{ff}}\Phi]^{-1}\nabla^2_{\mathbf{fg}}\Phi \tag{7.11}$$

$$\nabla_{\hat{\mathbf{s}}}\mathcal{O} = -[\nabla^2_{\mathbf{ff}}\Phi]^{-1}\nabla^2_{\mathbf{f}\hat{\mathbf{s}}}\Phi \tag{7.12}$$

The term $\nabla^2_{\mathbf{fg}}\Phi$ is an $N \times M$ second derivative matrix whose $(n,m)$th element is given by $\frac{\partial^2\Phi}{\partial f_n \partial g_m}$. Similar definitions obtain for $\nabla^2_{\mathbf{ff}}\Phi$ and $\nabla^2_{\mathbf{f}\hat{\mathbf{s}}}\Phi$. An evaluation of the terms in (7.11) and (7.12) yields

$$\nabla^2_{\mathbf{ff}}\Phi = -\mathcal{H}^T\text{diag}\Big(\frac{\bar{\mathbf{g}}}{(\mathcal{H}\bar{\hat{\mathbf{f}}}+\bar{\hat{\mathbf{s}}})^2}\Big)\mathcal{H} - \beta\mathcal{R} \tag{7.13}$$

$$\nabla^2_{\mathbf{fg}}\Phi = \mathcal{H}^T\text{diag}\Big(\frac{1}{\mathcal{H}\bar{\hat{\mathbf{f}}}+\bar{\hat{\mathbf{s}}}}\Big) \tag{7.14}$$

$$\nabla^2_{\mathbf{f}\hat{\mathbf{s}}}\Phi = -\mathcal{H}^T\text{diag}\Big(\frac{\bar{\mathbf{g}}}{(\mathcal{H}\bar{\hat{\mathbf{f}}}+\bar{\hat{\mathbf{s}}})^2}\Big) \tag{7.15}$$

So far, our equations (7.9) and (7.13)-(7.15) appear, albeit in a slightly different context, in [184] sec. 2.3.

With the results in (7.9)-(7.15), we can address our first goal, a calculation of $\mathcal{K}_{\hat{\mathbf{f}}}$ that includes the effects of scatter. From (7.9), it is readily seen that

$$\mathcal{K}_{\hat{\mathbf{f}}} \approx (\nabla_{\mathbf{g}}\mathcal{O})\mathcal{K}_{\mathbf{g}}(\nabla_{\mathbf{g}}\mathcal{O})^T + (\nabla_{\hat{\mathbf{s}}}\mathcal{O})\mathcal{K}_{\hat{\mathbf{s}}}(\nabla_{\hat{\mathbf{s}}}\mathcal{O})^T$$

$$
\begin{aligned}
&+(\nabla_{\mathbf{g}}\mathcal{O}) < (\mathbf{g}-\bar{\mathbf{g}})(\hat{\mathbf{s}}-\bar{\hat{\mathbf{s}}})^T > (\nabla_{\hat{\mathbf{s}}}\mathcal{O})^T \\
&+(\nabla_{\hat{\mathbf{s}}}\mathcal{O}) < (\hat{\mathbf{s}}-\bar{\hat{\mathbf{s}}})(\mathbf{g}-\bar{\mathbf{g}})^T > (\nabla_{\mathbf{g}}\mathcal{O})^T \qquad (7.16)
\end{aligned}
$$

where $<>$ indicates an average over noise realizations. (Thus $\bar{\mathbf{x}} \equiv < \mathbf{x} >$).

In the third term of (7.16), we need to evaluate the cross-covariance $< (\mathbf{g} - \bar{\mathbf{g}})(\hat{\mathbf{s}}-\bar{\hat{\mathbf{s}}})^T >$. Since the fourth term in (7.16) is the transpose of the third, then this evaluation gets us the fourth term as well. Let the counts in that part of the left (right) window that overlap the photopeak window be given by $\mathbf{g}_{l-ovp}$ ($\mathbf{g}_{r-ovp}$). Then it is easy to show that

$$
\begin{aligned}
& < (\mathbf{g}-\bar{\mathbf{g}})(\hat{\mathbf{s}}-\bar{\hat{\mathbf{s}}})^T > \\
= \; & \frac{W_m}{2W_s} < (\mathbf{g}-\bar{\mathbf{g}})(\mathbf{g}_l-\bar{\mathbf{g}}_l+\mathbf{g}_r-\bar{\mathbf{g}}_r)^T > \mathbf{B}^T \\
= \; & \frac{W_m}{2W_s} < (\mathbf{g}_{l-ovp}-\bar{\mathbf{g}}_{l-ovp}+\mathbf{g}_{r-ovp}-\bar{\mathbf{g}}_{r-ovp}) \times \\
& (\mathbf{g}_{l-ovp}-\bar{\mathbf{g}}_{l-ovp}+\mathbf{g}_{r-ovp}-\bar{\mathbf{g}}_{r-ovp})^T > \mathbf{B}^T \\
= \; & \frac{W_m}{2W_s}\mathrm{diag}(\bar{\mathbf{g}}_{l-ovp}+\bar{\mathbf{g}}_{r-ovp})\mathbf{B}^T \qquad (7.17)
\end{aligned}
$$

where we have used the fact that counts in non-overlapping windows are uncorrelated and Poisson distributed. Note also in the case of satellite windows that do not overlap the main window, (7.17) vanishes.

With (7.10)-(7.17), we can now evaluate all four terms in (7.16). It will be convenient to introduce a Fisher information matrix [69] appropriate for this problem, and this is given by

$$
\mathcal{F} \equiv \mathcal{H}^T \mathrm{diag}\Big(\frac{\bar{\mathbf{g}}}{(\mathcal{H}\bar{\hat{\mathbf{f}}}+\bar{\hat{\mathbf{s}}})^2}\Big)\mathcal{H} \qquad (7.18)
$$

The first term in (7.16) becomes

$$
\begin{aligned}
& (\nabla_{\mathbf{g}}\mathcal{O})\mathcal{K}_{\mathbf{g}}(\nabla_{\mathbf{g}}\mathcal{O})^T \\
= \; & [\mathcal{F}+\beta\mathcal{R}]^{-1}\mathcal{F}[\mathcal{F}+\beta\mathcal{R}]^{-1} \qquad (7.19)
\end{aligned}
$$

The second term in (7.16) becomes

$$\begin{aligned}&(\nabla_{\hat{\mathbf{s}}}\mathcal{O})\mathcal{K}_{\hat{\mathbf{s}}}(\nabla_{\hat{\mathbf{s}}}\mathcal{O})^T\\ =\ & \frac{W_m^2}{4W_s^2}[\mathcal{F}+\beta\mathcal{R}]^{-1}\mathcal{H}^T\mathrm{diag}\Big(\frac{\bar{\mathbf{g}}}{(\mathcal{H}\bar{\hat{\mathbf{f}}}+\bar{\hat{\mathbf{s}}})^2}\Big)\mathbf{B}\times\\ & \mathrm{diag}(\bar{\mathbf{g}}_l+\bar{\mathbf{g}}_r)\mathbf{B}^T\mathrm{diag}\Big(\frac{\bar{\mathbf{g}}}{(\mathcal{H}\bar{\hat{\mathbf{f}}}+\bar{\hat{\mathbf{s}}})^2}\Big)\mathcal{H}[\mathcal{F}+\beta\mathcal{R}]^{-1} \qquad (7.20)\end{aligned}$$

The third term in (7.16) becomes

$$\begin{aligned}&(\nabla_{\mathbf{g}}\mathcal{O}) < (\mathbf{g}-\bar{\mathbf{g}})(\hat{\mathbf{s}}-\bar{\hat{\mathbf{s}}})^T > (\nabla_{\hat{\mathbf{s}}}\mathcal{O})^T\\ =\ & -\frac{W_m}{2W_s}[\mathcal{F}+\beta\mathcal{R}]^{-1}\mathcal{H}^T\mathrm{diag}\Big(\frac{\mathbf{1}}{\mathcal{H}\bar{\hat{\mathbf{f}}}+\bar{\hat{\mathbf{s}}}}\Big)\mathrm{diag}(\bar{\mathbf{g}}_{l-ovp}+\\ & \bar{\mathbf{g}}_{r-ovp})\mathbf{B}^T\mathrm{diag}\Big(\frac{\bar{\mathbf{g}}}{(\mathcal{H}\bar{\hat{\mathbf{f}}}+\bar{\hat{\mathbf{s}}})^2}\Big)\mathcal{H}[\mathcal{F}+\beta\mathcal{R}]^{-1} \qquad (7.21)\end{aligned}$$

Note that the fourth term is simply the transpose of the third.

Equation (7.19), which is the first term of (7.16), corresponds to the contribution to the covariance from the Poisson noise in $\mathbf{g}$. This Poisson noise is that due to primary and scatter photons in the photopeak window. Equations (7.20) and (7.21), as well as the transpose of (7.21), correspond to the last three terms of (7.16). These represent *added* covariance due to the noise in the scatter estimate.

For a nonlinear shift-variant MAP reconstruction, resolution is characterized by an lpsf that is object and position dependent. The lpsf is defined operationally [69] as the noise-averaged difference of two reconstructions: one of the object and another of the object plus a vanishingly small point source at position $j$. If $\mathbf{e}_j$ is a unit vector at $j$, then the lpsf at $j$ is defined as

$$\bar{\hat{\mathbf{e}}}_j \equiv \lim_{\delta\to 0}\frac{1}{\delta}\Big( < \mathcal{O}\{\mathbf{g}(\mathbf{f}+\delta\mathbf{e}_j),\hat{\mathbf{s}}(\mathbf{f}+\delta\mathbf{e}_j)\} > - < \mathcal{O}\{\mathbf{g}(\mathbf{f}),\hat{\mathbf{s}}(\mathbf{f})\} > \Big) \qquad (7.22)$$

Using (7.10), one can approximate (7.22) as a difference of reconstructions of mean data:

$$\bar{\hat{\mathbf{e}}}_j \approx \lim_{\delta\to 0}\frac{1}{\delta}\Big(\mathcal{O}\{\bar{\mathbf{g}}(\mathbf{f}+\delta\mathbf{e}_j),\bar{\hat{\mathbf{s}}}(\mathbf{f}+\delta\mathbf{e}_j)\} - \mathcal{O}\{\bar{\mathbf{g}}(\mathbf{f}),\bar{\hat{\mathbf{s}}}(\mathbf{f})\}\Big) \qquad (7.23)$$

A method (7.24) to approximate the lpsf that is faster than the two-reconstruction methods (7.23) can be derived using (7.23) and (7.9)-(7.15). The first step in deriving (7.24) below can be obtained from (7.23) by expanding $\mathcal{O}\{\bar{\mathbf{g}}(\mathbf{f}+\delta\mathbf{e}_j), \bar{\hat{\mathbf{s}}}(\mathbf{f}+\delta\mathbf{e}_j)\}$ about $\mathcal{O}\{\bar{\mathbf{g}}(\mathbf{f}), \bar{\hat{\mathbf{s}}}(\mathbf{f})\}$ using (7.9). To see the second step of (7.24), define $\mathrm{H}^l$ and $\mathrm{H}^r$ as the system matrices for photon propagation into the left and right satellite windows. Then using the expressions $\bar{\mathbf{g}}(\mathbf{f}) = \mathrm{H}^P\mathbf{f} + \mathrm{H}^S\mathbf{f}$ and a version of (7.7) rewritten as $\bar{\hat{\mathbf{s}}}(\mathbf{f}) = \frac{W_m}{2W_s}\mathbf{B}(\mathrm{H}^l\mathbf{f} + \mathrm{H}^r\mathbf{f})$, we obtain the second step. The third step follows immediately from the second. Using (7.11)-(7.15) we obtain the final step of (7.24).

$$\begin{aligned}
&\bar{\hat{\mathbf{e}}}_j \\
\approx\;& \lim_{\delta\to 0}\frac{1}{\delta}\Big(\nabla_{\mathbf{g}}\mathcal{O}(\bar{\mathbf{g}}(\mathbf{f}+\delta\mathbf{e}_j) - \bar{\mathbf{g}}(\mathbf{f})) \\
& +\nabla_{\hat{\mathbf{s}}}\mathcal{O}(\bar{\hat{\mathbf{s}}}(\mathbf{f}+\delta\mathbf{e}_j) - \bar{\hat{\mathbf{s}}}(\mathbf{f}))\Big) \\
=\;& \lim_{\delta\to 0}\frac{1}{\delta}(\nabla_{\mathbf{g}}\mathcal{O}(\mathrm{H}^P(\mathbf{f}+\delta\mathbf{e}_j) - \mathrm{H}^P\mathbf{f} + \mathrm{H}^S(\mathbf{f}+\delta\mathbf{e}_j) - \mathrm{H}^S\mathbf{f}) \\
& +\nabla_{\hat{\mathbf{s}}}\mathcal{O}\frac{W_m}{2W_s}\mathbf{B}(\mathrm{H}^l(\mathbf{f}+\delta\mathbf{e}_j) - \mathrm{H}^l\mathbf{f} + \mathrm{H}^r(\mathbf{f}+\delta\mathbf{e}_j) - \mathrm{H}^r\mathbf{f})) \\
=\;& \nabla_{\mathbf{g}}\mathcal{O}(\mathrm{H}^P + \mathrm{H}^S)\mathbf{e}_j + \nabla_{\hat{\mathbf{s}}}\mathcal{O}\frac{W_m}{2W_s}\mathbf{B}(\mathrm{H}^l + \mathrm{H}^r)\mathbf{e}_j \\
=\;& (\mathcal{F}+\beta\mathcal{R})^{-1}\mathcal{H}^T\mathrm{diag}\Big(\frac{1}{\mathcal{H}\bar{\hat{\mathbf{f}}} + \bar{\hat{\mathbf{s}}}}\Big)(\mathrm{H}^P + \mathrm{H}^S)\mathbf{e}_j \\
-&\frac{W_m}{2W_s}(\mathcal{F}+\beta\mathcal{R})^{-1}\mathcal{H}^T\mathrm{diag}\Big(\frac{\bar{\mathbf{g}}}{(\mathcal{H}\bar{\hat{\mathbf{f}}} + \bar{\hat{\mathbf{s}}})^2}\Big)\mathbf{B}(\mathrm{H}^l + \mathrm{H}^r)\mathbf{e}_j \qquad (7.24)
\end{aligned}$$

Thus our main theoretical results are equations (7.16), (7.19), (7.20), (7.21) for covariance and (7.24) for lpsf.

## 7.5 Validation of Theory via Sample Methods

In this section, we use sample reconstruction methods to validate our theory expressions. We will first describe computational techniques for evaluating various theoretical and sample based expressions, then apply these to a 3D SPECT simulation. We reserve a discussion of the computational complexity of theory vs sample methods for section 7.6.1.

### 7.5.1 Computational Techniques for Theory and Sample Methods

We first discuss computational methods for theory expressions. Although we have an expression for $\mathcal{K}_{\hat{\mathbf{f}}}$ in equations (7.19)-(7.21), this matrix is too large for practical computation. Often, for FOM calculations, one is interested in constructs of the form $\mathcal{K}_{\hat{\mathbf{f}}}\mathbf{x}$ where $\mathbf{x}$ is a vector [96, 185, 119, 150, 115, 94, 109, 106]. In particular, we shall compute a quantity of interest, the local covariance about the point $j$, that is given by $\mathcal{K}_{\hat{\mathbf{f}}}\mathbf{e}_j$. This is the $j^{th}$ column of the covariance matrix. We shall consider a second quantity, the variance map, given by $\mathbf{e}_j^T\mathcal{K}_{\hat{\mathbf{f}}}\mathbf{e}_j = \sigma_j^2$ for a set of points $j$. This is the diagonal of the covariance matrix. For our simulations, we consider a case where satellite windows do not overlap the photopeak, so that the covariance is given by the sum of the two expressions in (7.19) and (7.20). For local covariance these are of the form $(\mathcal{F} + \beta\mathcal{R})^{-1}\mathcal{F}'(\mathcal{F} + \beta\mathcal{R})^{-1}\mathbf{e}_j$ where $\mathcal{F}' = \mathcal{F}$ for equation (7.19) and $\mathcal{F}' = \mathcal{H}^T\text{diag}\Big(\frac{\bar{\mathbf{g}}}{(\mathcal{H}\bar{\hat{\mathbf{f}}}+\bar{\hat{\mathbf{s}}})^2}\Big)\mathbf{B}\text{diag}(\bar{\mathbf{g}}_l + \bar{\mathbf{g}}_r)\mathbf{B}^T\text{diag}\Big(\frac{\bar{\mathbf{g}}}{(\mathcal{H}\bar{\hat{\mathbf{f}}}+\bar{\hat{\mathbf{s}}})^2}\Big)\mathcal{H}$ for (7.20). The computation of these sorts of expressions via Fourier techniques has been studied previously in [114, 116]. The main idea is that for a point $j$, one can form a triply block-circulant approximation $\mathcal{K}_{\hat{\mathbf{f}}}^j$ that closely approximates $\mathcal{K}_{\hat{\mathbf{f}}}$ in the vicinity of $j$. The main step in forming $\mathcal{K}_{\hat{\mathbf{f}}}^j$ is to approximate $\mathcal{F}$ or $\mathcal{F}'$ by a local triply block-circulant approximation $\mathcal{F}(j)$ or $\mathcal{F}'(j)$. Since $\mathcal{R}$ is itself triply block-circulant, the matrix constructs in $(\mathcal{F}(j) + \beta\mathcal{R}(j))^{-1}\mathcal{F}'(j)(\mathcal{F}(j) + \beta\mathcal{R}(j))^{-1}\mathbf{e}_j$ are amenable to calculations by rapid Fourier techniques. The variance map calculation requires only an additional inner product operation. We shall also evaluate the lpsf (7.24). Note that this is of the form $(\mathcal{F} + \beta\mathcal{R})^{-1}\mathbf{v}_j$ where vector $\mathbf{v}_j = \mathcal{H}^T\Big(\text{diag}\Big(\frac{1}{\mathcal{H}\bar{\hat{\mathbf{f}}}+\bar{\hat{\mathbf{s}}}}\Big)(\text{H}^P + \text{H}^S)\mathbf{e}_j - \frac{W_m}{2W_s}\text{diag}\Big(\frac{\bar{\mathbf{g}}}{(\mathcal{H}\bar{\hat{\mathbf{f}}}+\bar{\hat{\mathbf{s}}})^2}\Big)\mathbf{B}(\text{H}^l + \text{H}^r)\mathbf{e}_j\Big)$. Again, by using $\mathcal{F}(j)$, rapid Fourier techniques can be used to evaluate the lpsf. As far as the mean $\bar{\hat{\mathbf{f}}}$, the relevant expression is equation (7.10).

We now discuss evaluation of the local covariance and variance with sample-based methods. One first computes $N_{samp}$ reconstructions $\hat{\mathbf{f}}^k$, $k = 1, \ldots, N_{samp}$. Then clearly the sample mean is given by $\bar{\hat{\mathbf{f}}} = \frac{1}{N_{samp}} \sum_{k=1}^{N_{samp}} \hat{\mathbf{f}}^k$. An element of $[\mathcal{K}_{\hat{\mathbf{f}}}]_{jj'}$ of the covariance matrix can be computed by the sample expression

$$[\mathcal{K}_{\hat{\mathbf{f}}}]_{jj'} = \frac{1}{N_{samp} - 1} \sum_{k=1}^{N_{samp}} (\hat{\mathbf{f}}_j^k - \bar{\hat{\mathbf{f}}}_j)(\hat{\mathbf{f}}_{j'}^k - \bar{\hat{\mathbf{f}}}_{j'}) \tag{7.25}$$

With suitable choices for $j$ and $j'$, one can compute the local covariance about $j$ or a variance map. Clearly $N_{samp}$ must be chosen large enough to achieve an acceptable amount of sample error.

### 7.5.2 Simulation Results

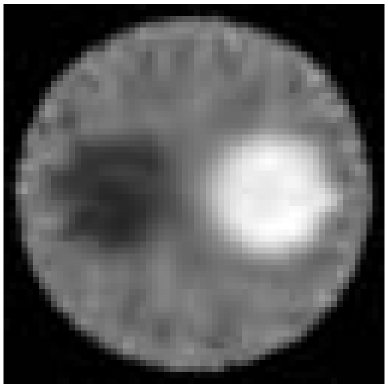

Figure 7.2: Anecdotal reconstruction of object including data and model (scatter) noise. Illustrated is slice 9.

We used a $3D$ $64 \times 64 \times 16$ object with cubic voxels of size 0.625 cm. The object was cylindrically symmetric except for the end slices 1 and 16, wherein the activity $\mathbf{f}$ was set to zero. In each of the remaining slices, the object activity comprised a background circle with circular hot and cold inserts of ratios background:hot:cold $= 2 : 4 : 1$. Attenuation was uniform in all 16 slices with attenuation set to that of $H_2O$ at 140Kev ($\mu = 0.146\ cm^{-1}$). Each camera face comprised $96 \times 32$ square bins of size 0.625 cm. We simulated a parallel-beam geometry with 65 equispaced projection angles. Figure 7.3 shows the object within the simulation setup.

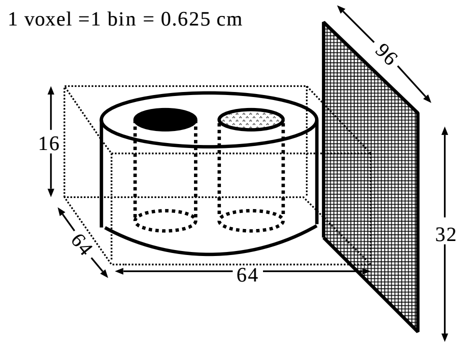

Figure 7.3: Simulation geometry with camera face in one position (not to scale). Object with background:hot:cold= 2:4:1.

We designed our simulation to approximately reflect the geometry and count level of some types of clinical acquisitions. We used SIMSET [209] to simulate a parallel hole collimator with bore radius and length of 0.1 cm and 3.0 cm, respectively, and a radius of rotation (measured from the center of the object to the collimator face) of 30 cm. These parameters were consistent with a depth-dependent resolution having a Gaussian psf whose $\sigma$ was modeled as $\sigma\ (cm) = 0.026\ d\ (cm) + 0.0392\ cm$ where $d$ is depth (measured from the camera face). The photopeak energy window was $128-152$ KeV and the single non-overlapping low-energy satellite window was $124-128$ KeV. (Note that for a single-energy radionuclide such as $\mathrm{Tc}^{99m}$, only one satellite window [49, 180] is needed.) The energy response curve of the detector was Gaussian with an energy resolution given by a FWHM of 10% for $\mathrm{Tc}^{99m}$. We generated $10^{11}$ source events scaled to yield 5.6M counts in the photopeak window and $4.14 \times 10^5$ counts in the left satellite window. We used enough source events so that these MC generated counts were effectively noiseless, thus obtaining $\bar{\mathbf{g}}$ and $\bar{\mathbf{g}}_l$.

To accomplish the sample reconstructions of (7.4), we used a $\mathbf{g}$ obtained by adding Poisson noise to $\bar{\mathbf{g}}$, and an $\hat{\mathbf{s}}$ obtained from (7.6), where in (7.6), $\mathbf{g}_l$ is itself a Poisson noise realization using $\bar{\mathbf{g}}_l$. In (7.6), we did not implement a sinogram smoothing filter $\mathbf{B}$. We used smoothing parameter $\beta = 0.005$ for a reasonable noise-resolution trade-off. The reconstruction used the COSEM-MAP algorithm [84] run to 100 iterations, using 16 subsets and an initial estimate corresponding to a noiseless reconstruction of the object. Fig. 7.2 shows one slice (slice #9) of a noisy reconstruction.

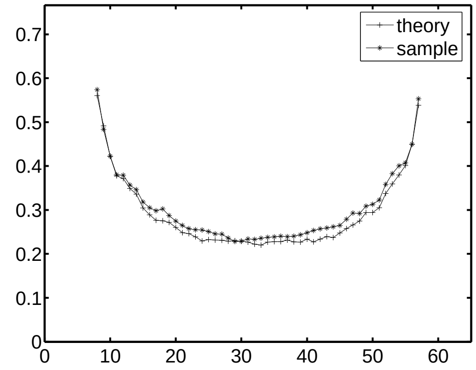

Figure 7.4: Profile through row 48 of slice 9 of the variance map. Theory and sample curves are shown.

To evaluate the theory expressions for local covariance and variance, we used techniques described above in sec. 7.5.1 and aforementioned procedures used for obtaining $\bar{\mathbf{g}}$, $\bar{\hat{\mathbf{f}}}$ and $\bar{\hat{\mathbf{s}}}$. As shown in Fig. 7.4 and Fig. 7.5, we have evaluated theory expressions for the variance map (the diagonal of $\mathcal{K}_{\hat{\mathbf{f}}}$) and also the local covariance at one pixel (a column of $\mathcal{K}_{\hat{\mathbf{f}}}$).

To validate the theory by sample methods, we generated noisy reconstructions and used these to obtain a sample estimate of variance and local covariance. A total of 8100 noisy data realizations was obtained by generating 8100 Poisson noise realizations

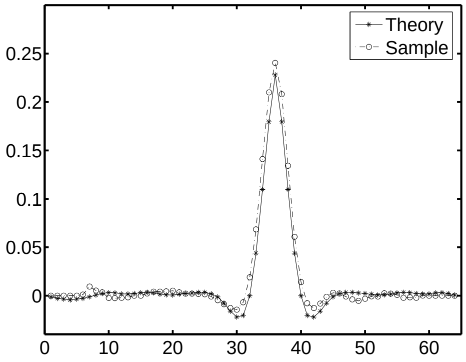

Figure 7.5: Profile through row 48 of slice 9 of local covariance image corresponding to voxel (48,36,9). Theory and sample curves are shown.

of $\bar{\mathbf{g}}$, and 8100 noisy scatter estimates obtained by generating 8100 Poisson noise realizations of $\bar{\mathbf{g}}_l$ and then applying (7.6). Figures 7.4 and 7.5 include profiles of the sample local covariance and variance images. The correspondence of sample and theory profiles is close.

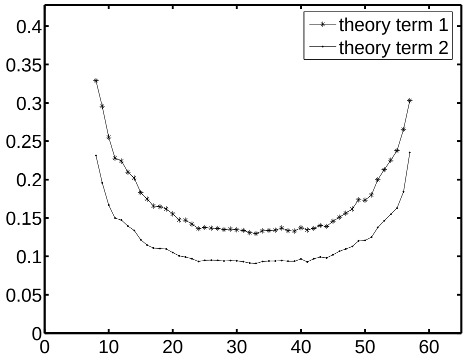

Figure 7.6: Profile through row 48 of slice 9 of the variance image decomposed into it's constituent components.

Equations (7.19) and (7.20) give the two contributions to the covariance of the reconstruction, one due to Poisson noise in $\mathbf{g}$ and the other due to the noise in the scatter estimate. Equations (7.19) and (7.20) were evaluated separately and the separate contributions are shown in figure 7.6, which corresponds to the net profile shown in figure 7.4, and in figure 7.7, which corresponds to the net profile shown in figure 7.5. For the imaging system that we have modelled, we observe that the component of variance and local covariance due to scatter (i.e. due to equation (7.20)) is comparable to that due to the Poisson noise in $\mathbf{g}$ given by equation (7.19). Thus we observe that the noise in the scatter estimate adds considerable variance to the reconstruction.

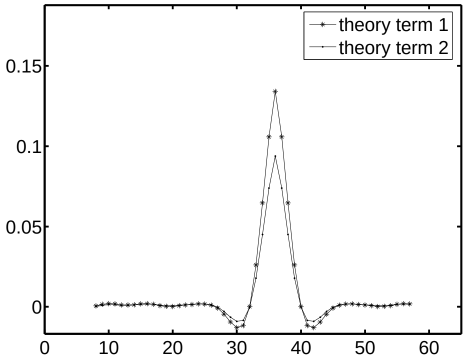

Figure 7.7: Profile through row 48 of slice 9 of the covariance image corresponding to voxel (48,36,9) decomposed into its constituent components.

We evaluated lpsf about a single point (48,36,9) using theory methods described above in sec. 7.5.1. A profile is shown in figure 7.8. To evaluate lpsf by sample methods one could use (7.22). While (7.22) involves all $2N_{samp}$ reconstructions, the simpler expression (7.23) for lpsf, involving only *two* reconstructions of mean data could be used instead. Note that the evaluation of (7.22) and (7.23) both need the terms $(\mathrm{H}^P + \mathrm{H}^S)\mathbf{e}_j$ and $\mathrm{H}^l\mathbf{e}_j$ along with $\bar{\mathbf{g}}(\mathbf{f})$ and $\bar{\hat{\mathbf{s}}}(\mathbf{f})$ to get $\bar{\mathbf{g}}(\mathbf{f} + \delta\mathbf{e}_j)$ and $\bar{\hat{\mathbf{s}}}(\mathbf{f} + \delta\mathbf{e}_j)$. These terms are calculated using an MC simulator. Note that (7.23) is obtained from (7.22) via (7.10).

Before comparing lpsf-theory vs lpsf-sample we compared lpsf via (7.22) to the ap-

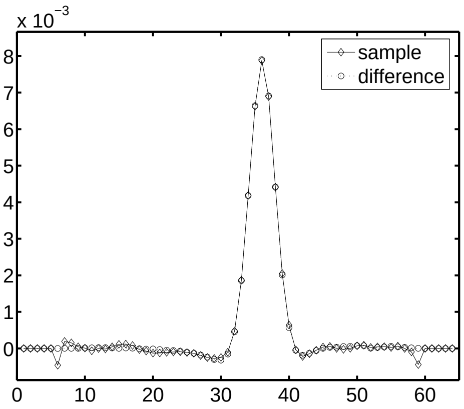

Figure 7.8: Profile through row 48 of slice 9 of lpsf at one location (48,36,9) (in the background). The sample curve computed via (7.22) and the difference of mean reconstruction curves computed via (7.23) correspond very well.

proximate lpsf via (7.23). This latter comparison is a test of the accuracy of the mean approximation (7.10). To evaluate the expression for lpsf using the sample method expressed in (7.22) we need $< \mathcal{O}\{\mathbf{g}(\mathbf{f} + \delta\mathbf{e}_j), \hat{\mathbf{s}}(\mathbf{f} + \delta\mathbf{e}_j)\} >$ and $< \mathcal{O}\{\mathbf{g}(\mathbf{f}), \hat{\mathbf{s}}(\mathbf{f})\} >$. To obtain $< \mathcal{O}\{\mathbf{g}(\mathbf{f} + \delta\mathbf{e}_j), \hat{\mathbf{s}}(\mathbf{f} + \delta\mathbf{e}_j)\} >$ we reconstructed 2000 noisy data realizations obtained by generating 2000 Poisson noise realizations of $\bar{\mathbf{g}}(\mathbf{f} + \delta\mathbf{e}_j)$, along with 2000 noisy scatter estimates $\hat{\mathbf{s}}(\mathbf{f} + \delta\mathbf{e}_j)$ obtained by generating 2000 Poisson noise realizations of $\bar{\mathbf{g}}_l(\mathbf{f} + \delta\mathbf{e}_j)$ and then applying (7.6). We took $\delta = 20\%$ of the local background. In order to get $< \mathcal{O}\{\mathbf{g}(\mathbf{f}), \hat{\mathbf{s}}(\mathbf{f})\} >$ we used the mean of 8100 reconstructions. Figure 7.8 shows both lpsf profiles for one location. The difference of reconstructions using (7.23) and the sample validation curves using (7.22) match very closely.

Finally we compared the lpsf theory expression with that due to the sample method in (7.22). The results, a profile of which is shown in figure 7.9, show a good correspondence.

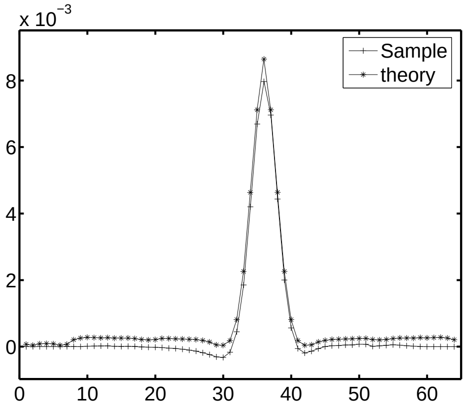

Figure 7.9: Profile through row 48 of slice 9 of lpsf at one location (48,36,9) (in the background). Sample curve versus theory curve.

## 7.6 Discussion

We have developed and validated theoretical expressions for mean, lpsf and covariance for SPECT MAP reconstructions driven by data noise and noise in the TEW WSC estimate. Below we discuss computational complexity of the theory expressions vs that of sample-based methods, and include comments on the applicability of our methods.

### 7.6.1 Complexity of Theory Methods vs Sample Methods

In general, a precise comparison of computational complexity of theory vs sample methods for computing a performance FOM depends on the specific FOM. We have addressed only quantities mean, lpsf and covariance that often comprise such FOM's. Nevertheless, it is useful to consider the complexity for these quantities. First, consider a fixed object $\mathbf{f}$, attenuation map $\boldsymbol{\mu}$, and imaging system H. Consider the evaluation of lpsf and a covariance-related quantity $\mathcal{K}_{\hat{\mathbf{f}}}\mathbf{x}$ at single location $j$. We consider the TEW WSC method.

All of the relevant theory and sample expressions will require $\bar{\mathbf{g}}$, $\bar{\mathbf{g}}_l$ and $\bar{\mathbf{g}}_r$ as well as $\mathrm{H}^r\mathbf{e}_j$, $\mathrm{H}^l\mathbf{e}_j$ and $\mathrm{H}^P\mathbf{e}_j$. These mean sinograms need be generated by an MC simulation using a sufficient number of source events so that the noise due to limited source events is far less than the Poisson noise added to these mean sinograms. The complexity of the required MC operation, dominated by $\bar{\mathbf{g}}, \bar{\mathbf{g}}_l$ and $\bar{\mathbf{g}}_r$, will be implementation dependent, but let us denote the number of operations by $N_{MC}$.

We now consider the complexity of sample-reconstruction (SR) based methods. From (7.10), one may as well use a single reconstruction of noiseless data to get the mean reconstruction, and from the discussion in section 7.5.2, use two noiseless reconstructions to obtain lpsf at a single location. As mentioned previously, constructs of the form $\mathcal{K}_{\hat{\mathbf{f}}}\mathbf{x}$ including lpsf and variance, can be calculated using variants of (7.25). This equation is dominated by the calculation of the $N_{samp}$ sample reconstructions. Thus considering the Monte Carlo calculations, the complexity of SR methods for such quantities at a single $j$ goes as $N_{samp}$ reconstructions $+N_{MC}$.

We now consider the computation complexity of the corresponding theory expressions, again for a single $j$. The mean reconstruction using (7.10) amounts to a single reconstruction. For covariance, as previously mentioned, we need only deal with a matrix vector product of the form $\mathcal{K}_{\hat{\mathbf{f}}}\mathbf{x}^j$ where $\mathbf{x}^j$ is a compact signal centered at location $j$. In this case one may replace with only small error $\mathcal{K}_{\hat{\mathbf{f}}}$ by $\mathcal{K}_{\hat{\mathbf{f}}}^j$. As mentioned in section 7.5.1, the complexity in computing $\mathcal{K}_{\hat{\mathbf{f}}}^j$ resides in the computation of the term $(\mathcal{F}(j) + \beta\mathcal{R}(j))^{-1}$. The computation of this inverse can be done with Fourier techniques, but the complexity of the Fourier operations is small relative to the computation of $\mathcal{F}(j)$ itself. In [114] it is shown that the computational complexity of $\mathcal{F}(j)$ is approximately equal to a single backprojection. (Approximate versions of $\mathcal{F}(j)$ for SPECT may be computed much more rapidly using techniques in [116].) If in (7.19), (7.20) and (7.21) we ascribe a complexity equal to a single backprojection to the appearance of the term $(\mathcal{F}+\beta\mathcal{R})^{-1}$, one might ask what are the remaining significant computationally complex operations. The answer is that there is an addition backprojection in (7.20) and (7.21). Thus to compute, for a given location $j$, a product of the form $\mathcal{K}_{\hat{\mathbf{f}}}^{j}\mathbf{x}^{j}$, the effort (once the sinograms have been computed) is approximately 2 backprojections if there is no satellite window overlap and 3 backprojections if there is satellite window overlap.

For the lpsf in (7.24) we noted in section 7.5.1 that it is of the form $(\mathcal{F}+\beta\mathcal{R})^{-1}\mathbf{v}_j$. We can again replace $\mathcal{F}$ and $\mathcal{R}$ by $\mathcal{F}(j)$ and $\mathcal{R}(j)$. If $(\mathcal{F}(j)+\beta\mathcal{R}(j))^{-1}$, using Fourier tricks, has already been computed for covariance purposes, there is no extra computation for this term. However the computation for $\mathbf{v}_j$ is dominated by the computation of a single backprojection. In sum, for a given location $j$ the lpsf involves only one backprojection if the corresponding covariance term has been computed.

Now consider, instead of a single location $j$, multiple locations $j=1,\ldots,J$. To calculate by SR methods any covariance related quantity at a single $j$ one needs $N_{samp}$ reconstructions. One iteration of an iterative reconstruction such as MAP is dominated by one projection and one backprojection (approximately 2 backprojections). If a reconstruction involves $L$ iterations, then the complexity is $2LN_{samp}$ backprojections. From previous arguments, the calculation of an lpsf or covariance related quantity for theory would need (for no window overlap) three backprojections. Thus for a single $j$, SR methods have a complexity of $2LN_{samp}$ backprojections + $N_{MC}$ and theory methods 3 backprojections + $N_{MC}$. If the calculation is done for $J$ separate locations, then the SR method does not require any extra reconstructions for covariance-related quantities. Note that lpsf calculation by SR methods using (7.23) would involve $(1+J)2L$ backprojections, but this number is far less than $2LN_{samp}$ backprojections. The theory calculation must be repeated at all $J$ locations. Therefore, the SR method retains a complexity of $2LN_{samp}$ (backprojections) + $N_{MC}$ but the theory method now involves $3J$ backprojections + $N_{MC}$. Since $L \sim 10 - 100$ and $N_{samp}$ is often $10^2 - 10^3$, then $3J$ is typically far less than $2LN_{samp}$, thus giving an apparent speed advantage for theory methods.

The aforementioned speed differences become insignificant if the MC sinogram calculations common to both methods are more computationally complex than sample reconstructions or the theory calculations. However the speed comparison in the above paragraph was considered in the context of calculation of the statistical quantities of $\hat{\mathbf{f}}$ for a fixed set of reconstruction parameters. For TEW these parameters are: count levels, $\mathcal{H}$, $\beta$, $\mathbf{B}$ and widths and positions of the photopeak and satellite windows. A natural goal is to explore this parameter space and develop an optimal set of parameters according to some image quality FOM. For SR methods one would have to do $N_{samp}$ reconstructions to get a FOM for *each* such member of the parameter set. For either method the investment in the initial MC calculation of the sinograms need be done only once. If $N_P$ is the number of sets of reconstruction parameters being explored (e.g. two $\mathcal{H}$'s and 3 $\beta$'s $\Rightarrow N_P = 6$), then the effort for SR methods goes as $2LN_{samp}N_P$ backprojections $+N_{MC}$ and for theory goes as $3JN_P$ backprojections $+N_{MC}$. If $N_{MC} < 2LN_{samp}N_P$ backprojections then the SR method is dominated by the reconstructions and not the Monte-Carlo calculations. In this case, theory methods will be faster than SR methods whether or not $N_{MC}$ is greater or less that $3JN_P$ backprojections. The inequality is dependent on the MC implementation, number of source events and size ($N_P$) of the search space.

### 7.6.2 Applications

One clear application of these results is in the optimization of TEW based scatter estimation methods as was done using sample methods in [179]. In this paper we have focused on familiar TEW SC method and its single satellite window variant. TEW is but one example of WSC. Our methods are applicable to other WSC methods with the restriction that the scatter estimate be modeled as an affine term. Any scatter estimate which is a linear combination of counts in adjacent windows of the form $\hat{\mathbf{s}} = \mathbf{B} \sum_k a_k \mathbf{g}_k$ where $\mathbf{g}_k$ is the counts in the $k^{th}$ energy window, $a_k$ a weight factor, and $\mathbf{B}$ a linear filtering operator. Examples include the generalized linear method in [166], the Compton scatter estimation method in [159], the Extended TEW in [181], TEW with scaling as in [175] and other variants of TEW [182, 183].

# Chapter 8

# Discussion and Future Work

In this work, we proposed our computational methods to theoretically predict the noise properties of MAP reconstructions of a SPECT system, and then the lesion detectability for the SPECT reconstructed images. It primarily dealt with the application of model observers to image quality in the context of lesion detectability which can be used to compare, optimize and improve imaging systems and SPECT reconstructions. Our results show the good coincidence between the theoretical predictions and the Monte Carlo simulations and human observer tests. We focused on SKE tasks where the lesion location is known. Though SKE is a simplistic task, the theoretical computations can be extended to more complex tasks with location uncertainty. We discuss this briefly in 8.1. We also proposed method for theoretical computation of first-and second order moments of SPECT reconstructions that model more realistic systems including scatter. Theoretical calculation of these quantities (mean, covariance, lpsf) can be used to rapidly calculate figures of merit (FOM) that summarize performance of detection and estimation tasks for reconstructed images. The main contributions comprise Chapter 5, 6 and 7.

In Chapter 5 we estimated the validity of the human emulating mathematical model observer the CHO in predicting human performance for SKE tasks. The context involved was the optimization of a crucial parameter which controls the noise/resolution trade-off in SPECT MAP reconstruction. This parameter extensively affects lesion detectability and was confirmed with human observer 2AFC tests. We also went on the show the effectiveness of the CHO adjusted for internal noise in predicting this human performance. We also observed that the noise in the background, i.e., object variability, is a very important factor that deteriorates the detection performance. We made an interesting observation in the performance of CHO in the presence of object variability. We saw in the presence of OV that the CHO predicts human performance without being tweaked for internal noise. To make our mathematical observer better in predicting human observer, we needed to include the quantization noise. The CHO in the SKE task acts directly on reconstructed images of continuous values, whereas, human observers act on displayed images in practice which are quantized. We saw quantization noise hardly affects the performance of the CHO.

In Chapter 6 we have observed, using 3D SPECT simulations, model observers, and a rapid means to evaluate SNR, that lesion detectability is not affected by anatomical boundary information. We extended our work by carrying out more realistic simulations involving the effect of anatomical boundaries on detection of a lesion in a 2D slice extracted from a 3D reconstruction of a 3D object. In the simulation described we assumed perfect knowledge of anatomical boundaries with no misalignments or anatomy-function resolution mismatch. We investigated whether the use of anatomical priors with organ boundaries alone or with perfect lesion boundaries alone would change lesion detectability relative to the case of a prior with no anatomical information. Furthermore, we investigated whether any such detectability changes for the organ-boundary case would be a function of the distance of the lesion to the organ boundary. We also investigated whether any detectability changes for the lesion-boundary case would be a function of the degree of proximity, i.e. a difference in the radius of the true functional lesion and the radius of the anatomical lesion boundary. Our results showed almost no detectability difference with vs without organ boundaries at any lesion-to-organ boundary distance. Our results also showed no difference in lesion detectability with and without lesion boundaries, and no variation of lesion detectability with degree of proximity.

Chapter 7 we tacked a somewhat different problem of rapid computation of covariance and lpsfs of 3D SPECT MAP reconstructions in the presence of scattered photons in the projection data. Chapters 5 and 6 dealt with controlling and predicting the effect of these noise/resolution tradeoff quantities on SKE human performance. We knew for the literature survey in Chapter 7 that the presence of scatter affects image quality. The MAP reconstruction incorporated a window-based scatter correction method TEW for modeling this scatter in the reconstruction. The scatter in the projection data was obtained using SIMSET an MC simulator. We showed that MAP reconstructions corrected for scatter was one form of a mismatched model error which increased the variance of 3D SPECT reconstructions. We developed fast theoretical expression which obviate the need of sample reconstructions for computing means and lpsf. These expressions can then be used in the computation of model observer FOMs. We validated our rapid theory results versus laborious sample methods and showed very good concordance between computations and sample methods.

We reviewed the image formation equation $\mathbf{g} = \mathrm{H}\mathbf{f} + \mathbf{n}$ and the MAP reconstruction operator $\hat{\mathbf{f}} = \mathcal{O}(\mathbf{g})$. We studied the effects of Poisson noise $\mathbf{n}$, the model mismatch between the real imaging model H and its approximation $\mathcal{H}$ used for reconstruction purposes. We also studied the effect of OV in affecting detection performance in case of human and model observers. Also Since $\mathcal{O}$ comprise a MAP algorithm we studied the effect of anatomical priors in affecting model observer SKE/BKE detection performance. Thus this was a broad study of the effects of noise resolution tradeoff, noise and reconstruction estimators in the context of SPECT “Image Quality”.

## 8.1 Future Work

### 8.1.1 Future work involving SKE task

We used the simplified non-realistic signal-known-exactly SKE detection task. For practical usage, there are several aspects we can focus on to improve our imaging system model and mathematical observer models for SKE tasks in the future. More detailed studies need to be done to take into account the more complicated geometrical factors, such as fan beam or even cone beam collimation. Long-range artifacts induced due to model mismatch in the form of inclusion/exclusion or attenuation correction and scatter correction can have an effect on lesion detectability. We would study the effects of these model errors on lesion detectability in the presence and absence of anatomical side information.

Further, in Chapter 6 each pixel belonged to a single tissue class giving rise to binary labeling of pixels. One way to compensate from misregistration errors and partial volume effects is to use "blurred" anatomical labels [132] as described in Sec. 6.1. We could show the effects of using binary as well as blurred labels to incorporate anatomical information in the MAP reconstruction in presence of either perfect or erroneous (imperfect) anatomical knowledge. Projection data of these experiments should be obtained with a Monte Carlo image generator SIMSET and the reconstruction should have imperfect knowledge of attenuation and scatter. We point out that the study discussed in Chapter 6 did not include the important feature of statistically variable backgrounds. Aside from their realism, the inclusion of background variability might lead to a change in conclusions regarding the efficacy of anatomical priors in some task contexts. Finally, Chapter 6 should obviously be extended to human observer testing. Preliminary results using human experiments with a 2AFC methodology (Barrett and Myers 2003) to measure SNR showed agreement of human and model observer for our lesion boundary experiment, but far more work is needed.

### 8.1.2 Extending the Task

While none of the studies described in Chapter 5 and 6 involved higher-order tasks, such as detection plus localization, it would be interesting to investigate the detection performance in the case of these tasks. SKE tasks are too simplistic and do not model the clinical realism of detection plus localization when the lesion location is unknown and variable. A physician in the clinic does not exactly know the lesion location and must predict the presence /or absence of the lesion along with its location within a certain appropriate search radius. In our group we have also done original work on signal-known-statistically/background-known-statistically (SKS/BKS) [28, 96, 97] but we do not discuss it in this thesis. However, we have only recently begun to apply this to practical 3D SPECT. My initial work in this area is [210], in which we address the problem of optimization and comparison of window-based scatter correction (SC) methods in SPECT for MAP (maximum *a posteriori*) reconstruction. It is a significant extension of two of our previous works [96, 155]. In [96], we introduced theory methods to rapidly evaluate performance of an observer for the task of detecting and localizing a signal in a SPECT MAP reconstruction. This had nothing to do with SC. However, in [210], we addressed the problem of formulating theoretical expressions for the additional bias and covariance (above that due to photon noise) in a SPECT MAP reconstruction that included window-based SC. Here, we extend [96] and combine it with [155] to address a problem of practical import.

This thesis has used statistical decision theory and other tools of signal processing to quantitatively analyze image quality in the medical imaging modality SPECT. Since for radiation-based imaging such as nuclear imaging and X-ray, one always tries to lower the dose of radiation administered to the patient, this starves the system of detected counts which results in the increase of quantum noise. Together with object variability and model error, this noise ensures that the reconstructed images will always be noisy and this offers challenges in Image Quality.

# References

[1] J.D. Bronzino, *The Biomedical Engineering Handbook*, CRC press and IEEE press, 1995.

[2] Z Cho, J.P. Jones, and M. Singh, *Fundamentals of Medical Imaging*, John Wiley & Sons, 1992.

[3] P.J. Early and D.B. Sodee, *Principles and Practice of Nuclear Medicine*, Mosby-Year Book, Inc, 1995.

[4] Ronald J. Jaszczak, SPECT: Single Photon Emission Computed Tomography, *IEEE Trans. Nuc. Sci.*, 27(3), pp. 1137–1153, 1980.

[5] B. Bendriem and D.W. Townsend, *The Theory and Practice of 3D PET*, Kluwer, 1998.

[6] H.H. Barrett and W. Swindell, *Radiological Imaging: The Theory of Image Formation, Detection and Processing, vol I & II*, Academic Press, 1981.

[7] H.O. Anger, Scintillation Camera, *Rev. Sci. Instrum*, 29, pp. 27–33, 1958.

[8] M.N. Wernick and J.N. Aarsvold, *Emission Tomography: The Fundamentals of PET and SPECT*, Elsevier Academic Press, 2004.

[9] Yuxiang Xing, *Rapid Calculation of Image Quality for Maximum a Posteriori Reconstructions in SPECT*, PhD thesis, State University of New York at Stony Brook, 2003.

[10] A. Rosenfeld and A. Kak, *Digital Picture Processing*, volume 1, Academic Press, New York, 1982.

[11] M.D. Maeseneer, L. Lencbik, H. Everaert, S. Marcelis, A. Bossuyt, M. Osteaux, and F. Beeckman, Evaluation of Lower Back Pain with Bone Scintigraphy and SPECT, *Radiographics*, 19(4), pp. 901–912, 1999.

[12] G.F. Gates, Bone SPECT Imaging of the Painful Back, *Clin. Nucl. Med.*, 21(7), pp. 560–571, Jul. 1996.

[13] G.F. Gates, SPECT Bone Scanning of the Spine, *Semin. Nucl. Med.*, 28(1), pp. 78–94, 1998.

[14] L.J. Han, T.K. Au-Yong, W.C. Tong, K.S. Chu, L.T. Szeto, and C.P. Wong, Comparison of Bone Single-Photon Emission Tomography and Planar Imaging in the Detection of Vertebral Metastases in Patients with Back Pain, *Eur. J. Nucl. Med.*, 25(6), pp. 635–638, 1998.

[15] B.M.W. Tsui and E.C. Frey, Three-dimensional Image Reconstruction Methods for Quantitative Myocardial Perfusion SPECT, In *Proceeding of the 20th Annual International Conference of the IEEE Engineering in Medicine and Biology Society*, volume 1, pp. 502–505, Hong Kong, 1998.

[16] R.C. Hendel, D.S. Berman, S.J. Cullom, W. Follansbee, G.V. Heller, H. Kiat, M.W. Groch, and J.J. Mahmarian, Multicenter Clinical Trial to Evaluate the Efficacy of Correction for Photon Attenuation and Scatter in SPECT Myocardial Perfusion Imaging, *Circulation*, 94, pp. 2742–2749, Dec 1999.

[17] N. Tamaki, Y. Kuge, and E. Tsukamoto, The Road to Quantitation of Regional Myocardial Uptake of Tracer, *J. Nuc. Med.*, 42(5), pp. 780–781, May 2001.

[18] K. Nakajima, J. Taki, M. Kawano, T. Higuchi, S. Sato, C. Nishijima, K. Takehara, and N. Tonami, Diastolic Dysfunction in Patients with Systemic Sclerosis Detected by Gated Myocardial Perfusion SPECT: An Early Sign of Cardiac Involvement, *J. Nuc. Med.*, 42(2), pp. 183–188, Feb. 2001.

[19] H.J. Biersack, H. Stefan, K. Reichman, B. Hunermann, K. Kuhnen, A. Bockisch, H. Penin, F.F. Knapp, and C. Winckler, Brain Imaging with $^{99m}$Tc-HMPAO SPECT, CT, and NMR Results in Epilepsy, *J. Nuc. Med.*, 27, pp. 1028, 1986.

[20] T.C. Yen, K.Y. Tzen, W.Y. Lin, W.P. Chen, and C.Y. Lin, Identification of New Renal Scanning in Repeated Episodes of Acute Pyelonephritis Using TC-99m DMSA Renel SPECT, *Clinical Nuclear Medicine*, 23(12), pp. 828–831, 1998.

[21] J. Park and S. Gambhir, Multimodality Radionuclide, Fluorescence, and Bioluminescence Small-Animal Imaging, *Proceedings of the IEEE*, 93(4), pp. 771–783, April 2005.

[22] G. Kastis, L. Furenlid, D. Wilson, T. Peterson, H. Barber, and H. Barrett, Compact CT/SPECT Small-Animal Imaging System, *IEEE Trans. Nuclear Science*, 51(1), pp. 63–67, Feb. 2004.

[23] S. R. Cherry, Y. Shao, R. W. Silverman, K. Meadors, S. Siegel, A. Chatziioannou, J. W. Young, W. Jones, J. C. Moyers, D. Newport, A. Boutefnouchet, T. H. Farquhar, M. Andreaco, M. J. Paulus, D. M. Binkley, R. Nutt, and M. E. Phelps, MicroPET: A High Resolution PET Scanner for Imaging Small Animals, *IEEE Trans. Nuclear Science*, 44, pp. 1161–1166, June 1997.

[24] G. K. Kastis, H. B. Barber, H. H. Barrett, H. C. Gifford, I. W. Pang, D. D. Patton, J. D. Sain, G. Stevenson, and D. W. Wilson, High Resolution SPECT Imager for Three-Dimensional Imaging of Small Animals, *J. Nuc. Med.*, 39(5), pp. 9P, May 1998.

[25] G. A. Kastis, M. C. Wu, S. J. Balzer, D. W. Wilson, L. Furenlid, G. Stevenson, H. H. Barrett, H. B. Barber, M. Woolfenden, P. Kelly, and M. Appleby, Tomographic Small-Animal Imaging Using a High-Resolution Semiconductor Camera, *IEEE Trans. Nuclear Science*, 49(1), pp. 172–175, Feb. 2002.

[26] M. A. Brown and R. C. Semelka, *MRI: Basic Principles and Applications*, Wiley-Liss, New York, NY, 1995.

[27] H. H. Barrett, J. Yao, J. P. Rolland, and K. J. Myers, Model Observers for Assessment of Image Quality, *Proc. Nat. Acad. Sci.*, 90, pp. 9758–9765, November 1993.

[28] P. Khurd and G. Gindi, Decision Strategies That Maximize the Area Under the LROC Curve, *IEEE Trans. Med. Imaging*, 24(12), pp. 1626–1636, Dec 2005.

[29] H.H. Barrett and K.J. Myers, *Foundations of Image Science*, John Wiley & Sons, 2004.

[30] C. K. Abbey and H. H. Barrett, Human- and Model-Observer Performance in Ramp-spectrum Noise: Effects of Regularization and Object Variability, *Journal of the Optical Society of America, A*, 18(3), pp. 473–488, March 2001.

[31] H. H. Barrett, Objective Assessment of Image Quality: Effects of Quantum Noise and Object Variability, *J. Opt. Soc. Am. A*, 7(7), pp. 1266–1278, July 1990.

[32] H. H. Barrett, C. K. Abbey, and E. Clarkson, Objective Assessment of Image Quality. III. ROC Metrics, Ideal Observers, and Likelihood-Generating Functions, *J. Opt. Soc. Am. A*, 15(6), pp. 1520–1534, June 1998.

[33] C. K. Abbey, *Assessment of Reconstructed Images*, PhD thesis, University of Arizona, 1998.

[34] M. F. Smith, M. E. Daube-Witherspoon, P. S. Plascjak, L. P. Szajek, R. E. Carson, J. R. Everett, S. L. Green, P. R. Territo, Robert S. Balaban, S. L. Bacharach, and W. C. Eckelman, Device-dependent Activity Estimation and Decay Correction of Radionuclide Mixtures with Application to Tc-94m PET Studies, *Medical Physics*, 28(1), pp. 36–45, January 2001.

[35] B. W. Reutter, G. T. Gullberg, and R. H. Huesman, Direct Least-squares Estimation of Spatiotemporal Distributions from Dynamic SPECT Projections Using a Spatial Segmentation and Temporal B-splines, *IEEE Trans. Med. Imaging*, 19(5), pp. 434–450, May 2000.

[36] R. R. Fulton, S. R. Meikle, S. Eberl, J. Pfeiffer, R. T. Constable, and J. M. Fullham, Correction for Head Movements in Positron Emission Tomography, *IEEE Trans. Nuclear Science*, 49(1), pp. 116–123, Feb. 2002.

[37] R. D. Beach, P. H. Pretorius, G. Boening, P. P. Bruyant, B. Feng, R. R. Fulton, M. A. Gennert, S. Nadella, and M. King, Feasibility of Stereo-infrared Tracking to Monitor Patient Motion during Cardiac SPECT Imaging, *IEEE Trans. Nuclear Science*, 51(5), pp. 2693–2698, Oct. 2004.

[38] D. Lalush and B. M. W. Tsui, Block-iterative Techniques for Fast 4D Reconstruction Using a Priori Motion Models in Gated Cardiac SPECT, *Phys. Med. Biol.*, 43(4), pp. 875–886, April 1998.

[39] H. C. Gifford, M. A. King, D. J. deVries, and E. J. Soares, Channelized Hotelling and Human Observer Correlation for Lesion Detection in Hepatic SPECT Imaging, *Journal of Nuclear Medicine*, 41(3), pp. 514–521, March 2000.

[40] W. Wang, *Noise Analysis of Bayesian Reconstruction Algorithms in Emission Tomography*, PhD thesis, State University of New York at Stony Brook, 1997.

[41] G. Grimmett and D. Strirzaker, *Probability and Random Process*, Oxford University Press, 2001.

[42] R M Lewitt, Alternatives to Voxels for Image Representation in Iterative Reconstruction Algorithms, *Phys. Med. Biol.*, 37(3), pp. 705–716, April 1992.

[43] W. Wang and G. Gindi, Noise Analysis of MAP-EM Reconstruction Algorithms in Emission Tomography, *Phys. Med. Biol.*, 42(11), pp. 2215–2232, 1997.

[44] U Engeland, T Striker, and H Luig, Count-Rate Statistics of the Gamma Camera, *Phys. Med. Biol.*, 43(10), pp. 2939–2947, Oct. 1998.

[45] D. Yu and J. Fessler, Mean and Variance of Singles Photon Counting with Deadtime, *Phys. Med. Biol.*, 45(7), pp. 2043–2056, 2000.

[46] M. Ljungberg, S. Strand, and M. King, *Monte Carlo Calculations in Nuclear Medicine Applications in Diagnostic Imaging*, Institute of Physics Publishing, Bristol, UK, 1998.

[47] B.M.W. Tsui, X. Zhao, E.C. Frey, and W.H. McCartney, Quantitative Single-Photon Emission Computed Tomography: Basics and Clinical Considerations, *Seminars in Nuclear Medicine*, 24(1), pp. 38–65, Jan. 1995.

[48] J.M. Boone, X-ray Production, Interaction, and Detection in Diagnostic Imaging, In J. Beutel, H.L. Kundel, and R.L. V. Metter, editors, *Handbook of Medical Imaging: volume 1. Physics and Psychophysics*, SPIE-The International Society for Optical Engineering, 2000.

[49] M. A. King, D. J. deVries, T. S. Pan, P. Pretorius, and J. Case, An Investigation of Filtering of TEW Scatter Estimates Used to Compensate for Scatter with Ordered Subset Reconstructions, *IEEE Trans. Nuclear Science*, 44(3), pp. 1140–1145023, June 1997.

[50] G. L. Zeng, G. T. Gullberg, C. Bai, P. E. Christian, F. Trisjono, E. V. R. Di Bella, J. W. Tanner, and H. T. Morgan, Iterative Reconstruction of Fluorine-18 SPECT Using Geometric Point Response Correction, *J. of Nuclear Medicine*, 39(1), pp. 124–130, Jan. 1998.

[51] C.E. Metz, F.B. Atkins, and R.N. Beck, The Geometrical Transfer Function Component for Scintillation Camera Collimators with Straight Parallel Holes, *Phys. Med. Biol.*, 25(6), pp. 1059–1070, 1980.

[52] A.R. Formiconi, Geometrical Response of Multihole Collimators, *Phys. Med. Biol.*, 43, pp. 3359–3379, 1998.

[53] F. Beekman, H. de Jong, and S. van Geloven, Efficient Fully 3-D Iterative SPECT Reconstruction with Monte Carlo-based Scatter Compensation, *IEEE Trans. Med. Imaging*, 21(8), pp. 867–877, Aug. 2002.

[54] E. Frey and B. Tsui, A New Method for Modeling the Spatially-Variant, Object-Dependent Scatter Response Function in SPECT, In *Conf. Rec. IEEE Nuc. Sci. Sym. Med. Imaging Conf.*, pp. 1082 – 1086, Nov. 1996.

[55] Y. Dewaraja, M. Ljungberg, and J. Fessler, 3-D Monte Carlo-based Scatter Compensation in Quantitative I-131 SPECT Reconstruction, In *Conf. Rec. IEEE Nuc. Sci. Sym. Med. Imaging Conf.*, IEEE, Oct. 2004.

[56] R. Leahy and J. Qi, Statistical Approaches in Quantitative Positron Emission Tomography, *Statistics and Computing*, 10, pp. 147–165, 2000.

[57] J. Llacer and E. Veklerov, Feasible Images and Practical Stopping Rules for Iterative Algorithms in Emission Tomography, *IEEE Trans. Med. Imaging*, 8(2), pp. 186–193, Jun. 1989.

[58] J. Nuyts and J. Fessler, A Penalized-Likelihood Image Reconstruction Method for Emission Tomography Compared to Postsmoothed Maximum-Likelihood With Matched Spatial Resolution, *IEEE Trans. Med. Imaging*, 22(9), pp. 1042–1052, Sep 2003.

[59] M. V. Narayanan, H. C. Gifford, M. A. King, P. H. Pretorius, T. H. Farncombe, P. Bruyant, and M. N. Wernick, Optimization of Iterative Reconstructions of $^{99m}$Tc Cardiac SPECT Studies Using Numerical Observers, *IEEE Trans. Nuc. Sci.*, 49(5), pp. 2355–2360, 2002.

[60] T. Hebert and R. Leahy, A Generalized EM Algorithm for 3-D Bayesian Reconstruction from Poisson Data using Gibbs Priors, *IEEE Trans. Med. Imaging*, 8(2), pp. 194–202, Jun 1989.

[61] S.J. Lee, A. Rangarajan, and G. Gindi, Bayesian Image Reconstruction in SPECT Using Higher Order Mechanical Models as Priors, *IEEE Trans. Med. Imaging*, 14(4), pp. 669 –680, 1995.

[62] K. Lange, M. Bahn, and R. Little, A Theoretical Study of Some Maximum Likelihood Algorithms for Emission and Transmission Tomography, *IEEE Trans. Med. Imaging*, MI-6(2), pp. 106–114, June 1987.

[63] V.E. Johnson, W.H. Wong, X. Hu, and C.T. Chen, Image Restoration Using Gibbs Priors: Boundary Modeling, Treatment of Blurring and Selection of Hyperparameter, *IEEE Trans. Pattern Analysis and Machine Intelligence*, 13(5), pp. 413–525, May 1991.

[64] W. Wang, C. Goldstein, and G. Gindi, Noise and Resolution Properties of Gamma-Penalized Likelihood Reconstruction, In *Conf. Rec. IEEE Nuc. Sci. Sym. Med. Imaging Conf.*, pp. 1136–1141, Toronto, Ontario, Canada, Nov. 1998, IEEE.

[65] S. Alenius, *On Noise Reduction in Iterative Image Reconstruction Algorithms for Emission Tomography: Median Root Prior*, PhD thesis, Tampere University of Technology, Finland, 1999.

[66] S.J. Lee, G.R. Gindi, I.G. Zubal, and A. Rangarajan, Using Ground-Truth Data to Design Priors in Bayesian SPECT Reconstruction, In Y. Bizais, C. Barillot, and R.D. Paola, editors, *Information Processing in Medical Imaging*, pp. 27–38, Kluwer Academic Publishers, 1995.

[67] S. Geman and D. Geman, Stochastic Relaxation, Gibbs Distributions, and the Bayesian Restoration of Images, *IEEE Trans. Pattern Analysis and Machine Intelligence*, 6(6), pp. 721–741, Nov. 1984.

[68] S. J. Lee, *Bayesian Image Reconstruction in Emission Computed Tomography Using Mechanical Models as Priors*, PhD thesis, State University of New York at Stony Brook, 1995.

[69] J. A. Fessler and W. L. Rogers, Spatial Resolution Properties of Penalized-Likelihood Image Reconstruction: Space-Invariant Tomographs, *IEEE Trans. Image Proc.*, 5(9), pp. 1346–1358, Sep. 1996.

[70] G. H. Golub and C. F. Van Loan, *Matrix Computation*, John Hopkins Univ. Press, 1989.

[71] E. Mumcuoglu, R. Leahy, S. Cherry, and Z. Zhou, Fast Gradient-Based Methods for Bayesian Reconstruction of Transmission and Emission PET Images, *IEEE Trans. Med. Imaging*, 13(4), pp. 687–701, December 1994.

[72] J. A. Fessler and S. C. Booth, Conjugate-Gradient Preconditioning Methods for Shift-Variant PET Image Reconstruction, *IEEE Trans. Image Proc.*, 8(5), May 1999.

[73] P. Khurd, Y. Xing, I. Hsiao, and G. Gindi, Fast Preconditioned Conjugate Gradient Reconstruction for 2D SPECT, In *Conf. Rec. IEEE Nuc. Sci. Sym. Med. Imaging Conf.*, volume 2, pp. 741–745, IEEE, Nov. 2002.

[74] A.P. Dempster, N.M. Laird, and D.B. Rubin, Maximum Likelihood for Incomplete Data Via The EM Algorithm, *Journal of the Royal Statistical Society. Series B(Methodological)*, 39(1), pp. 1–38, 1977.

[75] L.A. Shepp and Y. Vardi, Maximum Likelihood Reconstruction for Emission Tomography, *IEEE Trans. Med. Imaging*, MI-1, pp. 113–122, 1982.

[76] K. Lange and R. Carson, EM Reconstruction Algorithms for Emission and Transmission Tomography, *J. Comp. Assisted Tomography*, 8(2), pp. 306–316, Apr. 1984.

[77] A. R. De Pierro, A Modified Expectation Maximization Algorithm for Penalized Likelihood Estimation in Emission Tomography, *IEEE Trans. Med. Imaging*, 14(1), pp. 132–137, Mar. 1995.

[78] A. R. De Pierro, On the Convergence of an EM-Type Algorithm for Penalized Likelihood Estimation in Emission Tomography, *IEEE Trans. Med. Imaging*, 14(4), pp. 762–765, Dec. 1995.

[79] H. M. Hudson and R. M. Larkin, Accelerated Image Reconstruction using Ordered Subsets of Projection Data, *IEEE Trans. Med. Imaging*, 13(4), pp. 601–609, Dec. 1994.

[80] J. Browne and A. R. De Pierro, A Row-Action Alternative to the EM Algorithm for Maximizing Likelihood in Emission Tomography, *IEEE Trans. Med. Imaging*, 15(5), pp. 687–699, Oct. 1996.

[81] A. R. De Pierro and M. E. B. Yamagishi, Fast EM-like Methods for Maximum "a posteriori" Estimates in Emission Tomography, *IEEE Trans. Med. Imaging*, 20(4), pp. 280–288, April 2001.

[82] S. Ahn and J. Fessler, Globally Convergent Ordered Subsets Algorithms for Emission Tomography Using Relaxed Ordered Subsets algorithms, *IEEE Trans. Med. Imaging*, 22(5), pp. 613–626, May 2003.

[83] I. T. Hsiao, A. Rangarajan, and G. Gindi, A Provably Convergent OS-EM Like Reconstruction Algorithm for Emission Tomography, In *Conf. Rec. SPIE Med. Imaging*, volume 4684, pp. 10–19, SPIE, Feb. 2002.

[84] I. T. Hsiao, A. Rangarajan, and G. Gindi, A New Convergent MAP Reconstruction Algorithm for Emission Tomography Using Ordered Subsets and Separable Surrogates, In *Conf. Rec. IEEE Int. Symp. Biomed. Imaging*, pp. 409–412, IEEE, July 2002.

[85] A. Rangarajan, P. Khurd, I.-T. Hsiao, and G. Gindi, Convergence Proofs for the COSEM-ML and COSEM-MAP Algorithms, Technical Report MIPL-03-1, Medical Image Processing Lab, Depts. of Radiology and Electrical Engineering, State University of New York at Stony Brook. Web URL: http://www.mil.sunysb.edu/mipl/publications.html, Dec. 2003.

[86] R. Gordon, R. Bender, and G.T. Herman, Algebraic Reconstruction Techniques (ART) for Three-Dimensional Electron Microscopy and X-Ray Photography, *J. Theoretical Biology*, 29, pp. 471–481, 1970.

[87] C.L. Byrne, Block-Iterative Interior Point Optimization Methods for Image Reconstruction From Limited Data, *Inverse Problems*, 16, pp. 1405–1419, 2000.

[88] A. K. Jain, *Fundamentals of Digital Image Processing*, Prentice-Hall, Inc., 1989.

[89] W. Xia, R. M. Lewitt, and P. R. Edholm, Fourier Correction for Spatially Variant Collimator Blurring in SPECT, *IEEE Trans. Med. Imag.*, 14(1), pp. 100–115, Mar. 1995.

[90] L. T. Chang, A Method For Attenuation Correction in Radionuclide Computed Tomography, *IEEE Trans. Nuc. Sci.*, 25(1), pp. 638–643, Feb. 1978.

[91] X. He, E. C. Frey, J. M. Links, K. L. Gilland, W. P. Segars, and B. M. W. Tsui, A Mathematical Observer Study for the Evaluation and Optimization of Compensation Methods for Myocardial SPECT Using a Phantom Population That Realistically Models Patient Variability, *IEEE Trans. Nuclear Science*, 51(1), pp. 218–224, Feb. 2004.

[92] S. L. Faris, D. W. Wilson, H. H. Barrett, D. Dougherty, G. R. Gindi, and I. T. Hsiao, Using a Digital Anatomical Phantom to Optimize an Imaging System, In J. M. Boone and J. T. Dobbins, editors, *SPIE-Physics of Medical Imaging*, volume 3659, San Diego, CA, February 1999.

[93] J.P. Rolland and H.H. Barrett, Effect of Random Background Inhomogeneity on Observer Detection Performance, *J. Opt. Soc. Am. A*, 9, pp. 649–658, May 1992.

[94] J. Qi, Analysis of Lesion Detectability in Bayesian Emission Reconstruction With Nonstationary Object Variability, *IEEE Trans. Med. Imaging*, 2316(3), pp. 321–329, April 2004.

[95] J. Oldan, S. Kulkarni, Y. Xing, P. Khurd, and G. Gindi, Channelized Hotelling and Human Observer Study of Optimal Smoothing in SPECT MAP Reconstruction, *IEEE Trans. Nuclear Science*, 51(3), pp. 733–741, June 2004.

[96] P. Khurd and G. Gindi, Fast LROC Analysis of Bayesian Reconstructed Emission Tomographic Images Using Model Observers, *Phys. Med. Biol.*, 50(11), pp. 1519–1532, March 2005.

[97] P. Khurd and G. Gindi, Rapid Computation of LROC Figures of Merit Using Numerical Observers (for SPECT/PET Reconstruction), *IEEE Trans. Nuclear Science*, 52(3), pp. 518–526, June 2005.

[98] H. Van Trees, *Detection, Estimation and Modulation Theory*, John Wiley & Sons, 1968.

[99] S. Kay, *Fundamentals of Statistical Signal Processing, Volume 2: Detection Theory*, Prentice Hall, 1998.

[100] E. J. Soares, *Attenuation, Nose, and Image Quality in Single Photon Emission Computed Tomography*, PhD thesis, University of Arizona, 1994.

[101] C.E. Metz, ROC Methodology in Radiologic Imaging, *Invest. Radio*, 21, pp. 720–732, 1986.

[102] D.R. Gilland, B.M.W. Tsui, C.E. Metz, R.J. Jaszczak, and J.R. Perry, An Evaluation of Maximum Likelihood-Expectation Maximization Reconstruction for SPECT by ROC Analysis, *J. Nuc. Med.*, 33, pp. 451–457, 1992.

[103] P. Khurd, *On Reconstruction Methods and Image Quality in Emission Tomography*, PhD thesis, Dept of Electrical Engineering, State Univ. of New York at Stony Brook, Stony Brook, New York 11784, USA, August 2005.

[104] M. A. Kupinski, J. W. Hoppin, E. Clarkson, and H. H. Barrett, Ideal-Observer Compuation in Medical Imaging with Use of Markov-chain Monte Carlo Techniques, *J. Opt. Soc. Am. A*, 20(3), pp. 430–438, March 2003.

[105] X. He, B. S. Caffo, and E. C. Frey, Markov Chain Monte Carlo (MCMC) based Ideal Observer Estimation using a Parametrized Phantom and a Pre-calculated Dataset, In *Conf. Rec. SPIE Med. Imag.*, volume 6515, SPIE, Feb. 2007.

[106] A. Yendiki and J. Fessler, Analysis of Observer Performance in Known-Location Tasks for Tomographic Image Reconstruction, *IEEE Trans. Med. Imaging*, 25(1), pp. 28–41, Jan. 2006.

[107] S. D. Wollenweber, B. M. W. Tsui, D. S. Lalush, E. C. Frey, K. J. LaCroix, and G. T. Gullberg, Comparision of Hotelling Observer Models and Human Observers in Defect Detection from Myocardial SPECT Imaging, *IEEE Transactions on Nuclear Science*, 46(6), pp. 2098–2103, December 1999.

[108] S. Sankaran, E.C. Frey, K.L. Gilland, and B.M.W. Tusi, Optimum Compensation Method and Filter Cutoff Frequency in Myocardial SPECT: A Human Observer Study, *J. Nuc. Med.*, 43(3), pp. 432–438, March 2002.

[109] P. Bonetto, J. Qi, and R. M. Leahy, Covariance Approximation for Fast and Accurate Computation of Channelized Hotelling Observer Statistics, *IEEE Trans. Nuc. Sci.*, 47(4), pp. 1567–1572, Aug. 2000.

[110] C. K. Abbey, H. H. Barrett, and M. Eckstein, Practical Issues and Methodology in Assessment of Image Quality using Model Observers, In *Physics of Medical Imaging*, volume 3032, pp. 182–194, SPIE, February 1997.

[111] A. M. Zoubir and B. Boashash, The Bootstrap and Its Application in Signal Processing, *IEEE Signal Processing Magazine*, 15(1), pp. 56–76, 1998.

[112] J. A. Fessler, Mean and Variance of Implicitly Defined Biased Estimators (Such as Penalized Maximum Likelihood): Applications to Tomography, *IEEE Trans. Image Proc.*, 5(3), pp. 493–506, Mar. 1996.

[113] J. Qi and R. M. Leahy, A Theoretical Study of the Contrast Recovery and Variance of MAP Reconstructions from PET Data, *IEEE Trans. Med. Imag.*, 18(4), Apr. 1999.

[114] J. Qi and R. M. Leahy, Resolution and Noise Properties of MAP Reconstruction for Fully 3-D PET, *IEEE Trans. Med. Imag.*, 19(5), pp. 493–505, May 2000.

[115] Y. Xing, I. T. Hsiao, and G. Gindi, Rapid Calculation of Detectability in Bayesian SPECT, *Phys. Med. Biol.*, 48, pp. 3755–3773, Nov 2003.

[116] J. W. Stayman and J. Fessler, Efficient Calculation of Resolution and Covariance for Penalized-likelihood Reconstruction in Fully 3-D SPECT, *IEEE Trans. Med. Imaging*, 23(12), pp. 1543–1556, Dec. 2004.

[117] K. J. Myers and H. H. Barrett, The Addition of a Channel Mechanism to the Ideal-Observer Model, *J Opt Soc Am A*, 4, pp. 2447–2457, 1987.

[118] E. C. Frey, K. L. Gilland, and B. M. W. Tsui, Application of Task-Based Measures of Image Quality to Optimization and Evaluation of Three -Dimensional Reconstruction-Based Compensation Methods in Myocardial Perfusion SPECT, *IEEE Transactions on Medical Imaging*, 21(9), pp. 1040–1050, September 2002.

[119] J. Qi and R. Huesman, Penalized Maximum-Likelihood Image Reconstruction for Lesion Detection, *Phys. Med. Biol.*, 51, pp. 4017–4029, 2006.

[120] K. L. Gilland, Y. Qi, B. M. W. Tsui, and G. T. Gullberg, Comparison of Channelized Hotelling and Human Observers in Determining the Optimum OSEM Reconstruction Parameters for Myocardial SPECT, In *Nuclear Science Symposium and Medical Imaging Conference*, pp. M11–287, IEEE, 2003.

[121] S. D. Gilland, B. M. W. Tsui, Y. Qi, and G. T. Gullberg, Comparision of Channelized Hotelling and Human Observers in Determining Optimum OS-EM Reconstruction Parameters for Myocardial SPECT, *IEEE Transactions on Nuclear Science*, 53(3), pp. 1200–1204, June 2006.

[122] S. Kulkarni, P. Khurd, I. Hsiao, L. Zhou, and G. Gindi, A Channelized Hotelling Observer Study of Lesion Detection in SPECT MAP Reconstruction Using Anatomical Priors, *Phys. Med. Biol.*, 52(12), pp. 3601–3617, 2007.

[123] G. Gindi, M. Lee, A. Rangarajan, and G. Zubal, Bayesian Reconstruction of Functional Images Using Anatomical Information as Priors, *IEEE Trans. on Medical Imaging*, 12, pp. 670–680, Dec. 1993.

[124] P. P. Bruyant, H. C. Gifford, G. Gindi, and M. A. King, Numerical Observer Study of MAP-OSEM Regularization Methods With Anatomical Priors for Lesion Detection in $^{67}$Ga Images, *IEEE Trans. Nuclear Science*, 51(1), pp. 193–197, Feb. 2004.

[125] K. Baete, J. Nuyts, K. Van Laere, W. Van Paesschen, S. Ceyssens, L. De Ceuninck, O. Gheysens, A. Kelles, J. Van den Eynden, P. Suetens, and P. Dupont, Evaluation of Anatomy Based Reconstruction for Partial Volume Correction in Brain FDG-PET, *NeuroImage*, 23, pp. 305–317, 2004.

[126] T. Beyer, D.W. Townsend, T. Brun, P.E. Kinahan, M. Charron, R. Roddy, J. Israel, J. Jerin, J. Young, L. Byars, and R. Nutt, A Combined PET/CT Scanner for Clinical Oncology, *J. Nuc. Med.*, 41(8), pp. 1369–1379, Aug 2000.

[127] B.H. Hasegawa, T.F. Lang, J.K. Brown, E.L. Gingold, S.M. Reilly, S.C. Blankespoor, S.C. Liew, B.M.W. Tsui, and C. Ramanathan, Object-Specific Attenuation Correction of SPECT with Correlated Dual-Energy X-Ray CT, *IEEE Trans. Nuc. Sci.*, 40(4), pp. 1242–1252, Aug. 1993.

[128] H.W. Muller-Gartner, J.M. Links, J.L. Prince, R.N. Bryan, E. Mcveigh, J.P. Leal, C. Davatzikos, and J.J. Frost, Measurement of Radiotracer Concentration in Brain Gray Matter Using Positron Emission Tomography: MRI-Based Correction for Partial Volume Effects, *J. Cereb. Blood Flow Metab.*, 12(4), pp. 571–583, 1992.

[129] O. G. Rousset, Y. Ma, and A. C. Evans, Correction of Partial Volume Effects in PET: Principle and Validation, *J. Nuc. Med.*, 39(5), pp. 904–911, May 1998.

[130] C. Meltzer, J. P. Leal, H. S. Mayberg, H. N. Wagner, and J. J. Frost, Correction of PET Data for Partial Volume Effects in Human Cerebral Cortex by MR Imaging, *J. of Computer Assisted Tomography*, 14(4), pp. 561–570, July/August 1990.

[131] T. O. Videen, J. S. Perlmutter, M. A. Mintun, and M. E. Raichle, Regional Correction of Positron Emission Tomography Data for the Effects of Cerebral Atrophy, *Journal of Cerebral Blood Flow and Metabolism*, 8(5), pp. 662–670, 1988.

[132] C. Comtat, P. E. Kinahan, J. A. Fessler, T. Beyer, D. W. Townsend, M. Defrise, and C. Michel, Clinically Feasible Reconstruction of 3D Whole-Body PET/CT Data Using Blurred Anatomical Labels, *Phys. Med. Biol.*, 47(1), pp. 1–20, 2002.

[133] K. Baete, J. Nuyts, W. Van Paesschen, P. Suetens, and P. Dupont, Anatomical-Based FDG-PET Reconstruction for the Detection of Hypo-Metabolic Regions in Epilepsy, *IEEE Trans. Med. Imaging*, 23(4), pp. 510–519, April 2004.

[134] J. Nuyts, D. Beque, P. Dupont, and L. Mortelmans, A Concave Prior Penalizing Relative Differences for *Maximum-a-Posteriori* Reconstruction in Emission Tomography, *IEEE Trans. Nuclear Science*, 49(1), pp. 56–60, Feb 2002.

[135] R. Leahy and X. Yan, Incorporation of Anatomical MR Data for Improved Functional Imaging with PET, In A. C. F. Colchester and D. J. Hawkes, editors, *Information Processing in Medical Imaging*, pp. 105–120, Springer–Verlag, 1991.

[136] B. Lipinski, H. Herzog, E. Rota Kops, W. Oberschelp, and H. W. Muller-Gartner, Expectation Maximization Reconstruction of Positron Emission Tomography Images Using Anatomical Magnetic Resonance Information, *IEEE Trans. Med. Imaging*, MI-16(2), pp. 129–136, Apr. 1997.

[137] X. Ouyang, W. H. Wong, V.E. Johnson, X. Hu, and C.T. Chen, Incorporation of Correlated Structural Images in PET Image Reconstruction, *IEEE Trans. Med. Imaging*, MI-13(4), pp. 627–640, Dec. 1994.

[138] B. A. Ardekani, M. Braun, B. F. Hutton, I. Kanno, and H. Iida, Minimum Cross-Entropy Reconstruction of PET Images Using Prior Anatomical Information, *Phys. Med. Biol.*, 41(11), pp. 2497–2517, Nov. 1996.

[139] C. H. Hsu and R. Leahy, PET Image Reconstruction Incorporation Anatomical Information Using Segmented Regression, In K. Hanson, editor, *Proc. SPIE: Medical Imaging - Image Processing*, volume 3034, pp. 381–392, Newport Beach, CA, Feb. 1997, SPIE.

[140] J. Bowsher, V. Johnson, T. Turkington, R. Jaszczak, C. Floyd Jr, and R. Coleman, Bayesian Reconstruction and Use of Anatomical *a Priori* Information for Emission Tomography, *IEEE Trans. Med. Imaging*, 15(5), pp. 673–686, Oct. 1996.

[141] S. Sastry and R. E. Carson, Multimodality Bayesian Algorithm for Image Reconstruction in PET: A Tissue Composition Model, *IEEE Trans. Med. Imaging*, 16(6), pp. 750–761, Dec. 1997.

[142] A. Rangarajan, I. T. Hsiao, and G. R. Gindi, A Bayesian Joint Mixture Framework for the Integration of Anatomical Information in Functional Image Reconstruction, *Journal of Mathematical Imaging and Vision*, 12(3), pp. 199–217, June 2000.

[143] J.E. Bowsher, D.M. DeLong, T.G. Turkington, and R.J.P. Jaszczak, Aligning Emission Tomography and MRI Images by Optimizing the Emission-Tomography Image Reconstruction Objective Function, In *Conf. Rec. IEEE Nuc. Sci. Sym. Med. Imaging Conf.*, volume 4, pp. 2562–2565, Portland, OR, Oct. 2003.

[144] L.N. Trefethen and D. Bau, *Numerical Linear Algebra*, SIAM, 1997.

[145] B. M. W. Tsui, X. D. Zhao, G. K. Gregoriou, D. S. Lalush, E. C. Frey, R. E. Johnston, and W. H. P. McCartney, Quantitative Cardiac SPECT Reconstruction with Reduced Image Degradation Due to Patient Anatomy, *IEEE Trans. Nuc. Sci.*, 41, pp. 2838–2844, 1994.

[146] J. A. Terry, *A Comparison of Three Collimator Designs for Cardiac SPECT Imaging*, PhD thesis, University of North Carolina at Chapel Hill, 1992.

[147] P. H. Pretorius, M. A. King, B. M. Tsui, K. J. LaCroix, and W. Xia, A Mathematical Model of the Motion of the Heart for Use in Generating Source and Attenuation Maps for Simulating Emission Imaging, *Medical Physics*, 26(11), pp. 2323–2332, November 1999.

[148] J. Qi, Comparison of Statistical Reconstruction With Isotropic and Anisotropic Resolution in PET, *IEEE Trans. Nuclear Science*, 53(1), pp. 147–151, Feb. 2006.

[149] J. Nuyts, K. Baete, D. Beque, and P. Dupont, Comparison Between MAP and Postprocessed ML for Image Reconstruction in Emission Tomography when Anatomical Knowledge is Available, *IEEE Trans. Med. Imaging*, 24(5), pp. 667–675, May 2005.

[150] J. Qi and R. Huesman, Theoretical Study of Lesion Detectability of MAP Reconstruction Using Computer Observers, *IEEE Trans. Med. Imag.*, 20(8), pp. 815–822, 2001.

[151] P. Bruyant, H. Gifford, G. Gindi, and M. King, Investigation of Observer Perfermance in MAP-EM Reconstruction with Anatomical Priors and Scatter Correction for Lesion Detection in $^{67}$Ga Images, In *Conf. Rec. IEEE Nuc. Sci. Sym. Med. Imaging Conf.*, volume 5, pp. 3166–3169, Portland, OR, Oct. 2003.

[152] P. P. Bruyant, H. C. Gifford, G. Gindi, P. H. Pretorius, and M. A. King, Human and Numerical Observer Studies of Lesion Detection in Ga-67 Images Obtained with MAP-EM Reconstructions and Anatomical Priors, In *Proc. Nuclear Science Symposium and IEEE Medical Imaging Conference*, volume 7, pp. 4072–4075, Rome, Oct 2004.

[153] A. Lehovich, P. P. Bruyant, H. C. Gifford, G. Gindi, P. B. Schneider, S. Squires, and M. A. King, Human-Observer LROC Study of Lesion Detection in Ga-67 SPECT Images Reconstructed Using MAP with Anatomical Priors, In *Conf. Rec. IEEE Nuc. Sci. Sym. Med. Imaging Conf.*, pp. M03–5 (submitted), San Diego, Nov 2006.

[154] H. C. Gifford, P. H. Pretorius, and M. A. King, Comparison of Human- and Model-observer LROC Studies, In *Conf. Rec. SPIE Med. Imaging*, volume 5034, pp. 112–122, Feb. 2003.

[155] S. Kulkarni, P. Khurd, L. Zhou, and G. Gindi, Statistical Properties of SPECT MAP Reconstruction Incorporating Window Based Scatter Correction, *IEEE Trans. Nuclear Science*, 56(1), pp. 97–107, Feb 2009.

[156] P. Khurd, S. Kulkarni, and G. Gindi, Noise Propagation from Scatter Correction in SPECT MAP Reconstruction, In *Proc 8th Intl Meeting on Fully Three-Dimensional Image Reconstruction in Radiology and Nuclear Medicine*, pp. 97–100, F. Noo, H. Kudo, L. Zeng, Eds., July 2005.

[157] H. Zaidi and K. Koral, Scatter Modelling and Compensation in Emission Tomography, *Eur. J. Nucl. Med. Mol. Imaging*, 31(5), pp. 761–781, May 2004.

[158] H. Zaidi, *Quantitative Analysis in Nuclear Medicine Imaging*, Springer, 2006.

[159] R. J. Jaszczak, K. L. Greer, and C. E. Floyd, Jr., Improved SPECT Quantification Using Compensation for scattered Photons, *J. Nuc. Med.*, 25, pp. 893–900, 1984.

[160] D. Gagnon, A. Todd-Pokropek, A. Arsenaualt, and G. Dupras, Introduction to Holospectral Imaging in Nuclear Medicine for Scatter Subtraction, *IEEE Trans. Med. Imaging*, 8(3), pp. 245–250, Sept. 1989.

[161] K. F. Koral, X. Wang, L. Rogers, N. Clinthrone, and X. Wang, SPECT Compton-Scattering Correction by Analysis of Energy Spectra, *J. Nuc. Med.*, 29, pp. 195–202, 1988.

[162] K. Ogawa, Y. Harata, T. Ichihara, A. Kubo, and S. Hashimoto, A Practical Method for Position-dependent Compton-scatter Correction in Single Photon Emission CT, *IEEE Trans. Med. Imaging*, 10(3), pp. 408–412, Sep. 1991.

[163] X. Wang and K. Koral, A Regularized Deconvolution-Fitting Method for Compton-Scatter in SPECT, *IEEE Trans. Med. Imaging*, 11(3), pp. 351–360, Sept. 1992.

[164] M. A. King, G. J. Hademenos, and S. J. Glick, A Dual-Photopeak Window Method for Scatter Correction, *J. Nuc. Med.*, 33, pp. 605–612, 1992.

[165] P. H. Pretorius, A. J. van Rensburg, A. van Aswegen, M. G. Lotter, D. E. Serfontein, and C. P. Herbst, The Channel Ratio Method of Scatter Correction for Radionuclide Image Quantitation, *J. Nuc. Med.*, 34, pp. 330–335, 1992.

[166] D. R. Haynor, M. S. Kaplan, R. S. Miyaoka, and Thomas K. Lewellen, Multiwindow Scatter Correction Techniques in Single-Photon Imaging, *Medical Physics*, 22(12), pp. 2015–2024, December 1995.

[167] K. Ogawa and N. Nishizaki, Accurate Scatter Compensation using Neural Networks in Radionuclide Imaging, *IEEE Trans. Nuclear Science*, 40(4), pp. 1020–1025, June 1993.

[168] G. E. Fakhri, S. C. Moore, and P. Maksud, A New Scatter Compensation Method for Ga-67 Imaging Using Artificial Neural Networks, *IEEE Trans. Nuclear Science*, 48(3), pp. 799–804, June 2001.

[169] M. Ljungberg, M.A. King, G.J. Hademenos, and S.E. Strand, Comparison of Four Scatter Correction Methods Using Monte Carlo Simulated Source Distributions, *J. Nuc. Med.*, 35, pp. 143–151, 1994.

[170] I. Buvat, M. Rodrigues-Villafuerte, A. Todd-Pokropek, H. Benali, and R. Di Paola, Comparative Assessment of Nine Scatter Correction Methods Based on Spectral Analysis Using Monte Carlo Simulations, *J. Nuc. Med.*, 36, pp. 1476–1488, 1995.

[171] S. Moore, M. Kijewski, S. Mueller, F. Rybicki, and R. Zimmerman, Evaluation of Scatter Compensation Methods by their Effects on Parameter Estimation from SPECT Projections, *Medical Physics*, 28(2), pp. 278–287, February 2001.

[172] C. Bai, G. L. Zeng, and G. T Gullberg, A Slice-by-Slice Blurring model and Kernel Evaluation Using the Klein-Nishina Formula for 3D Scatter Compensation in Parallel and Converging Beam SPECT, *Phys. Med. Biol.*, 45(5), pp. 1275–1307, May 2000.

[173] J. Xiao, T. C. de Wit, S. G. Staelens, and F. J. Beekman, Evaluation of 3D Monte Carlo-Based Scatter Correction for $^{99m}$Tc Cardiac Perfusion SPECT, *J. Nuc. Med.*, 47, pp. 1662–1669, 2006.

[174] D.J. Kadrmas, E.C. Frey, S.S. Karimi, and B.M.W. Tsui, Fast Implementations of Reconstruction-Based Scatter Compensation in Fully 3D SPECT Image Reconstruction, *Phys. Med. Biol.*, 43, pp. 857–873, 1998.

[175] Y. Dewaraja, M. Ljungberg, and J. Fessler, 3-D Monte Carlo-based Scatter Compensation in Quantitative I-131 SPECT Reconstruction, *IEEE Trans. Nuclear Science*, 53, pp. 181–188, Feb. 2006.

[176] S. R. Meikle, B. F. Hutton, and D. L. Bailey, A Transmission Dependent Method for Scatter Correction in SPECT, *J. Nuc. Med.*, 35, pp. 360–367, 1994.

[177] Y. Narita, S. Eberl, H. Iida, B. Hutton, M. Braun, T. Nakamura, and G. Bautovich, Monte Carlo and Experimental Evaluation of Accuracy and Noise Properties of Two Scatter Correction Methods for SPECT, *Phys. Med. Biol.*, 41, pp. 2481–2496, 1996.

[178] M.V. Narayanan, P. H. Pretorius, S. T. Dahlberg, J. A. Leppo, N. Botkin, J. Krasnow, W. Berndt, E. Frey, and M. King, Evaluation of Scatter Compensation Strategies and Their Impact on Human Detection Performance in Tc-99m Myocardial Perfusion Imaging, *IEEE Trans. Nuclear Science*, 50(5), pp. 1522–1527, 2003.

[179] T. Farncombe, H. C. Gifford, M. Narayanan, H. Pretorius, E. Frey, and M. A. King, Assessment of Scatter Compensation Strategies for Ga-67 SPECT Using Numerical Observers and Human LROC Studies, *J. Nuc. Med.*, 45(5), pp. 802–812, May 2004.

[180] T. Ichihara, K. Ogawa, N. Motomura, A. Kubo, and S. Hashimoto, Compton Scatter Compensation Using the Triple-Energy Window Method for Single and Dual Isotope SPECT, *J. Nuc. Med.*, 34, pp. 2216–2221, 1993.

[181] J. Bong, H. Son, J. D. Lee, and H. Kim, Improved Scatter Correction for SPECT Images: A Monte Carlo Study, *IEEE Trans. Nuclear Science*, 52(5), pp. 1263–1270, Feb. 2005.

[182] M. H. Bourguignon, M. Wartski, H. Berrah, H. Valette, M. Crouzel, B. Bendriem, J. Delforge, and A. Syrota, A Scatter Correction Method from Spectral Imaging over Standard Acquisition Energy Window, *J. Nuc. Med.*, 33, May 1992, p. 888.

[183] X. Li, G. Han, H. Lu, L. Li, and Z. Liang, A New Scatter Estimation Method Using Triple Energy Window Acquisition to Fit Energy Spectrum, *J. Nuc. Med.*, 42, 2001, Abstract 194P.

[184] J. Qi and R. Huesman, Scatter Correction for Positron Emission Mammography, *Phys. Med. Biol.*, 42(15), pp. 2759–2771, Aug. 2002.

[185] J. Qi and R. Huesman, A Theoretical Study of the Penalized-Likelihood Image Reconstruction for Region-of-Interest Quantification, *IEEE Trans. Med. Imag.*, 25(5), May 2006.

[186] S. Ahn and R. M. Leahy, Analysis of Region-of-Interest Quantification for PET Image Reconstruction with Selective Regularization., In *Conf. Rec. IEEE Nuc. Sci. Sym. Med. Imaging Conf.*, pp. 1781–1786, Oct. 2006.

[187] M. Tamal, P. Markiewicz, P. Julyan, D. Hastings, and A. Reader, Impact of Scatter Modeling Error in 3D Maximum Likelihood Reconstruction in PET, In *Conf. Rec. IEEE Nuc. Sci. Sym. Med. Imaging Conf.*, pp. M14–213, IEEE, Oct. 2006.

[188] K. F. Koral, F. M. Swailem, S. Buchbinder, N. H. Clinthorne, W. L. Rogers, and B. M. W. Tsui, SPECT Dual-Energy-Window Compton Correction: Scatter Multiplier Required for Quantification, *J. Nuc. Med.*, 31, pp. 90–98, 1990.

[189] J.Q. Luo, K.F. Koral, M. Ljungberg, C.E. Floyd, and R.J. Jaszczak, A Monte Carlo Investigation of Dual-Energy-Window Scatter Correction for Volume-Of-Interest Quantification in $^{99m}$Tc SPECT, *Phys. Med. Biol.*, 40(1), pp. 181–199, Jan. 1995.

[190] Y. Dewaraja, L. Jia, and K. Koral, Quantitative $^{131}$I SPECT with Triple Energy Window Compton Scatter Correction, *IEEE Trans. Nuclear Science*, 45(6), pp. 3109–3114, Aug. 1998.

[191] P. Maksud, B. Fertil, C. Rica, G. El Fakhri, and A. Aurengo, Artificial Neural Network as a Tool to Compensate for Scatter and Attenuation in Radionuclide Imaging, *J. Nuc. Med.*, 39, pp. 735–745, 1998.

[192] D. Gagnon, N. Pouliot, and L. Laperriere, Statistical and Physical Content of Low-Energy Photons in Holospectral Imaging, *IEEE Trans. Med. Imaging*, 10(3), pp. 284–289, Sept. 1991.

[193] B. Axelsson, P. Msaki, and A. Israelson, Subtraction of Compton Scattered Photons in Single Photon Emission Computed Tomography, *J. Nuc. Med.*, 25, pp. 490–494, 1984.

[194] P. Msaki, B. Axelsson, C.M. Dahl, and S.A. Larsson, Generalized Scatter Correction Method in SPECT Using Point Scatter Distribution Functions, *J. Nuc. Med.*, 28(12), pp. 1861–1869, 1987.

[195] D.L. Bailey and S.R. Meikle, A Convolution-Subtraction Scatter Correction Method for 3D PET, *Phys. Med. Biol.*, 39, pp. 411–424, 1994.

[196] M. Ljungberg and Sven-Erik Strand, Scatter and Attenuation Correction in SPECT Using Density Maps and Monte Carlo Simulated Scatter Functions, *J. Nuc. Med.*, 31, pp. 1560–1567, 1990.

[197] M. Ljungberg and Sven-Erik Strand, Attenuation and Scatter Correction in SPECT for Sources in a Nonhomogeneous Object: A Monte Carlo Study, *J. Nuc. Med.*, 32, pp. 1278–1284, 1991.

[198] A. Welch, G. T. Gullberg, P. E. Christian, and F. L. Datz, A Transmission-Map-Based Scatter Correction Technique for SPECT in Inhomogeneous Media, *Med. Phys.*, 22, pp. 1627–1635, 1995.

[199] M. Shidahara, H. Watabe, K. M. Kim, T. Kato, S. Kawatsu, R. Kato, K. Yoshimura, Hidehiro Iida, and Kengo Ito, Development of a Practical Image-Based Scatter Correction Method for Brain Perfusion SPECT: Comparison with the TEW Method, *Eur. J. Nucl. Med. Mol. Imaging*, 31(10), pp. 1193–1198, Sept. 2005.

[200] H. M. Deloar, H. Watabe, K. M Kim, T. Aoi, E. Kunieda, H. Fujii, and H. Iida, Optimization of the Width of the Photopeak Energy Window in the TDCS Technique for Scatter Correction in Quantitative SPECT, *IEEE Trans. Nuclear Science*, 51(3), pp. 625–630, 2004.

[201] G. L. Zeng, C. Bai, and G. T. Gullberg, A Projector/Backprojector with Slice-to-Slice Blurring for Efficient Three-Dimensional Scatter Modeling, *IEEE Trans. Med. Imaging*, 18, pp. 722–732, 1999.

[202] D. J. Kadrmas, E. C. Frey, and B. M. W. Tsui, Application of Reconstruction-Based Scatter Compensation to Thallium-201 SPECT: Implementations for Reduced Reconstruction Noise, *IEEE Trans. Med. Imaging*, 17(3), pp. 325–333, June 1998.

[203] H. W. de Jong, E. T. Slijpen, and F. J. Beekman, Acceleration of Monte Carlo SPECT Simulation Using Convolution-Based Forced Detection, *IEEE Trans. Nuclear Science*, 48, pp. 58–64, 2001.

[204] M. Narayanan, M. King, P. Pretorius, S. Dahlberg, F. Spencer, E. Simon, E. Ewald, E. Healy, K. MacNaught, and J. Leppo, Human-Observer Receiver-Operating-Characteristic Evaluation of Attenuation, Scatter, and Resolution Compensation Strategies for 99mTc Myocardial Perfusion Imaging, *J. Nuc. Med.*, 44, pp. 1725–1734, 2003.

[205] D. de Vries, M. A. King, E. J. Soares, B. M.W. Tsui, and C. E. Metz, Effects of Scatter Subtraction on Detection and Quantitation in Hepatic SPECT, *J. Nuc. Med.*, 40(6), pp. 1011–1023, June 1999.

[206] F.J. Beekman, C. Kamphuis, and E.C. Frey, Scatter Compensation Methods in 3D Iterative SPECT Reconstruction: A Simulation Study, *Phys. Med. Biol.*, 42, pp. 1619–1632, 1997.

[207] T. Farncombe, H. C. Gifford, M. Narayanan, E. Frey, and M. A. King, A Comparison of Triple Energy Window Scatter Compensation Methods for Ga-67 Tumor Imaging, *J. Nuc. Med.*, 43, 2002, Abstract 54P.

[208] S. Ahn and J. A. Fessler, Emission Image Reconstruction for Randoms-Precorrected PET Allowing Negative Sinogram Values, *IEEE Trans. Med. Imaging*, 23(5), pp. 591–601, May 2004.

[209] R. L. Harrison, S. D. Vannoy, D. R. Haynor, S. B. Gillispie, M. S. Kaplan, and T. K. Lewellen, Preliminary Experience with the Photon History Generator Module of a Public-Domain Simulation System for Emission Tomography, In *Conf. Rec. IEEE Nuc. Sci. Sym. Med. Imaging Conf.*, pp. 1154 – 1158, 1993.

[210] S. Kulkarni, P. Khurd, G. Gindi, and L. Zhou, Rapid Optimization of SPECT Scatter Correction Using Model LROC Observer, In *Conf. Rec. IEEE Nuc. Sci. Sym. Med. Imaging Conf.*, pp. 3986–3993, Honolulu, Oct. 2007.